

UNIVERSIDADE FEDERAL DE MINAS GERAIS
Escola de Engenharia
Programa de Pós-graduação em Engenharia Elétrica

Rafael Mario da Silva

**CONTRIBUTION OF FULL CONVERTER WIND TURBINES TO POWER
SYSTEM DURING LOW VOLTAGE RIDE THROUGH**

Belo Horizonte
2024



UNIVERSIDADE FEDERAL DE MINAS GERAIS - UFMG

ESCOLA DE ENGENHARIA

GRADUATE PROGRAM IN ELECTRICAL ENGINEERING

Rafael Mario da Silva.

**CONTRIBUTION OF FULL CONVERTER WIND TURBINES TO POWER SYSTEM DURING LOW
VOLTAGE RIDE THROUGH**

Thesis presented to the Graduate Program in Electrical Engineering at the Universidade Federal de Minas Gerais, as a part of requirements for obtaining the degree of Doctor in Electrical Engineering.

Supervisor: Prof. Dr. Victor Flores Mendes,

Co-supervisor: Prof. Dr. Clodualdo Venicio de Sousa,

Co-supervisor: Prof. Dr. Ivan Paulo de Faria.

Belo Horizonte,
2024

S586c	<p>Silva, Rafael Mario da.</p> <p><i>Contribution of full converter wind turbines to power system during low voltage ride through</i> [recurso eletrônico] / Rafael Mario da Silva. – 2024.</p> <p>1 recurso online (162 f. : il., color.) : pdf.</p> <p>Orientador: Victor Flores Mendes. Coorientador: Clodualdo Venicio de Sousa. Coorientador: Ivan Paulo de Faria.</p> <p>Tese (doutorado) – Universidade Federal de Minas Gerais, Escola de Engenharia.</p> <p>Apêndices: f. 131-162.</p> <p>Bibliografia: f. 119-130.</p> <p>1. Engenharia elétrica – Teses. 2. Energia elétrica – Qualidade – Monitoração – Teses. 3. Eletrônica de potência – Teses. 4. Energia eólica – Teses. 5. Turbina eólica – Teses. I. Mendes, Victor Flores. II. Sousa, Clodualdo Venicio de. III. Faria, Ivan Paulo de. IV. Universidade Federal de Minas Gerais. Escola de Engenharia. V. Título.</p>
	CDU: 621.3(043)



UNIVERSIDADE FEDERAL DE MINAS GERAIS

**"CONTRIBUTION OF FULL CONVERTER WIND TURBINES TO POWER SYSTEM
DURING LOW VOLTAGE RIDE THROUGH"**

RAFAEL MARIO DA SILVA

Tese de Doutorado submetida à Banca Examinadora designada pelo Colegiado do Programa de Pós-Graduação em Engenharia Elétrica da Escola de Engenharia da Universidade Federal de Minas Gerais, como requisito para obtenção do grau de Doutor em Engenharia Elétrica. Aprovada em 23 de maio de 2024. Por:

Prof. Dr. Victor Flores Mendes
DEE (UFMG) - Orientador

Prof. Dr. Clodualdo Venicio de Sousa
UNIFEI - Coorientador

Prof. Dr. Ivan Paulo de Faria
UNIFEI - Coorientador

Prof. Dr. Danilo Iglesias Brandão
DEE (UFMG)

Prof. Drª. Maria Helena Murta Vale
DEE (UFMG)

Prof. Dr. Heverton Augusto Pereira
UFV

Prof. Dr. Tiago de Sá Ferreira
UNIFEI



Documento assinado eletronicamente por **Victor Flores Mendes, Professor do Magistério Superior**, em 23/05/2024, às 12:15, conforme horário oficial de Brasília, com fundamento no art. 5º do [Decreto nº 10.543, de 13 de novembro de 2020](#).



Documento assinado eletronicamente por **Heverton Augusto Pereira, Usuário Externo**, em 24/05/2024, às 16:51, conforme horário oficial de Brasília, com fundamento no art. 5º do [Decreto nº 10.543, de 13 de novembro de 2020](#).

Documento assinado eletronicamente por **Maria Helena Murta Vale, Membro de comissão**,



em 27/05/2024, às 12:40, conforme horário oficial de Brasília, com fundamento no art. 5º do [Decreto nº 10.543, de 13 de novembro de 2020](#).



Documento assinado eletronicamente por **Clodualdo Venicio de Sousa, Usuário Externo**, em 27/05/2024, às 15:52, conforme horário oficial de Brasília, com fundamento no art. 5º do [Decreto nº 10.543, de 13 de novembro de 2020](#).



Documento assinado eletronicamente por **Danilo Iglesias Brandao, Professor do Magistério Superior**, em 28/05/2024, às 15:37, conforme horário oficial de Brasília, com fundamento no art. 5º do [Decreto nº 10.543, de 13 de novembro de 2020](#).



Documento assinado eletronicamente por **Ivan Paulo de Faria, Usuário Externo**, em 04/06/2024, às 11:58, conforme horário oficial de Brasília, com fundamento no art. 5º do [Decreto nº 10.543, de 13 de novembro de 2020](#).



Documento assinado eletronicamente por **Tiago de Sá Ferreira, Usuário Externo**, em 10/06/2024, às 17:51, conforme horário oficial de Brasília, com fundamento no art. 5º do [Decreto nº 10.543, de 13 de novembro de 2020](#).



A autenticidade deste documento pode ser conferida no site https://sei.ufmg.br/sei/controlador_externo.php?acao=documento_conferir&id_orgao_acesso_externo=0, informando o código verificador 3254512 e o código CRC **13B19399**.

Acknowledgements

Primeiro, gostaria de agradecer a Deus, por me dar a oportunidade de acordar todos os dias, a oportunidade de cometer erros e acertos e aprender a partir deles. Agradecer por me permitir conhecer pessoas boas e ruins que, de uma forma ou de outra, me ajudam a tornar uma pessoa melhor, um dia após o outro.

Agradeço a minha família, especialmente a minha mãe Edilene por ter dedicado sua vida pelo meu irmão e por mim, por ter lutado para que eu tivesse uma educação e me ensinado o valor de lutar por aqueles que amamos, apesar das adversidades da vida. Obrigado Mãe por ser o pilar da minha existência e sua dedicação incondicional para comigo, jamais terei como retribuir.

Gostaria de agradecer a meus amigos da Universidade Federal de Itajubá. Agradeço ao Prof. Waner Wodson, Prof. Guilherme Monteiro, aos senhores Modesto, Caetano, Jhonathan e Antônio e também a minha amiga Gleicimares Mas um agradecimento especial ao Moisés Gonçalves e ao Prof. Geovane Reis pelo suporte e conselhos, eles que me aturam desde a graduação e me mostraram o significado de uma amizade verdadeira.

Agradeço também aos meus amigos da Universidade Federal de Minas Gerais, Lucas Santana, André (Badaia), Adilson e todos aqueles que me auxiliaram nesta jornada.

Agradeço aos meus professores do SENAI Daniel e Eugênio por terem me ensinado o amor pela engenharia elétrica.

También quiero expresar un agradecimiento especial a la Ingeniera Natalia Sánchez, quien durante un corto pero intenso período de este doctorado fue un gran apoyo y compañía. Su dedicación, inteligencia y amor por la ingeniería y, especialmente, por las personas, fueron una gran inspiración. Espero que esta determinación y amor siempre te acompañen, a pesar de los obstáculos de la vida. Gracias, Natalia, tus palabras y consejos siempre estarán en mi mente y corazón, tu es la mejor.

Por fim, gostaria de agradecer meus orientadores Prof. Ivan, mas principalmente aos professores Clodualdo e Frederico, obrigado por terem acreditado em mim, por seus auxílios e conselhos desde o começo de tudo.

A todos, meu eterno agradecimento.

“We must all do the best we can in whatever situation we’re in. Never give up.”
Stephen Hawking in interview to StarTalk/National Geographic Channel in 2018

Resumo

Nos últimos anos, a integração de fontes de energia renovável na matriz energética global tem sido impulsionada tanto por questões econômicas quanto ambientais, destacando-se as tecnologias eólica e solar fotovoltaica. Essas tecnologias dependem da eletrônica de potência para sua integração com a rede elétrica, diferenciando-as dos sistemas convencionais, principalmente quanto ao desempenho durante afundamentos momentâneos de tensão, comumente conhecidos como eventos de "*Low Voltage Ride Through*" (LVRT). Em comparação com os geradores síncronos, os conversores eletrônicos possuem limitações devido às características dos dispositivos semicondutores, mas apresentam maior flexibilidade na síntese de corrente. Este estudo foca na tecnologia de turbinas eólicas com conversores de potência plena, devido a maior robustez frente a distúrbios. Para melhorar o desempenho operacional dessa tecnologia durante afundamentos de tensão, o objetivo deste trabalho é propor um algoritmo de saturação de potência ativa que priorize as seguintes tarefas: primeiro, atender aos requisitos do código de rede; segundo, limitar a corrente do conversor ao seu valor nominal; terceiro, produzir potência ativa; e, sempre que possível, compensar oscilações de potência instantâneas durante faltas assimétricas. Investigou-se o impacto das oscilações instantâneas de potência nos conversores eletrônicos e os efeitos da mitigação dessas oscilações, através da injeção de correntes de sequência negativa, no suporte de tensão e na operação do sistema elétrico de potência durante transitórios. As proposições apresentadas neste estudo foram avaliadas por meio de estudos de caso utilizando simulações computacionais de sistemas reais. Inicialmente, examinou-se a implementação do algoritmo proposto em um sistema de geração de 2,1[MVA], e posteriormente em uma fazenda eólica de 73,5[MVA] integrada ao sistema padrão de 9 barras WSCC. Os modelos e resultados mostraram que anular oscilações instantâneas de potência ativa não só beneficia o conversor eletrônico, reduzindo o estresse nos dispositivos semicondutores e capacitores, como também permite reduzir o desequilíbrio entre as tensões durante faltas assimétricas.

Palavras-chave: afundamentos de tensão, conversores eletrônicos de potência, geração eólica, injeção de corrente reativa, qualidade da energia, suporte de tensão, *voltage ride through*.

Abstract

In recent years, the integration of renewable energy sources into the global energy matrix has been driven by both economic and environmental factors, highlighting wind and solar photovoltaic technologies. These technologies rely on power electronics for their integration with the electrical grid, distinguishing them from conventional systems, particularly regarding performance during momentary voltage sags, commonly known as Low Voltage Ride Through (LVRT) events. Compared to synchronous generators, electronic converters have limitations due to the characteristics of semiconductor devices, but they offer greater flexibility in current synthesis. This study focuses on wind turbine technology with full power converters due to their greater robustness against disturbances. To improve the operational performance of this technology during voltage sags, the objective of this work is to propose an active power saturation algorithm that prioritizes the following tasks: firstly, to meet grid code requirements; secondly, to limit the converter current to its nominal value; thirdly, to produce active power; and whenever possible, to compensate for instantaneous power oscillations during asymmetric faults. The impact of instantaneous power oscillations on electronic converters and the effects of mitigating these oscillations through the injection of negative sequence currents on voltage support and power system operation during transients were investigated. The propositions presented in this study were evaluated through case studies using computational simulations of real systems. Initially, the implementation of the proposed algorithm in a 2.1 MVA generation system was examined, and subsequently in a 73.5 MVA wind farm integrated into the standard WSCC 9-bus system. The models and results showed that canceling instantaneous active power oscillations not only benefits the electronic converter by reducing stress on semiconductor devices and capacitors but also helps reduce voltage imbalance during asymmetric faults.

Keywords: grid-connected converters, power quality, reactive current injection, voltage sag, voltage support, voltage ride through, wind energy.

Figure list

Fig. 1.1: Brazilian energy production in (a) 2011 and (b) 2022.....	21
Fig. 1.2: Deutschland energy production in (a) 2011 and (b) 2023.....	21
Fig. 1.3: Wind energy cost per kWh corrected for 2019 for different countries.....	22
Fig. 1.4 WEC system Type III - Double Fed Induction Generator (DFIG) diagram	23
Fig. 1.5: WEC system Type IV - Full-scale converter block diagram	24
Fig. 1.6: Onshore wind farm simple diagram.....	26
Fig. 1.7: Spain typical week (May 05 of 2019) day (a) demand and (b) generation hourly curve.	28
Fig. 1.8: Voltage limits requirements for different grid codes	30
Fig. 1.9: Reactive Current Injection requirements for different grid codes	31
Fig. 1.10: VDE ARN 4120 requirement of reactive current injection	34
Fig. 2.1: Grid voltage vector representation trajectory.....	44
Fig. 2.2: BPSC current trajectory in stationary reference frame and instantaneous power (a), (b) for $u = 0,182$ and (c), (d) for $u = 0,333$	46
Fig. 2.3: APOC current trajectory in stationary reference frame and instantaneous power (a), (b) for $u = 0,182$ and (c), (d) for $u = 0,333$	47
Fig. 2.4: RPOC current path in stationary frame and instantaneous power (a), (b) for $u = 0,182$ and (c), (d) for v	48
Fig. 2.5: AARC current path in stationary reference frame and instantaneous power (a), (b) for $u = 0,182$ and (c), (d) for $u = 0,333$	49
Fig. 2.6: PNSC current path in stationary reference frame and instantaneous power (a), (b) for $u = 0,182$ and (c), (d) for $u = 0,333$	51
Fig. 2.7: PARPC (a) active and (b) reactive power oscillation magnitude for coefficients $kp = -kq$	54
Fig. 2.8: PARPC (a) active and (b) reactive power oscillation magnitude for coefficients $kp = kq$	55
Fig. 2.9: (a) active and (b) reactive instantaneous and average power in positive and negative sequencies for AARC strategy with $P^* = 0.6[\text{pu}]$ and $Q^* = 0.8[\text{pu}]$ and $u = 0.3333$	58
Fig. 2.10: (a) active and (b) reactive instantaneous and average power in positive and negative sequencies for PNSC strategy with $P^* = 0.6[\text{pu}]$ and $Q^* = 0.8[\text{pu}]$ and $u = 0.3333$	58

Fig. 2.11: (a) active and (b) reactive instantaneous and average power in positive and negative sequencies for BPSC strategy with $P^* = 0.6[\text{pu}]$ and $Q^* = 0.8[\text{pu}]$ and $u = 0.3333$	58
Fig. 2.12: (a) active and (b) reactive instantaneous and average power in positive and negative sequencies for APOC strategy with $P^* = 0.6[\text{pu}]$ and $Q^* = 0.8[\text{pu}]$ and $u = 0.3333$	59
Fig. 2.13: (a) active and (b) reactive instantaneous and average power in positive and negative sequencies for APOC strategy with $P^* = 0.6[\text{pu}]$ and $Q^* = 0.8[\text{pu}]$ and $u = 0.3333$	59
Fig. 2.14: Instantaneous power flow.	60
Fig. 3.1: Grid Side Converter elements.	63
Fig. 3.2: Grid Side Converter control loops.	64
Fig. 3.3: Grid code voltage ride through operation.	65
Fig. 3.4: Active power curtailment algorithm flowchart	71
Fig. 3.5: Grid Side Converter elements.	73
Fig. 3.6: Simulation diagram	76
Fig. 3.7: (a) mains voltage profile for algorithm evaluation and (b) resulting positive sequence voltage and unbalance factor (values normalized by the converter rated voltage).	77
Fig. 3.8: (a) reference currents generated by the proposed algorithm and (b) mains currents for BPSC (values normalized by the converter rated current).	78
Fig. 3.9: (a) DC bus voltage and (b) mains active and reactive power for BPSC (values normalized by the converter rated parameters).	78
Fig. 3.10: (a) reference currents generated by the proposed algorithm and (b) mains currents for APOC (values normalized by the converter rated current).....	79
Fig. 3.11: (a) DC bus voltage and (b) mains active and reactive power for APOC (values normalized by the converter rated parameters).	79
Fig. 3.12: (a) reference currents generated by the proposed algorithm and (b) mains currents for RPOC (values normalized by the converter rated current).....	80
Fig. 3.13: (a) DC bus voltage and (b) mains active and reactive power for RPOC (values normalized by the converter rated parameters).	80
Fig. 3.14: Start sag GSC overcurrent for (a) APOC, (b) RPOC and (c) BPSC (values normalized by the converter rated current).....	81
Fig. 3.15: Start sag DC bus overvoltage for (a) APOC, (b) RPOC and (c) BPSC (values normalized by the converter DC bus setpoint).....	81
Fig. 3.16: Example of voltage change for several simulations (values normalized by the converter rated voltage).....	82

Fig. 3.17: Positive sequence active and reactive reference currents magnitudes for different operating points (values normalized by the converter rated current).....	82
Fig. 3.18: Voltage profile for simulations results, $ v _+ = 0.6[\text{pu}]$ and $u = 0.333$ (values normalized by the converter rated voltage).....	83
Fig. 3.19: BPSC (a) mains currents profile instantaneous (b) active and (c) reactive power for $ v _+ = 0.6[\text{pu}]$ and $u = 0.3333$ (values normalized by the converter rated parameters).....	84
Fig. 3.20: BPSC DC bus (a) capacitor current spectrum and (b) voltage for $ v _+ = 0.6[\text{pu}]$ and $u = 0.3333$ (values normalized by the converter rated parameters).....	85
Fig. 3.21: APOC (a) mains currents profile instantaneous (b) active and (c) reactive power for $ v _+ = 0.6[\text{pu}]$ and $u = 0.3333$ (values normalized by the converter rated parameters).....	85
Fig. 3.22: APOC DC bus (a) capacitor current spectrum and (b) voltage for $ v _+ = 0.6[\text{pu}]$ and $u = 0.3333$. (values normalized by the converter rated parameters).....	86
Fig. 3.23: RPOC (a) mains currents profile instantaneous (b) active and (c) reactive power for $ v _+ = 0.6[\text{pu}]$ and $u = 0.3333$. (values normalized by the converter rated parameters).....	87
Fig. 3.24: RPOC DC bus (a) capacitor current spectrum and (b) voltage for $ v _+ = 0.6[\text{pu}]$ and $u = 0.3333$. (values normalized by the converter rated parameters).....	87
Fig. 3.25: Conduction losses in the (a) diode and (b) IGBT for $ v _+ = 0.6[\text{pu}]$ and $u = 0.3333$. (values normalized by the converter nominal losses).....	88
Fig. 3.26: Comparisons of DC bus capacitors (a) 120[Hz] current ripple and (b) average voltage oscillations magnitude (values normalized by the converter rated parameters).....	89
Fig. 3.27: Comparisons of (a) diode and (b) IGBT average conduction losses (values normalized by the converter nominal losses)	89
Fig. 4.1: Effects of reactance and voltage on active power transfer limit.	92
Fig. 4.2: Synchronous generator model for unbalanced short-circuit analysis.	94
Fig. 4.3: Simplified representation of point of generator connection during an unbalanced sag.	96
Fig. 4.4: (a) positive and (b) negative sequence voltage and current vectors projections	99
Fig. 4.5: (a) wind generator and power system short circuit equivalent circuit and (b) Thevenin equivalent circuit in relation to the point of fault.....	100
Fig. 4.6: (a) Phase-to-ground, (b) phase-to-phase and (c) phase-to-phase-to-ground circuits.	101
Fig. 4.7: Modified 9 Bus WSCC power system.	102

Fig. 4.8: WEC currents during the fault for (a) BPSC, (b) APOC and (c) RPOC (values normalized by the wind generator rated current).....	104
Fig. 4.9: WECS instantaneous power during the fault for (a) BPSC, (b) APOC and (c) RPOC (Values normalized by the wind generator rated power).	104
Fig. 4.10: WECS (a) positive, (b) negative and (c) unbalance factor for different power control strategies. (Values normalized by the grid converter rated voltage).....	105
Fig. 4.11: Bus 11 instantaneous real power during the fault for (a) BPSC, (b) APOC and (c) RPOC (Values normalized by the wind generator rated power).....	106
Fig. 4.12: Bus 11 average voltage magnitude for different power control strategies (Values normalized by the wind generator rated power).....	106
Fig. 4.13: Moving average active power during the fault for generator at (a) bus 1, (b) bus 2 and (c) bus 3 (Values normalized by the respective generator nominal apparent power).....	107
Fig. 4.14: Moving average reactive power during the fault for generator at (a) bus 1, (b) bus 2 and (c) bus 3 (Values normalized by the respective generator nominal apparent power).....	107
Fig. 4.15: Angular opening of (a) bus 2 and (b) bus 3 for different power control strategies (angle values in reference to bus 1 (slack bus)).....	108
Fig. 4.16: Generators average voltage at (a) bus 1, (b) bus 2 and (c) bus 3 for different power control strategies (Values normalized by the respective generator rated voltage).....	109
Fig. 4.17: WEC average (a) active and (b) reactive power during the fault for different power control strategies (Values normalized by the converter rated power).....	109
Fig. 4.18: Generator at bus 1 short-circuit current for (a) BPSC, (b) APOC and (c) RPOC. (Values normalized by the generator rated current).....	110
Fig. 4.19: Generator at bus 2 short-circuit current for (a) BPSC, (b) APOC and (c) RPOC. (Values normalized by the generator rated current).....	110
Fig. 4.20: Generator at bus 3 short-circuit current for (a) BPSC, (b) APOC and (c) RPOC. (Values normalized by the generator rated current).....	111
Fig. 4.21: WEC (a) positive, (b) negative and (c) unbalance factor for different power control strategies changing the location of wind farm. (Values normalized by the grid converter rated voltage).....	113
Fig. 4.22: WEC average (a) active and (b) reactive power during the short-circuit. (Values normalized by the generator nominal power).....	113
Fig. 4.23: Synchronous generator at bus 3 average (a) active and (b) reactive power during the short-circuit. (Values normalized by the generator nominal power).....	114

Fig. A.1: (a) voltages and (b) reference currents in natural frame, (c) active and (d) reactive instantaneous power for IARC strategy.....	132
Fig. A.2: Harmonic distortion for (a) $u = 0.182$, (b) $u = 0.333$ and (c) $u = 0.571$ using IARC strategy.	132
Fig. A.3: Current and voltage vector path during the voltage sag for (a) $u = 0.182$, (b) $u = 0.333$ and (c) $u = 0.571$ for IARC strategy.....	133
Fig. A.4: (a) voltages and (b) reference currents in natural frame, (c) active and (d) reactive instantaneous for ICPS strategy.....	134
Fig. A.5: Harmonic distortion for (a) $u = 0.182$, (b) $u = 0.333$ and (c) $u = 0.571$ instantaneous for ICPS strategy.	135
Fig. A.6: Current and voltage vector path during the voltage sag for (a) $u = 0.182$, (b) $u = 0.333$ and (c) $u = 0.571$ for ICPS strategy.....	136
Fig. B.1: Generic control loop	137
Fig. B.2: Open loop control frequency response	138
Fig. B.3: Second order system temporal characteristic response	139
Fig. B.4: Resonant controller frequency response.....	142
Fig. B.5: Bilinear mapping of s-plane in z-plane.	143
Fig. B.6: Discrete time PI controller block diagram.....	144
Fig. B.7: Discrete time PI controller block diagram with anti-wind-up diagram.....	145
Fig. C.1: IGBT losses	150
Fig. C.2: Diode losses.....	150
Fig. C.3: ESR vs. frequency and permissible current ripple characteristic of a dielectric capacitor.....	152
Fig. C.4: Dielectric losses quantities graphical definition.....	152
Fig. C.5: Hysteresis control diagram.	153
Fig. C.6: PWM control diagram.	154
Fig. C.7: DC bus (a) voltage and (b) capacitors' current spectrum for chopper hysteresis control (values normalized by the converter rated values).....	155
Fig. C.8: DC bus (a) voltage and (b) capacitors' current spectrum for chopper PWM control (values normalized by the converter rated values)	156
Fig. D.1: WSCC 9-bus system single line diagram.....	160

Table list

Tab. 1.1: Comparison between voltage ride through from different transmission system operators	30
Tab. 1.2: Comparison of RCI requirement from GCs	31
Tab. 2.1: Relationship of PARPC and sinusoidal power control strategies	52
Tab. 2.2: Instantaneous power oscillation magnitude for different power control strategies ..	56
Tab. 2.3: Comparative summary of the sinusoidal reference currents power control strategies.	
.....	61
Tab. 4.1: Negative sequence voltage support for different power control strategies.	98
Tab. 4.2: Set points of power system generators.....	102
Tab. 4.3: Set points of power system generators.....	103
Tab. 4.4: WEC systems reactive power references for regulating the voltage at bus 11 in 1.03[pu] (values normalized by converter rated values)	112
Tab. 5.1: Summary results of power oscillation impact on the grid power converter.....	117
Tab. 5.2: Summary results of power control strategies on power system	118
Tab. C.1: Chopper components parameters	154
Tab. D.1: 2.1[MW] WEC system parameters	157
Tab. D.2: 2.1[MW] WEC system controllers' parameters	158
Tab. D.3: Transmission line (TL) parameters	158
Tab. D.4: Power transformer parameters.....	158
Tab. D.5: Wind farm medium voltage feeder.....	159
Tab. D.6: Wind generators interface transformer parameters	159
Tab. D.7: Bus 1 synchronous generator parameters	160
Tab. D.8: Bus 2 synchronous generator parameters	161
Tab. D.9: Bus 3 synchronous generator parameters	161
Tab. D.10: DC1A excitation system (AVR) parameters	161
Tab. D.11: 9-bus system transmission lines parameters.....	161
Tab. D.12: 9-bus system transmission lines parameters (zero sequency)	162
Tab. D.13: Generators' transformers parameters	162
Tab. D.14: 9-bus system loads parameters	162

List of acronyms

AARC	Average Active and Reactive Control
APCS	Adaptable power control strategies
APOC	Active Power Oscillation Cancels
AVR	Automatic Voltage Regulator
BPSC	Balanced Positive Sequence Control
DFIG	Double Fed Induction Generators
DSOGI	Double Second Order Generalized Integrator
ENTSOE	European Network of Transmission System Operators for Electricity
GC	Grid Codes
GSC	Grid-Connected Converters
GU	Generating unit
LVRT	Low Voltage Ride Through
MAV	moving average filters
MSC	Machine Side Converter
PARPC	Pliant Active and Reactive Power Control
PCC	Point of common coupling
PGC	Point of generator connection
PI	Proportional-integral
PIR	Proportional-Integral-Resonant
PLL	Phase Locked Loop
PNSC	Positive Negative Sequence Control
PNSE	Positive-Negative Sequence Extractor
POC	Point of connection
PWM	Pulse Width Modulation
RCI	Reactive Current Injection
RPOC	Reactive Power Oscillation Cancels
RPP	Renewable Power Plants
SRF-PLL	Synchronous reference frame Phase-locked loop
TSO	Transmission System Operator
VDE	Verband Deutscher Elektroingenieure

WECS Wind Energy Conversion System
WF Wind Farm

Summary

Chapter 1: Introduction	20
1.1 Renewable power generation scenario	20
1.2 Wind energy conversion technologies.....	22
1.2.1 WEC systems type III (DFIG)	23
1.2.2 WEC systems type IV (Full-scale converters).....	24
1.2.3 Wind power plants	26
1.3 Operational challenges with non-synchronous sources	27
1.4 Grid Codes and Voltage Ride Through	29
1.4.1 The provision of negative sequence currents and new scenario of RCI.....	32
1.5 Literature review and the state of art	35
1.5.1 The evolution of power control strategies and current saturation	36
1.6 Objectives	39
1.6.1 Specific objectives	40
1.7 Methodology	40
1.8 Thesis organization	41
Chapter 2: Power Control Strategies.....	42
2.1 Voltage sags in stationary reference frame	42
2.2 Instantaneous power oscillations	44
2.3 Power control strategies.....	45
2.3.1 Balanced Positive Sequence Control (BPSC).....	46
2.3.2 Active Power Oscillation Cancels (APOC)	47
2.3.3 Reactive Power Oscillation Cancels (RPOC)	48
2.3.4 Average Active and Reactive Control (AARC)	49
2.3.5 Positive Negative Sequence Control (PNSC)	50
2.4 Adaptable or flexible power control strategies (APCS)	50
2.5 Magnitude of instantaneous power oscillations	52
2.6 Power flow of the control strategies	57
2.7 Chapter conclusions	60
Chapter 3: Grid-connected converters	62
3.1 Full-power (Type IV) wind energy conversion systems	62

3.2 GSC control	63
3.3 Active power curtailment algorithm	64
3.3.1 Mathematical formulation for strategies with negative sequence currents.....	66
3.3.2 Mathematical formulation for strategies with only positive sequence	69
3.3.3 Algorithm description	70
3.4 Power oscillation impacts on the grid converter.....	72
3.4.1 Active power oscillations and DC capacitors losses	72
3.5 Simulation results	75
3.5.1 Algorithm evaluation	76
3.5.2 Analysis in different operational points.....	82
3.5.3 Power oscillations impact on the grid converters.	83
3.6 Chapter conclusions	89
Chapter 4: Voltage Support.....	91
4.1 Synchronous generators.....	91
4.1.1 Transient response	91
4.1.2 Short circuit response.....	93
4.2 VDE AR N 4120 and instantaneous power oscillations	93
4.3 Voltage support.....	95
4.3.1 Voltage support provided by the power control strategies.	97
4.3.2 Understanding the reactive power flow in negative sequence.....	98
4.4 Short-circuit contribution of full-power converters.....	99
4.5 Simulations results.....	101
4.5.1 WF located at 50% of TL6-9	103
4.5.2 Short-circuit contribution.....	109
4.5.3 Changing the WF location.	111
4.6 Chapter conclusion	114
Chapter 5: Conclusions	116
5.1.1 Thesis conclusions	116
5.1.2 Author publications.....	118
5.2 Work continuity	118
References.....	119
Appendix A: Non-sinusoidal Power Control Strategy	131

A.a Instantaneous active and reactive control (IARC)	131
A.b Instantaneously controlled positive sequence (ICSP).....	133
Appendix B: Modeling and Control	137
B.a Control Loop transfer function.....	137
B.b Proportional-Integral controller tuning	140
B.c Resonant controller tuning	141
B.d Controller discretization.....	142
B.d.i Proportional-integral controller discretization	143
B.d.ii Anti-wind-up implementation.....	144
B.d.iii Resonant controller discretization.....	145
B.e GSC modelling	145
B.e.i GSC current control loop	146
B.e.ii DC voltage control loop	146
B.e.iii Reactive power control loop	147
B.f Appointments.....	148
Appendix C: WEC losses and breaking chopper.....	149
C.a Semiconductor losses	149
C.b DC bus capacitors losses	150
C.b.i Power losses in DC capacitors	151
C.c Braking chopper	152
C.c.i Hysteresis control	153
C.c.ii PWM control.....	153
C.d Simulations results	154
C.d.i Hysteresis control.....	154
C.d.ii PWM control.....	155
Appendix D: WEC and Power System Data	157
D.a Wind energy conversion system data.....	157
D.b Wind farm (WF).....	157
D.c WSSC 9-bus System	159

Chapter I

INTRODUCTION

RENEWABLE energy sources, such as wind and solar power, have been experiencing rapid growth in electrical power systems worldwide. This surge is primarily driven by economic and environmental factors. Nevertheless, the high integration of these non-synchronous energy sources poses various operational challenges, which will be thoroughly discussed in this study. The objective of this chapter is to provide an overview of present worldwide energy scenarios, as well as to outline the motivations and objectives of this research.

1.1 Renewable power generation scenario

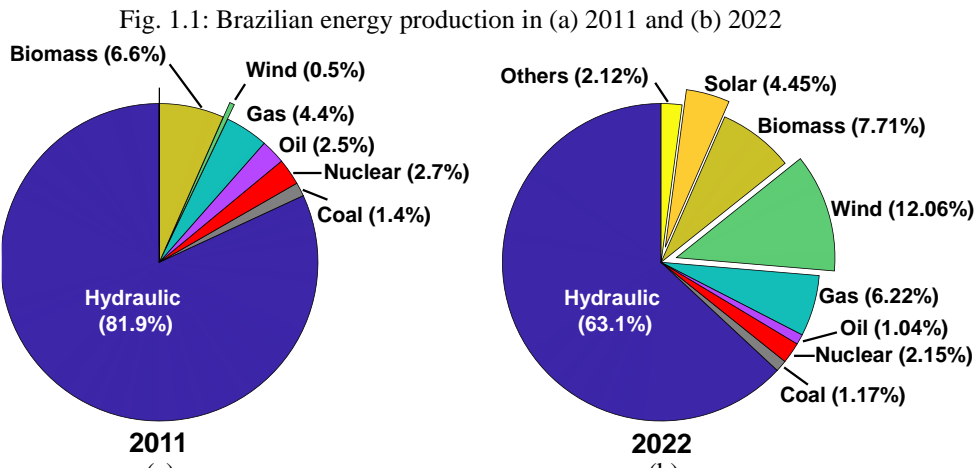
Over the past decade, there has been a notable increase in the integration of non-conventional electrical energy generation, with a significant emphasis on wind and photovoltaic technologies. These investments in alternative sources are primarily driven by the goal of sustainable development and the reduction of pollutant emissions. However, the quest for diversification in the energy matrix is not solely motivated by environmental concerns.

In Brazil, the electrical energy matrix, which is predominantly reliant on hydraulic generation, has faced challenges during various periods of drought. Additionally, fluctuations in commodity prices, such as oil and gas on the international market, have further spurred the adoption of alternative generation resources. Consequently, the share of wind energy in Brazil's energy matrix has risen remarkably from 0.5% to 12% between 2012 and 2023 (EPE, 2012, 2023). This significant increase is evident from the comparison of Brazilian energy generation in 2011 and 2022 depicted in Fig. 1.1.

In Germany, the government initiated a policy to phase out nuclear power following the 2011 nuclear accident at the Fukushima Power Plant in Japan. This policy shift has led to substantial investments in alternative energy sources (APPUNN, 2021; WNA, 2021). As a result, the contribution of wind energy to Germany's energy matrix has increased from 9.3% in 2011 to 32.2% in 2023 (ISE, [s.d.]), as shown in Fig. 1.2. Consequently, Germany has

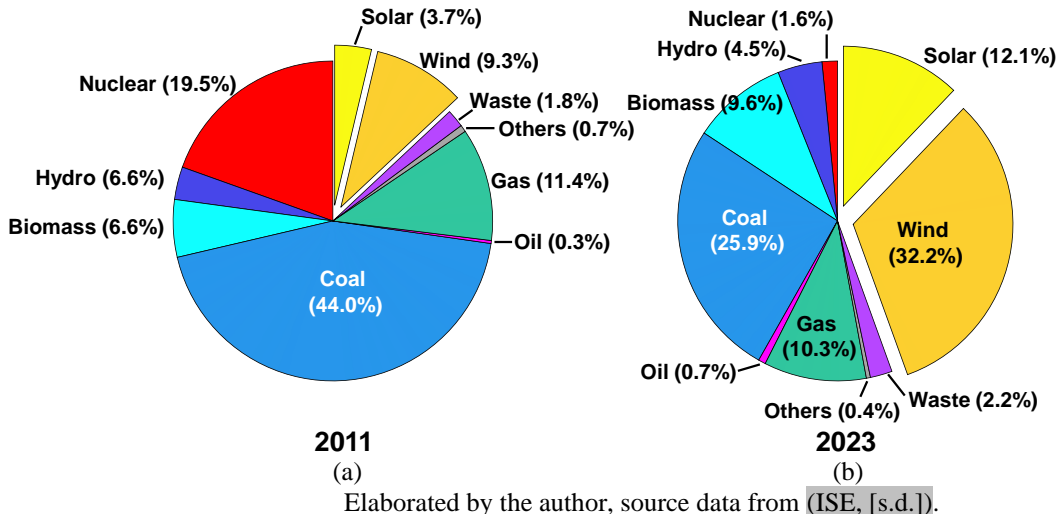
emerged as one of the European countries with the highest proportion of wind energy in its energy matrix (APPUNN, 2021; WNA, 2021).

In this context, government investments not only facilitate the diversification of the energy matrix but also promote the development of technologies and the reduction of costs associated with these projects. As illustrated in Fig. 1.3, the cost of wind power generation systems has significantly decreased over time, dropping from values exceeding 0.12[USD/kWh] to values below 0.08[USD/kWh] within the last decade.

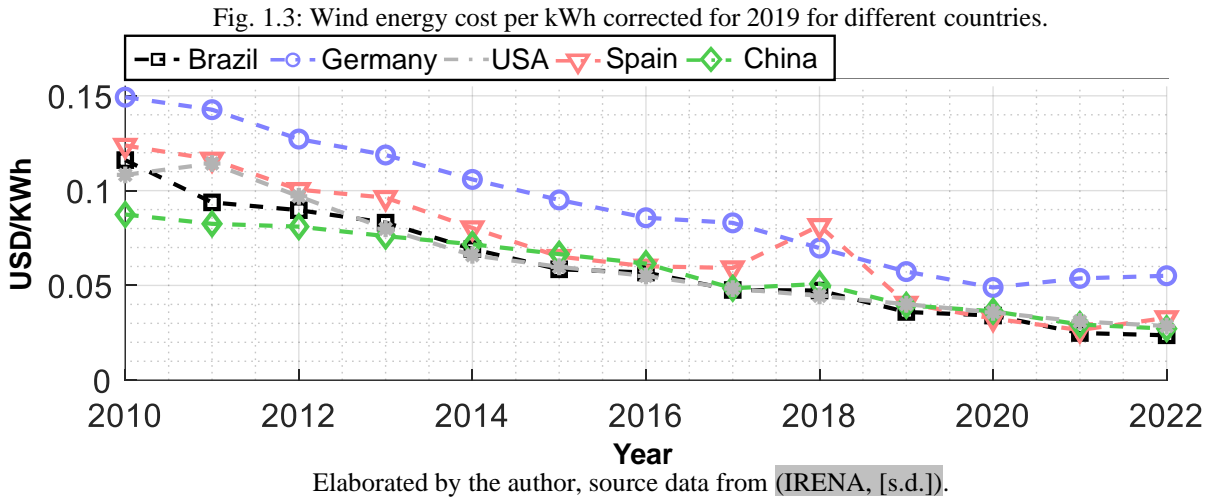


Elaborated by the author, source data from (EPE, 2012, 2023).

Fig. 1.2: Deutschland energy production in (a) 2011 and (b) 2023.



Elaborated by the author, source data from (ISE, [s.d.]).



1.2 Wind energy conversion technologies.

Still within the subject of technological development, according to the European Network of Transmission System Operators for Electricity (ENTSOE), Wind Energy Conversion (WEC) systems can be classified into four types based on their frequency control technology (ENTSOE, 2019):

- **Type I:** Utilizes squirrel cage induction generators with the stator connected to the grid via a step-up transformer. The turbine speed is regulated by the grid frequency, generating active power when the turbine shaft rotates faster than the grid frequency (negative slip).
- **Type II:** Employs wound rotor induction generators where speed is controlled through a variable resistor in the rotor circuit and the stator is connected to the grid via a step-up transformer. This resistor regulates currents to maintain a constant power output within specific wind speed conditions.
- **Type III:** Involves wound rotor induction generators where the rotor circuit connects to the grid through an AC-DC-AC (back-to-back) power electronics converter.
- **Type IV:** Features a machine completely isolated from the grid through a full power electronics converter.

It should be noted that wind energy generation technologies either use induction machines or the generator is isolated from the mains through a power electronic converter. In each case, the generator operates asynchronously from the electrical grid and in some literature, WEC are also referred to as non-synchronous sources or generators, and this nomenclature will also be employed on this work.

Originally, type I and II technologies were the predominant choices in wind generation due to their simplicity and low cost, mainly attributed to their lack of reliance on power electronics (POLINDER, 2011). However, as non-synchronous generators became integrated into grid codes (GCs), wind generation systems underwent significant development to meet stringent requirements and optimize energy conversion. These advances have surpassed the capabilities of type I and II technologies, and they will not be addressed in this work.

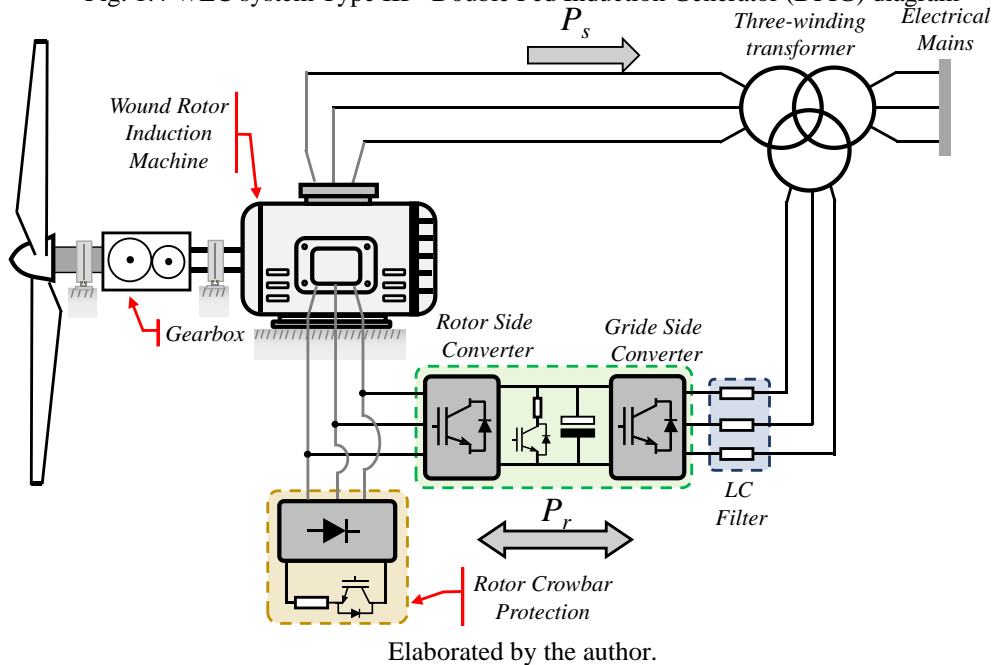
In contrast, type III and IV wind turbines, which are based on power electronics, not only enable more optimized wind energy conversion but also offer greater flexibility in supporting the electrical system and meeting the requirements established by the GCs.

1.2.1 WEC systems type III (DFIG)

WEC systems of type III, illustrated in Fig. 1.4, also referred as Double Fed Induction Generators (DFIG), feature a configuration where the stator of a wound rotor induction machine is directly connected to the mains, while the rotor currents are controlled by a back-to-back converter.

The rotor windings are accessed through slip rings and brushes, and by controlling the rotor currents and employing a gearbox to adapt the wind turbine speed to the rotation on the machine shaft, the generator can vary its speed within a range of approximately $\pm 30\%$ around the grid frequency (WANG et al., 2019). This capability enables the system to extract maximum power over a wider range of wind speeds.

Fig. 1.4 WEC system Type III - Double Fed Induction Generator (DFIG) diagram



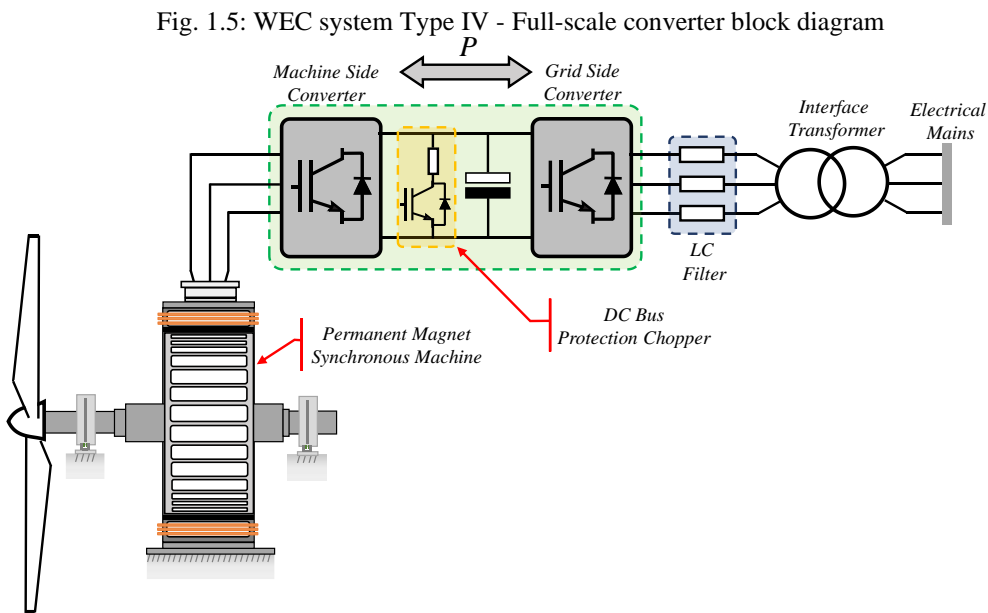
Elaborated by the author.

The main advantage of DFIG technology is the utilization of power electronics converters that are sized for a portion of the generator's rated power, resulting in cost reduction compared to type IV WEC (MENDES et al., 2015; PENA; CARDENAS; ASHER, 2013).

However, the direct connection of the induction machine stator to the mains makes it more vulnerable to power quality disturbances and make difficulties the compliance with grid codes (GCs) (SOUED; RAMADAN; BECHERIF, 2019). Additionally, the incorporation of gearboxes and slip rings reduces the average time between maintenance intervals (ISSAADI; HEMSAS; SOUALHI, 2023). Thus, type III wind turbines are being replaced by more resilient technologies that employ full-scale converters, especially in offshore power plants where wind turbines are difficult to access (RAJENDRAN et al., 2022).

1.2.2 WEC systems type IV (Full-scale converters)

In WEC systems of type IV, the power flow between the generator and the mains is accomplished by a full-power converter, as depicted in Fig. 1.5. and it is composed of the following subsystems:



Elaborated by the author.

- **Grid-Side Converter (GSC):** Typically, this component takes the form of a bidirectional active rectifier featuring two or more voltage levels. The GSC serves as the primary interface between the wind energy conversion (WEC) system and the electrical mains.
- **Machine-Side Converter (MSC):** The MSC is responsible for control and extraction of active power from the generator. It exhibits notable variability across different

manufacturers, which may encompass passive rectifiers combined with DC-DC converters or active rectifiers with multiple voltage levels.

- **DC Bus and Protection Chopper:** This set of components plays a pivotal role in the converter's operation. Its primary function is to assist the power equilibrium between the generator and the power dispatched to the grid, absorbing short-term surplus energy when the grid-side converter is unable to transmit the entirety of the generated power.

The full-power converter decouples the short-term dynamic response of the machine from the electrical mains. As a result, transient phenomena in the grid do not immediately affect the generator, enhancing reliability and simplifying the control in comparison to DFIG systems (SOUED; RAMADAN; BECHERIF, 2019).

Moreover, the power converters offers enhanced control flexibility over grid currents compared to DFIG systems (JIABING HU et al., 2015). The current control flexibility provides the opportunity to deploy diverse strategies aimed at mitigating the impacts of power quality while minimizing adverse effects on the turbine's mechanical components.

Another aspect of type IV wind turbines is the selection of the primary source generator. Since the machine operates isolated from the mains, there is a significant flexibility on its selection, although synchronous machines are predominantly used due to their higher efficiency compared to induction ones. Furthermore, synchronous machines can be designed with a larger number of poles, enabling them to operate at low speeds and eliminating the need for gearboxes (SILVA et al., 2018), which also allows for operation across a wider range of speeds and torque levels (ENTSOE, 2019).

Nonetheless, it must be taken into account that the elements that form the converter must be sized to support values greater than the generator power, resulting in an increase in both the implementation costs and the volume of the energy conversion system to values much higher than those observed for DFIG systems of similar power (SOUED; RAMADAN; BECHERIF, 2019).

Despite these disadvantages, type IV wind turbines will be the focus of this study because they are an increasingly expanding technology and present interface characteristics with the grid similar to photovoltaic generators and high-voltage direct current (HVDC) transmission systems, so the development of this work can be easily expanded to these technologies.

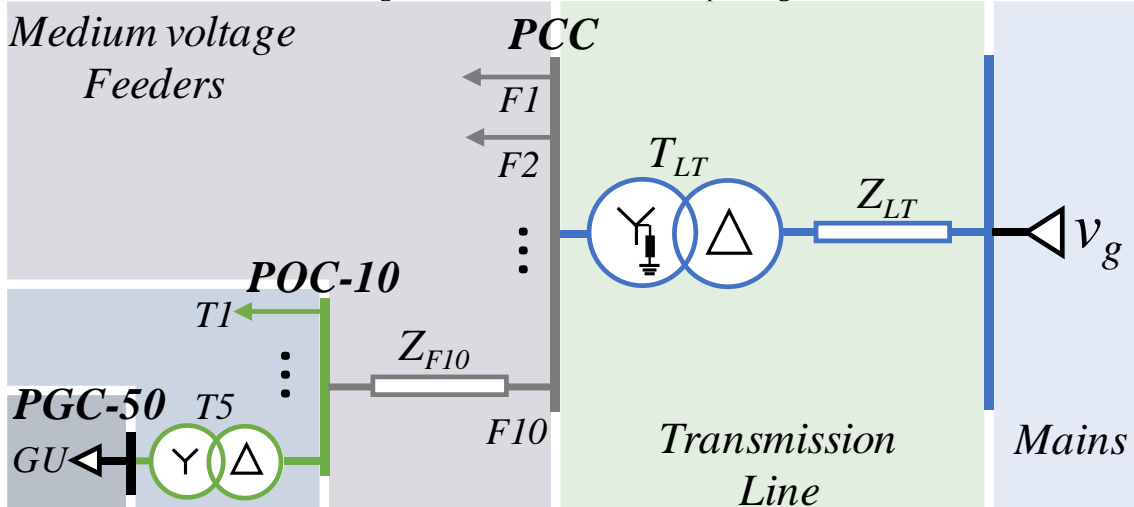
1.2.3 Wind power plants

The development of wind energy generation technologies is not only observed in the wind turbines themselves but also in the wind farms (WF) facilities, and currently, two types of assemblies are prevalent: onshore structures, where turbines are located on dry land, and offshore structures, where wind turbines are installed at sea.

Offshore WF have a significant advantage over onshore ones due to the efficiency and lower intermittency of the primary source, since there is minimal physical interference from the environment on the wind flow. However, their main disadvantages are the high implementation and maintenance costs, given the complexity of the structure and the challenging accessibility of their locations (DESALEGN et al., 2023).

This study will focus on the conventional structure of onshore wind farms, which a basic structure is illustrated in Fig. 1.6, because they are most common facility. The point of common coupling (PCC) serves as the interface connection between the WF and the transmission lines. A power transformer is utilized at the PCC, often employing a delta-wye configuration with a grounded neutral (Dyg), ensuring the separation of the WF and system grounding (CAMM et al., 2009) and connecting the WF to the mains through a transmission line with impedance Z_{LT} .

Fig. 1.6: Onshore wind farm simple diagram



- **PGC** – Point of Generator Connection

- **POC** – Point of Connection

- **PCC** – Point of Common Coupling.

Elaborated by the author.

Within the power plant, there exists a medium voltage grid comprising line feeders, denoted by impedances Z_{Fx} , where $x \in \{0,1,2, \dots, n\}$ and n is the number of feeders. These

feeders typically employ underground cables (MULJADI et al., 2013), connecting the point of connection (POC) of the generating units to the PCC. Finally, the point of generator connection (PGC) is linked to the POC via a transformer, responsible for stepping down the medium voltage to the levels required at the wind generator terminals.

1.3 Operational challenges with non-synchronous sources

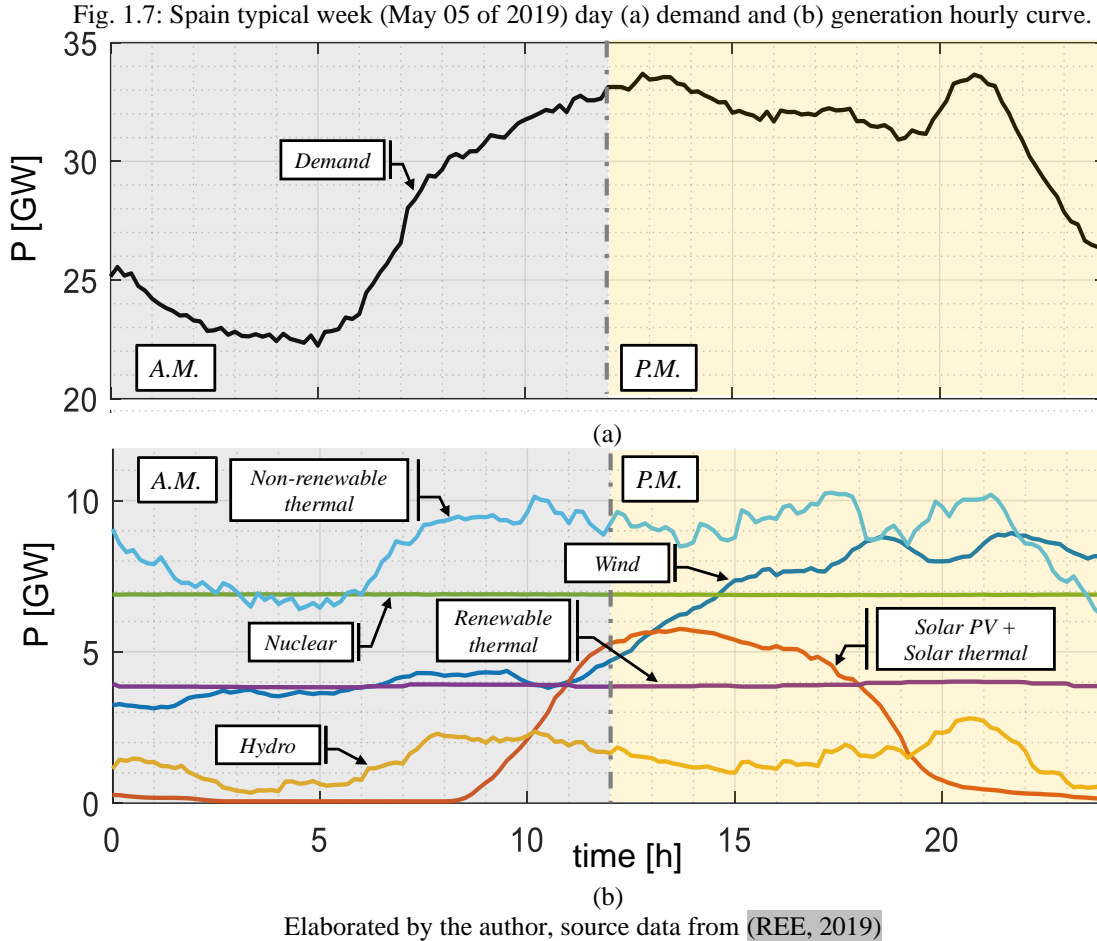
While renewable energy sources such as wind and solar offer significant environmental and economic benefits, they also introduce operational challenges related to the characteristics of the primary resource and the physical limitations of power electronic converters. The issues caused by these sources to the electrical power system can be categorized into two main areas of study: the impacts on small signal stability and the impacts on transient stability.

Small signal stability refers to the electrical power system's ability to remain stable in the face of continuous disturbances caused by small variations in load and/or generation. These disturbances can arise from a lack of damping or an inability to maintain the system's energy balance (ENTSOE, 2017). This relationship is elucidated through equation (1.1), which describes system frequency variations as a function of the active power generated (P_g) and the power demand (P_d), where f_n is the nominal frequency, and H is a constant time related to the system inertia (KARBOUJ; RATHER, 2019).

$$\frac{df}{dt} = (P_g - P_d) \cdot \frac{f_n}{2H}, \quad (1.1)$$

Unlike thermal and hydraulic sources, solar irradiation and wind speed exhibit stochastic patterns and have low forecast accuracy, and it is not possible to store these primary resources, consequently, the energy dispatch control is limited (QUAN; SRINIVASAN; KHOSRAVI, 2015). Then, the power balance of wind and photovoltaics changes continuously, rather than stepwise with an hourly schedule (DEETJEN; RHODES; WEBBER, 2017), resulting in greater variations in the terms P_d and P_g of (1.1).

Fig. 1.7 presenting a typical weekday in Spain in 2019, where wind and solar energy contributed 21.4% and 5.7% to the generated capacity in that year, respectively. This example illustrate how the integration of non-dispatchable sources leads to a mismatch between generation and demand, necessitating continuous compensation (TOLMASQUIM, 2016). Despite the capacity of other sources to absorb energy variations, this doesn't happen instantaneously, and the fluctuations in energy production result in-frequency variations (BU et al., 2012; KAUSHAL; HERTEM, 2019; QUINTERO et al., 2014)



Elaborated by the author, source data from (REE, 2019)

In relation to transient stability, it refers to the power system's capacity to maintain operation in the face of large disturbances, where the system response is no longer linear. Such disturbances or faults include short-circuits, sudden transmission line openings, or the loss of large blocks of load or generators (KUNDUR; BALU; LAUBY, 1994; SHAIR et al., 2021), and their effects are perceived by the generators through sudden variations in voltage and/or frequency at their terminals.

The resilience of type III and IV wind turbines during faults is constrained by the physical limitations of the power electronic converters. In the early days of wind resource integration, regulations were not well-defined, the wind turbines could be disconnected from the electrical mains (HIREMATH; MOGER, 2020). However, as WECS began contributing a significant portion of the energy supply, substantial energy losses occurred near fault locations, resulting in deteriorating power system frequency and/or voltage (HIREMATH; MOGER, 2020). These local energy losses triggered a cascade effect, causing generators in other areas to disconnect from the grid in response to the disturbance propagation (NASIRI; MILIMONFARED; FATHI, 2015).

In response to the challenges posed by the non-synchronous generators, transmission system operators (TSOs) have been developing more restrictive criteria for incorporating these technologies into the electrical power system, known as grid codes (GCs). The GCs define basic operational criteria for all types of generators connected to transmission systems, establishing, for example, the expected behavior of a wind turbine's transient response to voltage and frequency disturbances.

1.4 Grid Codes and Voltage Ride Through

Under normal operating conditions, WEC systems must have the ability to operate in two control modes:

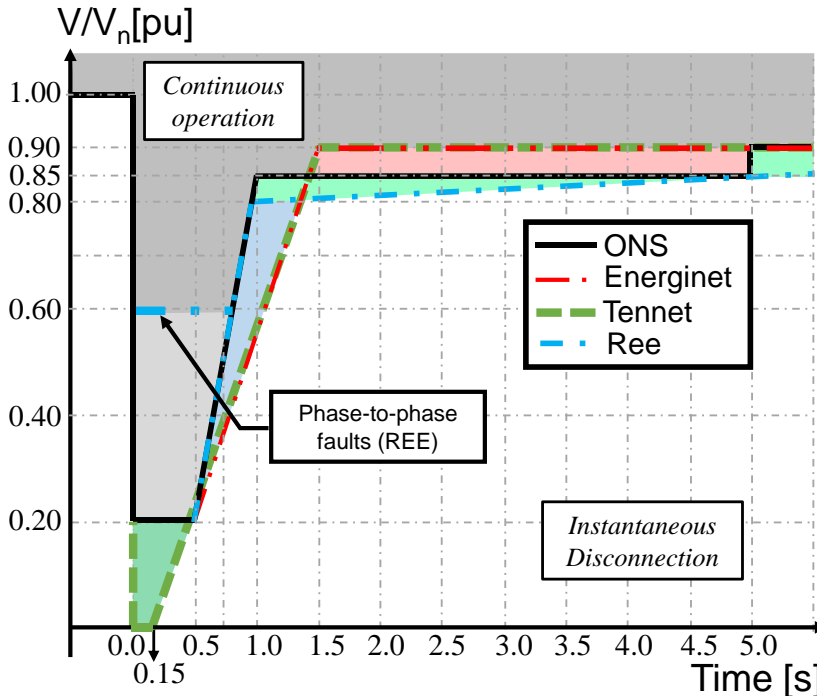
- PV control: Producing active power and regulating the voltage in PGC bus through indirect control of reactive power, it is the main control mode.
- PQ Control: Producing active power and reactive power or regulating power its factor at a value predefined by the TSO.

However, as previously mentioned, transient events cause sudden changes in the voltage and/or frequency values of the electrical mains. Regarding voltage deviations, the operation of wind turbines during momentary voltage sags is one of the main operational challenges due to the current restrictions imposed by semiconductor devices (VARTANIAN et al., 2018). The grid codes stipulate that wind generating units must remain connected to the grid as long as the voltage magnitude at their terminals remains above predetermined values for a specified period, a requirement known as Low Voltage Ride Through (LVRT).

Fig. 1.8 provides a comparative illustration of LVRT requirements from different TSOs, including the Brazilian *Operador Nacional do Sistema* (ONS) (ONS, 2020a), Danish Energinet (ENERGINET, 2016), German/Netherlands Tennet (TENNET TSO GMBH, 2015), and Spanish *Red Electrica de España* (REE) (REE, 2006).

When comparing the parameters of the LVRT curves in Tab. 1.1, it is evident that the TEENET GC presents the most stringent criteria, requiring the system to withstand up to 150[ms] with zero phase-to-phase voltage. Moreover, only REE differentiates symmetric from asymmetric faults, with the minimum voltage requirement in the latter case being 0.6[pu].

Fig. 1.8: Voltage limits requirements for different grid codes



Elaborated by the author, source data from (ENERGINET, 2016; ONS, 2020a; REE, 2006; TENNET TSO GMBH, 2015)

Tab. 1.1: Comparison between voltage ride through from different transmission system operators.

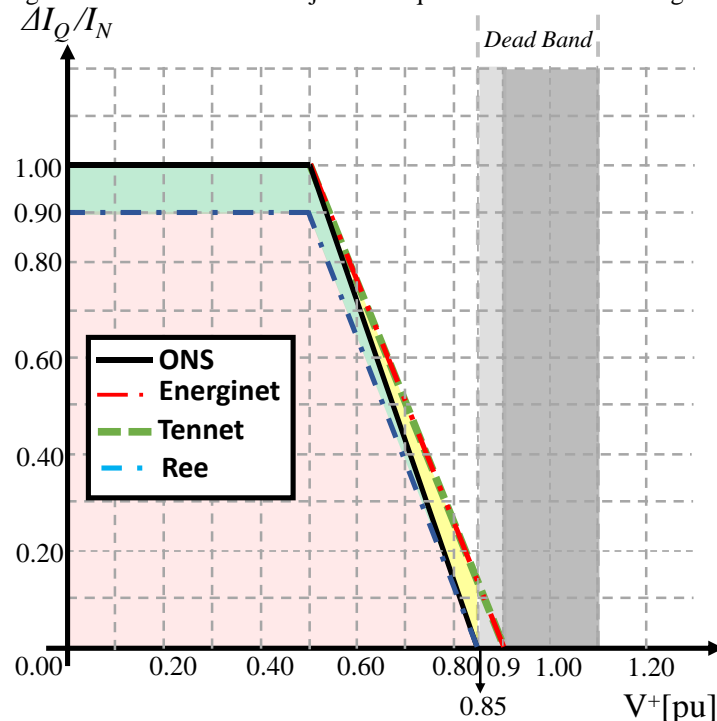
TSO	Y-axis (voltage)	Minimum value [pu]	Time lapsed on minimum voltage [ms]	Different for symmetrical and asymmetrical faults
ONS	Phase-to-ground voltages corresponding to the faulted phase	0.2	500	No
REE	Phase-to-ground voltages corresponding to the faulted phase	0.2	500	Yes
TEENET	Highest value of the phase-to-phase grid voltage.	0.0	150	No
ENERGINET	Smallest line-to-line voltage for the grid fundamental frequency component.	0.2	500	No

Elaborated by the author.

In more recent years, in addition to non-disconnection, the WECs must inject positive sequence reactive current (RCI), and this requirement takes precedence over any other function, including active power generation (ENERGINET, 2016; ONS, 2020a; REE, 2006; TENNET TSO GMBH, 2015). The aim RCI support is to increase the voltage at the WEC terminals and consequently prevent an unintentional shutdown of power generation, thereby averting a threat to grid stability in the event of brief voltage dips or increases (VDE, 2018).

Fig. 1.9 provides a comparison of RCI requirements across grid codes requirements from Brazilian *Operador Nacional do Sistema* (ONS) (ONS, 2020a), Danish Energinet (ENERGINET, 2016), German/Netherlands Tennet (TENNET TSO GMBH, 2015), and Spanish *Red Electrica de España* (REE) (REE, 2006). The y-axis represents the magnitude of the additional positive sequence component of reactive current (I_Q), the x-axis represents the positive sequence voltage at the WEC system's terminals, and I_N denotes the rated current of the generation unit. It should be noted that the analyzed TSOs, except for REE, require the WEC to provide its full current capacity in the case of sags with voltages below 0.5[pu], as described in Tab. 1.2.

Fig. 1.9: Reactive Current Injection requirements for different grid codes



Elaborated by the author, source data from (ENERGINET, 2016; ONS, 2020a; REE, 2006; TENNET TSO GMBH, 2015)

Tab. 1.2: Comparison of RCI requirement from GCs

TSO	Max. I_Q value [pu]	Dead-band min. range [pu]	Max. current voltage start [pu]
ONS	1.0	0.85	0.5
REE	0.9	0.85	0.5
TENNET	1.0	0.9	0.5
ENERGINET	1.0	0.9	0.5

Elaborated by the author.

Thus, the prioritization of LVRT requirements means that, from the mains' perspective, the behavior of the wind turbine during voltage transients is primarily influenced by the RCI

(KELLER; KROPOSKI, 2010), and the wind power generator can be considered as acting like controlled current sources in response to the positive sequence voltage at its terminals (ENTSOE, 2019).

During voltage sags, the transmission lines' power flow capacity becomes more constrained compared to normal conditions (KUNDUR; BALU; LAUBY, 1994), and the increase in current flow resulting from RCI requirements must be accounted for adjusting protections in areas near to WFs. An example of this problem occurred on August 15, 2023, in Brazil, where the overload of the transmission lines due to ineffective reactive current flow during a voltage sag led to the disconnection of the north and northwest region of the country from the main grid (ONS, 2023). This incident leaving more than 29 million people without electrical energy (PIMENTEL, 2023), and underscores the importance of considering the behavior of wind turbines during voltage transients and the need for appropriate protections to prevent widespread power outages.

For KARBOUI AND RATHER (2019), the emphasis on RCI and current limitation of power electronics converters can lead to almost negligible active power generation during short circuits and may result in more significant frequency excursions in power systems with high integration of non-synchronous sources. But, according to ERLICH et al. (2009), injecting positive sequence reactive current near conventional plants can enhance the voltage profile, enabling synchronous generators to increase active power transfer during grid faults and expand the stability margin.

In fact, the effectiveness of the RCI is influenced by the grid's X/R ratio and the sharing of wind converters in the energy matrix (GÖKSU et al., 2014; SWANDARU; ROTARU; SYKULSKI, 2017, 2021), and as the X/R ratio decreases, it becomes beneficial to reduce the slope of the RCI curve, prioritizing the injection of active current (SWANDARU; ROTARU; SYKULSKI, 2021). However, the definition of the RCI curve slope is the responsibility of the TSO.

1.4.1 The provision of negative sequence currents and new scenario of RCI

An important highlight is the RCI requirement stipulates the injection of positive sequence currents regardless of whether the voltages are balanced or not. In GOKSU et al. (2013), it is demonstrated that, in specific cases, injecting balanced reactive currents during asymmetrical faults can lead to overvoltage in phases with higher magnitudes, resulting in undesirable disconnections. Thus, since the Reactive Current Injection (RCI) requirement aims to enhance

the supportability of wind turbines during voltage sags, this problem ultimately undermines the effectiveness of this functionality.

Since 2016, ongoing discussions have taken place within the European Union regarding the injection of negative sequence currents during asymmetrical faults, initiated by the publication of **COMMISSION REGULATION (EU) 2016/631 (2016)**. This publication aimed to harmonize the GCs across different entities of member states of the European Union, establishing the basic guidelines and facilitating energy exchange. These requirements are considered non-exhaustive, i.e., the specification is left to the decision of each member state.

One of the aspects addressed in **COMMISSION REGULATION (EU) 2016/631 (2016)** is the provision of fast fault current or the contribution of non-synchronous generators during asymmetrical faults. It stipulates that TSO shall have the right to specify a requirement for asymmetrical current injection and this requirement must be in accordance with the following principles in relation to robustness:

- Interdependency between fast fault current requirements active power recovery.
- Dependence between active power recovery times and duration of voltage deviations
- Specified limit of the maximum allowed time for active power recovery.
- Adequacy between the level of voltage recovery and the minimum magnitude for active power recovery.
- Adequate damping of active power oscillations.

Building upon this publication, **ENTSOE (2016)** anticipates that in networks with high penetration of non-synchronous generators, in the event of asymmetric faults, the provision of negative sequence reactive currents becomes optional but highly recommended.

Taking these new requirements, the VDE (*Verband Deutscher Elektroingenieure - Association of German Electrical Engineers*) in VDE ARN 4120 (**VDE, 2018**), proposes a new reactive current injection where wind generators must now supply both positive and negative reactive currents, described in Fig. 1.10. According to **VDE ARN 4120 (2018)**, the generating units must be capable of supplying a reactive current of at least 100% of the rated current in each phase, allowing the reduction of the active portion of the current.

The additional reactive current ($\Delta I_q^{+,-}$) for both sequences is directly proportional to the voltage deviation ($\Delta V^{+,-}$), as outlined in equation (1.2). Where, the TSO must specify the amplification factor k_{VDE} when planning the connection of the wind farm (WF) to the grid based on the impedances between the point of generator connection (PGC) and the point of

common connection (PCC) of the park with the high voltage network, where must be $2 \leq k_{VDE} \leq 6$.

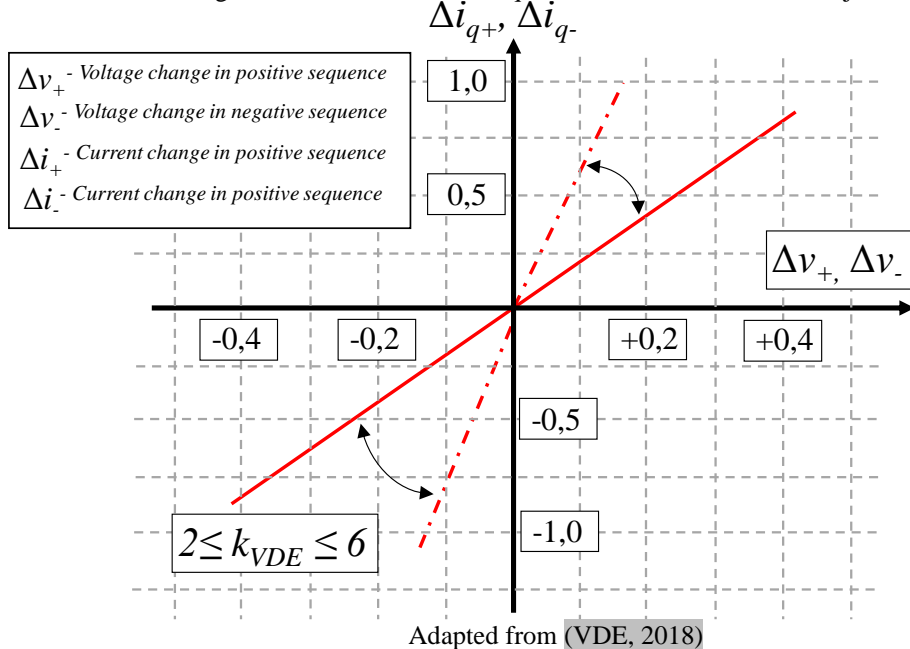
$$\Delta I_q^{+, -} = k_{VDE} \cdot \Delta V_{+, -}. \quad (1.2)$$

The calculations of voltage deviations are defined in equations (1.3) and (1.4), where V^+ and V^- represent the voltage amplitudes measured in the positive and negative sequences, respectively. Additionally, V_{1min} denotes the average voltage within a period of 1 minute before the fault, and V_n represents the nominal value of the voltage.

$$\Delta V^+ = \frac{V_{1min} - V^+}{V_n}, \quad (1.3)$$

$$\Delta V^- = \frac{V^-}{V_n}. \quad (1.4)$$

Fig. 1.10: VDE ARN 4120 requirement of reactive current injection



As stated by VDE ARN 4120 (2018), the objective of additional reactive current is to provide optimal support for both symmetrical and asymmetrical faults while minimizing surges in non-faulty phases. In line with GRAUNGAARD TAUL et al.(2020), the generation of current references by the positive and negative sequences, as established in VDE ARN 4120, does not solely focus on the converter's perspective but aims to enhance the flexibility of grid support functionalities. This is corroborated by ENTSOE (2016), which indicates that the injection of asymmetric currents is intended to help the balance of grid voltages.

Then at this juncture, it is worth questioning whether it would be possible to somehow mitigate the impacts of voltage sags for the electronic converter and assist the grid?

1.5 Literature review and the state of art

To answer the question above, due to the presence of semiconductor devices, it is necessary to take into account the limited overcurrent capacity of power electronic converters compared to conventional synchronous generators, as detailed in GOMES GUERREIRO et al. (2023) and GUERREIRO et al. (2024). Moreover, the reduction in voltage magnitude and the prioritization of RCI mean that it is not always practical to maintain the pre-fault grid active power supply (JIA; YANG; NIELSEN, 2018).

For WEC systems, the voltage ride through is a critical situation because, the slow dynamics of blade pitch control create an imbalance between the generated and delivered power to the grid, leading to a rapid increase in DC bus voltage (CONROY; WATSON, 2007; MENDES et al., 2016). And, to prevent undesirable disconnections or power converter damages, external hardware, such as a braking chopper, must be applied to balance the generator and grid feeding power, thus averting grid overcurrents and/or DC bus overvoltages (HIREMATH; MOGER, 2020). In asymmetric faults, in addition to the previously reported issues, there are instantaneous power oscillations with twice the grid fundamental frequency.

Currently, many studies focus on reducing the impacts of voltage sags on wind turbines through energy storage devices such as batteries and supercapacitors (AGHMADI; MOHAMMED, 2024; WEI et al., 2023). For instance, references KIM et al. (2021), (2020), ALGHAMDI (2023), and LI; LIU (2023) propose using Dynamic Voltage Restorers (DVR) to improve wind turbine performance during voltage sags. Similarly, references LETAIEF et al.(2024) and BERGER et al. (2022) suggest adding battery energy storage systems (BESS) to wind turbines, arguing that these systems would not only enhance performance during voltage sags but also increase the capacity to assist in primary frequency regulation by providing additional inertia.

However, the use of additional hardware with storage devices results in increased implementation costs, as well as higher maintenance costs and greater waste production from battery disposal (SAHOO; TIMMANN, 2023). In this thesis, the author intends to follow a different path by proposing improvements to the response capacity of wind turbines to voltage sags without the use of additional hardware.

1.5.1 The evolution of power control strategies and current saturation

In fact, the discussion of the impacts of unbalanced voltage sags on wind turbines came before the establishment of clear criteria for voltage ride-through in grid codes. References RODRIGUEZ et al. (2007), RODRÍGUEZ et al. (2009), RODRIGUEZ et al., (2011) and CASTILLA et al., (2010) define power control strategies, i.e., equations for calculating the reference currents necessary to impose reference values of active and reactive power on the grid and additionally, mitigating power quality issues during asymmetric faults, such as nullifying instantaneous power oscillations.

Adaptive or flexible strategies were subsequently proposed in RODRIGUES et al. (2011), FEI WANG et al. (2011), and SOSA et al. (2016). These strategies use gains to weight the relationship between the positive and negative sequence components in the calculation of reference currents. This approach allows for different power quality characteristics when interacting with unbalanced voltage and even enables the replication of characteristics from the strategies described in previous references.

With the emergence of RCI requirements during LVRT, the converter's operation becomes more complex. In addition to the current restrictions imposed by semiconductor devices, the converter must now prioritize compliance with the grid codes. Under these conditions, to avoid mechanical stress on the wind turbine shaft, the generator active power cannot be suddenly reduced to zero (ZHOU; LI; MOHAMED, 2021). Likewise, as maximum active power must be delivered to the mains to minimize the DC bus power imbalance and reduce the amount of energy dissipated by the braking chopper and its consequently degradation (NASIRI; ARZANI, 2022).

Thus, based on this scenario, a new research front emerges, named power curtailment or power saturation strategies. They aim to optimize compliance with the grid code (GC) and the injection of active power considering the converters' current restrictions. Additionally, the injection of negative sequence currents has been discussed to achieve diverse power quality objectives, even before the establishment of AR N 4120.

In this way, it is possible to outline the power curtailment methods into two main categories (JIA; YANG; NIELSEN, 2018):

- **Power-characteristic-oriented control:** These strategies focus on directly controlling oscillations in output power by regulating the DC bus voltage.

- **Voltage-support-oriented control:** This approach aims to adjust the relationship between positive and negative sequence power to support grid voltage during unbalanced faults, with an emphasis on phase voltage regulation.

CHOU et al. (2011) introduced a technique involving reactive current injection during LVRT using both positive and negative sequences to improve voltage support and fulfill the RCI requirement. However, this method does not consider instantaneous power oscillations and assumes that the active current injected during the voltage sag is null.

MA; LISERRE; BLAABJERG. (2013) addressed power oscillation and overcurrent issues in three-phase DC-AC power converters caused by unbalanced voltages. They proposed new control strategies utilizing zero-sequence components to enhance power control under adverse conditions, eliminating active power oscillations. The method can be used in both three-phase and four-wire networks but does not provide reactive current.

CAMACHO et al. (2018) aimed to maximize the lowest phase voltage by injecting the maximum permissible current of the inverter to support grid voltage during faults. This method balances active and reactive power references according to grid impedance (resistive or inductive) without using negative sequence currents, but it does not consider GCs requirements.

LÓPEZ et al. (2018) proposed strategies to meet LVRT and RCI requirements of grid codes. They focused on limiting the injected current to the maximum allowed by the inverter, ensuring active power control during normal operation and voltage sags, and preventing active power oscillations.

HASAN; AGARWAL. (2021) defined a voltage support scheme to provide necessary voltage support at the PGC during grid faults. This scheme ensures consistent voltage compensation irrespective of the nature of the injected current, especially when dealing with varying available active power levels, by adjusting the injected positive and negative sequence currents accordingly.

GARNICA et al. (2020) aimed to maximize the current injected by the inverter while limiting it to the maximum allowable value to protect the inverter from overcurrents. They optimized voltage support for three-phase three-wire inverters connected to RL grids during voltage sags, avoided oscillations in instantaneous active power, and reduced voltage imbalance by adjusting the amplitudes of positive and negative-sequence voltages, but did not consider the RCI requirement of grid codes.

CASTILLA et al. (2020) proposed a control scheme that combines flexible oscillating-power control with slope voltage control to prevent overvoltage, reduce cascade disconnection risks, and ensure compliance with grid-code requirements for reactive current injection during voltage sags.

Recent works, such as those by **FENG et al. (2020)**, aim to meet the requirements established by VDE AR N 4120. **FENG et al. (2020)** addressed limiting current, restraining active power oscillation, and injecting reactive current to comply with next-generation grid code requirements. Their strategy mathematically determines power allocations to fulfill these goals simultaneously, including injecting asymmetrical current to reduce voltage unbalance at the point of common coupling.

GRAUNGAARD TAUL et al. (2020) presented a flexible power control strategy for asymmetrical faults, proposing a current reference generation strategy that derives power references and flexible controller gains while complying with converter current limitations and the VDE AR N 4120 grid code requirement.

For both **FENG et al. (2020)** and **GRAUNGAARD TAUL et al. (2020)**, using the proposed methodologies to meet VDE requirements resulted in an increase in instantaneous power fluctuations.

When evaluating these works, it is evident that:

- **Tradeoff between voltage support and power oscillations:** There is a tradeoff between optimizing voltage support and cancelling instantaneous power oscillations. Achieving optimal voltage support requires injecting more negative sequence currents than needed to cancel power oscillations. This tradeoff will be discussed in this thesis.
- **Complexity of calculations:** The proposed methodologies require complex calculations, such as arc trigonometrical functions of temporal variables. Given that voltage dips are transient phenomena, high-performance processors are needed to ensure these calculations do not compromise the objectives of the algorithms.
- **Voltage support:** the RCI proposed in the GCs is highly dependent on the magnitude of the system impedance and the inductance-to-resistance ratio (X/R ratio). In systems with low equivalent impedance or more resistive characteristics, the injection of reactive current will not be effective.

Regarding the last topic, a third strand of research focuses on utilizing the capacity of electronic converters to restore voltage at the PCC. This is achieved through the control of positive and negative sequence currents to restore and balance voltage levels. This research,

presented in references such as CAMACHO et al. (2013a), GOKSU et al. (2013), MIRET et al. (2013), CASTILLA et al. (2014), CÉSAR A. SILVA (2014), CAMACHO et al. (2014), MIRET et al. (2015) and NEJABATKHAH et al. (2016), envisions a future scenario where the penetration of distributed generators with electronic converters is significant enough to potentially replace conventional generators.

It is essential to differentiate between two concepts: voltage support and voltage restoration. Voltage restoration refers to a closed-loop control action that attempts to return the voltage to pre-fault levels, both in magnitude and phase balance. In contrast, voltage support operates in an open loop, aiming to increase the converter's LVRT operating margin by injecting predefined values of reactive current, and is the focus of this thesis.

Another important consideration is why the converter's ability to cancel instantaneous power oscillations is crucial for enhancing wind turbines' low voltage ride through (LVRT) operation.

Losses in electrolytic capacitors are proportional to energy oscillations in the dielectric (CHEN et al., 2016; LENZ; PINHEIRO; SARTORI, 2017). Consequently, active power oscillations lead to increased dielectric losses in the GSC's capacitors. This results in a rise in operating temperature, which could reduce the lifetime of the converter's bus capacitors (CUPERTINO et al., 2019).

Additionally, an increase in reactive current results in higher losses in the diodes of the IGBT modules (DE ANDRADE et al., 2016; GANDHI et al., 2018; GRAB et al., 2022). The cancellation of reactive power oscillations can reduce losses in the diodes, as the power would be restricted to its average value.

In summary, reducing power fluctuations is directly related to mitigating the impacts of momentary voltage drops on the converter.

1.6 Objectives

Thus, in view of the problems reported in this chapter, the general objective of this thesis is to propose an algorithm for limiting active power during low voltage ride-through operation, establishing four control priorities:

- 1. Compliance with voltage ride-through and RCI requirement:** The primary goal is to ensure adherence to the voltage ride-through and reactive current injection (RCI) defined in grid codes (GCs).

2. **Limiting grid converter current to its rated value:** Maintaining the current within the converter's rated capacity is crucial to safeguard the power converter and prevent undesired disconnections from the mains.
3. **Control of active power production:** This priority enables the management of active power production during both normal operations and grid faults.
4. **Mitigation of power oscillations** During unbalanced voltage sags, whenever feasible, the algorithm aims to mitigate power oscillations that may arise during unbalanced voltage sags.

The proposed algorithm is characterized by its flexibility, allowing it to be applied to different power control strategies using only simple equations, ensuring compliance with current grid codes.

1.6.1 Specific objectives

Based on the general objective of this thesis, the following specific objectives can be listed:

- Develop a robust algorithm that ensures compliance with voltage ride-through, and reactive current injection (RCI) requirements as defined in current grid codes (GCs) and effectively manage active power production during both normal operating conditions and in the event of grid disturbances.
- Ensure the proposed algorithm is adaptable to different power control strategies, using straightforward equations to facilitate its integration with existing and future grid codes.
- Discuss the impacts of type IV generators on the transient behavior of electrical power systems.
- Propose improvements to existing grid codes with the aim of enhancing the participation of renewable sources based on power electronics systems in transient stability improvement.

1.7 Methodology

The proposed objectives will be accomplished through the following approaches:

- **Bibliographic Review:** An extensive review of relevant literature will be conducted throughout this work, guiding the development, and aiding in the interpretation of results.

- **Mathematical Models:** The formulations of mathematical models are proposed to provide insights into the discussions and propositions presented in this thesis.
- **Computational Simulation:** Detailed computational simulations will be conducted using *Plecs* software for a 2.1 MW type IV WEC, and a WF integrated into the WSCC 9-bus power system will be simulated using *MatLab/Simulink*. These simulations will be based on real data parameters and will be undertaken to evaluate the proposed objectives and introduce new insights.

1.8 Thesis organization

In a nutshell, this thesis is divided into the following chapters:

- **Chapter I:** Outlines the motivations and objectives of this research.
- **Chapter II:** Delves into the power control strategies during LVRT through development of mathematical formulations using instantaneous power theory.
- **Chapter III:** A strategy is proposed to prioritize the reactive current injection, restricting active power and flexibility to cancel instantaneous powers oscillations during LVRT.
- **Chapter IV:** Investigates the power control strategies influences over the voltage support and their consequence for other generation units of an electrical power system.
- **Chapter V:** Conclusions are made.

Chapter II

POWER CONTROL STRATEGIES

GRID-CONNECTED converters indeed provide enhanced flexibility in current synthesis compared to conventional generators with synchronous machines. Their ability to independently control active and reactive currents and synthesize unbalanced and harmonic currents opens possibilities for implementing power control strategies, which are valuable for mitigating power oscillations during unbalanced voltage sags. This chapter will delve into the advantages in power control strategies during LVRT through development of mathematical formulations using instantaneous power theory.

2.1 Voltage sags in stationary reference frame

Voltage sag is a sudden and temporary drop in voltage magnitude, often caused by load demand fluctuations or short circuits (IEEE-1159, [s.d.]). Most power system faults are either phase-to-ground or phase-to-phase, leading to unbalanced voltages, and the unbalance among the phases could be quantified using the unbalance factor u , defined as the ratio of the negative sequence voltage magnitude $|\mathbf{v}^-|$ over the positive sequence voltage magnitude $|\mathbf{v}^+|$ in (2.1)

$$u = \frac{|\mathbf{v}^-|}{|\mathbf{v}^+|}. \quad (2.1)$$

Most of the power electronics converters utilized in WECS operate in a three-phase to three-wire configuration, the analysis in this study will focus on this specific setup. This approach enables the modeling unbalanced voltages, through the summation of positive and negative sequence components, as detailed in equation (2.2) (CAMACHO et al., 2013b).

$$\begin{aligned} v_a &= v^+ \cos(\omega t + \phi^+) + v^- \cos(\omega t - \phi^-), \\ v_b &= v^+ \cos\left(\omega t + \phi^+ - \frac{2\pi}{3}\right) + v^- \cos\left(\omega t - \phi^- + \frac{2\pi}{3}\right), \\ v_c &= v^+ \cos\left(\omega t + \phi^+ + \frac{2\pi}{3}\right) + v^- \cos\left(\omega t - \phi^- - \frac{2\pi}{3}\right), \end{aligned} \quad (2.2)$$

As a convention of this text, the superscript “+” denotes quantities in the positive sequence, while “-“ represents the negative sequence. In equation (2.2), ϕ^+ and ϕ^- denote the phase angles, ω the fundamental frequency, and V^+ and V^- represent the voltage magnitudes.

Employing the linear transformation for the stationary frame (Clarke transform) in equation (2.2), as described by RODRIGUEZ et al. (2009), the grid voltages are represented by two quantities, v_α and v_β , orthogonal to each other, as outlined in equation (2.3). This simplification facilitates the derivation of mathematical equations without missing information.

$$\begin{aligned} v_\alpha &= V^+ \cos(\omega t + \phi^+) + V^- \cos(-\omega t + \phi^-), \\ v_\beta &= V^+ \sin(\omega t + \phi^+) + V^- \sin(-\omega t + \phi^-). \end{aligned} \quad (2.3)$$

To represent (2.3) in a vector notation, the set equations (2.4) are used.

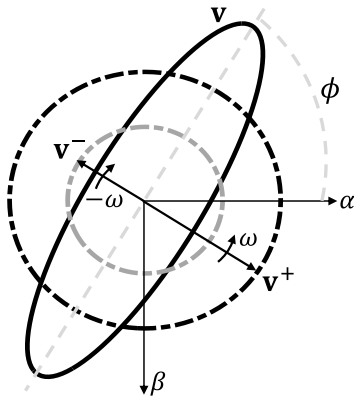
$$\begin{aligned} \mathbf{v}^+ &= [v_\alpha^+, v_\beta^+], \\ \mathbf{v}^- &= [v_\alpha^-, v_\beta^-], \\ \mathbf{v} &= \mathbf{v}^+ + \mathbf{v}^-. \end{aligned} \quad (2.4)$$

The relationship between the positive and negative sequence voltages in the stationary frame ($\alpha\beta$) is established using the Fortescue equations in Clark's transform (PINTO et al., 2021; RODRIGUEZ et al., 2006) resulting in (2.5), where the operator $q = e^{-j\pi/2}$.

$$\begin{aligned} \mathbf{v}^+ &= \frac{1}{2} \begin{bmatrix} 1 & -q \\ q & 1 \end{bmatrix} \cdot \mathbf{v}, \\ \mathbf{v}^- &= \frac{1}{2} \begin{bmatrix} 1 & q \\ -q & 1 \end{bmatrix} \cdot \mathbf{v}, \end{aligned} \quad (2.5)$$

The vectors \mathbf{v}^+ and \mathbf{v}^- have circular trajectories, albeit in opposite directions, and the instantaneous sum of them results in an elliptical path for \mathbf{v} , as depicted in Fig. 2.1. The eccentricity of this ellipse correlates with the negative sequence magnitude, while the angular disparity between ϕ^+ and ϕ^- introduces a displacement ϕ in the voltage trajectory relative to the α -axis.

Fig. 2.1: Grid voltage vector representation trajectory



Elaborated by the author.

Equation (2.6) expresses the magnitude of vector \mathbf{v} , where $|\mathbf{v}|^2$, $|\mathbf{v}^+|^2$ and $|\mathbf{v}^-|^2$ are defined in (2.7), and $\cos(\phi)$ and $\sin(\phi)$ in (2.8).

$$\begin{aligned} |\mathbf{v}|^2 &= (\mathbf{v}^+ + \mathbf{v}^-) \cdot (\mathbf{v}^+ + \mathbf{v}^-) = |\mathbf{v}^+|^2 + |\mathbf{v}^-|^2 + 2|\mathbf{v}^+||\mathbf{v}^-|\cos(2\omega t + \phi^+ - \phi^-), \quad (2.6) \\ |\mathbf{v}|^2 &= v_\alpha^2 + v_\beta^2, \\ |\mathbf{v}^+|^2 &= v_\alpha^+{}^2 + v_\beta^+{}^2, \\ |\mathbf{v}^-|^2 &= v_\alpha^-{}^2 + v_\beta^-{}^2, \end{aligned} \quad (2.7)$$

$$\begin{aligned} \cos(\phi) &= \cos(\phi^+ + \phi^-) = \frac{v_\alpha^+ v_\alpha^- - v_\beta^+ v_\beta^-}{|\mathbf{v}^+| |\mathbf{v}^-|} \\ \sin(\phi) &= \sin(\phi^+ + \phi^-) = \frac{v_\beta^+ v_\alpha^- - v_\alpha^+ v_\beta^-}{|\mathbf{v}^+| |\mathbf{v}^-|} \end{aligned} \quad (2.8)$$

2.2 Instantaneous power oscillations

In addition to positive (\mathbf{i}^+) and negative (\mathbf{i}^-) sequence, the current vector (\mathbf{i}) can also be decomposed into active (\mathbf{i}_p) and reactive (\mathbf{i}_q) components as described in (2.9).

$$\begin{aligned} \mathbf{i}_p &= \mathbf{i}_p^+ + \mathbf{i}_p^-, \\ \mathbf{i}_q &= \mathbf{i}_q^+ + \mathbf{i}_q^-, \\ \mathbf{i} &= \mathbf{i}_p + \mathbf{i}_q. \end{aligned} \quad (2.9)$$

In this work, to simplify the notation in the reactive or imaginary power computation, the orthogonal projection of vector \mathbf{v} , denoted by \mathbf{v}_\perp , is utilized, where it is defined in (2.10) (CAMACHO et al., 2013b).

$$\mathbf{v}_\perp = \begin{bmatrix} 0 & 1 \\ -1 & 0 \end{bmatrix} \mathbf{v}. \quad (2.10)$$

Thus, the instantaneous active or real power (p) are stated by the dot product (\cdot) of voltage (\mathbf{v}) by the current (\mathbf{i}) in (2.11), and the reactive or imaginary power (q) the dot product of orthogonal voltage projection (\mathbf{v}_\perp) by the current (\mathbf{i}) in (2.12). where P , Q the average powers and \tilde{p} , \tilde{q} the oscillatory values with twice fundamental frequency of active and reactive power.

$$p = (\mathbf{v}^+ + \mathbf{v}^-) \cdot (\mathbf{i}_p^+ + \mathbf{i}_p^- + \mathbf{i}_q^+ + \mathbf{i}_q^-) = \dots$$

$$\underbrace{\mathbf{v}^+ \cdot \mathbf{i}_p^+ + \mathbf{v}^- \cdot \mathbf{i}_p^-}_P + \underbrace{\mathbf{v}^+ \cdot \mathbf{i}_q^+ + \mathbf{v}^- \cdot \mathbf{i}_q^-}_0 + \underbrace{\mathbf{v}^- \cdot \mathbf{i}_p^+ + \mathbf{v}^+ \cdot \mathbf{i}_p^- + \mathbf{v}^+ \cdot \mathbf{i}_q^- + \mathbf{v}^- \cdot \mathbf{i}_q^+}_{\tilde{p}}, \quad (2.11)$$

$$q = (\mathbf{v}_\perp^+ + \mathbf{v}_\perp^-) \cdot (\mathbf{i}_p^+ + \mathbf{i}_p^- + \mathbf{i}_q^+ + \mathbf{i}_q^-) = \dots$$

$$\underbrace{\mathbf{v}_\perp^+ \cdot \mathbf{i}_q^+ + \mathbf{v}_\perp^- \cdot \mathbf{i}_q^-}_Q + \underbrace{\mathbf{v}_\perp^+ \cdot \mathbf{i}_p^+ + \mathbf{v}_\perp^- \cdot \mathbf{i}_p^-}_0 + \underbrace{\mathbf{v}_\perp^- \cdot \mathbf{i}_q^+ + \mathbf{v}_\perp^+ \cdot \mathbf{i}_q^- + \mathbf{v}_\perp^+ \cdot \mathbf{i}_p^- + \mathbf{v}_\perp^- \cdot \mathbf{i}_p^+}_{\tilde{q}}, \quad (2.12)$$

The expressions for instantaneous active and reactive powers demonstrate that the projection of \mathbf{i} over \mathbf{v} yields active power, while the projection of \mathbf{i} over the orthogonal vector \mathbf{v}_\perp produces reactive power and the interaction between voltages and currents from different sequences give rise to power oscillations \tilde{p} and \tilde{q} .

2.3 Power control strategies

The versatility of the power electronic converter allows current references to be computed to provide the grid with the average values of active (P^*) and reactive (Q^*) power, and additionally manage instantaneous power fluctuations at the voltage measurement point. The equations of reference currents to compensate power quality issues are termed power control strategies and can be categorized into those generating non-sinusoidal reference currents and those generating sinusoidal reference currents.

Given the harmonic distortion limits mandated by grid codes (GCs), this study emphasizes sinusoidal power control strategies, while providing a discussion of non-sinusoidal power control strategies in Appendix A. Various power control strategies have been proposed in the works of RODRIGUEZ et al. (2007), RODRIGUEZ et al. (2009), FEI WANG et al. (2011), RODRIGUEZ et al. (2011), which are detailed below.

To analyze the behavior of the strategies in this chapter, graphs illustrating the temporal behavior of the equations for the described conditions throughout will be presented, in other words, the graphs presented in this chapter are not simulations results.

2.3.1 Balanced Positive Sequence Control (BPSC)

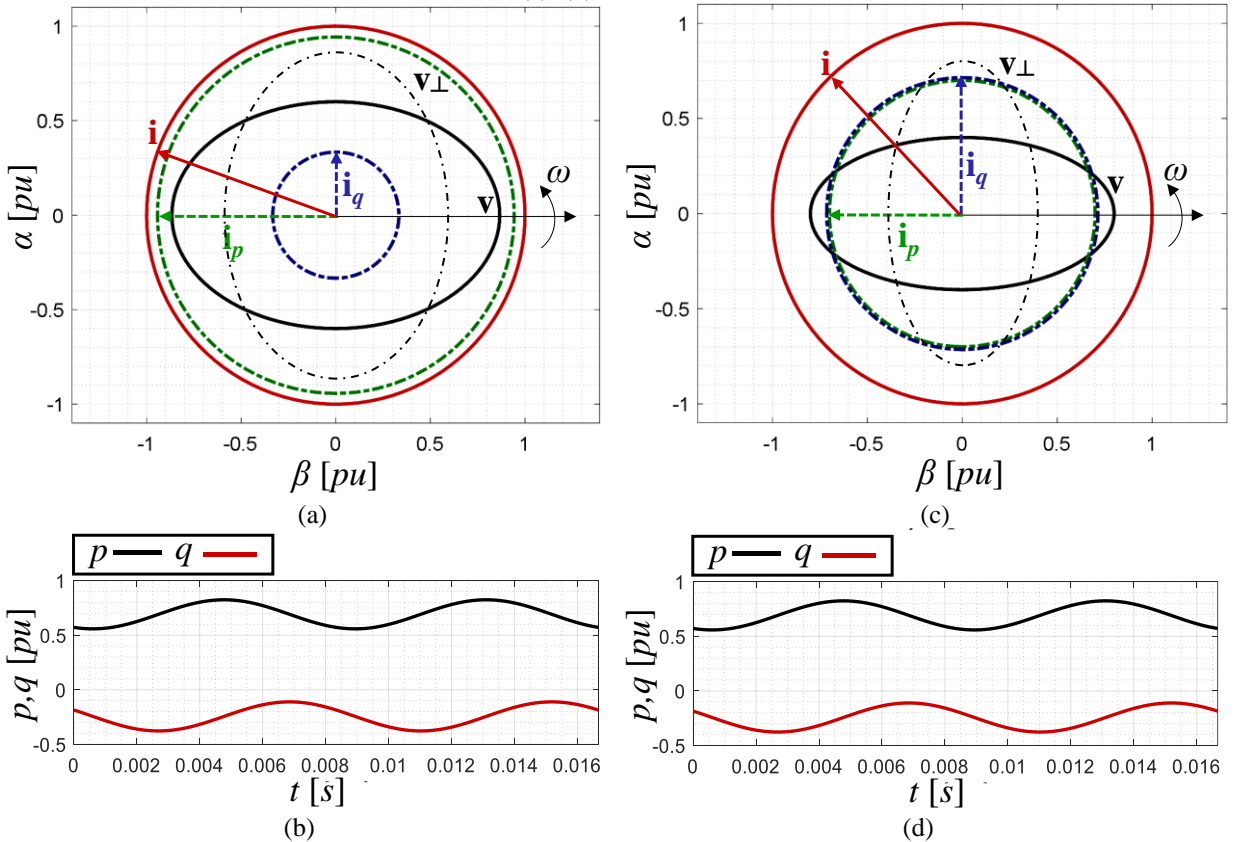
The Balanced Positive Sequence Control (BPSC), described in equations (2.13) and (2.14), exclusively utilizes the positive sequence voltage for computing reference currents. This approach yields a set of sinusoidal balanced currents, even in an unbalanced grid.

$$\mathbf{i}_p^* = \frac{P^*}{|\mathbf{v}^+|^2} \mathbf{v}^+, \quad (2.13)$$

$$\mathbf{i}_q^* = \frac{Q^*}{|\mathbf{v}^+|^2} \mathbf{v}_\perp^+. \quad (2.14)$$

The graphs on Fig. 2.2(a) and Fig. 2.2(c) illustrate the trajectories of currents and voltage in the stationary frame for two different unbalance factors and varying levels of active and reactive currents.

Fig. 2.2: BPSC current trajectory in stationary reference frame and instantaneous power (a), (b) for $u = 0,182$ and (c), (d) for $u = 0,333$



Elaborated by the author.

As the BPSC strategy exclusively utilizes the positive sequence, the dot product of the elliptical trajectory of voltage (\mathbf{v}) and orthogonal projection (\mathbf{v}_\perp) vectors, with the circular path of current vector (\mathbf{i}) leads to oscillations in both active and reactive powers, which is apparent in the instantaneous power profiles depicted in Fig. 2.2(b) and Fig. 2.2(d).

2.3.2 Active Power Oscillation Cancels (APOC).

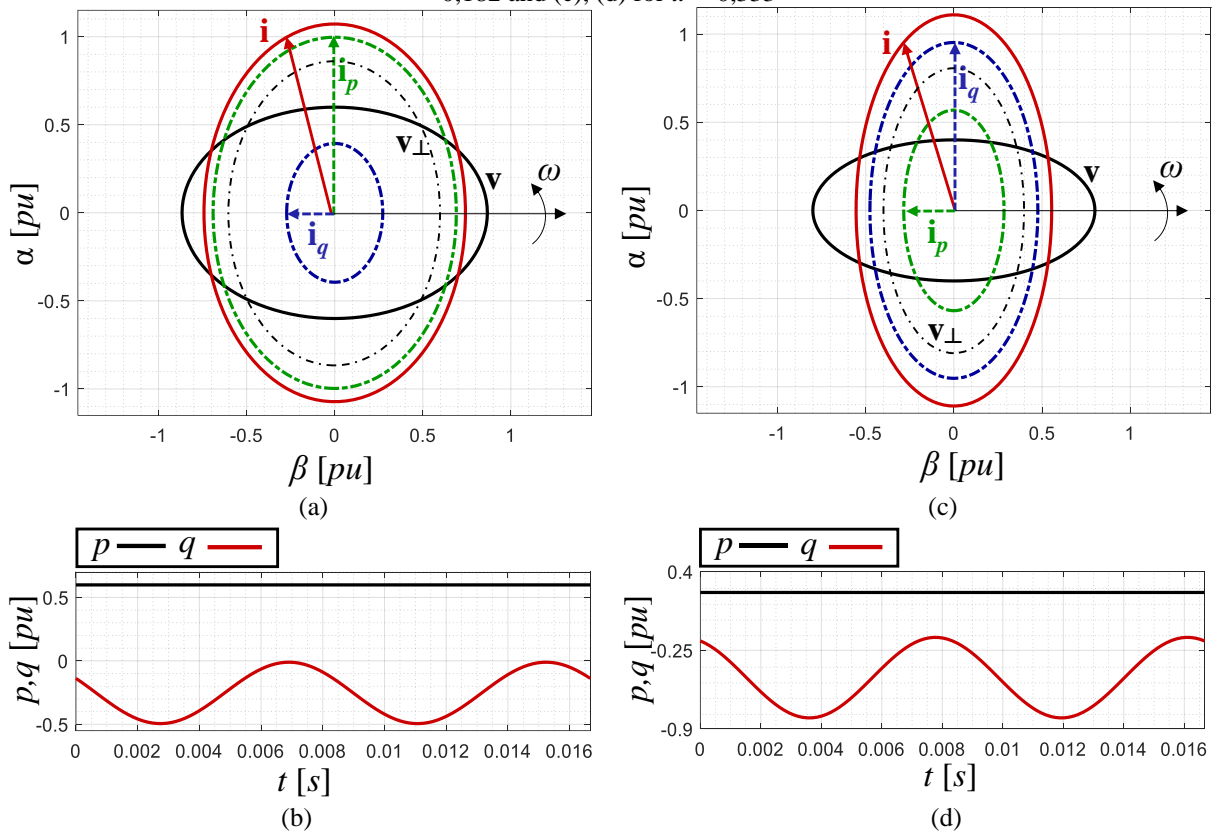
The Active Power Oscillation Cancels (APOC) (FEI WANG; DUARTE; HENDRIX, 2011) aims at the cancellation of active power oscillations by utilizing both positive and negative sequence currents. These currents are calculated in equations (2.15) and (2.16).

$$\mathbf{i}_p^* = \frac{P^*}{|\mathbf{v}^+|^2 - |\mathbf{v}^-|^2} (\mathbf{v}^+ - \mathbf{v}^-), \quad (2.15)$$

$$\mathbf{i}_q^* = \frac{Q^*}{|\mathbf{v}^+|^2 + |\mathbf{v}^-|^2} (\mathbf{v}_\perp^+ + \mathbf{v}_\perp^-). \quad (2.16)$$

In the case of APOC, the maximum magnitude of the voltage vector (\mathbf{v}) aligns with the minimum value of the current (\mathbf{i}), as illustrated in Fig. 2.3(a) and Fig. 2.3(c). Consequently, the dot product of these variables yields a continuous value of active power (p). Conversely, the maximum values of the orthogonal projection (\mathbf{v}_\perp) of voltage and current (\mathbf{i}) coincide, giving rise to oscillations in reactive power (q), as shown in Fig. 2.3(b) and Fig. 2.3(d). These outcomes are consistent regardless of the magnitudes of currents (\mathbf{i}_p) and (\mathbf{i}_q) and the degree of voltage unbalance.

Fig. 2.3: APOC current trajectory in stationary reference frame and instantaneous power (a), (b) for $u = 0,182$ and (c), (d) for $u = 0,333$



Elaborated by the author.

2.3.3 Reactive Power Oscillation Cancels (RPOC).

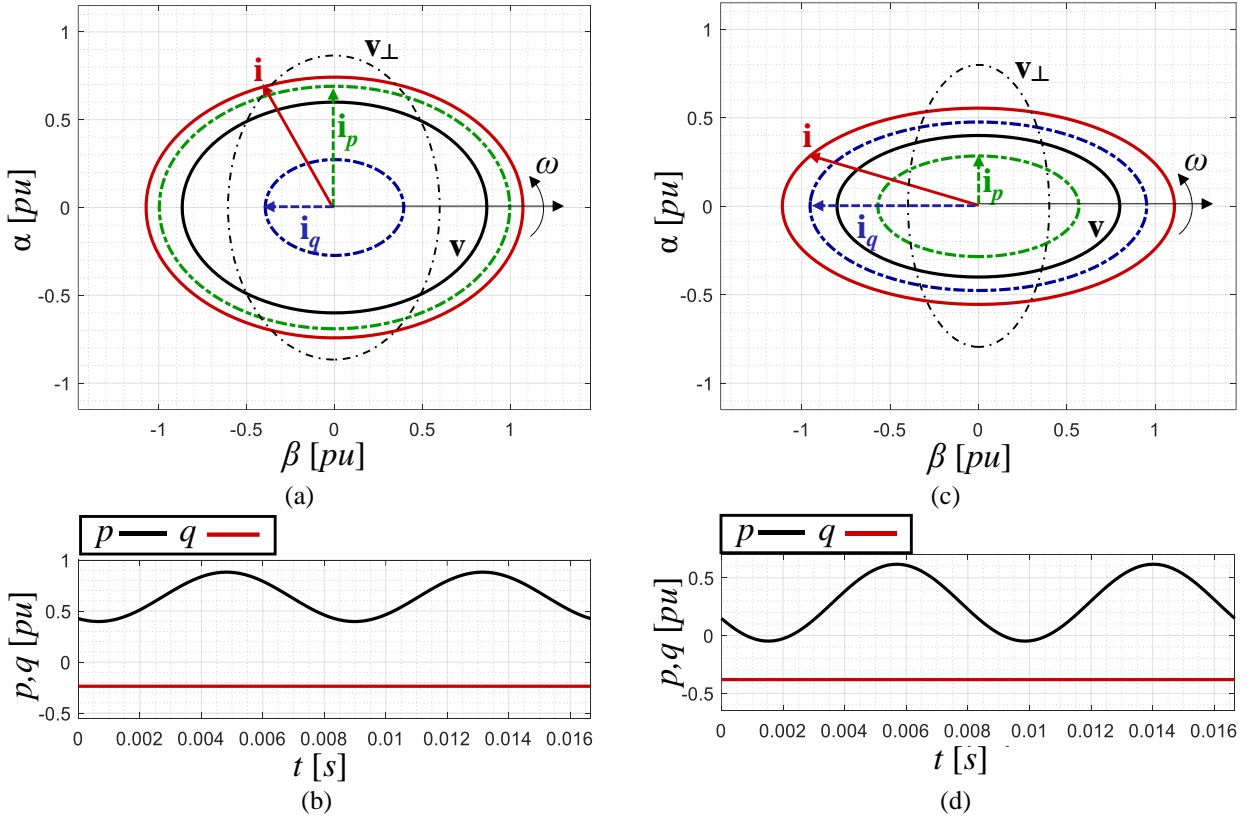
The objective of the Reactive Power Oscillation Cancels (RPOC) strategy (FEI WANG; DUARTE; HENDRIX, 2011), described in equations (2.17) and (2.18), is eliminate the reactive power oscillations by utilizing positive and negative sequence currents.

$$\mathbf{i}_p^* = \frac{P^*}{|\mathbf{v}^+|^2 + |\mathbf{v}^-|^2} (\mathbf{v}^+ + \mathbf{v}^-), \quad (2.17)$$

$$\mathbf{i}_q^* = \frac{Q^*}{|\mathbf{v}^+|^2 - |\mathbf{v}^-|^2} (\mathbf{v}_\perp^+ - \mathbf{v}_\perp^-). \quad (2.18)$$

In the stationary plane, in Fig. 2.4(a) and Fig. 2.4(c), the behavior of the currents differs from that of the APOC strategy. In this scenario, the maximum magnitude of current (\mathbf{i}) aligns with the maximum of voltage (\mathbf{v}) and with the minimum of the orthogonal projection (\mathbf{v}_\perp). Consequently, the reactive power remains constant, while the active power oscillates independent of the magnitudes of currents (\mathbf{i}_p) and (\mathbf{i}_q) and the degree of voltage unbalance, as described in Fig. 2.4(b) and Fig. 2.4(d).

Fig. 2.4: RPOC current path in stationary frame and instantaneous power (a), (b) for $u = 0,182$ and (c), (d) for v



Elaborated by the author.

2.3.4 Average Active and Reactive Control (AARC)

The Average Active and Reactive Control (AARC) strategy (RODRIGUEZ et al., 2007; RODRÍGUEZ et al., 2009), calculates the reference currents using the collective root-mean-square (RMS) norm $\|\mathbf{v}\|$ (CZARNECKI, 1988). In a three-phase three-wire unbalanced grid, $\|\mathbf{v}\|$ is defined by equation (2.19), where T represents the fundamental period.

$$\|\mathbf{v}\|^2 = \frac{1}{T} \int_0^T (v_a^2 + v_b^2 + v_c^2) dt = \frac{1}{T} \int_0^T |\mathbf{v}|^2 dt = |\mathbf{v}^+|^2 + |\mathbf{v}^-|^2, \quad (2.19)$$

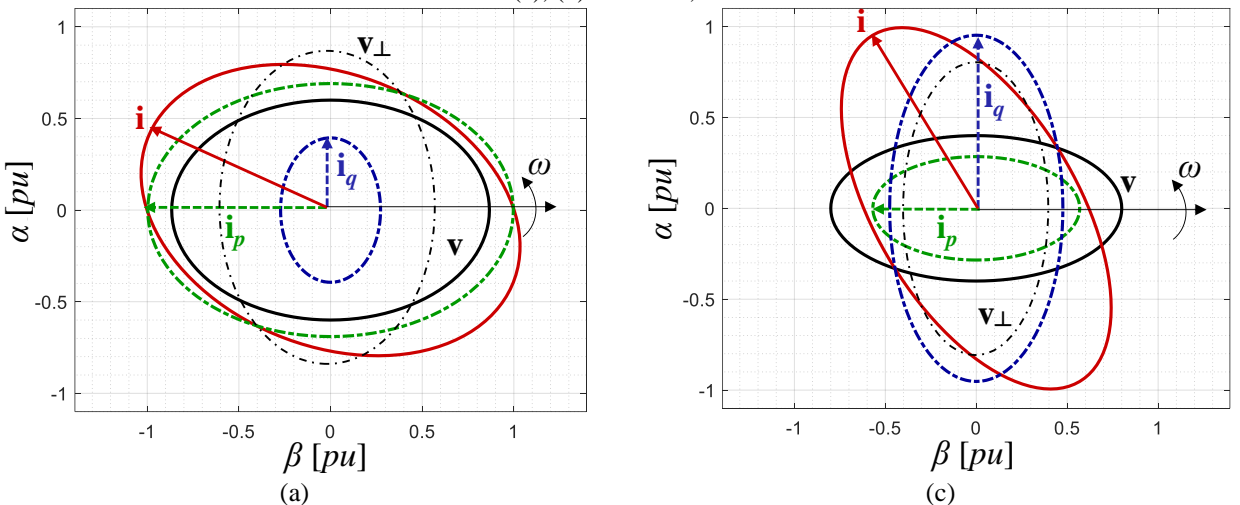
Subsequently, the reference currents obtained through equations (2.20) and (2.21) imply the smaller collective RMS current value necessary for feed-into the grid the average values of P^* and Q^* over a single fundamental grid cycle (CUPERTINO et al., 2019).

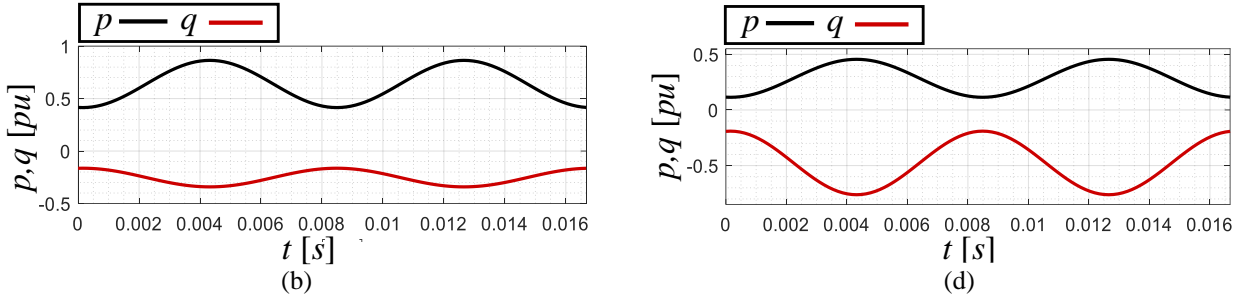
$$\mathbf{i}_p^* = \frac{P^*}{\|\mathbf{v}\|^2} \mathbf{v} = \frac{P^*}{|\mathbf{v}^+|^2 + |\mathbf{v}^-|^2} (\mathbf{v}^+ + \mathbf{v}^-), \quad (2.20)$$

$$\mathbf{i}_q^* = \frac{Q^*}{\|\mathbf{v}\|^2} \mathbf{v}_\perp = \frac{Q^*}{|\mathbf{v}^+|^2 + |\mathbf{v}^-|^2} (\mathbf{v}_\perp^+ + \mathbf{v}_\perp^-), \quad (2.21)$$

In the stationary frame Fig. 2.5(a) and Fig. 2.5(c), the current (\mathbf{i}_p) align with the voltage (\mathbf{v}) and (\mathbf{i}_q) with the orthogonal projection (\mathbf{v}_\perp). The higher is (\mathbf{i}_p) value in relation to (\mathbf{i}_q), the current vector (\mathbf{i}) tends to align its maximum with the maximum of voltage vector (\mathbf{v}). Consequently, active power oscillations are proportional to (\mathbf{i}_p), while reactive power oscillations are proportional do (\mathbf{i}_q), as depicted in Fig. 2.5(b) and Fig. 2.5(d).

Fig. 2.5: AARC current path in stationary reference frame and instantaneous power (a), (b) for $u = 0,182$ and (c), (d) for $u = 0,333$





Elaborated by the author.

2.3.5 Positive Negative Sequence Control (PNSC)

The Positive Negative Sequence Control (PNSC) strategy enables the computation of a set of currents that includes both positive and negative sequences. This calculation aims to counteract the cosine terms found in instantaneous power oscillations (equations **Error!** **Reference source not found.**). This cancellation is attainable only when one of the power references is adjusted to zero in equations (2.22) and (2.23).

$$\mathbf{i}_p^* = \frac{P^*}{|\mathbf{v}^+|^2 - |\mathbf{v}^-|^2} (\mathbf{v}^+ - \mathbf{v}^-), \quad (2.22)$$

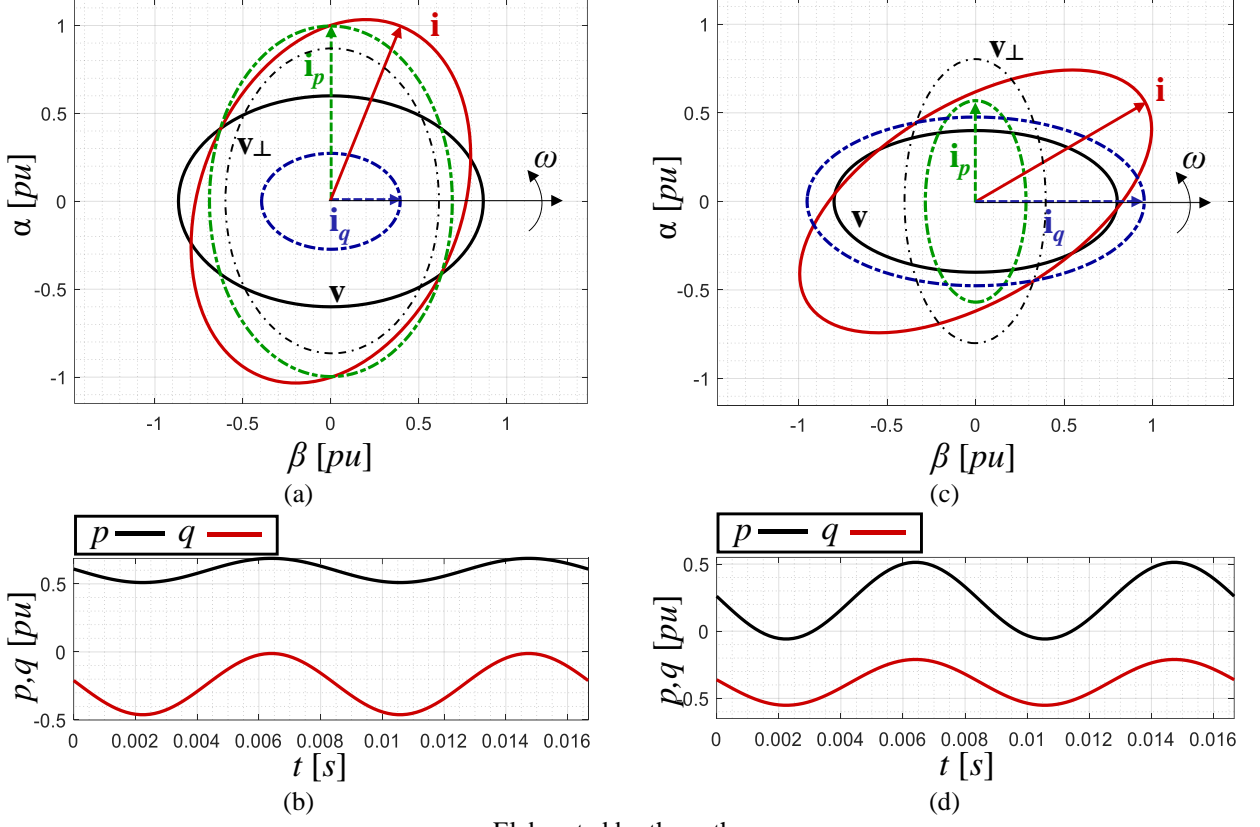
$$\mathbf{i}_q^* = \frac{Q^*}{|\mathbf{v}^+|^2 - |\mathbf{v}^-|^2} (\mathbf{v}_\perp^+ - \mathbf{v}_\perp^-). \quad (2.23)$$

In the $\alpha\beta$, depicted in Fig. 2.6(a) and Fig. 2.6(c), the active current (\mathbf{i}_p) has its maximum value aligned with minimum voltage (\mathbf{v}) magnitude, while the maximum value of reactive current (\mathbf{i}_q) and voltage (\mathbf{v}) are lined up. The higher is (\mathbf{i}_q) value in relation to (\mathbf{i}_p), the current vector (\mathbf{i}) tends to align its maximum value with the maximum of voltage vector (\mathbf{v}). Then, higher the value of (\mathbf{i}_p), greater are the oscillations of reactive power (q), meanwhile, higher the value of reactive current (\mathbf{i}_p), the greater are the oscillations in the active (p) power, as demonstrated in Fig. 2.6(b) and Fig. 2.6(d).

2.4 Adaptable or flexible power control strategies (APCS)

Adaptable or flexible power control strategies employ coefficients to modulate the interaction between positive and negative sequences. Several strategies of this nature have been proposed in works such as (CASTILLA et al., 2010; FEI WANG; DUARTE; HENDRIX, 2011; RODRIGUEZ et al., 2011; SOSA et al., 2016).

Fig. 2.6: PNSC current path in stationary reference frame and instantaneous power (a), (b) for $u = 0,182$ and (c), (d) for $u = 0,333$



Elaborated by the author.

This work will concentrate on the formulation of the Pliant Active and Reactive Power Control (PARPC) (FEI WANG; DUARTE; HENDRIX, 2011). The PARPC strategy, in equations (2.24) and (2.25), involves the utilization of coefficients, denoted as (k_p) and (k_q) , to regulate the interaction of active and reactive currents with positive and negative sequences. The PARPC strategy has the capability to replicate any of the sinusoidal reference current generation control methods discussed earlier. The relationship of (k_p) and (k_q) coefficients with previous control strategies is described in Tab. 2.1.

$$\mathbf{i}_p^* = \frac{P^*}{|\mathbf{v}^+|^2 + k_p |\mathbf{v}^-|^2} (\mathbf{v}^+ + k_p \mathbf{v}^-), \quad (2.24)$$

$$\mathbf{i}_q^* = \frac{Q^*}{|\mathbf{v}^+|^2 + k_q |\mathbf{v}^-|^2} (\mathbf{v}_\perp^+ + k_q \mathbf{v}_\perp^-). \quad (2.25)$$

Tab. 2.1: Relationship of PARPC and sinusoidal power control strategies

PARPC		
Strategy	k_p	k_q
AARC	1	1
BPSC	0	0
PNSC	-1	-1
APOC	-1	1
RPOC	1	-1

Elaborated by the author.

2.5 Magnitude of instantaneous power oscillations

In the preceding analyses, the instantaneous power oscillations were assessed visually by observing the patterns of voltage and current trajectories in the stationary reference frame. By utilizing the PARPC adaptive strategy equations, it becomes feasible to formulate mathematical expressions that quantify the magnitudes of these oscillations. The subsequent equations are contributions of this thesis and are also detailed in the paper SILVA et al. (2020).

First, replacing PARPC equations (2.24) and (2.25) in the oscillation terms of instantaneous power equations (2.11) and (2.12) it is obtained the equations (2.26) and (2.27).

$$\tilde{p} = \mathbf{v}^- \cdot \underbrace{\left(\frac{P^* \mathbf{v}^+}{|\mathbf{v}^+|^2 + k_p |\mathbf{v}^-|^2} \right)}_{i_p^+} + \mathbf{v}^+ \cdot \underbrace{\left(\frac{k_p P^* \mathbf{v}^-}{|\mathbf{v}^+|^2 + k_p |\mathbf{v}^-|^2} \right)}_{i_p^-} + \dots \\ \mathbf{v}^+ \cdot \underbrace{\left(\frac{k_q Q^* \mathbf{v}_\perp^-}{|\mathbf{v}^+|^2 + k_q |\mathbf{v}^-|^2} \right)}_{i_q^-} + \mathbf{v}^- \cdot \underbrace{\left(\frac{Q^* \mathbf{v}_\perp^+}{|\mathbf{v}^+|^2 + k_q |\mathbf{v}^-|^2} \right)}_{i_q^+}, \quad (2.26)$$

$$\tilde{q} = \mathbf{v}_\perp^- \cdot \underbrace{\left(\frac{Q^* \mathbf{v}_\perp^+}{|\mathbf{v}^+|^2 + k_q |\mathbf{v}^-|^2} \right)}_{i_q^+} + \mathbf{v}_\perp^+ \cdot \underbrace{\left(\frac{k_q Q^* \mathbf{v}_\perp^-}{|\mathbf{v}^+|^2 + k_q |\mathbf{v}^-|^2} \right)}_{i_q^-} + \dots \\ \mathbf{v}_\perp^+ \cdot \underbrace{\left(\frac{k_p P^* \mathbf{v}^-}{|\mathbf{v}^+|^2 + k_p |\mathbf{v}^-|^2} \right)}_{i_p^-} + \mathbf{v}_\perp^- \cdot \underbrace{\left(\frac{P^* \mathbf{v}^+}{|\mathbf{v}^+|^2 + k_p |\mathbf{v}^-|^2} \right)}_{i_p^+}. \quad (2.27)$$

According to the principle of dot product for orthogonal variables:

$$\begin{aligned}
 \mathbf{v} \cdot \mathbf{v}_\perp &= 0 \\
 (\mathbf{v}^+ + \mathbf{v}^-) \cdot (\mathbf{v}_\perp^+ + \mathbf{v}_\perp^-) &= 0 \\
 \underbrace{(\mathbf{v}^+ \cdot \mathbf{v}_\perp^+ + \mathbf{v}_\perp^- \cdot \mathbf{v}^-)}_0 \cdot (\mathbf{v}^- \cdot \mathbf{v}_\perp^+ + \mathbf{v}_\perp^- \cdot \mathbf{v}^+) &= 0 \\
 \mathbf{v}^- \cdot \mathbf{v}_\perp^+ &= -\mathbf{v}_\perp^- \cdot \mathbf{v}^+
 \end{aligned} \tag{2.28}$$

Then, using (2.28) on (2.26) and (2.27), the instantaneous power oscillations for PARPC is resumed on equations (2.29) and (2.30).

$$\tilde{p} = \left(\frac{(1+k_p)P^*}{|\mathbf{v}^+|^2 + k_p |\mathbf{v}^-|^2} \right) \mathbf{v}^+ \cdot \mathbf{v}^- + \left(\frac{(1-k_q)Q^*}{|\mathbf{v}^+|^2 + k_p |\mathbf{v}^-|^2} \right) \mathbf{v}_\perp^+ \cdot \mathbf{v}^-, \tag{2.29}$$

$$\tilde{q} = \left(\frac{(1+k_q)Q^*}{|\mathbf{v}^+|^2 + k_q |\mathbf{v}^-|^2} \right) \mathbf{v}_\perp^+ \cdot \mathbf{v}_\perp^- - \left(\frac{(1-k_p)P^*}{|\mathbf{v}^+|^2 + k_q |\mathbf{v}^-|^2} \right) \mathbf{v}_\perp^+ \cdot \mathbf{v}^-. \tag{2.30}$$

By substituting the set of equations (2.3) into (2.29) and (2.30) and associating the terms, equations (2.31) and (2.32) are obtained.

$$\begin{aligned}
 \tilde{p} &= \left(\frac{(1+k_p)|\mathbf{v}^+||\mathbf{v}^-| \cos(2\omega t + \phi^+ - \phi^-)}{|\mathbf{v}^+|^2 + k_p |\mathbf{v}^-|^2} \right) P^* + \dots \\
 &\quad \left(\frac{(1-k_q)|\mathbf{v}^+||\mathbf{v}^-| \sin(2\omega t + \phi^+ - \phi^-)}{|\mathbf{v}^+|^2 + k_q |\mathbf{v}^-|^2} \right) Q^*,
 \end{aligned} \tag{2.31}$$

$$\begin{aligned}
 \tilde{q} &= \left(\frac{(1+k_q)|\mathbf{v}^+||\mathbf{v}^-| \cos(2\omega t + \phi^+ - \phi^-)}{|\mathbf{v}^+|^2 + k_q |\mathbf{v}^-|^2} \right) Q^* - \dots \\
 &\quad \left(\frac{(1-k_p)|\mathbf{v}^+||\mathbf{v}^-| \sin(2\omega t + \phi^+ - \phi^-)}{|\mathbf{v}^+|^2 + k_p |\mathbf{v}^-|^2} \right) P^*.
 \end{aligned} \tag{2.32}$$

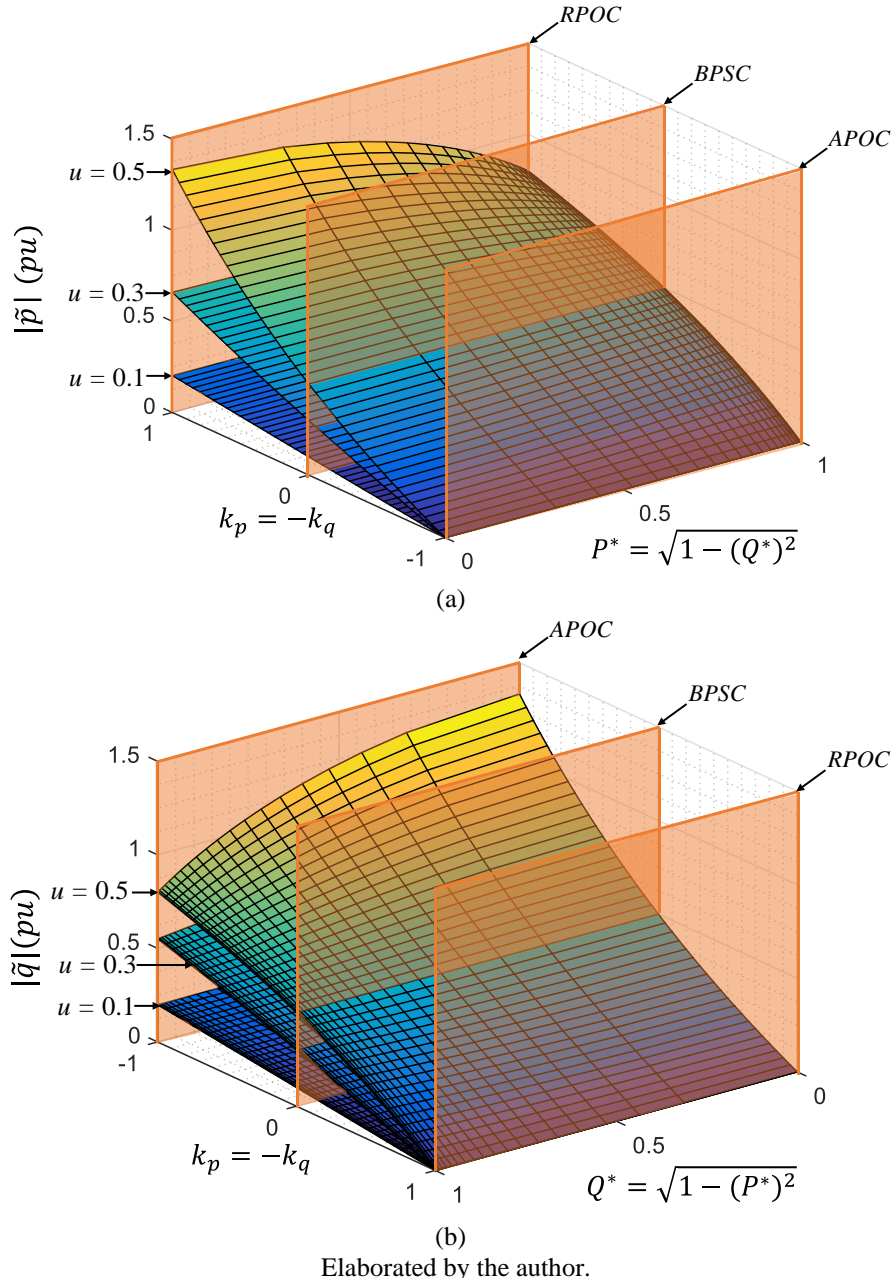
Finally, the orthogonal relation between sine and cosine functions in (2.31) and (2.32) allows for the calculation of power oscillation magnitudes through quadratic sums, resulting in equations (2.33) and (2.34), where $|\tilde{p}|$ and $|\tilde{q}|$ are the active and reactive power oscillation magnitude.

$$|\tilde{p}| = u \sqrt{\left(\frac{(1+k_p)P^*}{1+k_p u^2} \right)^2 + \left(\frac{(1-k_q)Q^*}{1+k_q u^2} \right)^2}, \tag{2.33}$$

$$|\tilde{q}| = u \sqrt{\left(\frac{(1+k_q)Q^*}{1+k_q u^2} \right)^2 + \left(\frac{(1-k_p)P^*}{1+k_p u^2} \right)^2}, \tag{2.34}$$

The graphical representations of equations (2.33) and (2.34), shown in Fig. 2.7(a) and Fig. 2.7(b), illustrate the magnitudes of active and reactive power oscillations. These calculations were conducted while keeping the total power at 1[pu], under varying levels of voltage unbalance, represented by the (u). The coefficients (k_p) and (k_q) were adjusted to adhere to the APOC, RPOC, and BPSC strategies, ensuring that they fall within the range of $-1 \leq k_p = -k_q \leq 1$.

Fig. 2.7: PARPC (a) active and (b) reactive power oscillation magnitude for coefficients $k_p = -k_q$.

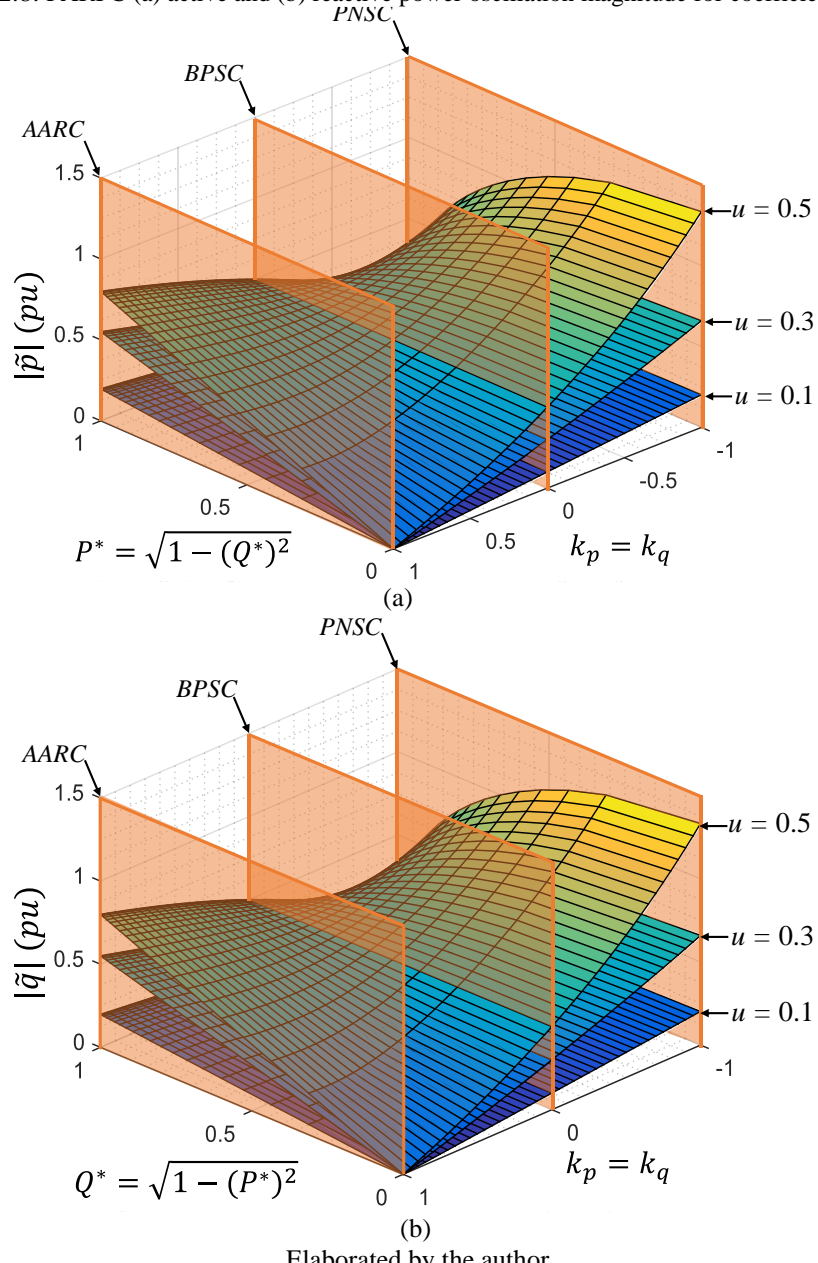


Elaborated by the author.

These graphs distinctly showcase that the use of APOC corresponds to higher values of reactive power oscillation magnitudes, while the employ of RPOC results in higher magnitudes of active power oscillations.

In line with the previous conditions, the graphs in Fig. 2.8(a) and Fig. 2.8(b) illustrate the magnitudes of active and reactive power oscillations, computed using equations (2.33) and (2.34). For these results, the coefficients (k_p) and (k_q) were adjusted to encompass the AARC, PNSC, and BPSC strategies, with $-1 \leq k_p = k_q \leq 1$. The total power is maintained at 1[pu] while varying the level of unbalance represented by the (u) factor.

Fig. 2.8: PARPC (a) active and (b) reactive power oscillation magnitude for coefficients $k_p = k_q$



Elaborated by the author.

Observations from these graphs reveal distinct behaviors. The AARC strategy demonstrates a linear relationship between the magnitude of power oscillation and its corresponding average value and u factor. In the PNSC strategy, the magnitude of the active power oscillation increases with the average reactive power value (Q^*), while the reactive power oscillation grows in tandem with the average active power value (P^*). This phenomenon becomes more pronounced as the u factor increases. Furthermore, any combination of (k_p) and (k_q) gains other than those resulting in the APOC and RPOC strategies fail to nullify power oscillations.

For a more in-depth assessment, by substituting the coefficients from Tab. 2.1 into equations (2.33) and (2.34), sets of equations presented in Tab. 2.2 were derived.

Tab. 2.2: Instantaneous power oscillation magnitude for different power control strategies

Strategy	$ \tilde{p} $	$ \tilde{q} $	
AARC	$\frac{2u}{1+u^2}P^*$	$\frac{2u}{1+u^2}Q^*$	(2.35)
PNSC	$\frac{2u}{1-u^2}Q^*$	$\frac{2u}{1-u^2}P^*$	(2.36)
BPSC	$u\sqrt{(P^*)^2 + (Q^*)^2}$	$u\sqrt{(P^*)^2 + (Q^*)^2}$	(2.37)
APOC	0	$u\sqrt{\left(\frac{2Q^*}{1+u^2}\right)^2 + \left(\frac{2P^*}{1-u^2}\right)^2}$	(2.38)
RPOC	$u\sqrt{\left(\frac{2P^*}{1+u^2}\right)^2 + \left(\frac{2Q^*}{1-u^2}\right)^2}$	0	(2.39)

Elaborated by the author.

These equations quantify the magnitudes of power oscillations for each strategy investigated in this chapter, and the conclusions drawn are as follows:

- **AARC:** The magnitude of the oscillations in (2.35) is linearly independent between the powers. In other words, the magnitude of active power oscillations depends on the reference value of active power, and the same applies to reactive power.
- **PNSC:** The magnitude of the oscillation of one power depends on the reference value of the other. Specifically, in (2.36), the magnitude of active power oscillations depends on the reactive power reference, and vice versa.
- **BPSC:** The magnitude of oscillations is the same for active and reactive power and depends on the total power reference in (2.37).

- **APOC:** The magnitude of reactive power oscillations has a nonlinear relationship with the total value of power (active and reactive) in (2.38), and presents the highest magnitude of reactive power oscillation among the evaluated strategies if compared in a same condition.
- **RPOC:** In opposite to APOC, the magnitude of active power oscillations has a nonlinear relationship with the total value of power (active and reactive) in (2.39), and exhibits the largest magnitude of active power oscillation among the evaluated strategies when they are compared in a same condition.

Finally, in all equations there is also a relationship with the unbalance factor, where strategies such as APOC, RPOC, and PNSC, due to the subtraction of (u) in the denominator of the equations, present oscillation magnitudes that increase more with the imbalance than the other ones.

2.6 Power flow of the control strategies

Upon observing the equations governing power control strategies, one encounters an intriguing aspect concerning the average values of active and reactive power across the symmetrical components and their correlation with the references P^* and Q^* . This observation stems from the fact that in certain strategies, the sequence components manifest values greater than zero, whereas in others, they are smaller than zero.

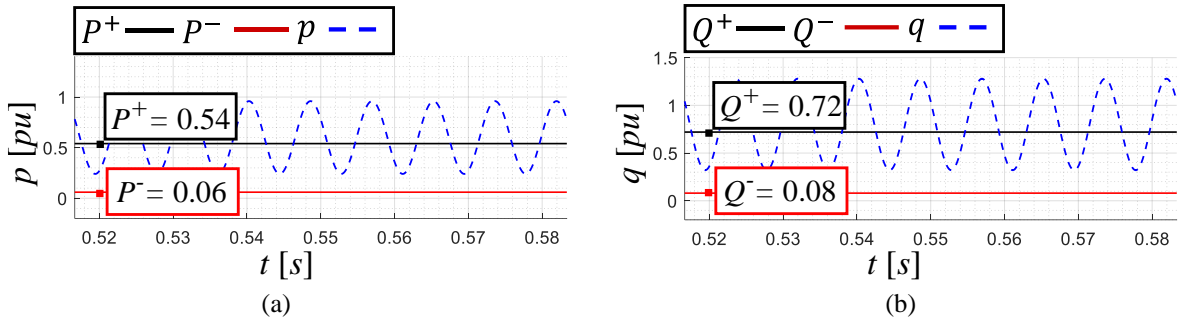
To elucidate the analysis, temporal values of the instantaneous power p and q , produced by the strategies for $P^* = 0.6$ [pu], $Q^* = 0.8$ [pu], and $u = 0.3333$ were plotted in Fig. 2.9 to Fig. 2.13. Additionally, the average values in the symmetric components were depicted on these graphs, with P^+ and Q^+ representing the average values in the positive sequence, and P^- and Q^- representing the average values in the negative sequence.

- **AARC:** As illustrated in Fig. 2.9 and consistent with equations (2.15) and (2.16), both $P^- > 0$ and $Q^- > 0$. Consequently, P^+ and Q^+ are smaller than the reference P^* and Q^* .
- **PNSC:** in Fig. 2.10 and corroborated by the equations (2.22) and (2.23), is observed $P^- < 0$ and $Q^- < 0$. Therefore, P^+ and Q^+ are higher than P^* and Q^* .
- **BPSC:** In equations (2.13) and (2.14), and described in Fig. 2.11, there is no production of negative sequence components ($P^- = 0$ and $Q^- = 0$). Then, P^+ and Q^+ are equal to P^* and Q^* , respectively.

- **APOC:** As shown in Fig. 2.12 and described by (2.15) and (2.16), $P^- < 0$ and $Q^+ > 0$, resulting in $P^+ > P^*$ and $Q^+ < Q^*$.
- **RPOC:** Finally, as shown in Fig. 2.13 and by equations (2.17) and (2.18), $P^- > 0$ and $Q^- < 0$, which is opposite to APOC. Consequently $P^+ < P^*$ and $Q^+ > Q^*$.

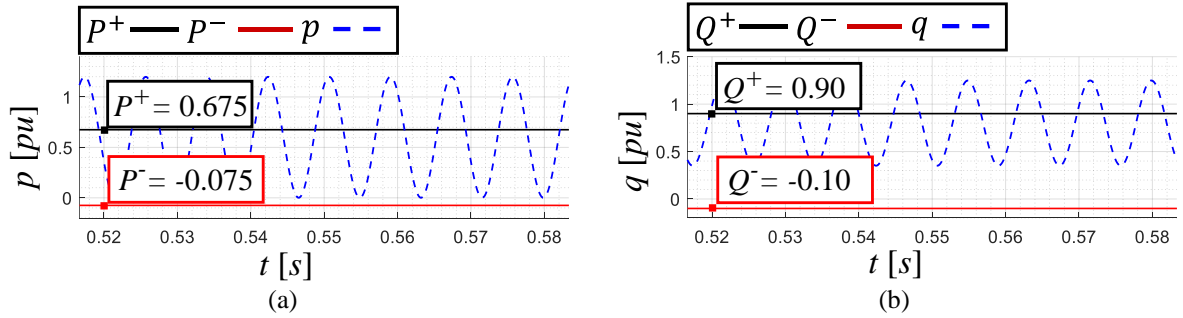
In this way, it is evident that some strategies exhibit greater power production through the positive sequence than others. This insight will enable a better assessment of the voltage support promoted by the power control strategies discussed in Chapter 4.

Fig. 2.9: (a) active and (b) reactive instantaneous and average power in positive and negative sequences for AARC strategy with $P^* = 0.6[\text{pu}]$ and $Q^* = 0.8[\text{pu}]$ and $u = 0.3333$.



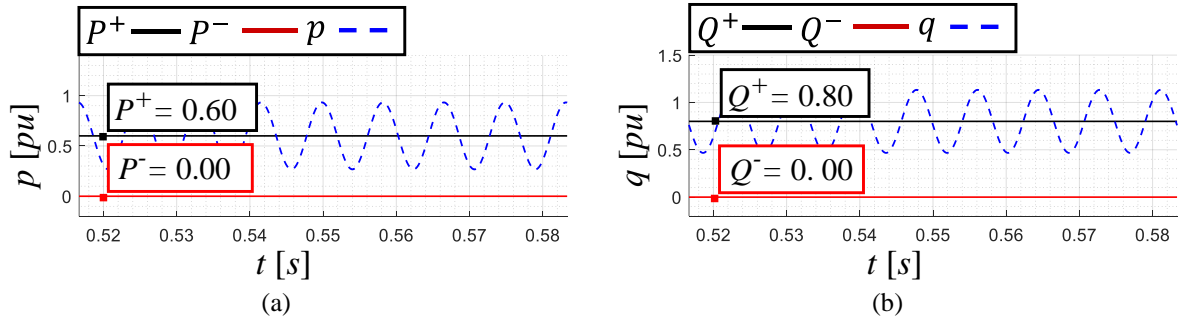
Elaborated by the author.

Fig. 2.10: (a) active and (b) reactive instantaneous and average power in positive and negative sequences for PNSC strategy with $P^* = 0.6[\text{pu}]$ and $Q^* = 0.8[\text{pu}]$ and $u = 0.3333$.



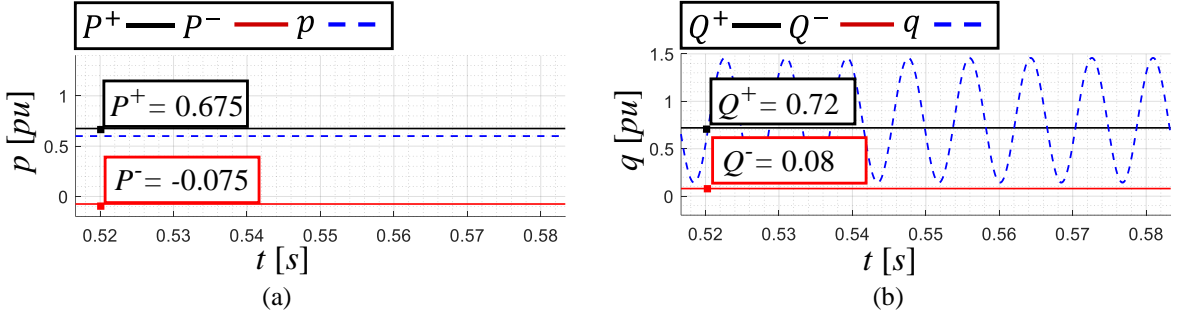
Elaborated by the author.

Fig. 2.11: (a) active and (b) reactive instantaneous and average power in positive and negative sequences for BPSC strategy with $P^* = 0.6[\text{pu}]$ and $Q^* = 0.8[\text{pu}]$ and $u = 0.3333$.



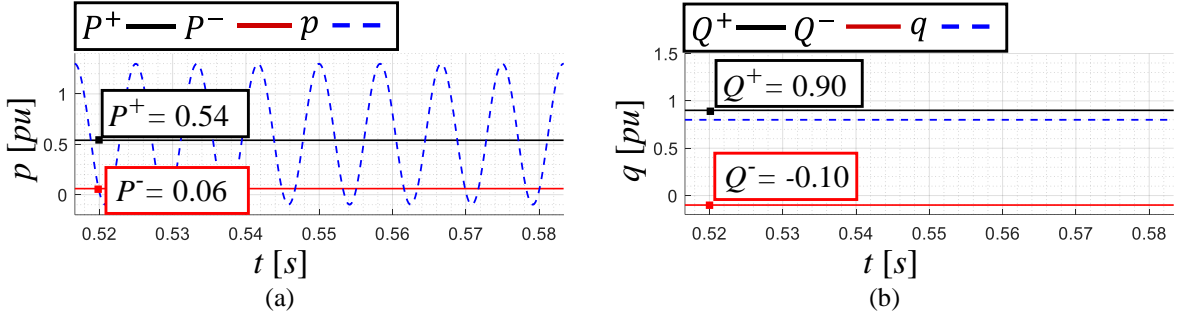
Elaborated by the author.

Fig. 2.12: (a) active and (b) reactive instantaneous and average power in positive and negative sequences for APOC strategy with $P^* = 0.6[\text{pu}]$ and $Q^* = 0.8[\text{pu}]$ and $u = 0.3333$.



Elaborated by the author.

Fig. 2.13: (a) active and (b) reactive instantaneous and average power in positive and negative sequences for APOC strategy with $P^* = 0.6[\text{pu}]$ and $Q^* = 0.8[\text{pu}]$ and $u = 0.3333$.



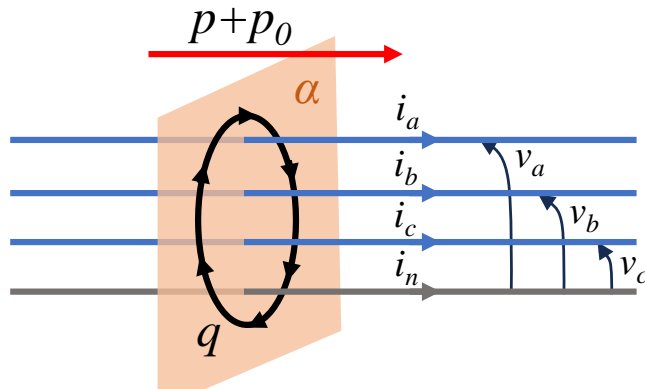
Elaborated by the author.

At this point, it's pertinent to question a nomenclature aspect: why refer to power values as greater or less than zero rather than indicating the direction of power flow, i.e., from the grid to the generator or vice versa? Addressing this query necessitates an understanding of the powers concept established in the instantaneous power theory, which serves as the theoretical foundation for the mathematical developments in this thesis.

Consider a generic four-wire system where the conductors pass through a surface α , as depicted in Fig. 2.14. According to AKAGI et al. (2017), in a three-phase system, whether with or without a neutral conductor, instantaneous active power, denoted as p , represents the total instantaneous energy per second crossing the surface α , exchanged between the source and the load.

In contrast, reactive, or imaginary power, denoted as q , is proportional to the amount of energy exchanged between the phases of the system, thereby not contributing to the effective transfer of energy between the source and the load. Consequently, assigning a direction to of reactive power flow is a misconception.

Fig. 2.14: Instantaneous power flow.



Adapted from AKAGI et al. (2017).

2.7 Chapter conclusions

The interplay between positive and negative sequence currents and voltages leads to instantaneous power oscillations in both active and reactive power at twice the fundamental frequency of the electrical mains.

It is important to note that when using sinusoidal currents, it is not possible to simultaneously eliminate both active and reactive power oscillations, but they can be applied to reduce or eliminate at least one of these oscillations.

The objective of this chapter is to provide the theoretical foundation for explaining power control strategies, utilizing the instantaneous powers theory. In addition, the author of this thesis has developed equations that depict power fluctuations by deriving them from the strategies' own equations. This approach enables a comprehensive description of the strategies' features and constraints, and part the results obtained in this chapter were published in the paper (SILVA et al., 2020)

Tab. 2.3 provides a summary of the key characteristics of the strategies explored in this chapter. The analysis reveals that AARC and PNSC strategies are only effective at canceling power fluctuations under specific conditions. As a result, the use of these strategies may not be justified when compared to the others. Consequently, the proposals presented in this work primarily concentrate on the APOC, RPOC, and BPSC. Nonetheless, all the mathematical formulations can be expanded to strategies with sinusoidal currents, incorporating the utilization of generic equations.

Tab. 2.3: Comparative summary of the sinusoidal reference currents power control strategies.

Strategy	Active reference	Reactive reference	Characteristics
AARC	$\mathbf{i}_p^{+*} = \frac{P^*}{ \mathbf{v}^+ ^2 + \mathbf{v}^- ^2} \mathbf{v}^+$ $\mathbf{i}_p^{-*} = \frac{P^*}{ \mathbf{v}^+ ^2 + \mathbf{v}^- ^2} \mathbf{v}^-$	$\mathbf{i}_q^{+*} = \frac{Q^*}{ \mathbf{v}^+ ^2 + \mathbf{v}^- ^2} \mathbf{v}_\perp^+$ $\mathbf{i}_q^{-*} = \frac{Q^*}{ \mathbf{v}^+ ^2 + \mathbf{v}^- ^2} \mathbf{v}_\perp^-$	<ul style="list-style-type: none"> • Unbalanced currents. • Cancels the sine terms of instantaneous power oscillations. • It always has active power oscillations, except when $P^* = 0$; • It always has reactive power oscillations, except when $Q^* = 0$; • The reference currents computed result in the smallest collective RMS value to deliver P^* and Q^* over one grid period.
PNSC	$\mathbf{i}_p^{+*} = \frac{P^*}{ \mathbf{v}^+ ^2 - \mathbf{v}^- ^2} \mathbf{v}^+$ $\mathbf{i}_p^{-*} = \frac{-P^*}{ \mathbf{v}^+ ^2 - \mathbf{v}^- ^2} \mathbf{v}^-$	$\mathbf{i}_q^{+*} = \frac{Q^*}{ \mathbf{v}^+ ^2 - \mathbf{v}^- ^2} \mathbf{v}_\perp^+$ $\mathbf{i}_q^{-*} = \frac{-Q^*}{ \mathbf{v}^+ ^2 - \mathbf{v}^- ^2} \mathbf{v}_\perp^-$	<ul style="list-style-type: none"> • Unbalanced currents. • Cancels the cosine terms of instantaneous power oscillations. • Singular point at $\mathbf{v}^+ = \mathbf{v}^-$; • Cancels the active power oscillations only if $Q^* = 0$; • Cancels the reactive power oscillations only if $P^* = 0$.
BPSC	$\mathbf{i}_p^{+*} = \frac{P^*}{ \mathbf{v}^+ ^2} \mathbf{v}^+$ $\mathbf{i}_p^{-*} = 0$	$\mathbf{i}_q^{+*} = \frac{Q^*}{ \mathbf{v}^+ ^2} \mathbf{v}_\perp^+$ $\mathbf{i}_q^{-*} = 0$	<ul style="list-style-type: none"> • Balanced currents. • It always has active and reactive power oscillations, except when $P^* = Q^* = 0$.
APOC	$\mathbf{i}_p^{+*} = \frac{P^*}{ \mathbf{v}^+ ^2 - \mathbf{v}^- ^2} \mathbf{v}^+$ $\mathbf{i}_p^{-*} = \frac{-P^*}{ \mathbf{v}^+ ^2 - \mathbf{v}^- ^2} \mathbf{v}^-$	$\mathbf{i}_q^{+*} = \frac{Q^*}{ \mathbf{v}^+ ^2 + \mathbf{v}^- ^2} \mathbf{v}_\perp^+$ $\mathbf{i}_q^{-*} = \frac{Q^*}{ \mathbf{v}^+ ^2 + \mathbf{v}^- ^2} \mathbf{v}_\perp^-$	<ul style="list-style-type: none"> • Unbalanced currents. • No active power oscillation. • Singular point at $\mathbf{v}^+ = \mathbf{v}^-$; • It always has reactive power oscillations, except when $P^* = Q^* = 0$; • Presents the sine and cosine terms of the reactive instantaneous power oscillation.
RPOC	$\mathbf{i}_p^{+*} = \frac{P^*}{ \mathbf{v}^+ ^2 + \mathbf{v}^- ^2} \mathbf{v}^+$ $\mathbf{i}_p^{-*} = \frac{P^*}{ \mathbf{v}^+ ^2 + \mathbf{v}^- ^2} \mathbf{v}^-$	$\mathbf{i}_q^{+*} = \frac{Q^*}{ \mathbf{v}^+ ^2 - \mathbf{v}^- ^2} \mathbf{v}_\perp^+$ $\mathbf{i}_q^{-*} = \frac{-Q^*}{ \mathbf{v}^+ ^2 - \mathbf{v}^- ^2} \mathbf{v}_\perp^-$	<ul style="list-style-type: none"> • Unbalanced currents. • No reactive power oscillations. • Singular point at $\mathbf{v}^+ = \mathbf{v}^-$; • It always has active power oscillations, except when $P^* = Q^* = 0$; • Presents the sine and cosine terms of the active instantaneous power oscillation.

Elaborated by the author.

Chapter III

GRID-CONNECTED CONVERTERS

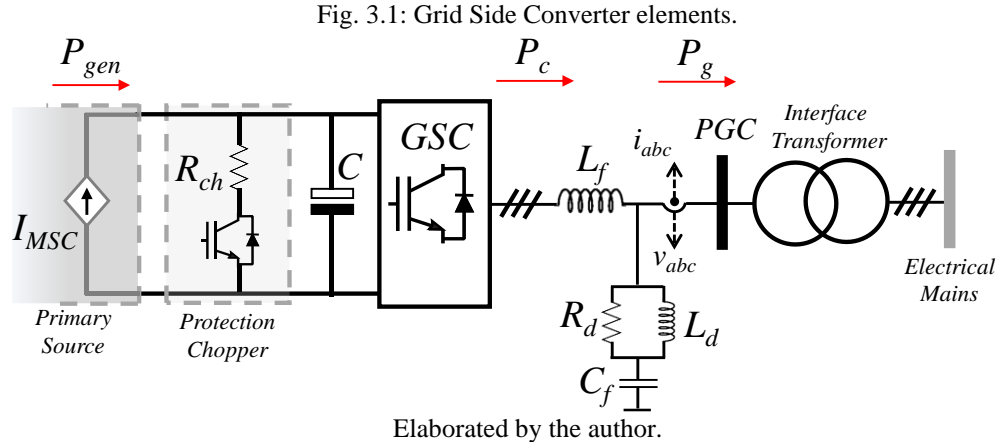
GRID-CONNECTED converters are subjected to electrical current limitations, typically constrained by the nominal ratings of their semiconductor switches. During low voltage ride-through (LVRT) operations, the voltage levels in the grid will impose restrictions on the maximum amount of power that the converter can supply to the grid. Grid codes mandate that priority should be given to injecting positive sequence reactive current during LVRT. In this chapter, a strategy is proposed to restrict active power delivery during LVRT events. This strategy aligns with grid codes, ensuring compliance, and can be applied in conjunction with power control strategies presented in the previous chapter. Finally, the examination of the impacts of different power control strategies on the power electronic converters is evaluated.

3.1 Full-power (Type IV) wind energy conversion systems

The full-scale converter plays a fundamental role in defining the dynamic behavior of the generation system from the grid's perspective. This is especially pertinent due to the mechanical components, which exhibit substantial inertia in contrast to the electrical one. Any sudden disparity between the generated active power and the one delivered to the grid is effectively managed by the protection chopper circuit to avoid the increasing of DC bus voltage (CONROY; WATSON, 2007; MENDES et al., 2016)

Hence, the forthcoming analyses in this work will focus on the GSC (Grid Side Converter), while the MSC (Machine Side Converter) will be represented as a controlled source responsible for injecting active power into the DC bus, as denoted in Fig. 3.1.

The LCL filter, is designed to reduce the high-order harmonics content in GSC currents (KOUCHAKI; NYMAND, 2018). The element $L1$ represents the inverter side inductor; $L2$ is the equivalent inductance from the transformer interface with PGC (point of generator connection), the filter shunt leg comprises the capacitor C_f in series with the high frequency damping resistance R_d and inductance L_d . Finally, the DC bus equivalent capacitance is symbolized by the capacitor C , and the chopper resistance by R_{ch} .



3.2 GSC control

The simplified control diagram for the GSC is illustrated in Fig. 3.2 and consists of cascaded control loops:

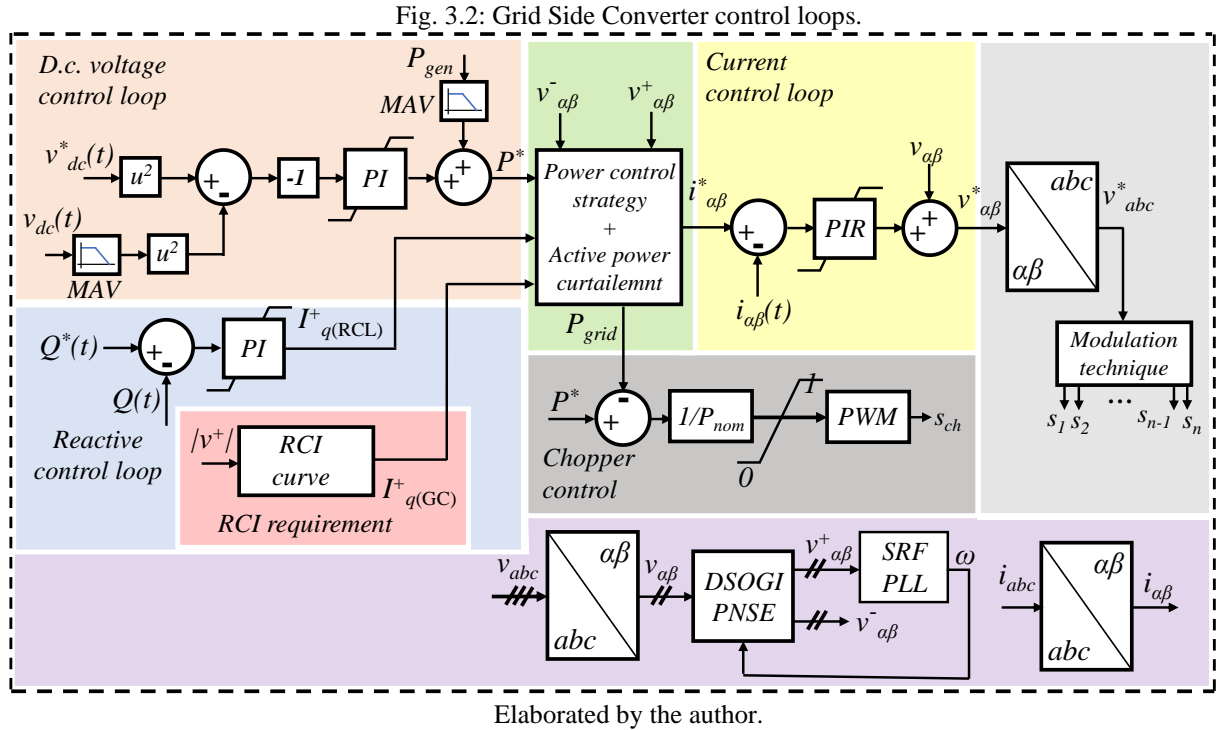
- **Current Control Loop:** This loop controls the output current and has the fastest dynamics among the control loops.
- **Voltage Control Loop:** This loop regulates the DC bus voltage using the quadratic value of the voltage.
- **Reactive Power Control:** This loop regulates reactive power under normal operating conditions but is disabled during voltage ride-through events.

The detailed models of these control loops are explained in Appendix B, and, the control is performed in the stationary frame ($\alpha\beta$) for the following reasons:

- **Reduced Linear Transformations:** The $\alpha\beta$ frame requires fewer linear transformations compared to the dq frame, thereby reducing computational workload.
- **Mitigated Dependency on Synchronism Structures:** Operating in the $\alpha\beta$ reference frame lessens the reliance on synchronism structures, which are used only for voltage sequence decomposition.
- **Reduced Control Structures:** This allows for the simultaneous control of positive and negative sequence currents with a single control structure.

The decomposition of mains voltage into sequence components is accomplished through the utilization of a Double Second Order Generalized Integrator (DSOGI), a Positive-Negative Sequence Extractor (PNSE) (RODRIGUEZ et al., 2008), and a Synchronous Reference Frame Phase-Locked Loop (SRF-PLL) (GOLESTAN; GUERRERO; VASQUEZ, 2017).

The intermediate block between the current loop and the outermost loops is the algorithm for limiting active power and generating reference currents through power control strategies. This algorithm represents one of the main contributions of this thesis and is explained in the following subsection.



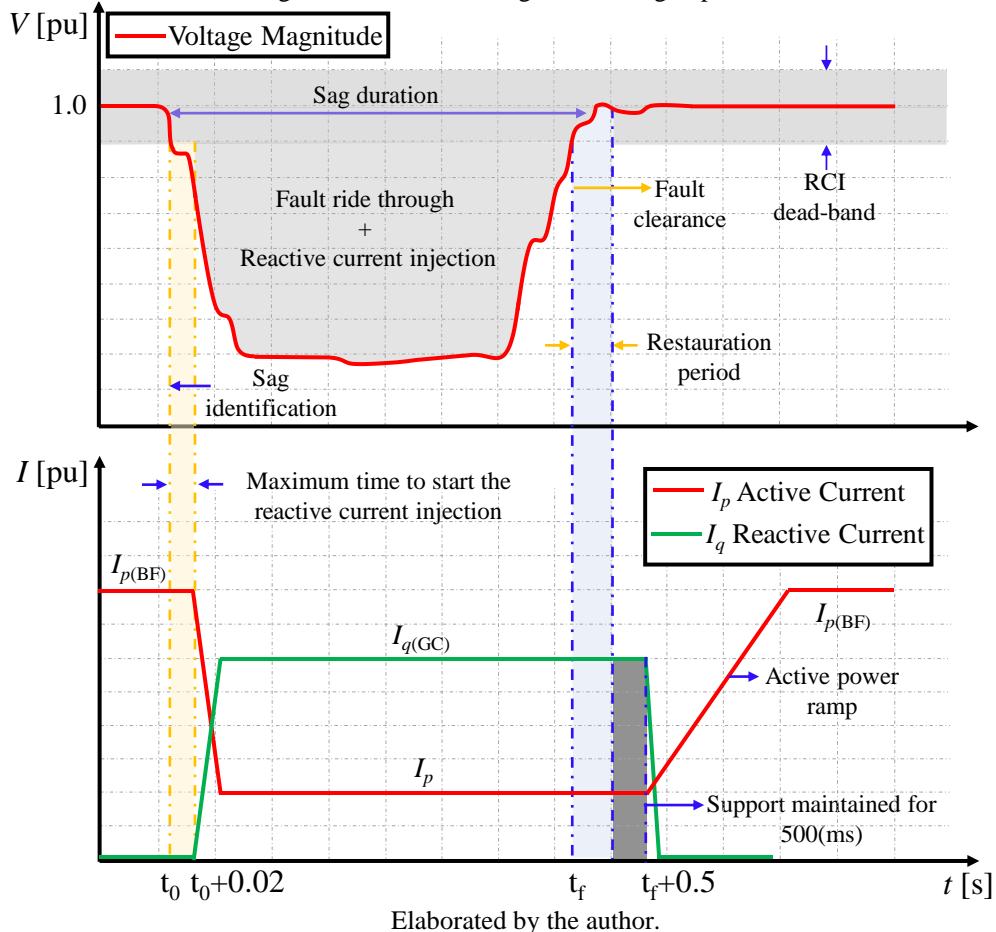
3.3 Active power curtailment algorithm

In a simplified representation, Fig. 3.3 illustrates the grid codes (GC) specifications of the wind turbine's response during voltage ride through operation. It is important to note that the graph is primarily based on the guidelines provided by **TENNET TSO GMBH (2015)**, which imposes stricter requirements compared to other GCs examined in this study, and a sequence of requirements are set as follows:

- Following the onset of a voltage sag, the generating unit (GU) is allowed a maximum of 20[ms] to start the reactive current injection.
- Throughout the fault occurrence and after the return of voltage within the dead-band range, the wind turbine must provide its maximal current capacity to the mains, even in pre-fault scenarios characterized by low active power production.
- During the restauration period, the provision of reactive support must be sustained for a duration of 500[ms].

- Upon the clearance of the fault, the wind turbine must promptly re-establish active power production and return to the pre-fault operational state, with active power ramp gradient of no less than 20% of the nominal power per second.

Fig. 3.3: Grid code voltage ride through operation.



Elaborated by the author.

Because of the inherent physical constraints of semiconductors, grid-connected converters have their current capacity restricted at the nominal rating of their static switches (JIA et al., 2021). Consequently, during voltage ride-through operation, characterized by a reduction in voltage magnitude and GCs emphasis on injecting reactive current, the active power supplied to the grid must be proportionally curtailed.

Then, in view of these restrictions, a contribution of this thesis is a dynamic active power curtailment algorithm, which is also described in SILVA; SOUSA AND MENDES, (2021). The proposed algorithm offers flexibility in its application with different power control strategies, and outlines four specific control priorities:

- 1. Compliance with voltage ride-through and RCI requirements:** The primary objective is to ensure observance to the voltage ride-through and RCI provisions defined in GCs.

2. **Limiting grid converter current to rated value:** Maintaining the current within converter rated capacity is of paramount importance to safeguard the power converter and avoid undesired disconnections from the mains.
3. **Control of Active Power Production:** This priority empowers the management of active power production under both normal operating conditions and in the event of grid faults.
4. **Mitigation of power oscillations during unbalanced voltage sags:** Whenever feasible, the algorithm seeks to mitigate power oscillations that may arise during unbalanced voltage sags.

3.3.1 Mathematical formulation for strategies with negative sequence currents

Power control strategies, such as APOC and RPOC, use negative sequence currents to manipulate power oscillations. Moreover, during voltage sags the grid voltage is not constant and the converter has limited current capacity, which makes it difficult to maintain the output power, and the RCI requirement itself is based on the magnitude of the current.

In view of these issues, the power control strategies should be reformulated in terms of currents. Then, using the PARPC equations (2.24) and (2.25), they are rewritten in (3.1) and (3.2).

$$\mathbf{i}_p^* = I_p^+ \frac{\mathbf{v}^+}{|\mathbf{v}^+|} + k_p I_P^- \frac{\mathbf{v}^-}{|\mathbf{v}^-|}, \quad (3.1)$$

$$\mathbf{i}_q^* = I_q^+ \frac{\mathbf{v}_\perp^+}{|\mathbf{v}^+|} + k_q I_q^- \frac{\mathbf{v}_\perp^-}{|\mathbf{v}^-|}, \quad (3.2)$$

With the currents magnitudes defined in (3.3) to (3.5)

$$I_p^+ = I_p = \frac{P^*}{|\mathbf{v}^+|^2 + k_p |\mathbf{v}^-|^2} |\mathbf{v}^+|, \quad (3.3)$$

$$I_q^+ = I_q = \frac{Q^*}{|\mathbf{v}^+|^2 + k_q |\mathbf{v}^-|^2} |\mathbf{v}^+|, \quad (3.4)$$

$$I_P^- = I_P^+ \frac{|\mathbf{v}^-|}{|\mathbf{v}^+|} = I_p u, \quad (3.5)$$

$$I_q^- = I_q^+ \frac{|\mathbf{v}^-|}{|\mathbf{v}^+|} = I_q u$$

Initially, to meet the RCI requirements, the magnitude of positive sequence reactive current I_q^+ should be computed in accordance with the provisions laid out in GCs, which is defined in equation (3.6).

$$I_{q(GC)}^+ = \begin{cases} 0 & \text{if } 0.85 < V^+ \leq 1.10 \text{ pu}, \\ mV^+ + c & \text{if } 0.50 < V^+ \leq 0.85 \text{ pu}, \\ I_{q(max)} & \text{if } 0.00 < V^+ \leq 0.50 \text{ pu}, \end{cases} \quad (3.6)$$

As an example, the RCI curve equation in Brazilian Grid Code (ONS, 2020a), the slope (m) is -2.8571[pu], the linear coefficient (c) is 2.4168 [pu], and a maximum reactive current ($I_{q(max)}$) of 1 [pu]. Therefore, for sags where the voltage falls below 0.5[pu], the entire converter current must be allocated to support the voltage, rendering any form of compensation or active power generation unfeasible.

The current magnitude can be determined through the vector path in the stationary frame in equation (3.7).

$$| \mathbf{i} | = \sqrt{I_\alpha^2 + I_\beta^2}, \quad (3.7)$$

where:

$$\begin{aligned} I_\alpha &= \sqrt{(i_{\alpha(p)})^2 + (i_{\alpha(q)})^2}, \\ I_\beta &= \sqrt{(i_{\beta(p)})^2 + (i_{\beta(q)})^2}. \end{aligned} \quad (3.8)$$

The subscripts p and q denoting the active and reactive components of the current. Then, applying the equations (3.1) to (3.5) in (3.7), it is obtained the current magnitude expression in (3.9).

$$| \mathbf{i} | = \sqrt{\frac{| \mathbf{v}^+ |^2 (I_p^{+2} + I_q^{+2}) + | \mathbf{v}^- |^2 (k_p^2 I_p^{+2} + k_q^2 I_q^{+2}) + 2(v_\alpha^+ v_\alpha^- + v_\beta^+ v_\beta^-)(k_p I_p^{+2} + k_q I_q^{+2})}{| \mathbf{v}^+ |^2}}. \quad (3.9)$$

Under the assumption $k_p \in \{-1, +1\}$ and $k_q \in \{-1, +1\}$, relating the approximation (3.10) and the equation (2.8), the current's magnitude in (3.9) can be calculated as a function of $\cos(\phi)$. Then, applying the Clarke's inverse transformation the current magnitude for each phase is defined by the set of equations (3.11).

$$v_\alpha^+ v_\alpha^- + v_\beta^+ v_\beta^- \approx v_\alpha^+ v_\alpha^- - v_\beta^+ v_\beta^-, \quad (3.10)$$

$$\begin{aligned}
I_a &= \sqrt{\frac{|\mathbf{v}^+|^2 + |\mathbf{v}^-|^2 - 2|\mathbf{v}^+||\mathbf{v}^-|\cos(\phi)}{|\mathbf{v}^+|^2}(I_p^{+2} + I_q^{+2})}, \\
I_b &= \sqrt{\frac{|\mathbf{v}^+|^2 + |\mathbf{v}^-|^2 - 2|\mathbf{v}^+||\mathbf{v}^-|\cos(\phi - 2\pi/3)}{|\mathbf{v}^+|^2}(I_p^{+2} + I_q^{+2})}, \\
I_c &= \sqrt{\frac{|\mathbf{v}^+|^2 + |\mathbf{v}^-|^2 - 2|\mathbf{v}^+||\mathbf{v}^-|\cos(\phi + 2\pi/3)}{|\mathbf{v}^+|^2}(I_p^{+2} + I_q^{+2})},
\end{aligned} \tag{3.11}$$

According to (3.11), the smaller cosine value result in the phase current with the greater magnitude. Then, decomposing the cosine function of each phase equations, maximum magnitude current can be formulated as a function of the phase angle ϕ in (3.12) and (3.13).

$$I_{max} = \sqrt{\frac{|\mathbf{v}^+|^2 + |\mathbf{v}^-|^2 - 2|\mathbf{v}^+||\mathbf{v}^-|x}{|\mathbf{v}^+|^2}(I_p^{+2} + I_q^{+2})}, \tag{3.12}$$

$$x = \min\left(-\frac{1}{2}\cos(\phi) + \frac{\sqrt{3}}{2}\sin(\phi), -\frac{1}{2}\cos(\phi) - \frac{\sqrt{3}}{2}\sin(\phi)\right). \tag{3.13}$$

Using the approximation (3.10) allows the derivation of analytical expressions (3.12) and (3.13) to calculate the maximum current (I_{max}). However, this approximation introduces inaccuracies, potentially leading to overcurrent in the converter. To mitigate this risk, it is crucial to constrain (I_{max}) to the rated current of the primary source (I_{rated}) which must be lower than the maximum current of the semiconductors (I_{sw}), as described by inequation (3.14).

$$I_{max} \leq I_{rated} < I_{sw}. \tag{3.14}$$

Owing to the priority of ensuring the RCI, it is necessary to curtail active power production. Consequently, by manipulating equation (3.12), the maximum magnitude of the positive sequence active current ($I_{p(max)}^+$) can be determined by (3.15).

$$I_{p(max)}^+ = \sqrt{\frac{(I_{max})^2|\mathbf{v}^+|^2}{|\mathbf{v}^+|^2 + |\mathbf{v}^-|^2 - 2|\mathbf{v}^+||\mathbf{v}^-|x} - (I_q^+)^2}, \tag{3.15}$$

The active current derived from the primary source can be defined using equation (3.16), and this value should be lower than or equal to the one calculated in equation (3.15).

$$I_p^+ = P^* \frac{|\mathbf{v}^+|}{|\mathbf{v}^+|^2 + k_p |\mathbf{v}^-|^2}. \quad (3.16)$$

In a pre-fault scenario characterized by low active power production, equation (3.12) can also be manipulated to recalculate the reactive current resulting in (3.17), the objective is optimizing voltage support.

$$I_q^+ = \sqrt{\frac{(I_{max})^2 |\mathbf{v}^+|^2}{|\mathbf{v}^+|^2 + |\mathbf{v}^-|^2 - 2|\mathbf{v}^+||\mathbf{v}^-|x} - (I_p^+)^2}. \quad (3.17)$$

After obtaining the positive sequence magnitudes, the negative sequence values are determined through the expressions (3.18).

$$\begin{aligned} I_p^- &= k_p u I_p^+, \\ I_q^- &= k_q u I_q^+. \end{aligned} \quad (3.18)$$

The maximum active power supplied to the grid following the algorithm's interactions is:

$$P_{grid} = I_p^+ \frac{|\mathbf{v}^+|^2 + k_p |\mathbf{v}^-|^2}{|\mathbf{v}^+|}. \quad (3.19)$$

3.3.2 Mathematical formulation for strategies with only positive sequence

The BPSC strategy relies solely on the positive sequence for reference current computation, resulting in a simplified maximum current calculation by equation (3.20).

$$I_{max} = \sqrt{I_p^+{}^2 + I_q^+{}^2}. \quad (3.20)$$

Hence, the maximum active current can be defined by (3.21).

$$I_{p(max)}^+ = \sqrt{I_{max}{}^2 - I_{q(GC)}^+{}^2}. \quad (3.21)$$

The active current derived from the primary source can be defined using equation (3.22).

$$I_p^+ = \frac{P_{gen}}{|\mathbf{v}^+|}. \quad (3.22)$$

In a pre-fault scenario characterized by low active power production, the reactive current should be recalculated using (3.23) to optimize the voltage support:

$$I_q^+ = \sqrt{I_{max}{}^2 - I_p^+{}^2}. \quad (3.23)$$

The negative sequence currents are null:

$$\begin{aligned} I_p^- &= 0, \\ I_q^- &= 0. \end{aligned} \tag{3.24}$$

Finally, the active power injected into the grid following the execution of the algorithm is computed using equation (3.25).

$$P_{grid} = I_p^+ \cdot |\mathbf{v}^+|. \tag{3.25}$$

3.3.3 Algorithm description

With equations established, it is crucial to outline the sequence in which they are employed within the algorithm's implementation. This process is elucidated in the flowchart presented in Fig. 3.4. The algorithm takes as input the values of active power from the DC bus control loop (P^*), the positive and negative sequence voltages ($v_{\alpha\beta}^+$ and $v_{\alpha\beta}^-$), the currents magnitude from reactive power control loop $I_{q(RCL)}$ and from RCI grid code $I_{q(GC)}$.

Subsequently, it calculates the unbalance factor u using equation (2.1), computes the magnitudes of the positive and negative sequence voltages $|\mathbf{v}^+|$ and $|\mathbf{v}^-|$ as defined in (2.7), and derives the $\cos(\phi)$ and $\sin(\phi)$ via the set of equations (2.8). Additionally, it calculates the active current I_p^+ using (3.16), or (3.22) if BPSC strategy is employed.

At this stage in the algorithm's execution, the decision-making process unfolds. Initially, it assesses whether the magnitude of the positive sequence voltage is less than the starting value of the RCI curve (V_{RCI}).

If the answer is yes, the algorithm proceeds as follows:

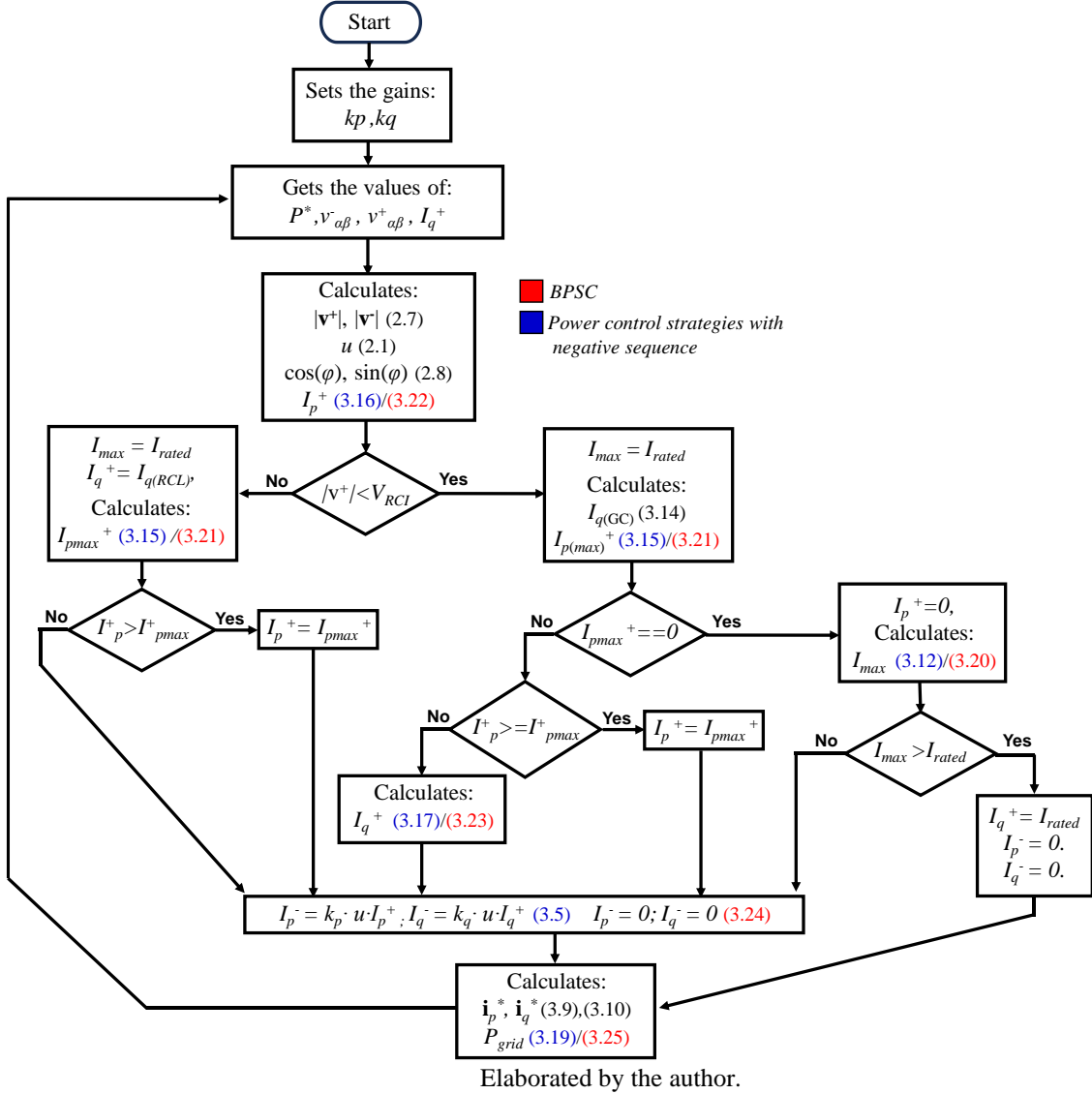
- The reactive power control loop is deactivated, and $I_{q(RCL)}$ is ignored.
- It sets the maximum current (I_{max}) to the GSC rated value (I_{rated}). The positive sequence reactive current is determined based on the RCI requirements ($I_{q(GC)}^+$).
- The algorithm calculates the value of maximum active positive sequence current $I_{p(max)}^+$, and checks if it is null.

If $I_{p(max)}^+$ is null:

- The positive sequence active current (I_p^+) is set to zero.
- I_{max} is recalculated, and the algorithm checks if I_{max} is greater than I_{rated} .

If I_{max} is greater than I_{rated} :

Fig. 3.4: Active power curtailment algorithm flowchart



- The positive sequence reactive current I_q^+ is limited at the value of I_{rated} , and the negative sequence components are set to null.

If I_{max} is not greater than I_{rated} , the algorithm proceeds to calculate the negative sequence components.

Returning to $I_{p(max)}^+$ is not null, the algorithm checks if I_p^+ is lower than $I_{p(max)}^+$.

- If yes, I_q^+ is recalculated to optimize grid support, and the negative sequence components are calculated.
- If no, I_p^+ is limited at the value of $I_{p(max)}^+$, and the negative sequence components are calculated.

Returning to the initial comparison, if positive sequence voltage is greater or equal than V_{RCL} , which could be 0.9 or 0.85, depends on GC:

- The reactive power control loop is activated (or still active), the grid code reactive current $I_{q(GC)}^+$ is null. Consequently, I_q^+ derived solely from $I_{q(RCL)}^+$.
- I_{max} is set to the GSC's I_{rated} .
- The algorithm calculates $I_{p(max)}^+$ and verifies if I_p^+ is greater than $I_{p(max)}^+$.

If I_p^+ is greater than $I_{p(max)}^+$:

- I_p^+ is limited at the value of $I_{p(max)}^+$, and the negative sequence components are calculated.

If not, the algorithm proceeds to calculate the negative sequence components.

After establishing the magnitudes, the current references are computed based on equations (3.1) and (3.2), along with the calculation of the active power P_{grid} supplied to the mains, using equation (3.19) (or (3.25) if BPSC is employed).

3.4 Power oscillation impacts on the grid converter

At this point, it is pertinent to ask: why cancel or reduce instantaneous power oscillations, given that grid codes do not address this issue? And what is their impact on the electronic converter?

As discussed in Chapter 2, it is possible to cancel either active or reactive power oscillations, but not both simultaneously. Moreover, canceling one type of oscillation results in a greater magnitude in the opposite component; for example, canceling instantaneous active power oscillations leads to greater reactive power oscillations and vice versa. And as explained in Appendix C, the losses in the power electronic converter elements are proportional to the magnitude of the current but also to the energy oscillations.

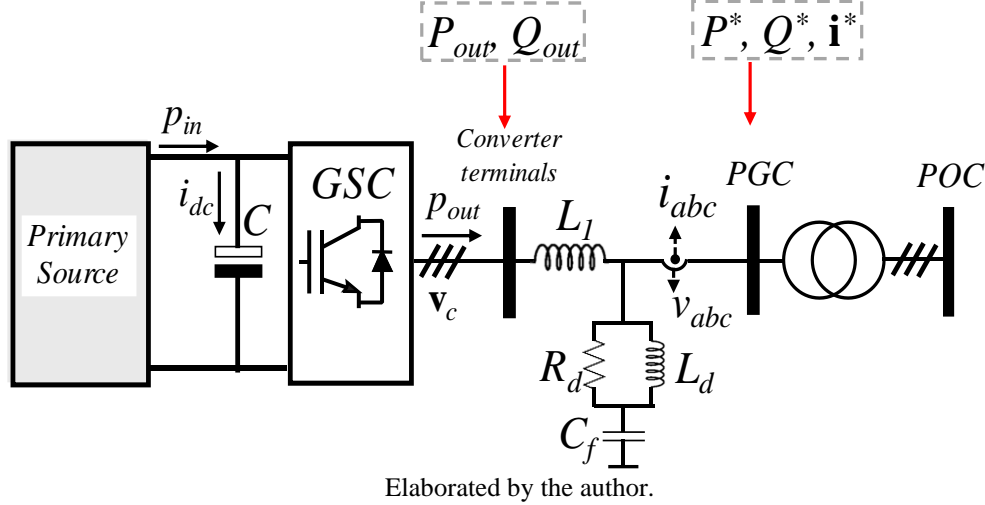
Regarding reactive power, the WEC are designed to operate with a high-power factor, therefore, the diodes of the semiconductor modules are slightly required. However, during LVRT operation, most of the converter current will be reactive, and the diodes will conduct for longer. For asymmetric faults, the current flowing through the diode can be even higher, considering that there is an instantaneous increase in the reactive current value due to the power oscillations.

3.4.1 Active power oscillations and DC capacitors losses

The grid active power and energy oscillations in the DC bus capacitors are directly related, as will be demonstrated in this section. Consider the representation of the GSC shown in Fig.

3.5, which describes the energy balance. In steady state, the GSC's instantaneous input active power (P_{in}) consists of a continuous value. And under balanced voltages, the instantaneous power at the GSC terminals (p_{out}) is also constant. Therefore, neglecting the converter losses, the input and output power are equal, and there is no energy flow through the DC bus capacitors.

Fig. 3.5: Grid Side Converter elements.



Elaborated by the author.

However, in an unbalanced fault, p_{out} is formed by the sum of average (P_{out}) and oscillatory (\tilde{p}_{out}) terms. Assuming the protection chopper can balance the power from the primary generator with the power delivered to the grid, i.e., $P_{in} = P_{out}$, the energy balance in the DC bus can be defined by (3.26). This means that the energy flowing through the capacitors corresponds to the oscillatory portion of the output power.

$$\Delta p = P_{in} - p_{out} = p_{in} - (P_{out} + \tilde{p}_{out}) = -\tilde{p}_{out}. \quad (3.26)$$

The power set-points and reference currents managed by the power control strategies correspond to the point where voltage and current measurements are taken. Consequently, the GSC output current will differ slightly from the reference values generated by the power control strategies, as it must also supply the currents consumed by the filter.

For simplicity, the current consumed by the capacitive branch of the LCL filter is ignored. Therefore, the GSC terminal output power oscillation (\tilde{p}_{out}) can be approximated by (3.27), where v_c^{+-} represents the positive and negative sequence voltages synthesized at the converter terminals.

$$\tilde{p}_{out} = v_c^- \cdot i_p^+ + v_c^+ \cdot i_p^- + v_c^- \cdot i_q^+ + v_c^+ \cdot i_q^-, \quad (3.27)$$

By substituting the PARPC equations (2.24) and (2.25) in (3.27) and manipulating the terms, the relation (3.28) is obtained. Then, the power oscillations at the converter terminals

depend not only on the adopted control strategy but also on the interaction between the voltages at the converter terminals and the measuring point, and to cancel the power oscillations at the converter terminals, the filter dynamics must be considered when calculating the reference currents.

$$\tilde{p}_{\text{out}} = \left(\frac{(\mathbf{v}^+ \cdot \mathbf{v}_c^- + k_p \mathbf{v}^- \cdot \mathbf{v}_c^+)}{|\mathbf{v}^+|^2 + k_p |\mathbf{v}^-|^2} \right) P^* + \left(\frac{(\mathbf{v}_\perp^+ \cdot \mathbf{v}_c^- - k_q \mathbf{v}_\perp^- \cdot \mathbf{v}_c^+)}{|\mathbf{v}^+|^2 + k_q |\mathbf{v}^-|^2} \right) Q^*. \quad (3.28)$$

In addition, the interaction between \mathbf{v} and \mathbf{v}_c does not allow to define an analytical equation that precisely determines \tilde{p}_{out} oscillations magnitude. Approximation could be done by rewriting (3.28) in terms of the variables at the converter terminals, resulting in (3.29). In this equation, ϕ_c^+ and ϕ_c^- represent the positive and negative sequence phase angles of the converter terminal voltages, respectively.

$$\begin{aligned} \tilde{p}_{\text{out}} \approx & \left(\frac{(1 + k_p)|\mathbf{v}_c^+||\mathbf{v}_c^-| \cos(2\omega t + \phi_c^+ - \phi_c^-)}{|\mathbf{v}_c^+|^2 + k_p |\mathbf{v}_c^-|^2} \right) P_{\text{out}} + \dots \\ & \left(\frac{(1 - k_q)|\mathbf{v}_c^+||\mathbf{v}_c^-| \sin(2\omega t + \phi_c^+ - \phi_c^-)}{|\mathbf{v}_c^+|^2 + k_q |\mathbf{v}_c^-|^2} \right) Q_{\text{out}}, \end{aligned} \quad (3.29)$$

The oscillation magnitude is described in (3.30) and u_c is the GSC terminal voltages unbalance factor

$$|\tilde{p}_{\text{out}}| \approx u_c \sqrt{\left(\frac{(k_p^+ + k_p^-)P_{\text{out}}}{k_p^+ + k_p^- u_c^2} \right)^2 + \left(\frac{(k_q^+ - k_q^-)Q_{\text{out}}}{k_q^+ + k_q^- u_c^2} \right)^2}, \quad (3.30)$$

Since \tilde{e}_{cap} is the instantaneous oscillation of energy in the DC bus, it can be calculated using the (3.31). Replacing (3.29) and performing the integral, \tilde{e}_{cap} is defined in equation (3.32).

$$\tilde{e}_{\text{cap}} = \int \Delta p \, dt = \int (-\tilde{p}_{\text{out}}) \, dt. \quad (3.31)$$

$$\begin{aligned} \tilde{e}_{\text{cap}} \approx & \dots \\ & \frac{u_c}{2\omega} \left\{ - \left(\frac{(1 + k_p) \sin(2\omega t + \phi_c^+ - \phi_c^-)}{1 + k_p u_c^2} \right) P_{\text{out}} \right. \\ & \left. + \left(\frac{(1 - k_p) \cos(2\omega t + \phi_c^+ - \phi_c^-)}{1 + k_q u_c^2} \right) Q_{\text{out}} \right\}, \end{aligned} \quad (3.32)$$

The magnitude of \tilde{e}_{cap} , denoted as ΔE_{cap} , is given by (3.33). This equation defines the proportional relationship between grid active power oscillations and the energy oscillations in the DC bus capacitors.

$$\Delta E_{cap} = \dots$$

$$\frac{u_c}{2\omega} \sqrt{\left(\frac{(1+k_p)P_{out}}{1+k_p u_c^2}\right)^2 + \left(\frac{(1-k_q)Q_{out}}{1+k_q u_u^2}\right)^2} = \frac{|\tilde{p}_{out}|}{2\omega}. \quad (3.33)$$

According to CUPERTINO et al. (2019), the bus voltage is defined in (3.34), where V_{dc} is the average value of the DC voltage, \tilde{v}_{dc} is the instantaneous oscillation around this average value and C is the bus equivalent capacitance. Thus, using (3.33), the magnitude $\Delta \tilde{v}_{dc}$ is approximated by (3.35).

$$v_{dc} = V_{dc} + \tilde{v}_{dc} = V_{dc} + \frac{1}{C V_{dc}} \int \Delta p \, dt = V_{dc} + \frac{\tilde{e}_{cap}}{C V_{dc}}, \quad (3.34)$$

$$\Delta \tilde{v}_{dc} \approx \frac{\Delta E}{C V_{dc}} = \frac{|\tilde{p}_{out}|}{2\omega C V_{dc}} \quad (3.35)$$

Some considerations must be made regarding (3.35). While it suggests that using the APOC strategy can potentially eliminate energy fluctuations in the DC bus capacitors, this ideal outcome is not achievable in practice. As demonstrated earlier, the presence of the filter introduces dynamics that prevent the complete elimination of these fluctuations. Therefore, $\Delta \tilde{v}_{dc}$ is:

- Directly proportional to magnitude of grid active power oscillations $|\tilde{p}_{out}|$.
- Inversely proportional to DC voltage level V_{dc} , bus capacitance C , grid frequency ω .

To mitigate the impacts of voltage sags on the grid converter, hardware improvements like increasing capacitance or raising the operating voltage of the capacitors can be considered. However, a safer and more cost-effective alternative is to reduce active power oscillations. Notably, energy oscillations and the resulting current components in the capacitors depend just on active power oscillations.

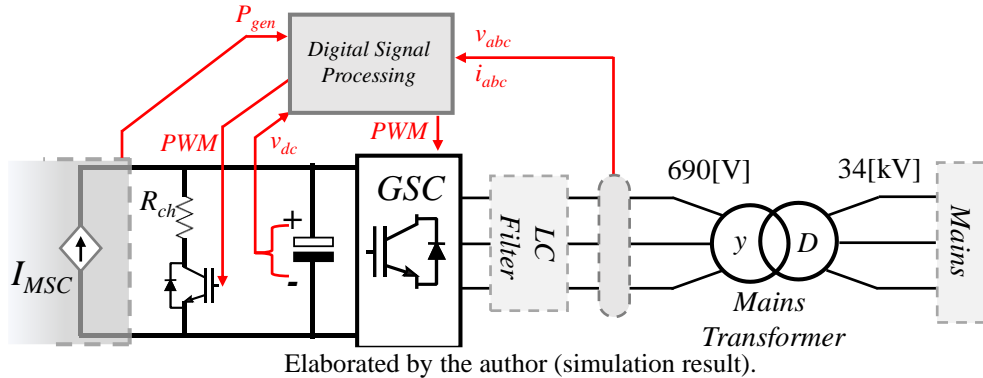
3.5 Simulation results

In this section, computational simulations were conducted using data from a real 2.1[MW] full power wind power generator using a power converter stack Infineon 6MS30017E43W33015 (INFINEON, 2012). The simulations were performed using PLECS software (version 4.5.6). PLECS stands out as a specialized software tailored specifically for power electronics simulation, offering distinct advantages over more generic simulation tools.

Detailed information about the simulated system data can be found in Appendix D, section D.a.

The simulation diagram is depicted in Fig. 3.6, where the primary source simulated as a power source injecting produced energy into the GSC DC bus. All control and signal processing were implemented in C language using a PLECS C-script block, with a sampling interval set at twice the switching frequency.

Fig. 3.6: Simulation diagram



To limit the DC bus voltage during voltage ride-through operation, PWM chopper control was employed, as further explained in Appendix C. Before and during the voltage sag, the MSC operates with generator nominal active power (2[MW]), and the reactive control loop regulates the grid reactive power in 0.0[Var], achieving unitary power factor, and the converter supply reactive power just to supplies the grid LCL filter.

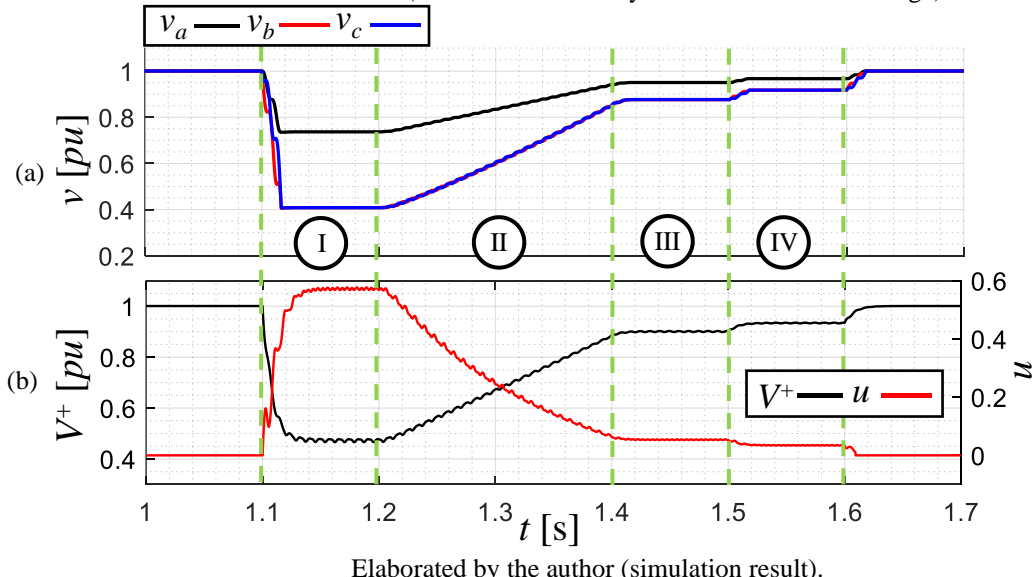
3.5.1 Algorithm evaluation

To evaluate the proposed active power curtailment algorithm, it is simulated a grid voltage profile as shown in Fig. 3.7(a). This profile is designed to address various operating scenarios stipulated in the Brazilian grid code voltage ride through and reactive current injection (ONS, 2020a). The resulting voltage profile leads to the positive sequence magnitude and unbalance factor described in Fig. 3.7(b), thereby defining the following intervals:

- **Interval I:** Positive sequence of 0.48 [pu] and an unbalance factor of 0.57. The entire converter's current capacity is allocated to RCI. It is not possible to produce active power or negative sequence currents.
- **Interval II:** As the voltage magnitude gradually increases, the converter can inject reactive current, generate active power, and mitigate power quality issues.

- **Interval III:** Positive sequence of 0.9[pu] and unbalance factor of 0.05, this interval encompasses operation within the threshold region between RCI requirement voltage support and normal operation.
- **Interval IV:** Positive sequence of 0.93[pu] and unbalance factor of 0.034. Operation takes place with unbalanced voltages but operates within the RCI requirement dead-band ($I_q = 0$).

Fig. 3.7: (a) mains voltage profile for algorithm evaluation and (b) resulting positive sequence voltage and unbalance factor (values normalized by the converter rated voltage).



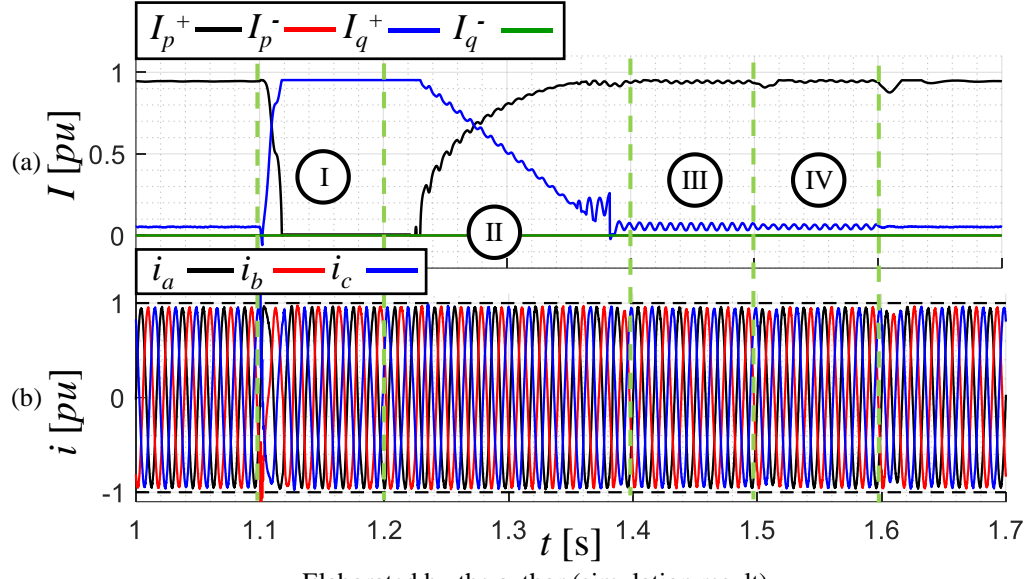
Elaborated by the author (simulation result).

The magnitudes of the currents generated by the active power curtailment algorithm applied with the BPSC strategy are depicted in Fig. 3.8(a). As detailed in the preceding chapter, the BPSC strategy computes reference current values exclusively using the positive sequence voltage, resulting in balanced currents, as illustrated in Fig. 3.8(b).

The interaction between balanced currents and unbalanced voltages generates oscillations in the voltage on the DC bus, as shown in Fig. 3.9(a). These oscillations are the result of instantaneous power oscillations present in the mains (Fig. 3.9(b)) and persist throughout the evaluated operating ranges.

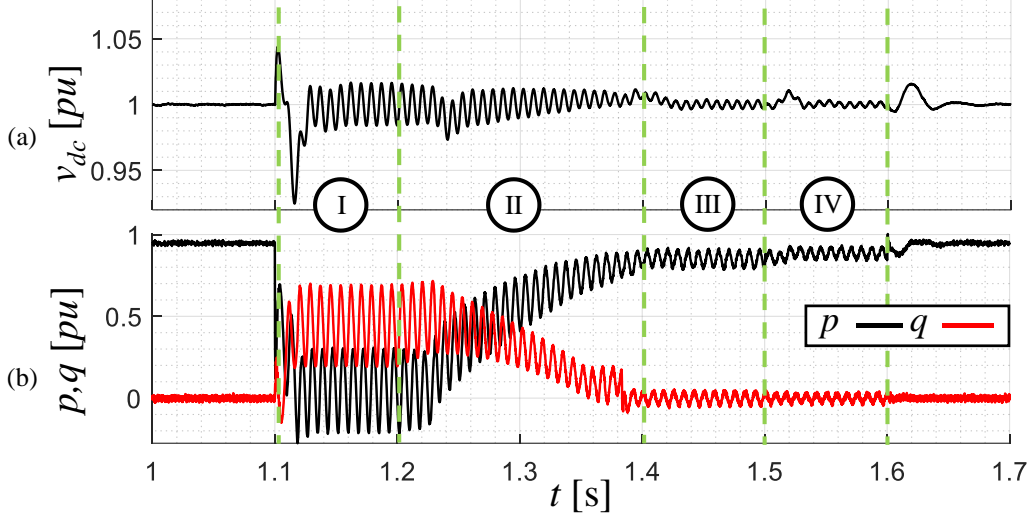
For the APOC strategy, the magnitude of the currents calculated by the algorithm and the resulting in the mains are shown in Fig. 3.10. The APOC strategy generates currents in the negative sequence to compensate active power oscillations. However, for **interval I**, due to the very low voltage level, the entire capacity of the converter must be used for the injection of positive sequence reactive current. Then, to ensure that the rated current of the converter is not exceeded, the algorithm reduces active and negative sequence currents to zero, acting with the same behavior of BPSC strategy.

Fig. 3.8: (a) reference currents generated by the proposed algorithm and (b) mains currents for BPSC (values normalized by the converter rated current).



Elaborated by the author (simulation result).

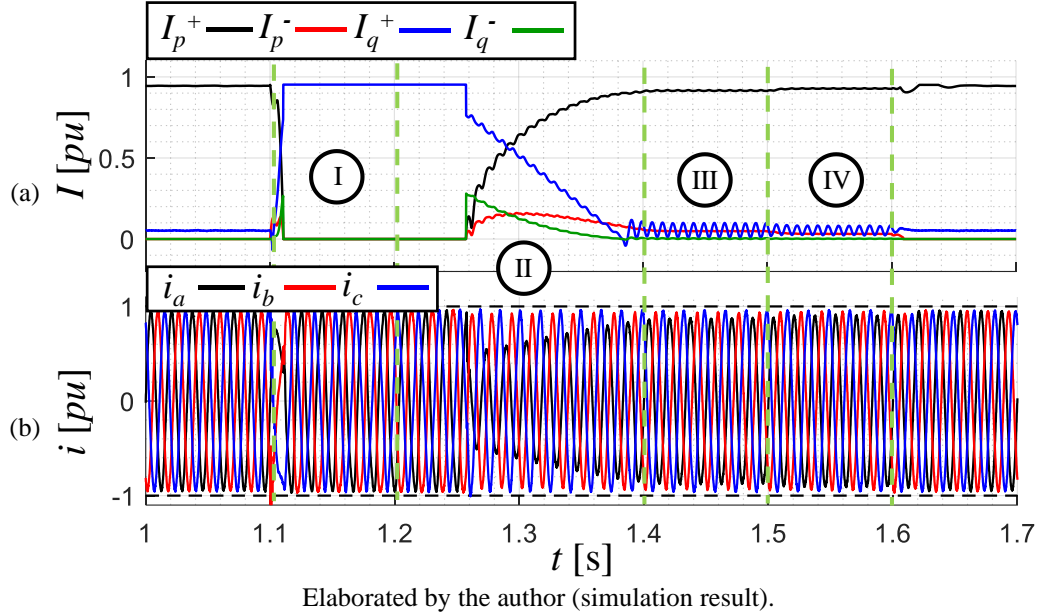
Fig. 3.9: (a) DC bus voltage and (b) mains active and reactive power for BPSC (values normalized by the converter rated parameters).



Elaborated by the author (simulation result).

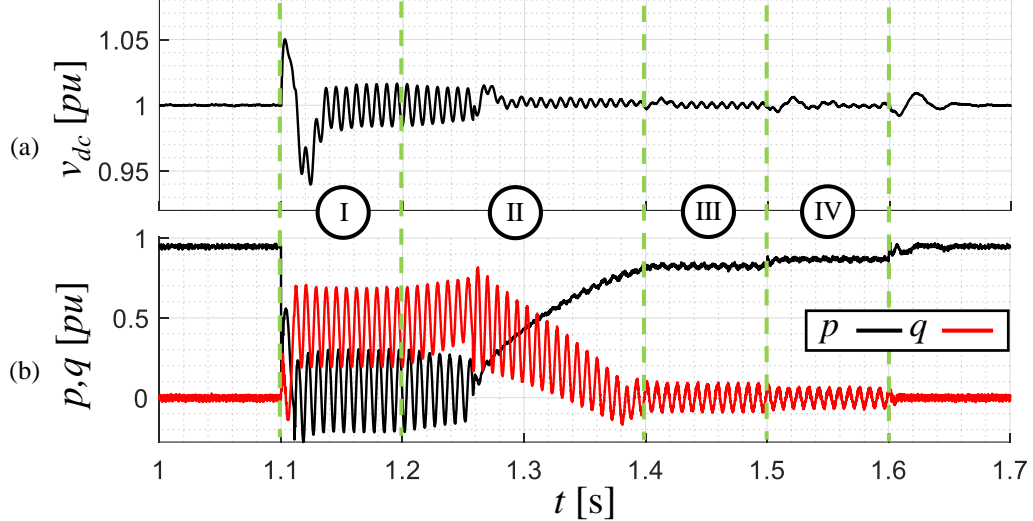
As the voltage level increases, active power generation increases, and the currents become unbalanced due to the negative sequence currents. Consequently, voltage oscillation on the DC bus occurs only in initial time interval, as shown in Fig. 3.11(a), and after that, there is compensation for the active power oscillation, as shown in Fig. 3.11(b).

Fig. 3.10: (a) reference currents generated by the proposed algorithm and (b) mains currents for APOC (values normalized by the converter rated current).



Elaborated by the author (simulation result).

Fig. 3.11: (a) DC bus voltage and (b) mains active and reactive power for APOC (values normalized by the converter rated parameters).

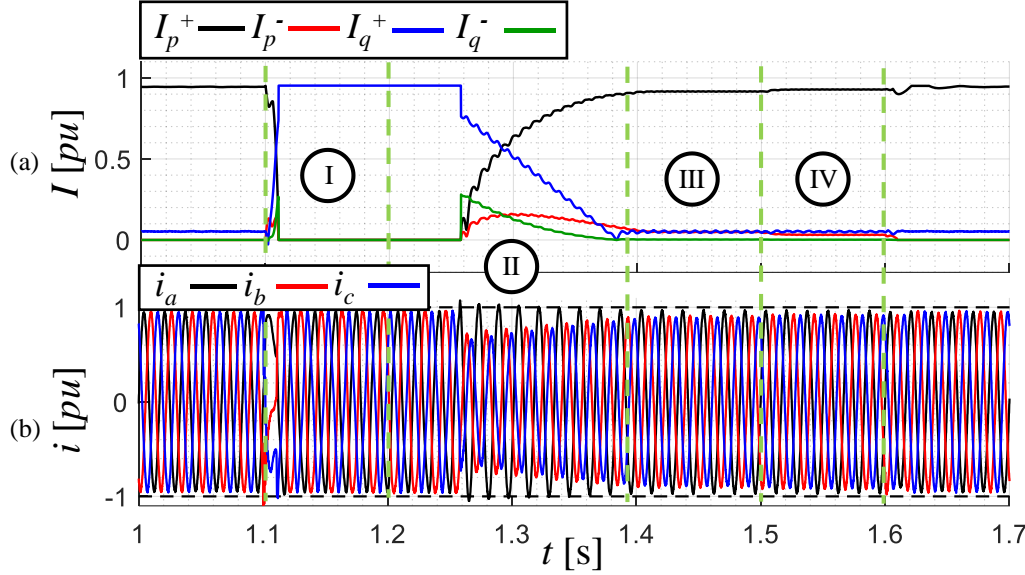


Elaborated by the author (simulation result).

The magnitude of the currents generated by the active power curtailment algorithm using RPOC strategy and their results in the mains are shown in Fig. 3.12. Except for the initial interval, the RPOC strategy also generates unbalanced currents; however, the objective is to nullify reactive power oscillations, and therefore, the mains currents profile (Fig. 3.12(a)) are different from that presented by the APOC (Fig. 3.10(b)). Nevertheless, the magnitude of the currents remains within the limits of the converter.

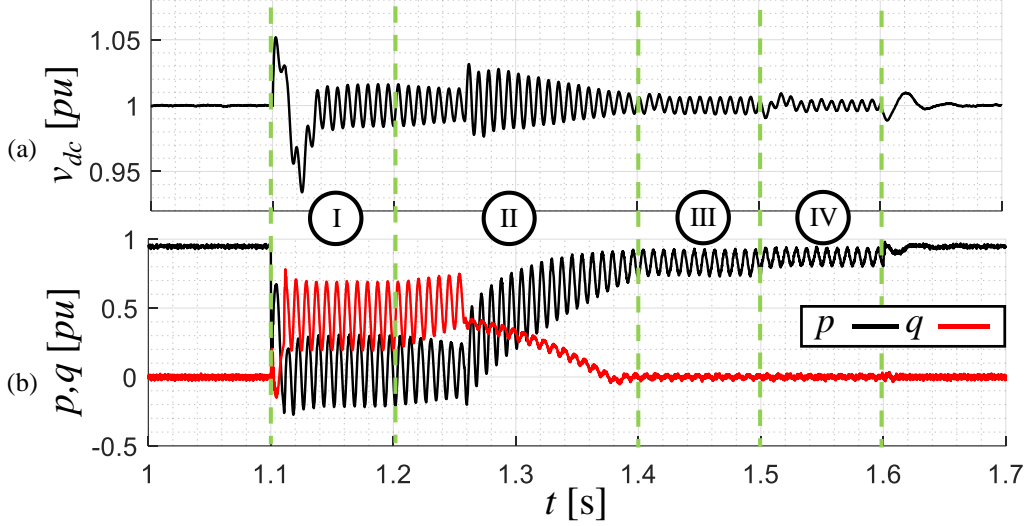
Another interesting point is the use of this strategy causes the largest voltage fluctuations in the DC bus among the strategies evaluated, as shown in Fig. 3.13(a), which is a result of the grid high active power oscillations, in Fig. 3.13(b).

Fig. 3.12: (a) reference currents generated by the proposed algorithm and (b) mains currents for RPOC (values normalized by the converter rated current).



Elaborated by the author (simulation result).

Fig. 3.13: (a) DC bus voltage and (b) mains active and reactive power for RPOC (values normalized by the converter rated parameters).



Elaborated by the author (simulation result).

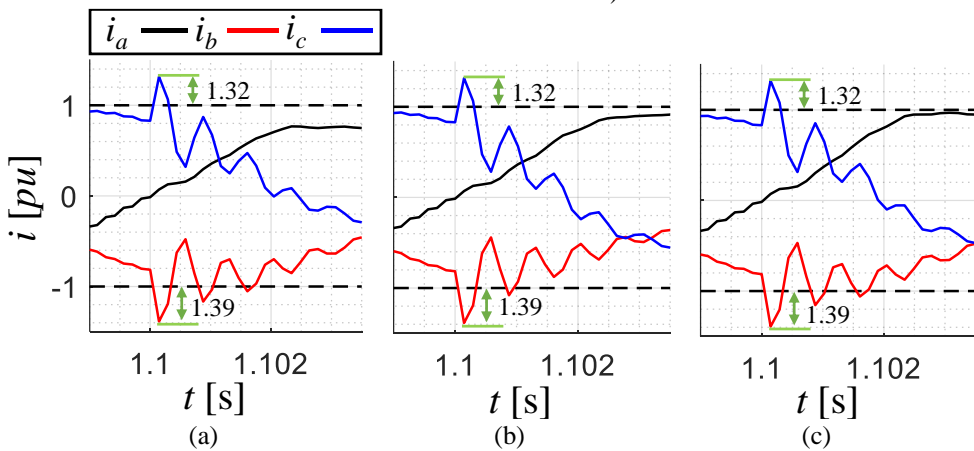
The preceding findings demonstrate that the proposed algorithm maintains current levels within the converter's operational limits during low voltage magnitude transients. However, it is imperative to highlight that during **Interval I**, overcurrents peaked at 1.39[pu], as illustrated in Fig. 3.14. Simultaneously, overvoltages on the DC bus reached magnitudes of up to 0.05[pu] (57.5[V]) in Fig. 3.15. These transients stem from both the abrupt variation in test

voltage (Fig. 3.7(a)) and the operation preceding fault start, during which the generator operates with nominal active power (2[MW]), constituting an extreme operating condition.

Despite these challenges, the algorithm proves effective as it requires only a few microseconds to compute current components and activate the protection chopper, effectively quelling overcurrents in less than 0.5[ms]. Moreover, according to the converter data sheets in (INFINEON, 2012), it is capable of supporting up to a repetitive peak collector current of 2.4[pu] for 1[ms] and overvoltages of up to 1.09[pu] for 150[μs].

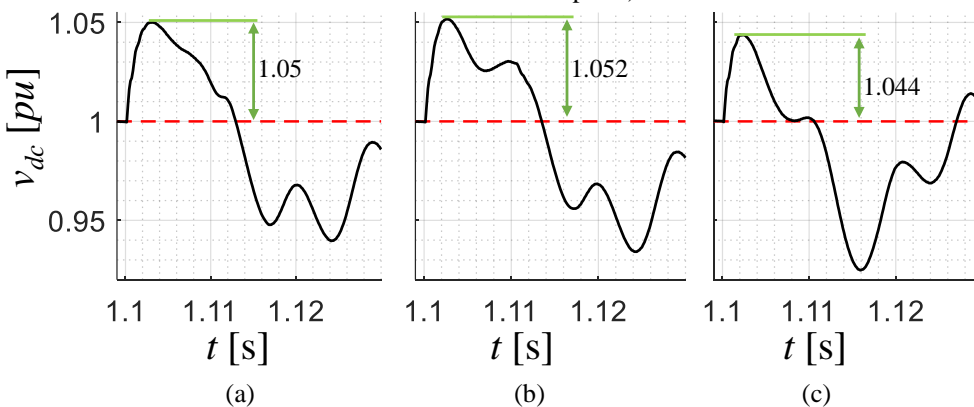
Then, while momentary overcurrents and overvoltages may occur during extreme conditions, the converter is designed to withstand such transients without suffering permanent damage, ensuring the algorithm achieves its objective of curtailing active power without compromising the integrity of the power converter.

Fig. 3.14: Start sag GSC overcurrent for (a) APOC, (b) RPOC and (c) BPSC (values normalized by the converter rated current).



Elaborated by the author (simulation results).

Fig. 3.15: Start sag DC bus overvoltage for (a) APOC, (b) RPOC and (c) BPSC (values normalized by the converter DC bus setpoint).

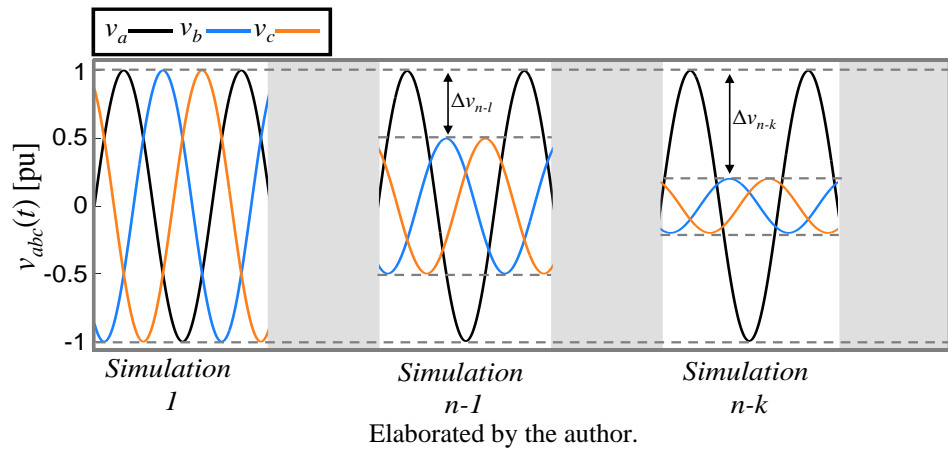


Elaborated by the author (simulation results).

3.5.2 Analysis in different operational points

To broaden the scope of the analysis, a series of simulations were conducted where the voltage magnitude of v_a remained constant at 1[pu], while v_b and v_c underwent systematic reductions in each simulation run, as illustrated in Fig. 3.16. Here, it is aimed to evaluate the system's response to diverse voltage conditions, and it is important to note the voltage limits stipulated by the ONS grid code were not considered. This decision was made to focus specifically on evaluating the active power curtailment algorithm in various operational conditions and demonstrating its operation.

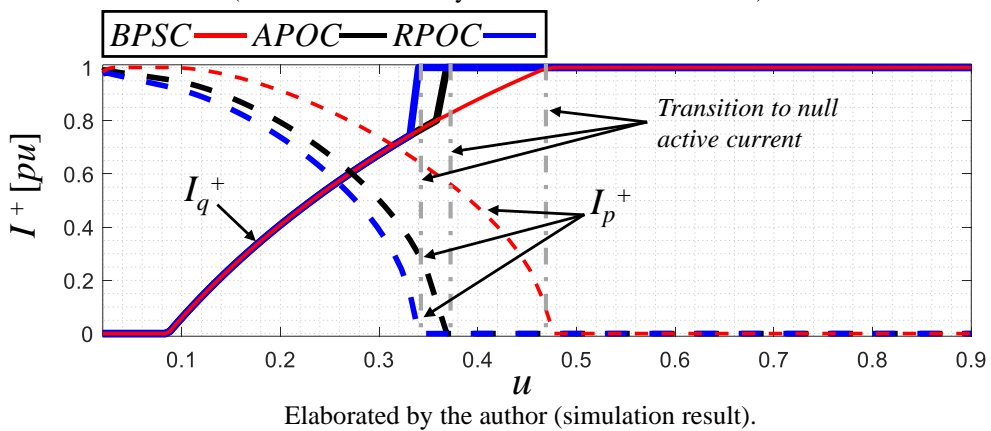
Fig. 3.16: Example of voltage change for several simulations (values normalized by the converter rated voltage).



Elaborated by the author.

The magnitudes of positive sequence reference currents calculated by the active power curtailment algorithm, concerning the unbalance factor u , for different power control strategies are illustrated in the graphs of Fig. 3.17. As defined in set of equations (3.5), positive and negative sequence currents are linked through the unbalance factor u , except for BPSC, where $I_p^- = I_q^- = 0$.

Fig. 3.17: Positive sequence active and reactive reference currents magnitudes for different operating points (values normalized by the converter rated current).



Elaborated by the author (simulation result).

Notably, the BPSC strategy consistently yields higher active current compared to others for the same value of u , while the RPOC strategy results in lower active current magnitudes. As discussed in Chapter 2, the APOC and RPOC strategies, to compensate the direction of power flow through the negative sequence, change the production of active power through the positive sequence. This adjustment ensures that the net value is equal to the reference value, which accounts for the differences in the active current references observed in the graphs.

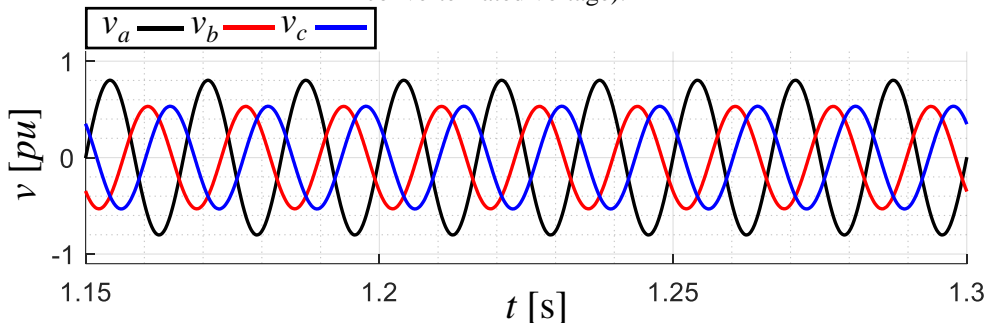
As the positive sequence reactive current is defined by the GC, the three strategies share the same value until the point where it becomes possible to compensate for power oscillations without exceeding the converter limits. However, during the transition to null active current, induced by the high values of I_q^+ and unbalance factor u , the converter becomes unable to inject negative sequence currents and active current without surpassing its capacity. As the remaining I_q^+ proves insufficient to optimize voltage support, the curtailment algorithm recalculates I_q^+ to maximize current capacity, elucidating the abrupt transition observed.

3.5.3 Power oscillations impact on the grid converters.

After validating the active power curtailment algorithm, two questions arise: Why mitigate instantaneous power oscillations? And what is the impact of these oscillations on the grid converter?

To discuss these issues, comparative simulations were carried out between the power control strategies BPSC, APOC, and RPOC subjected to the voltage profile in Fig. 3.18. This voltage results in a positive sequence voltage magnitude of $|\mathbf{v}|^+ = 0.6[\text{pu}]$ and an unbalance factor of $u = 0.3333$, and the generator operates with nominal active power (2[MW]).

Fig. 3.18: Voltage profile for simulations results, $|\mathbf{v}|^+ = 0.6[\text{pu}]$ and $u = 0.333$ (values normalized by the converter rated voltage).

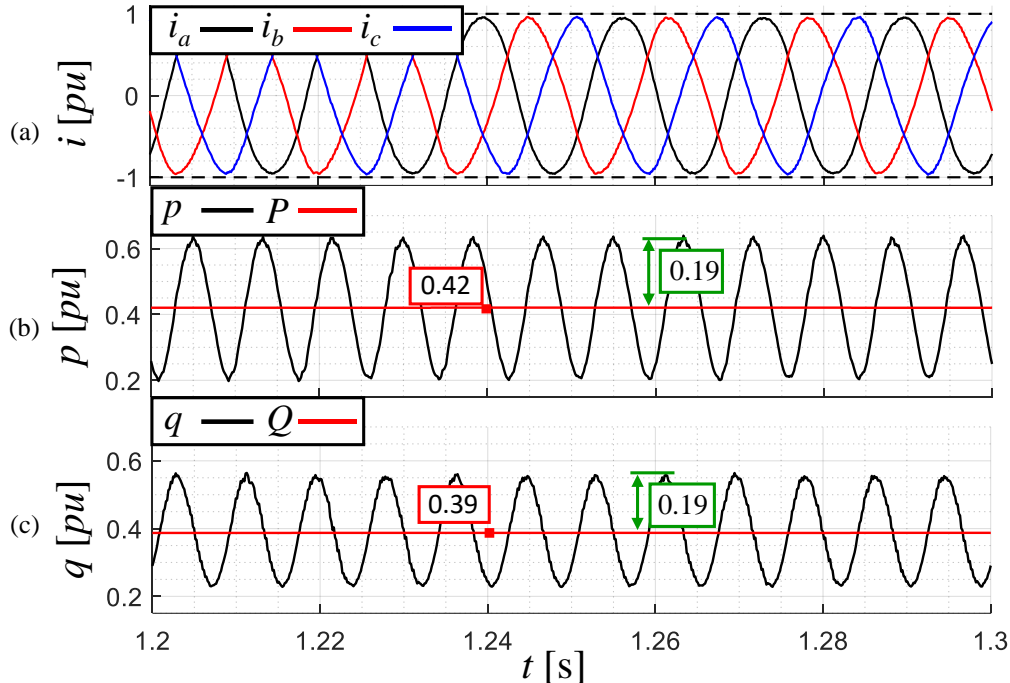


Elaborated by the author (simulation result)

The current profile generated by the BPSC strategy, and the resulting instantaneous active and reactive powers are shown in Fig. 3.19. The average active power feed in into the grid is

0.42[pu], and reactive power is 0.39[pu], with both powers oscillating with the same magnitude of 0.19[pu], corroborating with equations (2.37).

Fig. 3.19: BPSC (a) mains currents profile instantaneous (b) active and (c) reactive power for $|v|^+ = 0.6[\text{pu}]$ and $u = 0.3333$ (values normalized by the converter rated parameters).

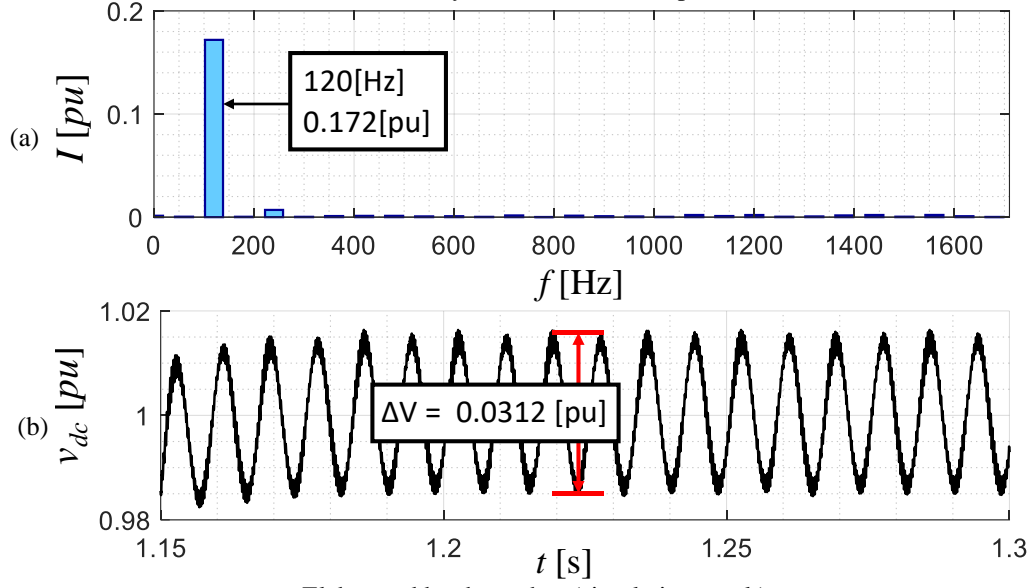


Elaborated by the author (simulation result).

Even though the BPSC strategy produces only balanced currents, active power oscillations generate energy oscillations of the same frequency in the converter's DC bus capacitors. Analyzing the frequency spectrum of the bus current, a component of 0.172[pu] magnitude at 120[Hz] stands out, in Fig. 3.20(a), in the same frequency oscillations in the bus voltage with a magnitude of 0.0312[pu] (approximately 36[V]) are also observed in Fig. 3.20(b).

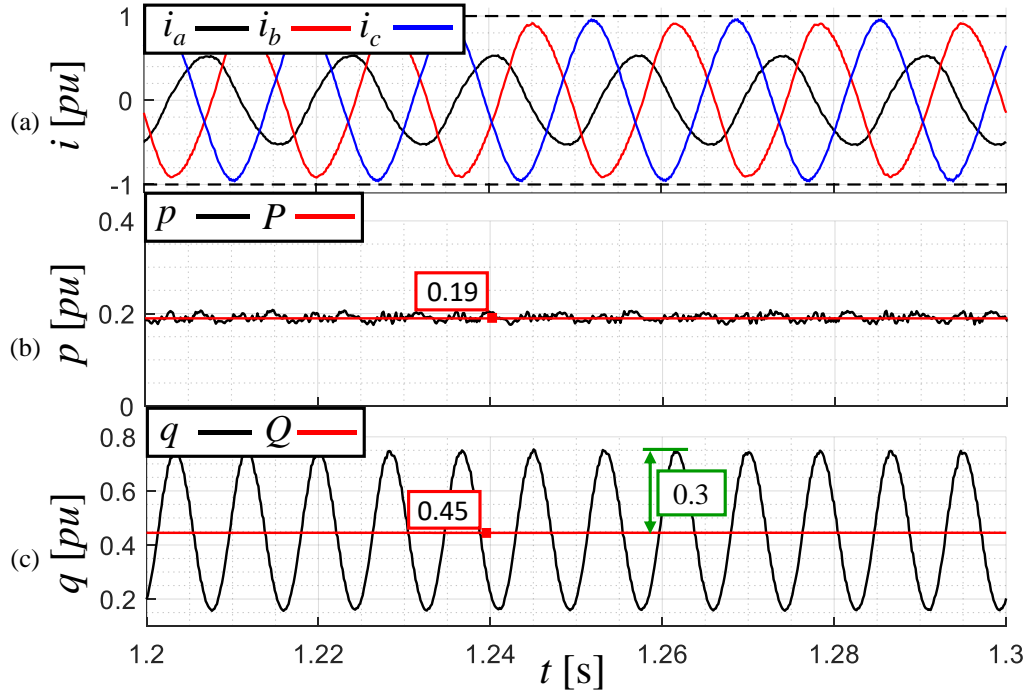
The currents produced by the APOC strategy in Fig. 3.21(a) have a complementary profile to that of the voltage in Fig. 3.18, meaning the phase which voltage has the highest magnitude has the current with the lowest peak value and vice versa. The average active power generated was 0.19[pu], less than half the value generated by the BPSC strategy, but the magnitudes of the oscillations are almost null, as shown in Fig. 3.21(b). For the reactive power in Fig. 3.21(c), the average value produced was 0.45[pu], with oscillations magnitudes of 0.3[pu].

Fig. 3.20: BPSC DC bus (a) capacitor current spectrum and (b) voltage for $|v^+| = 0.6[\text{pu}]$ and $u = 0.3333$ (values normalized by the converter rated parameters).



Elaborated by the author (simulation result).

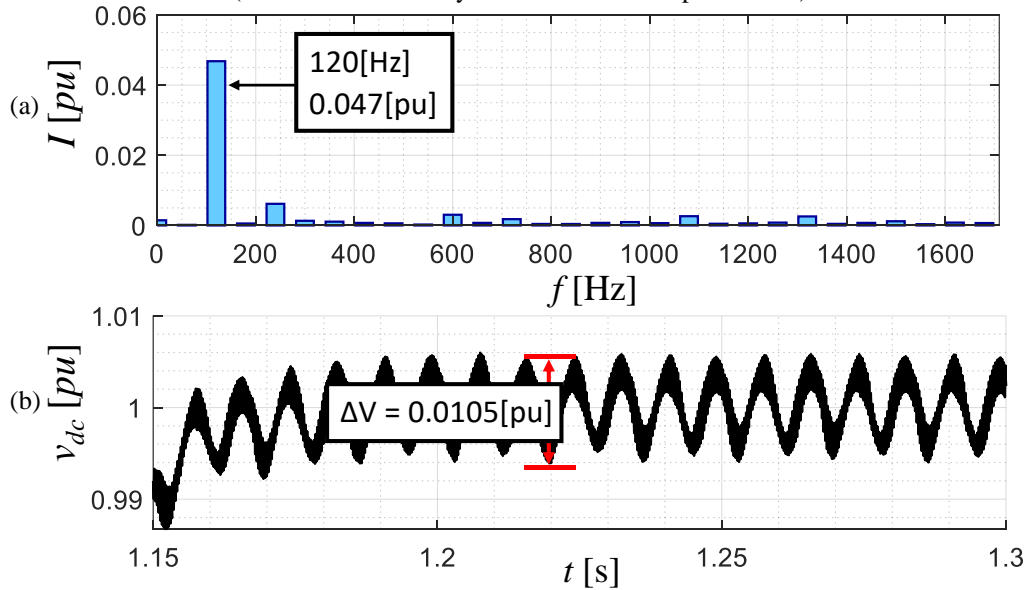
Fig. 3.21: APOC (a) mains currents profile instantaneous (b) active and (c) reactive power for $|v^+| = 0.6[\text{pu}]$ and $u = 0.3333$ (values normalized by the converter rated parameters).



Elaborated by the author (simulation result).

Since the active power oscillations are damped, when analyzing the current spectrum in the DC bus capacitors present in Fig. 3.22(a), the component at 120[Hz] has a magnitude of 0.047[pu], and the voltage oscillations in the DC have magnitudes of 0.0105[pu] (approximately 12[V]), as shown in Fig. 3.22(b).

Fig. 3.22: APOC DC bus (a) capacitor current spectrum and (b) voltage for $|v|^{+} = 0.6[\text{pu}]$ and $u = 0.3333$. (values normalized by the converter rated parameters).



Elaborated by the author (simulation result).

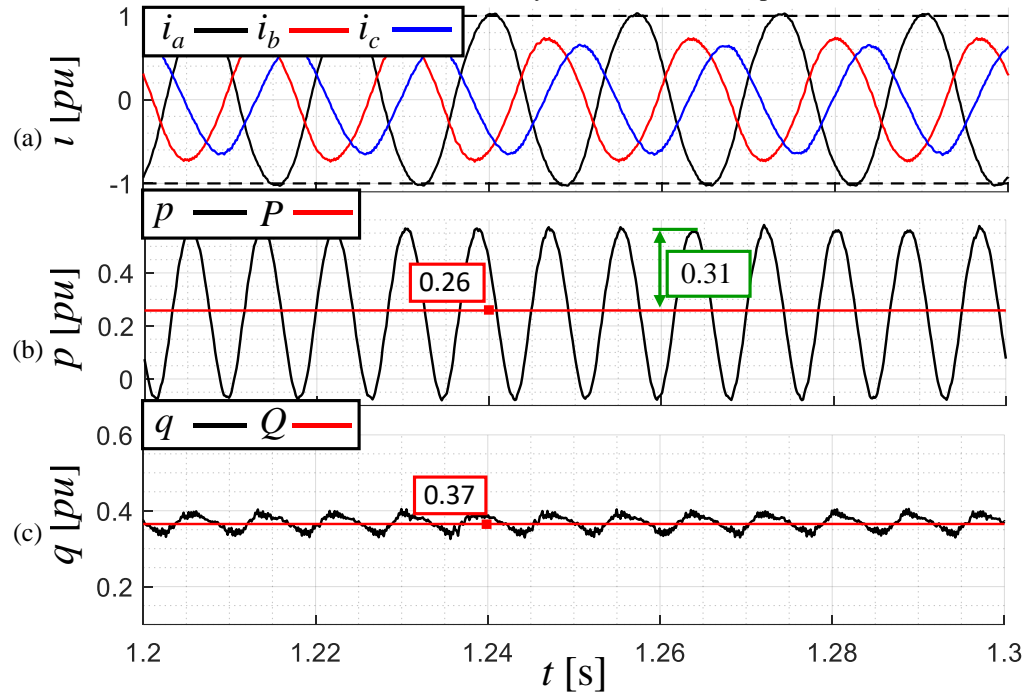
In the case of the RPOC strategy, the mains current in Fig. 3.23(a), follows the voltage profile. In other words, the phase with the maximum voltage magnitude exhibits the highest peak current, while the phase with the minimum magnitude has the lowest current. This results average active power of 0.26[pu] and oscillations magnitude of 0.31[pu] in Fig. 3.23(b). For reactive power, average value of 0.37[pu] and oscillations nearly zero in Fig. 3.23(c).

Because of high active power oscillations, the current spectrum in the DC bus capacitor, illustrated in Fig. 3.24(a), features a 120 Hz component with an amplitude of 0.314[pu], and the voltage oscillations on the DC bus have a magnitude of 0.0542[pu] (approximately 62[V]) in peak-to-peak value, as seen in Fig. 3.24(b).

Regarding semiconductor switch losses, Fig. 3.25 presents a comparison between the average losses measured in the diodes (Fig. 3.25(a)) and in the IGBTs (Fig. 3.25(b)) of the converter. The values are normalized to the average losses in the nominal (pre-fault) operating condition of the converter, which are $E_{diode} = 788.14[\text{W}]$ and $E_{igbt} = 13.662[\text{kW}]$, respectively.

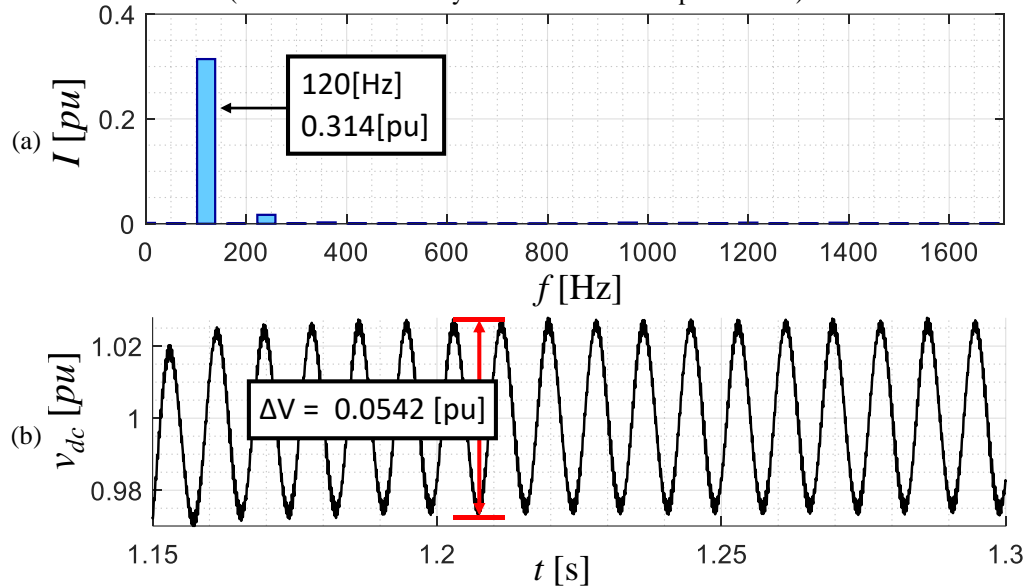
The results indicate that, as expected, with the increase in reactive current during voltage sags, diode losses nearly triple compared to the pre-fault condition. The RPOC strategy shows the lowest diode losses among the strategies analyzed. Conversely, a reduction in IGBT losses is observed, particularly with strategies that allow for the circulation of negative sequence currents. Notably, the APOC strategy exhibits the lowest IGBT loss values relative to the other strategies.

Fig. 3.23: RPOC (a) mains currents profile instantaneous (b) active and (c) reactive power for $|v|^{+} = 0.6[\text{pu}]$ and $u = 0.3333$. (values normalized by the converter rated parameters).



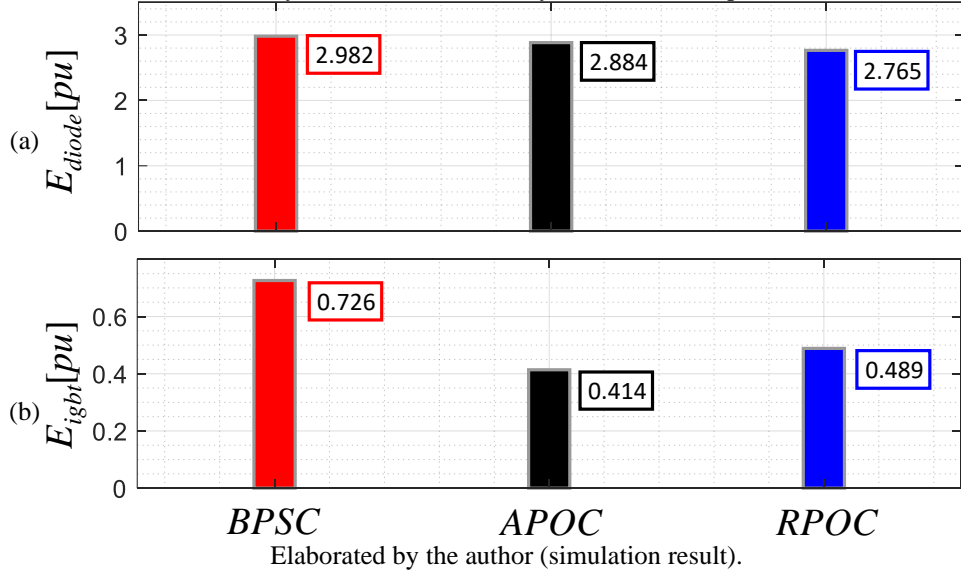
Elaborated by the author (simulation result).

Fig. 3.24: RPOC DC bus (a) capacitor current spectrum and (b) voltage for $|v|^{+} = 0.6[\text{pu}]$ and $u = 0.3333$. (values normalized by the converter rated parameters).



Elaborated by the author (simulation result).

Fig. 3.25: Conduction losses in the (a) diode and (b) IGBT for $|v|^{+} = 0.6[\text{pu}]$ and $u = 0.3333$. (values normalized by the devices losses in systems nominal operation).

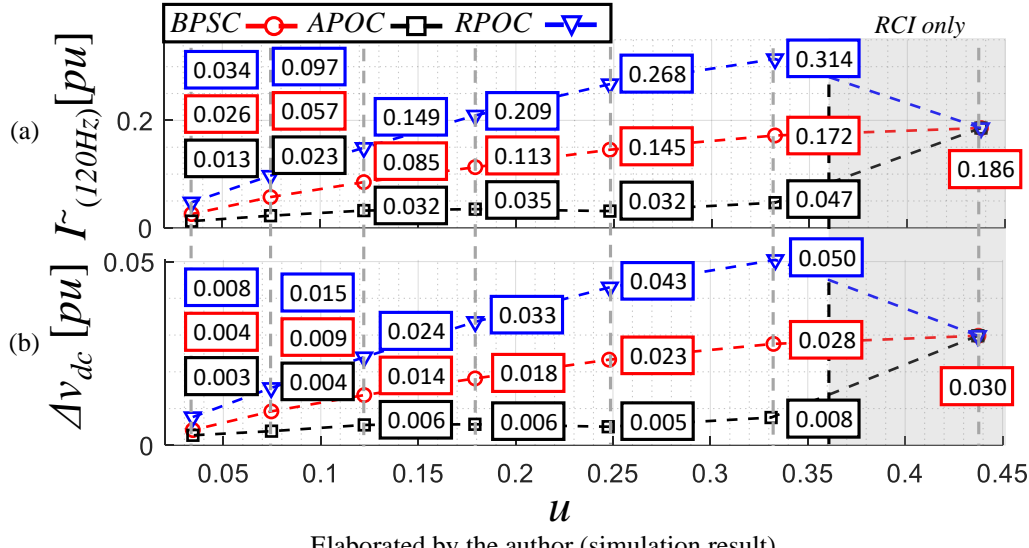


For a comprehensive analysis, Fig. 3.26(a) illustrates the magnitude of the 120Hz current ripple (I_{120}^{\sim}) and Fig. 3.26(b) the voltage oscillation magnitude (Δv_{dc}) in the DC bus capacitors for different unbalance voltage sag conditions. When it is possible to provide negative sequence currents, the APOC strategy proves to be the most beneficial for the converter, with $I_{120}^{\sim} = 0.047[\text{pu}]$ and $\Delta v_{dc} = 0.008$ being the highest values obtained at $u = 0.35$. For comparison, under the same conditions, the RPOC strategy reaches values of $I_{120}^{\sim} = 0.314[\text{pu}]$ and $\Delta v_{dc} = 0.05[\text{pu}]$.

Similarly, semiconductor losses are depicted in Fig. 3.27. When evaluating diode losses (Fig. 3.27(a)), it is observed that as the sag becomes more severe and reactive current increases, losses in the diode also increase. Among the strategies analyzed, the RPOC strategy stands out, showing the lowest diode losses. However, for the IGBT (Fig. 3.27(b)), the reduction in voltage and the increase in the reactive portion of the current lead to a reduction in IGBT losses. In this case, the APOC strategy is notable, presenting the greatest reduction in losses.

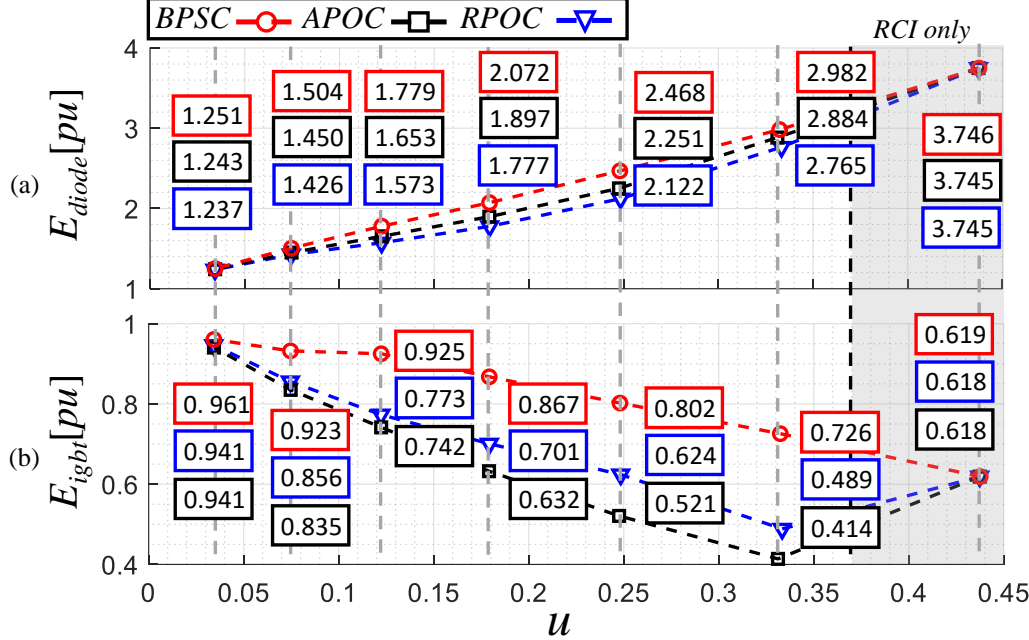
In both results, for deep sags ($u > 0.35$), the entire converter capacity is utilized for the RCI, and is not possible to make any type of compensation for power oscillations, and the three strategies lines converge to the same point.

Fig. 3.26: Comparisons of DC bus capacitors (a) 120[Hz] current ripple and (b) average voltage oscillations magnitude (values normalized by the converter rated parameters).



Elaborated by the author (simulation result).

Fig. 3.27: Comparisons of (a) diode and (b) IGBT average conduction losses. (values normalized by the devices losses in systems nominal operation).



Elaborated by the author (simulation result).

3.6 Chapter conclusions

The objective of this chapter was to propose an active power saturation algorithm with following objectives:

- Compliance with voltage ride-through and RCI requirements.
- Limiting grid converter current to its rated value.
- Control of active power production.

- Mitigation of power oscillations during unbalanced voltage sags.

Some results of the results of this chapter were published on (SILVA; SOUSA; MENDES, 2021).

The simulation results demonstrate that abrupt voltage variations lead to short-time grid overcurrents and overvoltage in the DC bus. These transients are influenced by various factors, e.g., the time required for the phase-locked loop (PLL) to estimate voltage components, the time the algorithm takes for processing and limiting the current and activating the chopper. However, it's worth noting that these voltage and current transients are controlled in less than a quarter of a grid cycle. And after the onset of the voltage sag, both currents and voltage remain within the operational limits of the grid converter.

It is important to emphasize that the simulations were conducted under the worst operating conditions for the system, very low voltage levels sag, fast transition rates and full pre-fault active power generation.

The results also show that canceling power oscillations reduces the impacts of unbalanced sags on the power converter, both by minimizing losses in the semiconductors and by reducing energy oscillations in the converter's DC bus capacitors.

While this discussion focuses on unbalanced voltage sags, a transient event, it is important to recognize that 120[Hz] current oscillations in the DC bus capacitors can be substantial, sometimes exceeding 30% of the converter's nominal current, depending on the chosen control strategy. Additionally, diodes losses can reach more than triple its pre-fault condition due the increase of reactive current.

From the converter's perspective, opting for the APOC strategy appears to be the most advantageous. By mitigating power oscillations, this strategy effectively dampens voltage and current oscillations within the converter's DC bus. Although the RPOC strategy presents better results in reducing diode losses, it must be considered that IGBT losses are much higher. Therefore, reducing losses in IGBTs is more beneficial overall.

Chapter IV

VOLTAGE SUPPORT

GRID codes instruct the injection of positive sequence reactive current to boost the voltage and enhance the operating margin of wind turbines during voltage ride-through operations. Power control strategies can utilize a portion of the wind turbine current to mitigate instantaneous power oscillations. However, it is essential to investigate the impact of these strategies on voltage support and other sources of energy generation in the system during transients. This chapter aims to address this objective.

4.1 Synchronous generators.

To comprehend the limitations of grid-connected converters and their impacts on the grid response in face of disturbances, it is necessary to briefly explain the behavior of conventional synchronous generators during same conditions.

The control of a synchronous generator connected to the grid typically involves two control systems: the automatic voltage regulator (AVR) and the speed governor. The AVR regulates reactive power and voltage by controlling the machine's field current, which exhibits high inductance (IEEE-421.5, [s.d.]). Conversely, the speed governor manages active power and frequency by controlling the high-inertia mechanical components that convert primary energy into mechanical energy on the generator shaft (IEEE-125, [s.d.]).

4.1.1 Transient response

Among the faults that disrupt the normal operation of the power system, short circuits are particularly detrimental due to their significant energy fluctuations, making them a focal point of analysis. High-voltage AC transmission systems are predominantly inductive, characterized by a high X/R ratio, resulting in short-circuit currents that are primarily reactive (ANDERSON, 1995). This increased flow of reactive power leads to voltage drops at various nodes within the power system. Additionally, sudden changes in active power result in instantaneous deviations in the grid frequency, with the magnitude of frequency excursion influenced by factors such as power system inertia and fault location.

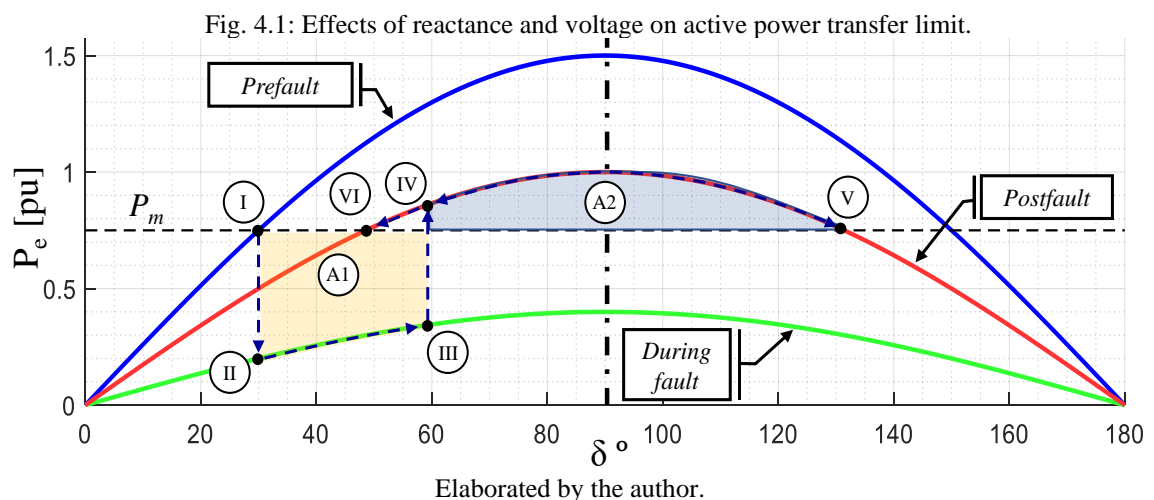
Fig. 4.1 illustrates a simple example of the behavior of electrical active power (P_e) as a function of load angle δ in a synchronous machine during and immediately after a three-phase short-circuit event. Due to the high time response of the speed governor, the mechanical power (P_m) sourced from primary machine can be considered constant during the analyzed period.

During the initial cycles of the short circuit, the reduction in grid voltage and the change of equivalent impedance (X_{eq}) at generators terminals lead to a sudden decrease in P_e . However, the rotor's inertia prevents the machine from accelerating, maintaining the load angle constant and shifting the operating point from *I* to *II*.

After some time, the rotor accelerates, as P_m exceeds P_e , causing an increase in the load angle until the fault is cleared at point *III*. At this juncture, the system experiences an increase in P_e due to the changes in voltage and X_{eq} and V , with the accumulated kinetic energy causing P_e to surpass P_m , transitioning from *III* to *IV*.

The generator's inertia continues to increase the load angle, shifting the operating point from *IV* to *V*, where the rotor speed matches the synchronous speed. At this stage, system stability is achieved only if the accumulated accelerating energy is fully transferred to the grid, satisfying the equal-area criterion ($A1 = A2$), otherwise, the machine continues to accelerate and lose its synchronization with the grid.

In stable condition, with the dissipation of kinetic energy, the rotor decelerates, causing the load angle to oscillate along the post-fault active power curve until it is completely damped. Eventually, the generator reaches a new equilibrium at point *VI*.



Therefore, the angular stability of synchronous machines is influenced by the following factors:

- **Equivalent voltage and impedance at the generator terminals:** During and after the fault, the voltage and impedance change and alters the power transfer capacity, resulting in instantaneous changes in the generator's output active power.
- **Generator's inertia:** The inertia of the generation system plays a crucial role in controlling the load angle and mitigating frequency deviations during transient events. Higher inertia leads to smaller load angle excursions and better stability.
- **Fault clearing time:** The time it takes to clear a fault has a direct impact on transient stability. A faster fault clearing time reduces the time available for the machine to accumulate excessive mechanical energy.

4.1.2 Short circuit response.

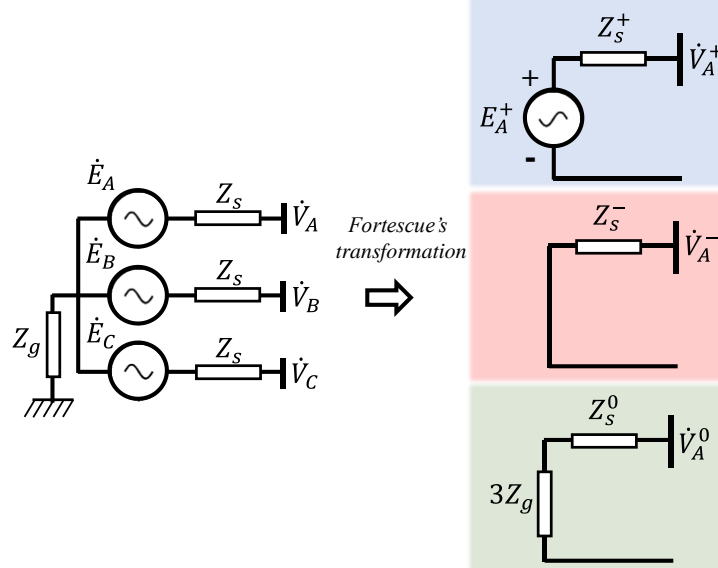
The slow response of the generator, in comparison to the transient period, permits the machine to be represented as a balanced voltage source during the initial stages of a short-circuit (ANDERSON, 1995). As a result, the fault currents are dictated by the equivalent impedance at the generator terminals, with synchronous machines engineered to endure up to fifteen times their rated current during the subtransient phase (IEEE-115, [s.d.]).

In the context of unbalanced faults, the machine model expands to include not only the positive sequence, characterized by a balanced voltage source and impedance, but also the negative and zero sequences, represented solely by impedances (KUNDUR; BALU; LAUBY, 1994) as depicted in Fig. 4.2, where z_s^+ , z_s^- and z_s^0 are the machine impedance of positive, negative and zero sequence and z_g^+ is the ground impedance. Then, with unbalanced short-circuits, the generator produces balanced currents and absorbs the unbalanced ones.

4.2 VDE AR N 4120 and instantaneous power oscillations

As discussed in Chapter 1, the injection of negative sequence currents by wind turbines during asymmetric faults has garnered attention following the publication of COMISSION REGULATION (EU) 2016/631 (2016). Building on this, VDE ARN 4120 (2018) introduced a new approach to reactive current injection during voltage sags, specifically addressing the injection of negative sequence reactive current in asymmetric faults.

Fig. 4.2: Synchronous generator model for unbalanced short-circuit analysis.



Adapted from (ANDERSON, 1995)

Assuming $V_{1min} = V_n$ and that the pre-fault reactive current is null, we can normalize the voltages by V_n , and rewrite equations (1.2), (1.3) and (1.4) as (4.1).

$$\begin{aligned} I_q^+ &= k_{VDE} \left(1 - \frac{|\mathbf{v}^+|}{V_n} \right), \\ I_q^- &= k_{VDE} \frac{|\mathbf{v}^-|}{V_n}, \end{aligned} \quad (4.1)$$

Since the VDE does not specify the behavior of the active components of current, we can assume that they have any magnitudes defined by I_p^+ and I_p^- . Therefore, we can replace them and equation (4.1) in the instantaneous power oscillation terms in equations (2.11) and (2.12), obtaining the expressions (4.2) and (4.3).

$$\begin{aligned} \tilde{p} &= \mathbf{v}^- \cdot I_p^+ \frac{\mathbf{v}^+}{|\mathbf{v}^+|} + \mathbf{v}^+ \cdot I_p^- \frac{\mathbf{v}^-}{|\mathbf{v}^-|} + \dots \\ &\quad \underbrace{\mathbf{v}^+ \cdot k_{VDE} \frac{|\mathbf{v}^-|}{V_n} \frac{\mathbf{v}_\perp^-}{|\mathbf{v}^-|}}_{I_q^-} + \mathbf{v}^- \cdot k_{VDE} \left(1 - \frac{|\mathbf{v}^+|}{V_n} \right) \frac{\mathbf{v}_\perp^+}{|\mathbf{v}^+|} \end{aligned} \quad (4.2)$$

$$\begin{aligned} \tilde{q} &= \mathbf{v}_\perp^- \cdot k_{VDE} \left(1 - \frac{|\mathbf{v}^+|}{V_n} \right) \frac{\mathbf{v}_\perp^+}{|\mathbf{v}^+|} + \mathbf{v}_\perp^+ \cdot k_{VDE} \frac{|\mathbf{v}^-|}{V_n} \frac{\mathbf{v}_\perp^-}{|\mathbf{v}^-|} + \dots \\ &\quad + \mathbf{v}_\perp^- \cdot I_p^+ \frac{\mathbf{v}^+}{|\mathbf{v}^+|} + \mathbf{v}_\perp^+ \cdot I_p^- \frac{\mathbf{v}^-}{|\mathbf{v}^-|} \end{aligned} \quad (4.3)$$

Then, using (2.28), the expressions for power oscillations resulting from the VDE AR N 4120 are described in (4.4) and (4.5).

$$\tilde{p} = \left(\frac{I_p^+}{|\mathbf{v}^+|} + \frac{I_p^-}{|\mathbf{v}^-|} \right) \mathbf{v}^- \cdot \mathbf{v}^+ + k_{VDE} \left(2 \frac{|\mathbf{v}^+|}{V_n} - 1 \right) \frac{\mathbf{v}_\perp^- \cdot \mathbf{v}^+}{|\mathbf{v}^+|}, \quad (4.4)$$

$$\tilde{q} = \left(\frac{I_p^+}{|\mathbf{v}^+|} - \frac{I_p^-}{|\mathbf{v}^-|} \right) \mathbf{v}_\perp^- \cdot \mathbf{v}^+ + k_{VDE} \frac{\mathbf{v}_\perp^+ \cdot \mathbf{v}_\perp^-}{|\mathbf{v}^+|}. \quad (4.5)$$

The cancellation of instantaneous power oscillations is achieved when the relations between the positive and negative sequence currents adhere to the set of equations (4.6) for APOC and the set (4.7) for RPOC, as discussed in chapters 3. In both cases, the magnitudes of the sequence components must be related through the unbalance factor u .

$$I_p^- = -u \cdot I_p^+, \quad (4.6)$$

$$I_q^- = u \cdot I_q^+.$$

$$I_p^- = u \cdot I_p^+, \quad (4.7)$$

$$I_q^- = -u \cdot I_q^+.$$

Then, the VDE recommendation specifies the behavior of I_q^+ and I_q^- , even if the active components I_p^+ and I_p^- adhere to the relationships established in equations (4.6) or (4.7), it is no longer possible to eliminate instantaneous power oscillations as before.

4.3 Voltage support.

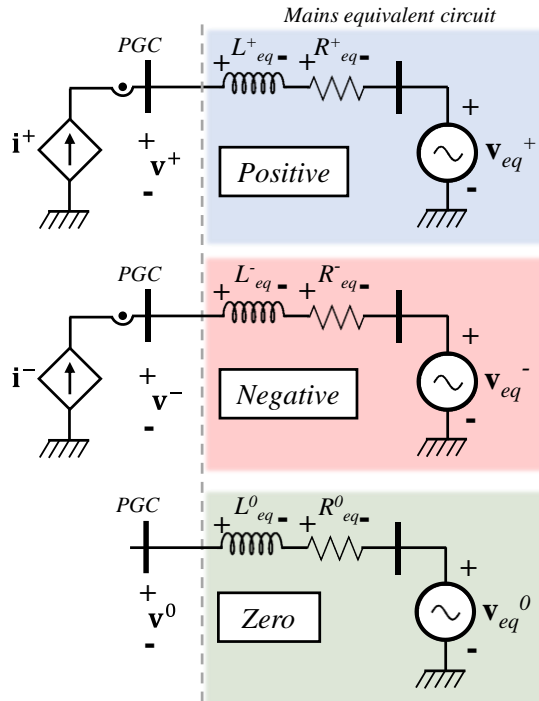
During unbalanced sags, the optimal voltage support scenario involves increasing the positive and simultaneously decreasing the negative sequence voltages. However, despite the enhanced flexibility, COMMISSION REGULATION (EU) 2016/631 (2016) also specifies that non-synchronous generators shall promote adequate damping of active power oscillations. While VDE AR N 4120 offers flexibility in voltage support, it does not assist power oscillations. Considering this, a pertinent question is: how do power control strategies influence voltage support during asymmetric faults? To answer this question, a mathematical model is developed to describe the voltages at the wind turbine terminals as a function of power control strategies.

Unlike synchronous generators, power electronic converters have current synthesis control because of the semiconductor devices current restriction. In the case of full power converters, it is appropriate to model them as controlled current sources. This modeling approach holds for both the positive and negative sequences. But, due to the configuration of transformer

windings, the WEC acts as an open circuit in the zero sequence (ENTSOE, 2019; HE; GENG; MU, 2021).

The illustration of the symmetrical components circuit in the time domain, utilizing the PGC as the reference point, is presented in Fig. 4.3. The electrical power system could be represented by its equivalent circuit elements L_{eq}^+ , R_{eq}^+ , L_{eq}^- , R_{eq}^- and \mathbf{v}_{eq}^+ , respectively positive sequence inductance, resistance, negative sequence inductance, resistance, and positive sequence equivalent voltage.

Fig. 4.3: Simplified representation of point of generator connection during an unbalanced sag.



Elaborated by the author.

Assuming $L_{eq}^+ = L_{eq}^- = L_{eq}$ and $R_{eq}^+ = R_{eq}^- = R_{eq}$ and formulating the voltage equations in the circuit, the PGC voltage are described in (4.8) and (4.9).

$$\mathbf{v}^+ = \mathbf{v}_{eq}^+ + R_{eq} \cdot \mathbf{i}^+ + L_{eq} \cdot \frac{d\mathbf{i}^+}{dt}, \quad (4.8)$$

$$\mathbf{v}^- = \mathbf{v}_{eq}^- + R_{eq} \cdot \mathbf{i}^- + L_{eq} \cdot \frac{d\mathbf{i}^-}{dt}, \quad (4.9)$$

Replacing (3.1), (3.2) in (4.8) and (4.9) it is obtained the equations (4.10) and (4.11).

$$\begin{aligned} \mathbf{v}^+ &= \mathbf{v}_{eq}^+ + R_{eq} \cdot \left(I_p^+ \frac{\mathbf{v}^+}{|\mathbf{v}^+|} + I_q^+ \frac{\mathbf{v}_\perp^+}{|\mathbf{v}^+|} \right) + \dots \\ &\quad L_{eq} \cdot \frac{d}{dt} \left(I_p^+ \frac{\mathbf{v}^+}{|\mathbf{v}^+|} + I_q^+ \frac{\mathbf{v}_\perp^+}{|\mathbf{v}^+|} \right), \end{aligned} \quad (4.10)$$

$$\begin{aligned}\mathbf{v}^- = \mathbf{v}_{eq}^- + R_{eq} \cdot \left(k_p I_p^- \frac{\mathbf{v}^-}{|\mathbf{v}^-|} + k_q I_q^- \frac{\mathbf{v}_\perp^-}{|\mathbf{v}^-|} \right) + \dots \\ L_{eq} \cdot \frac{d}{dt} \left(k_p I_p^- \frac{\mathbf{v}^-}{|\mathbf{v}^-|} + k_q I_q^- \frac{\mathbf{v}_\perp^-}{|\mathbf{v}^-|} \right),\end{aligned}\tag{4.11}$$

By employing the expressions (2.3) for the voltages in the stationary frame within equations (4.10) and (4.11), and manipulating the derivatives, the PGC voltage can be expressed as a function of the PARPC in (4.12) and (4.13).

$$\begin{aligned}\mathbf{v}^+ = \mathbf{v}_{eq}^+ + R_{eq} \left(I_p^+ \frac{\mathbf{v}^+}{|\mathbf{v}^+|} + I_q^+ \frac{\mathbf{v}_\perp^+}{|\mathbf{v}^+|} \right) + \dots \\ \omega L_{eq} \left(-I_p^+ \frac{\mathbf{v}_\perp^+}{|\mathbf{v}^+|} + I_q^+ \frac{\mathbf{v}^+}{|\mathbf{v}^+|} \right),\end{aligned}\tag{4.12}$$

$$\begin{aligned}\mathbf{v}^- = \mathbf{v}_{eq}^- + R_{eq} \left(k_p u I_p^- \frac{\mathbf{v}^-}{|\mathbf{v}^-|} + k_q u I_q^- \frac{\mathbf{v}_\perp^-}{|\mathbf{v}^-|} \right) + \dots \\ \omega L_{eq} \left(k_p u I_p^- \frac{\mathbf{v}_\perp^-}{|\mathbf{v}^-|} - k_q u I_q^- \frac{\mathbf{v}^-}{|\mathbf{v}^-|} \right).\end{aligned}\tag{4.13}$$

Once the equations (4.12) and (4.13) describing the voltage in the PGC have been established, an important observation can be made: the terms \mathbf{v}_\perp^+ and \mathbf{v}_\perp^- have less contributions to voltage support compared to \mathbf{v}^+ and \mathbf{v}^- , because they are orthogonal to the grid voltages \mathbf{v}_{eq}^+ and \mathbf{v}_{eq}^- . Consequently, the flow of active current across resistive elements and reactive current across inductive ones, or the ratio of inductance to resistance (X/R), greatly influences the voltage support.

4.3.1 Voltage support provided by the power control strategies.

While the equation (4.12) is independent of the gains k_p and k_q , it is important to note when employing the curtailment algorithm outlined in Chapter 3, the value of I_q^+ is determined by the RCI requirement. However, the value of I_p^+ is modified according to the power control strategy, as detailed in equation (3.3). Consequently, in a system predominantly characterized by inductance ($X/R \gg I$), the chosen strategy selection will exert minimal influence on voltage support in positive sequence.

In the negative sequence, represented by (4.13), the power control strategy selection not only influences the magnitude of the currents but also determines the direction of power flow and, consequently, the voltage drop across system elements. By substituting the values of k_p

and k_q corresponding to the APOC, RPOC, and BPSC strategies outlined in Tab. 2.1, the effects on the negative sequence voltage are described in the equations provided in Tab. 4.1.

Tab. 4.1: Negative sequence voltage support for different power control strategies.

Strategy	\mathbf{v}^-	
BPSC	\mathbf{v}_{eq}^-	(4.14)
APOC	$\mathbf{v}_{eq}^- + R_{eq} \left(-u I_p^+ \frac{\mathbf{v}^-}{ \mathbf{v}^- } + u I_q^+ \frac{\mathbf{v}_\perp^-}{ \mathbf{v}^- } \right) + \omega L_{eq} \left(-u I_p^+ \frac{\mathbf{v}_\perp^-}{ \mathbf{v}^- } - u I_q^+ \frac{\mathbf{v}^-}{ \mathbf{v}^- } \right)$	(4.15)
RPOC	$\mathbf{v}_{eq}^- + R_{eq} \left(u I_p^+ \frac{\mathbf{v}^-}{ \mathbf{v}^- } - u I_q^+ \frac{\mathbf{v}_\perp^-}{ \mathbf{v}^- } \right) + \omega L_{eq} \left(u I_p^+ \frac{\mathbf{v}_\perp^-}{ \mathbf{v}^- } + u I_q^+ \frac{\mathbf{v}^-}{ \mathbf{v}^- } \right)$	(4.16)

Elaborate by the author.

Assuming $I_q^+ > 0$ and $I_p^+ > 0$, the following conclusions can be drawn from the equations in Tab. 4.1:

- **BPSC:** The converter behaves as an open circuit in the negative sequence, and the voltage \mathbf{v}^- does not change in relation to \mathbf{v}_{eq}^- .
- **APOC:** The negative sequence current reduces the voltage regardless of the $\omega L_{eq}/R_{eq}$ ratio of the electrical system.
- **RPOC:** The negative sequence current increases the voltage regardless of the $\omega L_{th}/R_{th}$ ratio of the electrical system.

4.3.2 Understanding the reactive power flow in negative sequence.

From the equations in Tab. 4.1, the selection of the power control strategy influences the direction of current flow in the negative sequence. Assuming $I_q^+ > 0$, which implies $Q^+ > 0$, results in an increase in \mathbf{v}_{eq}^+ . Chapter 2, Section 2.6, with the equations in Tab. 4.1, $I_q^- > 0$, i.e., $k_q = 1$ and $Q^- > 0$, results in a decreasing of \mathbf{v}_{eq}^- , which is contrary to what is established in the positive sequence. But why?

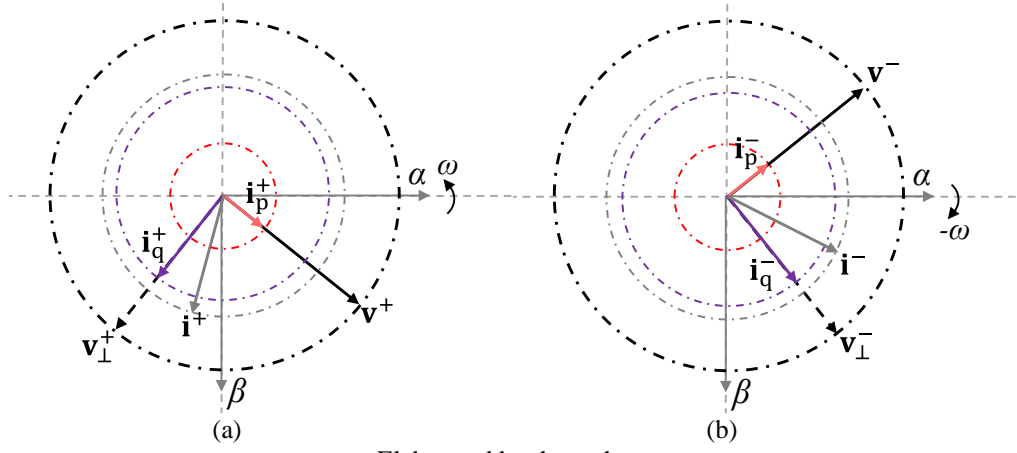
This can be elucidated by observing

Fig. 4.4. In the positive sequence (

Fig. 4.4(a)) the space vector \mathbf{v}^+ rotates counterclockwise, and applying (2.10) results in the orthogonal projection \mathbf{v}_\perp^+ lagging behind \mathbf{v}^+ , and the projection of \mathbf{i}^+ onto \mathbf{v}_\perp^+ , results in reactive power flowing from the generator towards the grid. Conversely, in the negative sequence,

Fig. 4.4(b), the space vector \mathbf{v}^- rotates in clockwise. Using (2.10) leads to the vector \mathbf{v}_\perp^- being ahead of \mathbf{v}^- , and vector \mathbf{i}^- projection onto \mathbf{v}_\perp^- to result in power flow from the grid to the generator.

Fig. 4.4: (a) positive and (b) negative sequence voltage and current vectors projections



Elaborated by the author.

4.4 Short-circuit contribution of full-power converters

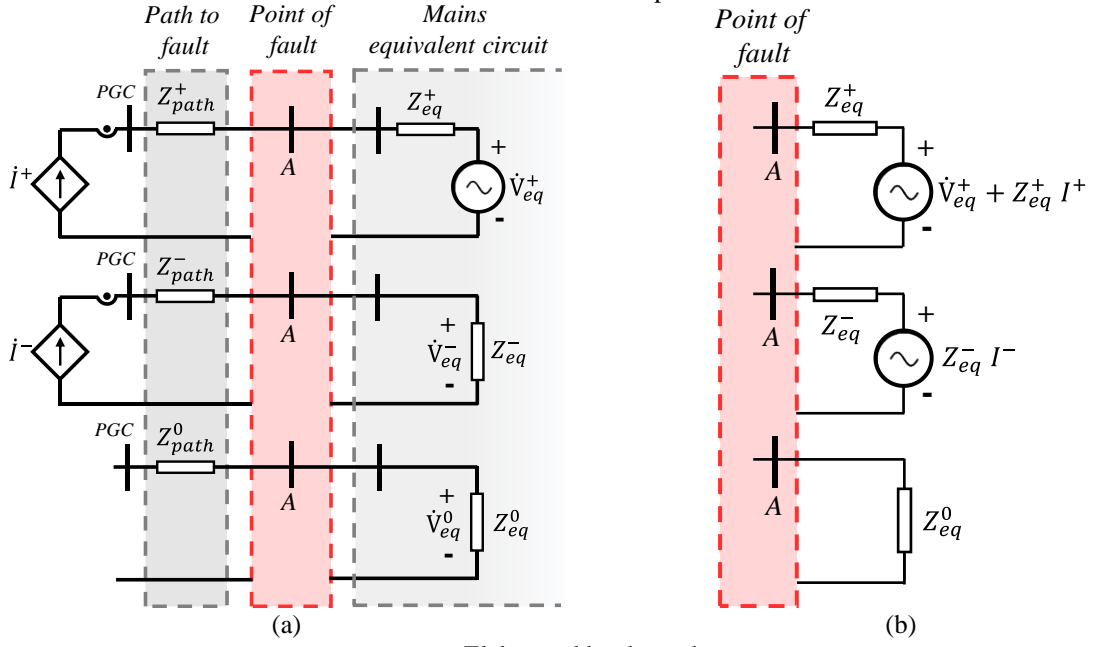
The behavior of the full power converter acting as a current source during a fault not only affects voltage support but also influences its contribution to the short circuit. In this study, it is considered the equivalent circuit concerning the PGC, as illustrated in Fig. 4.5(a), where the variables are represented in the frequency domain (phasors) and the upper scripts +, - and 0 refers to positive negative and zero sequence, respectively.

Within this framework, the various impedances along the path from the wind turbine to the fault location (point A) are denoted by Z_{path}^+ , Z_{path}^- and Z_{path}^0 . Additionally, the mains equivalent impedances and voltage are represented by Z_{eq}^+ , Z_{eq}^- , Z_{eq}^0 and V_{eq}^+ . The currents supplied by wind turbines during a fault in phasor notation are described in equations (4.17) and (4.18), with I_p the active and I_q the reactive current magnitude. Thus, the Thevenin equivalent circuit in relation to the fault point is represented by the circuit shown in Fig. 4.5(b).

$$\dot{I}^+ = I_p^+ + jI_q^+, \quad (4.17)$$

$$\dot{I}^- = I_p^- + jI_q^- = k_p u I_p^+ + j k_q u I_q^+. \quad (4.18)$$

Fig. 4.5: (a) wind generator and power system short circuit equivalent circuit and (b) Thevenin equivalent circuit in relation to the point of fault.



Elaborated by the author.

According to electrical power systems analysis (ANDERSON, 1995), the sequence connections change depending on the type of fault. Phase-to-ground (PG), phase-to-phase (PP), and phase-to-phase-to-ground (PPG) circuits are illustrated in Fig. 4.6(a), Fig. 4.6(b) and Fig. 4.6(c), respectively. Finally, the fault currents in phase A for these circuits are respectively described by (4.19), (4.20) and (4.21), correspondingly.

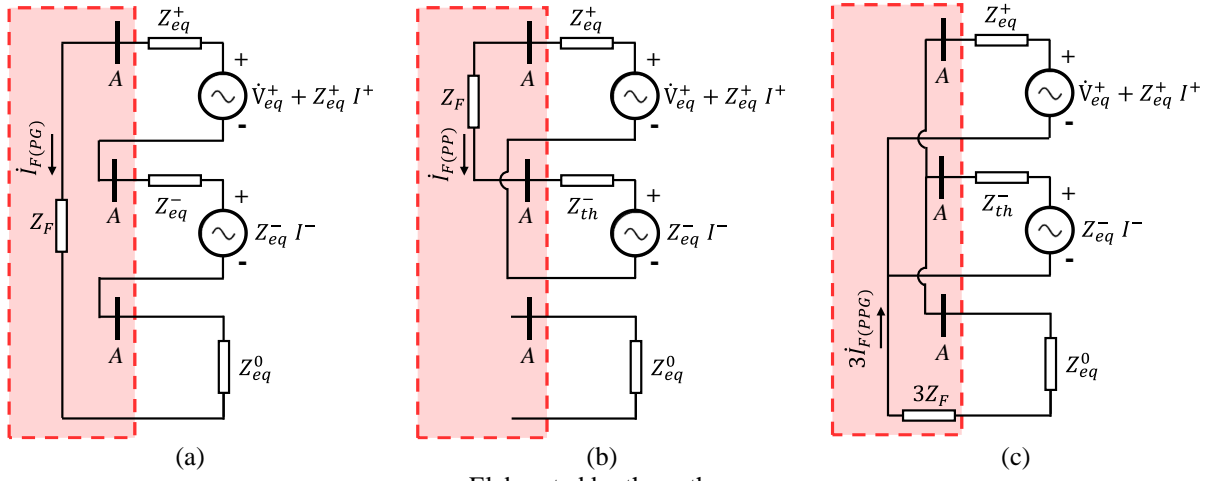
$$\dot{I}_{FA(PG)} = \frac{\dot{V}_{eq} + Z_{eq}^+ I^+ + Z_{eq}^- I^-}{Z_{eq}^+ + Z_{eq}^- + Z_{eq}^0 + 3Z_F}, \quad (4.19)$$

$$\dot{I}_{FA(PP)} = \frac{\dot{V}_{eq} + Z_{eq}^+ I^+ - Z_{eq}^- I^-}{Z_{eq}^+ + Z_{eq}^- + Z_F}. \quad (4.20)$$

$$\dot{I}_{FA(PPG)} = \frac{3}{\frac{Z_{eq}^0 + 3Z_F}{Z_{eq}^-} + \frac{Z_{eq}^0 + 3Z_F}{Z_{th}^+} + 1} \left(\frac{\dot{V}_{eq}}{Z_{eq}^+} + I^+ + I^- \right). \quad (4.21)$$

According to the equations (4.19), (4.20) and (4.21), regardless of the fault type, the wind turbine's contribution to the fault remains highly limited because the sum of active and reactive currents of WECS will not exceed 1[pu] (based on wind generation systems). The only degree of freedom lies in the ability to adjust the relationship between the active and reactive components of the current.

Fig. 4.6: (a) Phase-to-ground, (b) phase-to-phase and (c) phase-to-phase-to-ground circuits.



Elaborated by the author.

Unlike synchronous generators, wind turbines with full-power converters can actively control and restrict the negative sequence currents. However, it's essential to recognize that when employing power control strategies, the correlation between positive and negative sequence currents is bound by the unbalance factor $u \leq 1$ (equations (4.6) or (4.7)). Consequently, while the wind turbine's contribution in the positive sequence may be modest compared to a synchronous generator of similar capacity, it's even more marginal in the negative sequence.

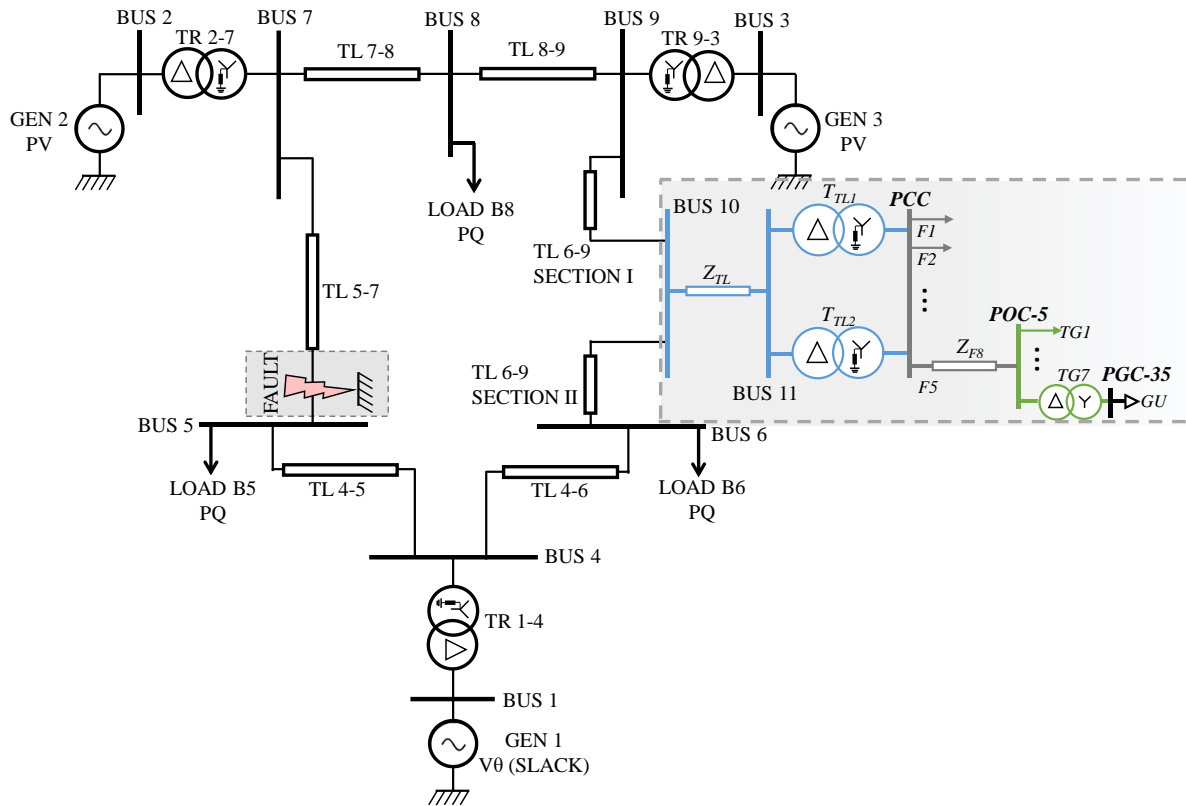
4.5 Simulations results

In this section, simulation results are presented. To evaluate and discuss the appointments made in this chapter, it is employed the standard power system, which represents a simple approximation of the Western System Coordinating Council (WSCC) to an equivalent system with nine buses and three generators, it is described in detail in [Appendix D, section D.c.](#)

For this thesis, the standard WSCC 9-bus system is modified by the inclusion of a WF located between buses 9 and 6, as illustrated in [Fig. 4.7](#). The power system simulations were implemented using *Matlab/Simulink®* software, which offers capabilities for task distribution among cores and optimized numerical solution methods, enabling the simulation of the system with the required level of detail.

The WF consists of 35 turbines, each turbine has 2.1[MVA] of capacity, the WEC systems employed in the simulations were the same models as those employed in [Chapter 3](#), described in [Appendix D, section D.a](#). As indicated in [Tab. 4.2](#), the wind farm represents 11.47% of the power system installed capacity, and its data is described on [Appendix D, section D.b](#)

Fig. 4.7: Modified 9 Bus WSCC power system.



Elaborated by the author.

Tab. 4.2: Set points of power system generators

Bus	Power [MVA]	Installed Capacity [%]
1	247.5	38.61
2	192	29.95
3	128	19.97
11	73.5	11.47

Elaborated by the author.

To simulate the power system entering in Low Voltage Ride Through (LVRT) with unbalanced voltages, faults are introduced between the phases B, C, and the ground at bus 5 (phase-phase-ground type fault) at $t = 5.9[\text{s}]$ after simulation start. The faults have duration of 100[ms], which is the maximum time limit for fault elimination by the protection systems in transmission lines and buses, as stipulated by the Brazilian TSO ONS (ONS, 2020b). In the fault elimination, the transmission line between buses 5 and 7 is removed, simulating the operation of the protection system.

According with references (ANDRADE; SORRENTINO, 2010; IEEE STD 80, [s.d.]), the fault impedance values to ground in substations vary depending on the grounding system, typically having a minimum value of $0.01[\Omega]$, which was utilized. The LVRT and RCI requirements utilized were established by the Brazilian TSO in (ONS, 2020a).

4.5.1 WF located at 50% of TL6-9

For the first analysis, the WF is allocated at 50% of the total length of the transmission line between buses 6 and 9. To evaluate the worst-case scenario, in the pre-fault condition the 35 turbines in the WF operate at their nominal active power (2[MW]).

The WF is modeled regulating active power and the voltage at bus 11 to 1.04[pu] (PV bus), which the system load flow yields a reactive power of -521.45[kVAr] for each WEC. Additionally, the load flow analysis reveals a power of 4.85[MW] at the slack bus, also regulating the voltage at bus 1 at 1.04[pu]. The operational condition specifications for the other generators in the power system are outlined in Tab. 4.3.

Tab. 4.3: Set points of power system generators.

Bus	Voltage set point [pu]	Active power set point [MW]
1	1.04	-
2	1.025	163
3	1.025	85
11	1.03	70

Elaborated by the author

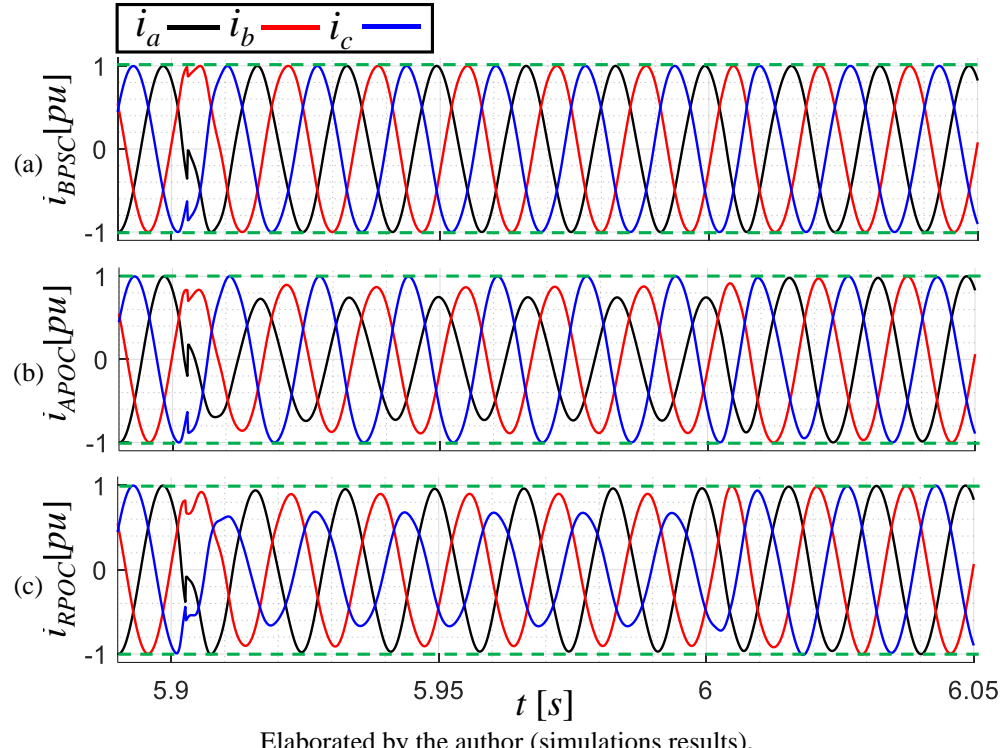
Fig. 4.8 and Fig. 4.9 depict the instantaneous current and power values at the terminals of one of the wind turbines within the WF. These readings align with the expected behavior of the power control strategies discussed in the preceding chapters, thus reinforcing the concepts and analyses established therein and the current remains within the limit of 1[pu] throughout the transient, a consequence of implementing the active power curtailment algorithm proposed in Chapter 3.

The voltage support promoted by the power control strategies at the WEC terminals is compared in Fig. 4.10. For reference, one of the simulations was conducted without the injection of reactive current during the fault, represented by a dashed gray line.

In the positive sequence, as shown in Fig. 4.10(a), the BPSC, APOC, and RPOC strategies exhibit similar behaviors. Due to the system's inductive characteristic ($X/R \gg 1$) and the prioritization of RCI, the choice of strategy has minimal impact on voltage support in the positive sequence, with values consistently above 0.75[pu].

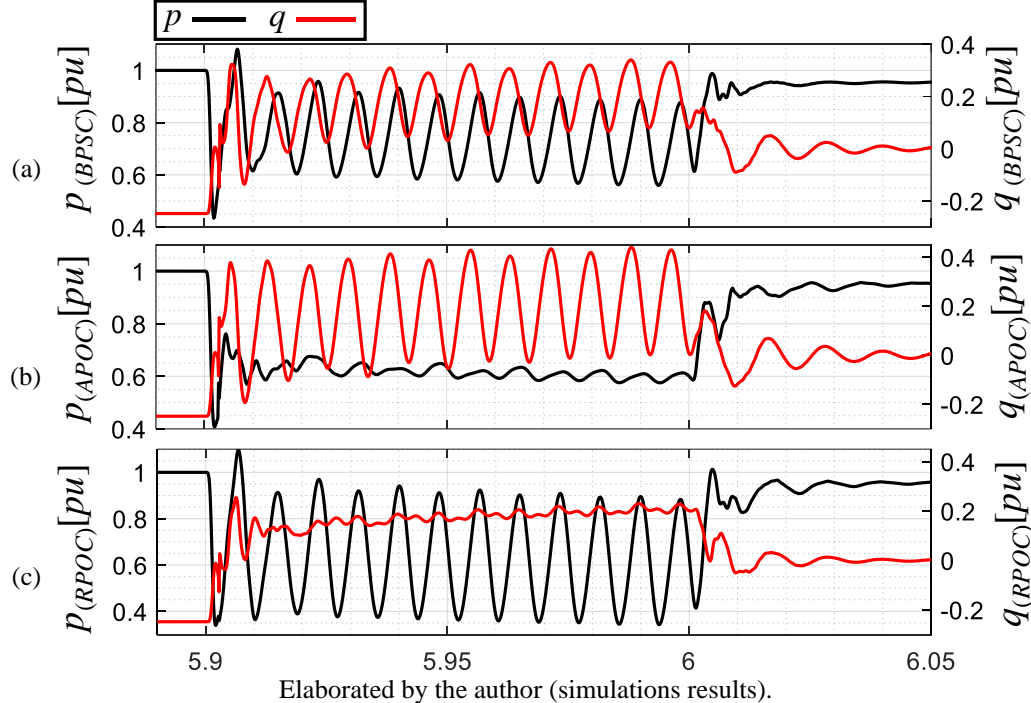
In contrast, for the simulation scenario without additional reactive current, the voltage at the wind turbine terminals drops below 0.69[pu]. This highlights the importance of the RCI requirement, as it increases the operating margin of the converter relative to the LVRT limits shown in Fig. 1.8, enabling it to operate for longer periods without disconnecting from the grid.

Fig. 4.8: WEC currents during the fault for (a) BPSC, (b) APOC and (c) RPOC (values normalized by the wind generator rated current).



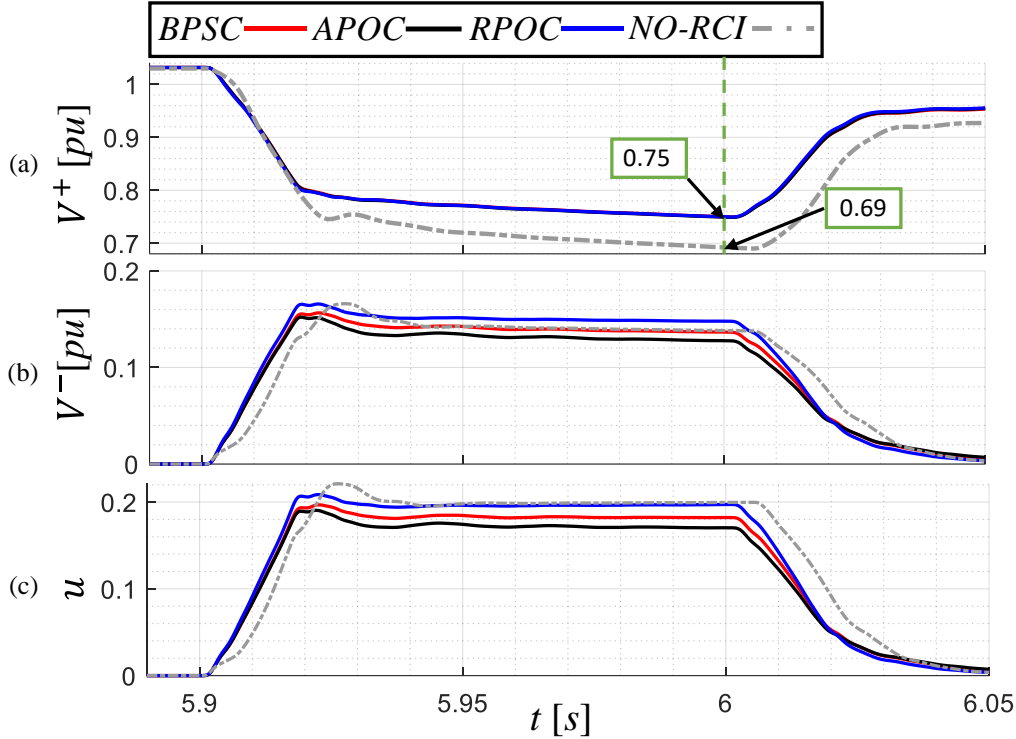
Elaborated by the author (simulations results).

Fig. 4.9: WECS instantaneous power during the fault for (a) BPSC, (b) APOC and (c) RPOC (Values normalized by the wind generator rated power).



Elaborated by the author (simulations results).

Fig. 4.10: WECS (a) positive, (b) negative and (c) unbalance factor for different power control strategies. (Values normalized by the grid converter rated voltage)



Elaborated by the author (simulations results).

For the negative sequence, depicted in Fig. 4.10(b), the choice of strategy significantly affects voltage support. Throughout the short-circuit duration, the APOC strategy exhibited the smallest magnitude, whereas the RPOC strategy showed the largest. For BPSC and no-RCI, there is no current injection in the negative sequence, resulting in similar characteristics.

Consequently, the APOC strategy has the lowest unbalance factor (Fig. 4.10(c)) among the analyzed strategies. Notably, due to the decrease in positive sequence voltage, even without altering the magnitude of the negative sequence, the unbalance factor for no-RCI is higher than for the RPOC strategy.

Fig. 4.11 illustrates the instantaneous power at bus 11, which is the connection point of the WF to the transmission line. At this level of the electrical system, none of the strategies promotes the cancellation of power oscillations, due to the existence of the zero sequence. However, voltage support is still observed, as shown in Fig. 4.12, which compares voltage values at bus 11, derived by averaging signals between the interval of $t = 5.95[s]$ and $t = 6.0[s]$. When employing the APOC strategy, the difference between the highest and lowest phase voltage magnitudes is $0.1695[pu]$, while for RPOC and BPSC, they are $0.1838[pu]$ and $0.1777[pu]$, respectively.

Fig. 4.11: Bus 11 instantaneous rea power during the fault for (a) BPSC, (b) APOC and (c) RPOC (Values normalized by the wind generator rated power).

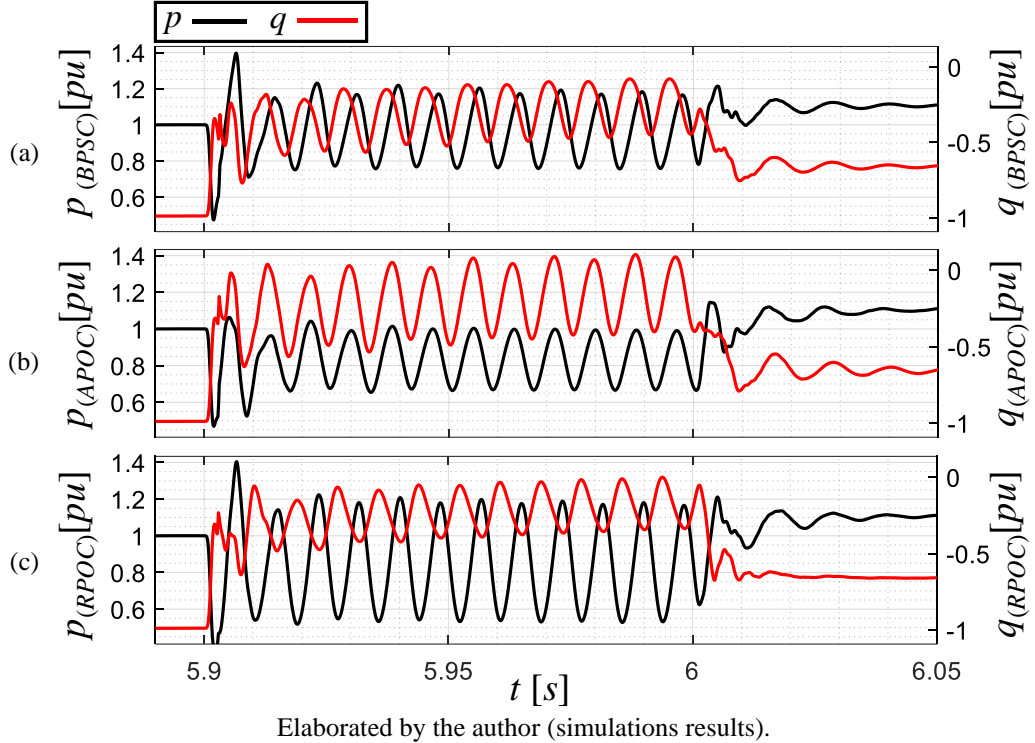
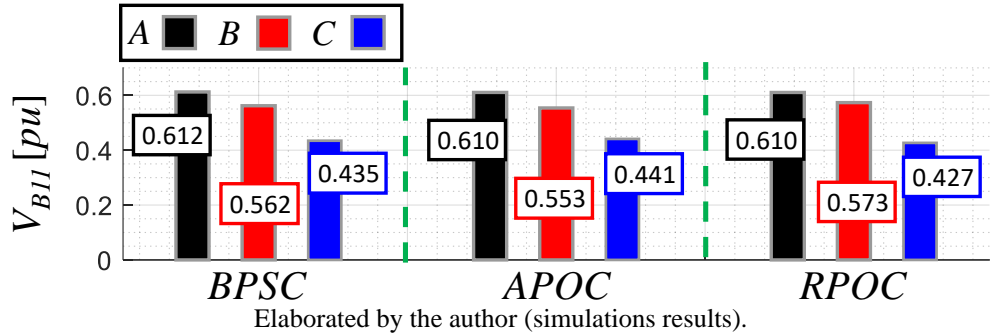
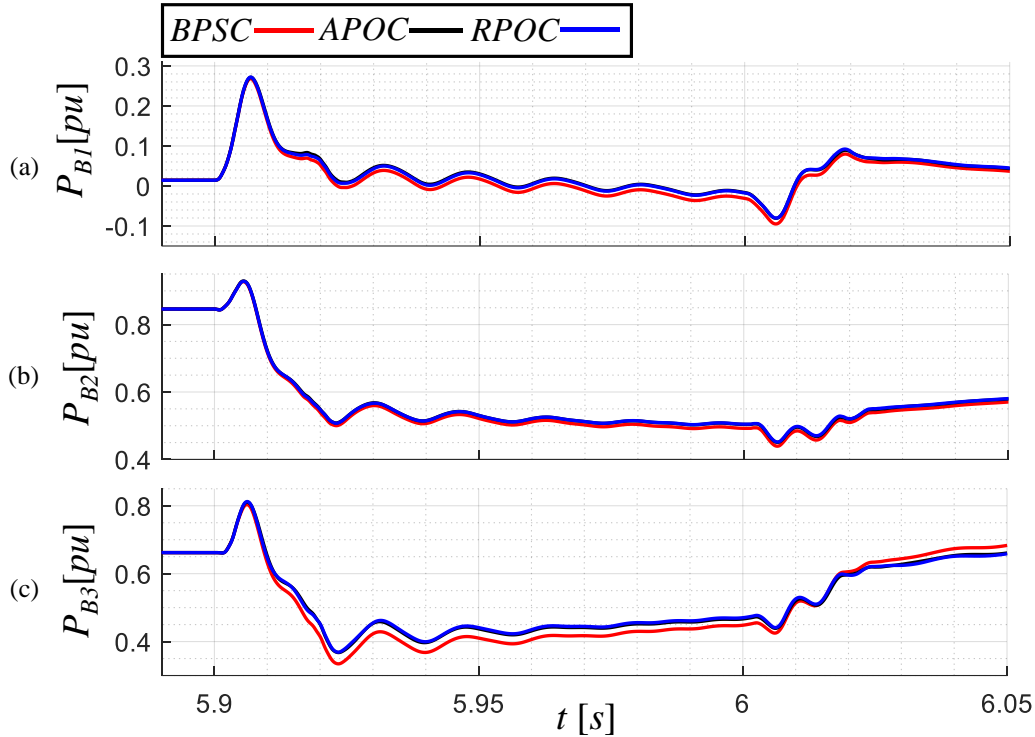


Fig. 4.12: Bus 11 average voltage magnitude for different power control strategies (Values normalized by the wind generator rated power).



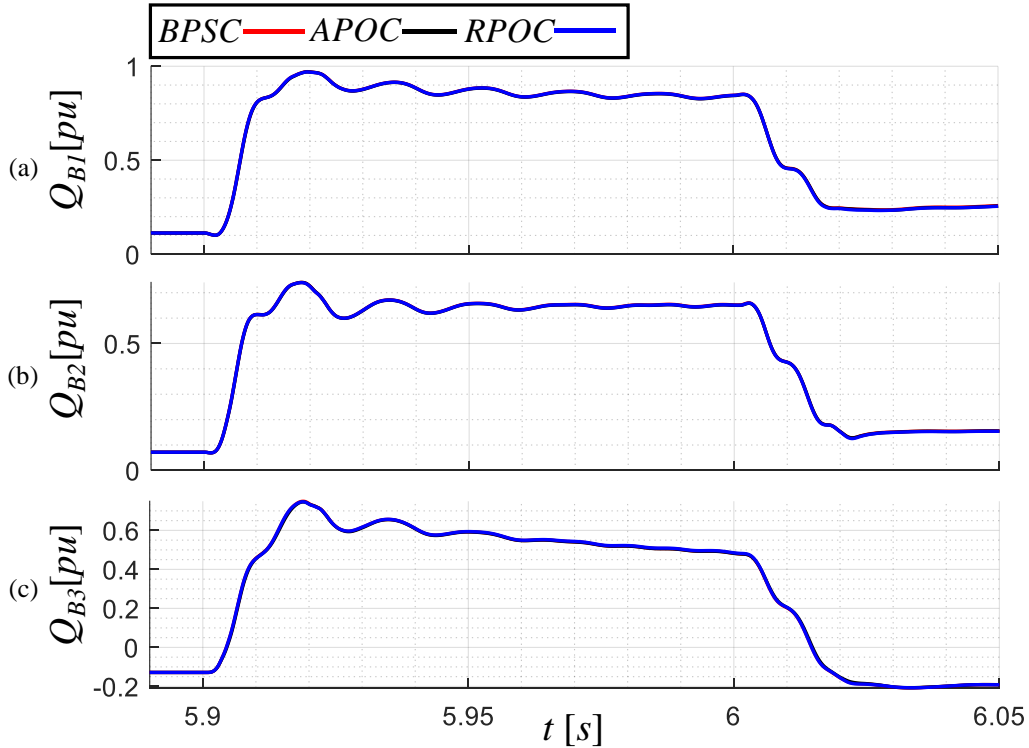
The moving average values of the active and reactive powers produced by the synchronous generators during the short circuit are shown in Fig. 4.13 and Fig. 4.14, respectively. For strategies involving negative sequence current injection, a slight increase in the active power (Fig. 4.13) of the synchronous machines is observed during the fault. This is particularly notable for the machine connected to bus 3, Fig. 4.13(c), which is the closest to the WF. In terms of reactive power, in Fig. 4.14, there is practically no difference among the strategies.

Fig. 4.13: Moving average active power during the fault for generator at (a) bus 1, (b) bus 2 and (c) bus 3 (Values normalized by the respective generator nominal apparent power).



Elaborated by the author (simulations results).

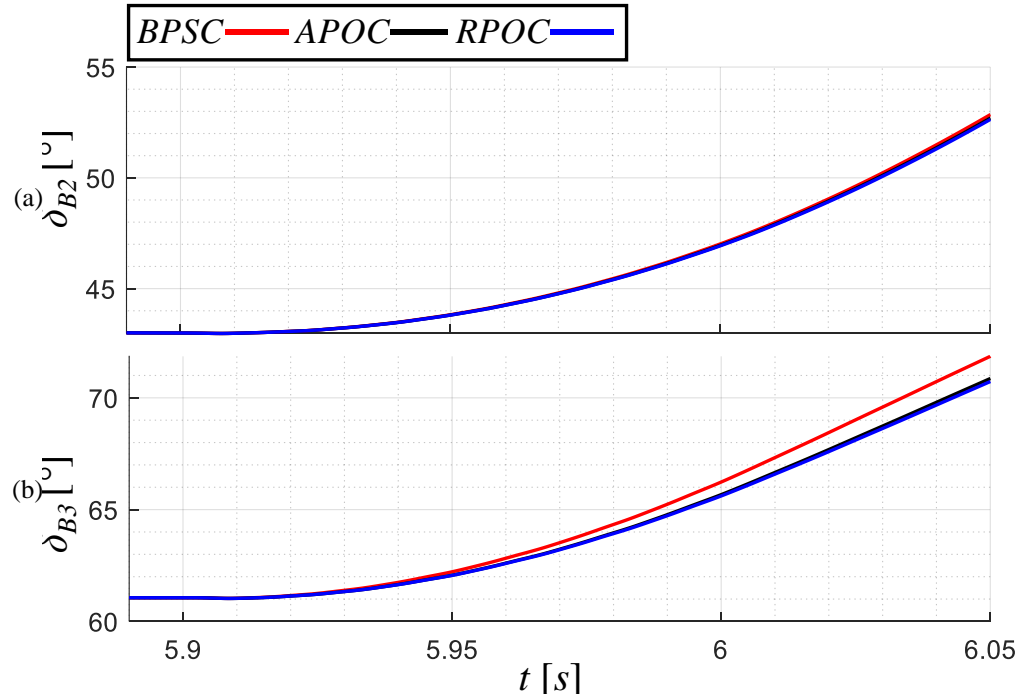
Fig. 4.14: Moving average reactive power during the fault for generator at (a) bus 1, (b) bus 2 and (c) bus 3 (Values normalized by the respective generator nominal apparent power).



Elaborated by the author (simulations results).

The increase in the active power of the synchronous generators during the fault is reflected in the load angle decrease, measured on the generators at buses 2 and 3 in relation to the reference (slack) bus 1 in Fig. 4.15. This reduction in angle is more prominent in generator 3, where the difference of the BPSC in relation to other strategies exceeds 1° at $t = 6.05[\text{s}]$.

Fig. 4.15: Angular opening of (a) bus 2 and (b) bus 3 for different power control strategies (angle values in reference to bus 1 (slack bus))



Elaborated by the author (simulations results).

It is necessary to understand the reasons why strategies that produce negative sequence currents allow synchronous generators to infeed more active power. Firstly, we can analyze the phase voltages of the generators in Fig. 4.17. The values represent the peak voltage average between the intervals $t = 5.95[\text{s}]$ and $t = 6.00[\text{s}]$. When comparing the values of the same phase, the maximum difference between one strategy and another does not exceed 0.007[pu]. Therefore, the answer doesn't lie in the voltage.

However, when comparing the moving average power values of the wind turbines in Fig. 4.17, the BPSC strategy produces a significantly higher amount of active power compared to the other strategies, because it does not generate current through the negative sequence. Consequently, with a greater amount of active power supplied by the wind farm, less will be demanded from the other generators, deteriorating the transient response.

Fig. 4.16: Generators average voltage at (a) bus 1, (b) bus 2 and (c) bus 3 for different power control strategies (Values normalized by the respective generator rated voltage).

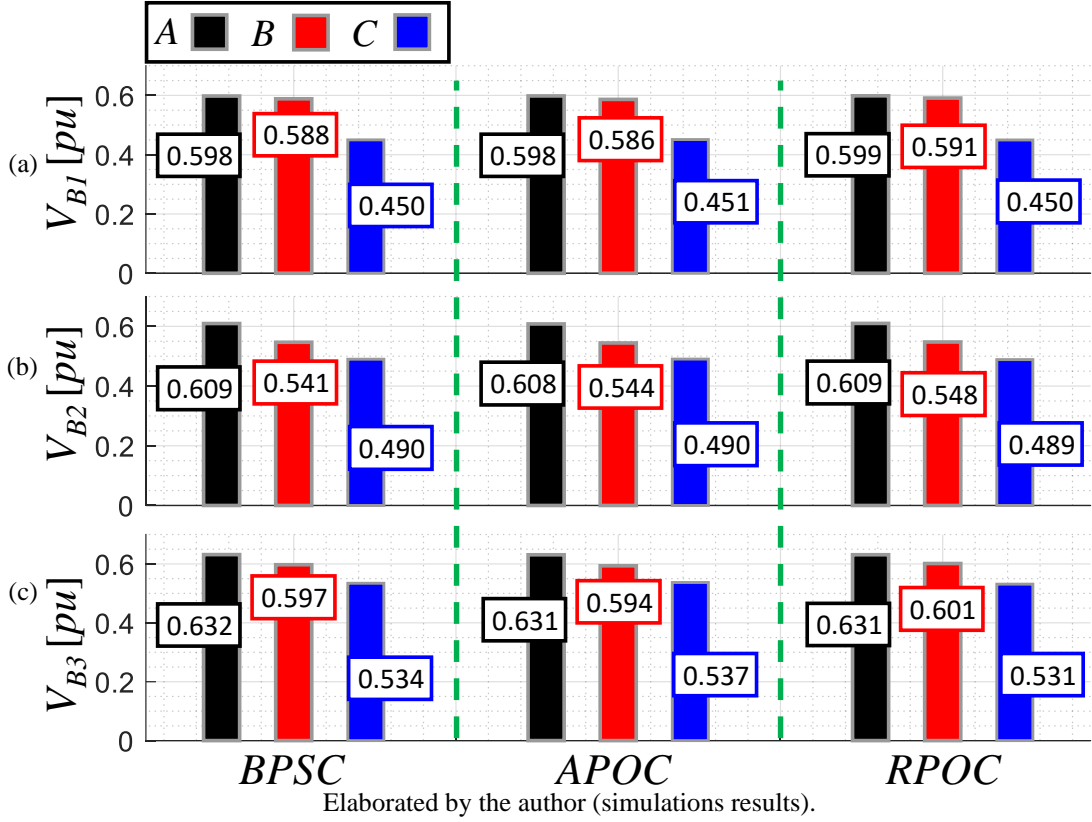
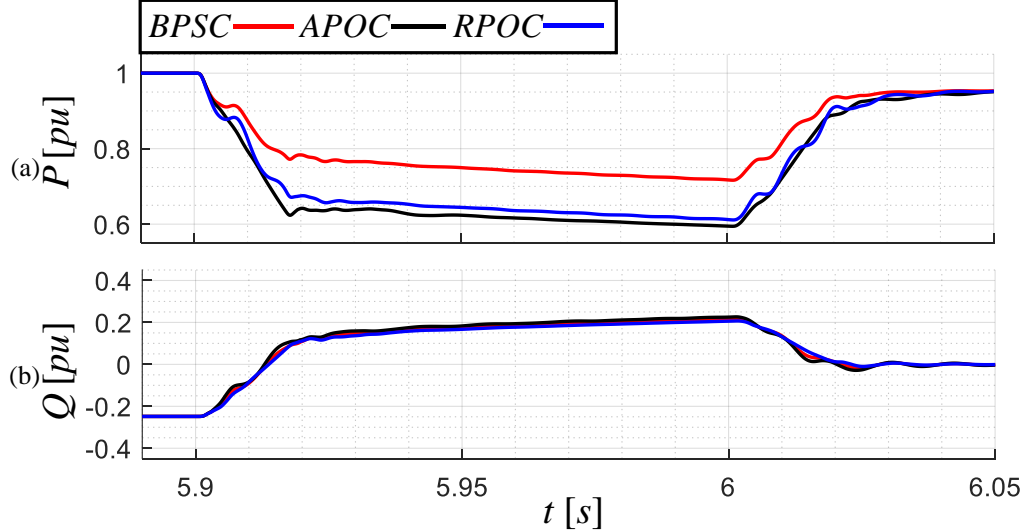


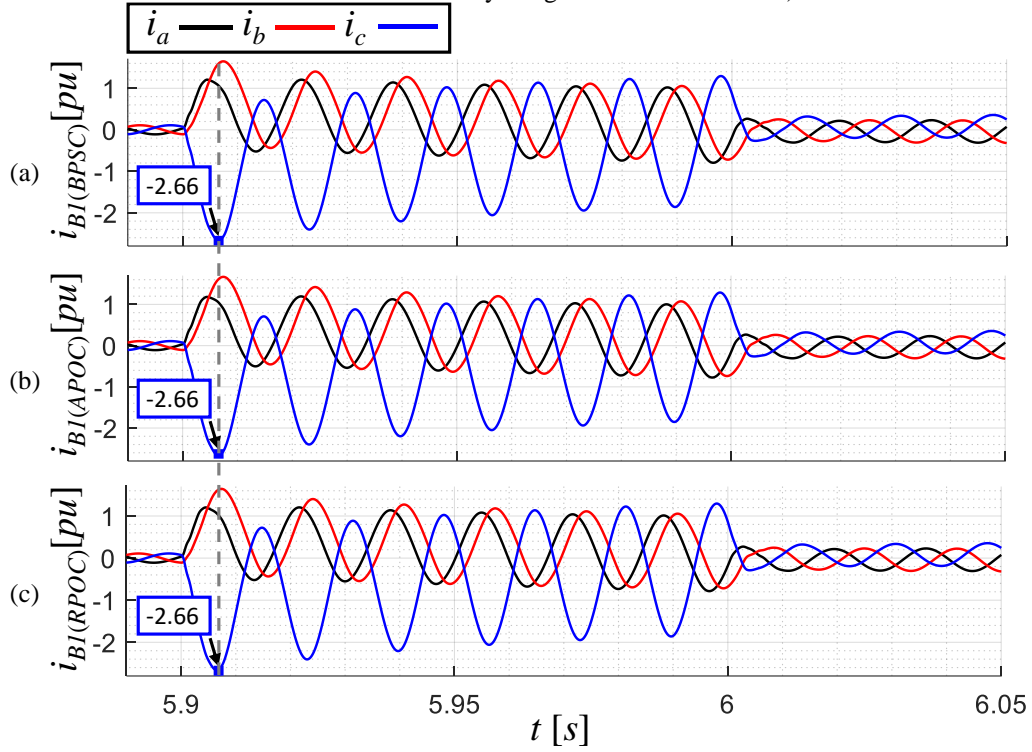
Fig. 4.17: WEC average (a) active and (b) reactive power during the fault for different power control strategies (Values normalized by the converter rated power).



4.5.2 Short-circuit contribution

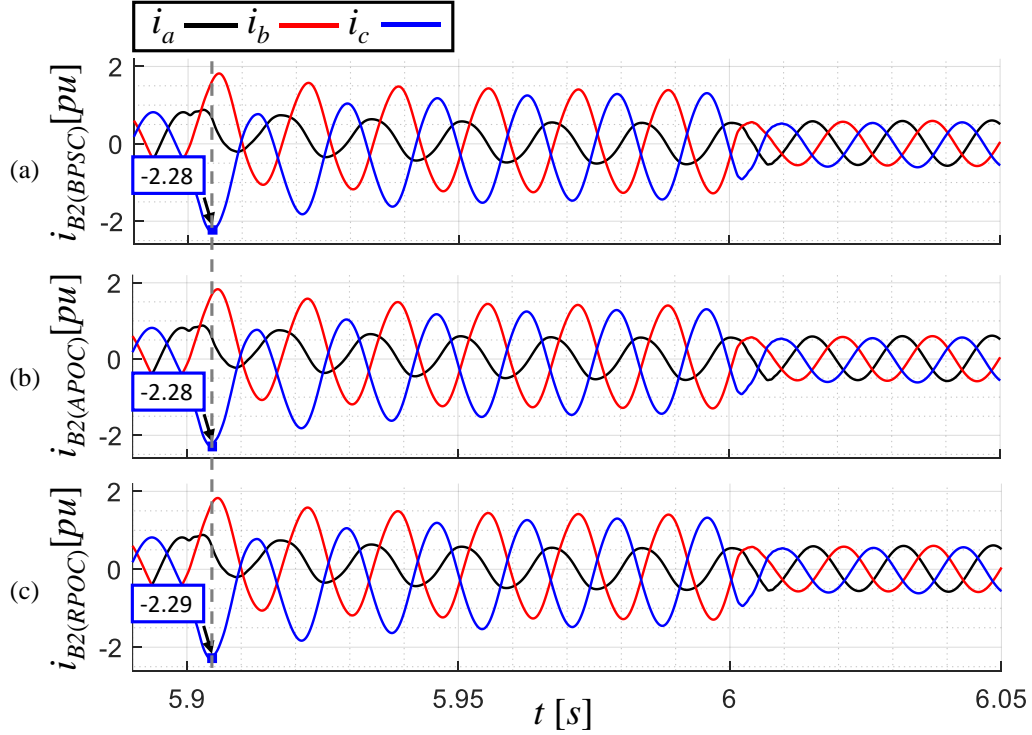
Another important point is the impact of wind farm power control strategies on the short-circuit currents of generators in the electrical power system. The graphs in Fig. 4.18, Fig. 4.19, and Fig. 4.20 show the currents temporal waveforms at buses 1, 2 and 3, respectively.

Fig. 4.18: Generator at bus 1 short-circuit current for (a) BPSC, (b) APOC and (c) RPOC. (Values normalized by the generator rated current).



Elaborated by the author (simulations results).

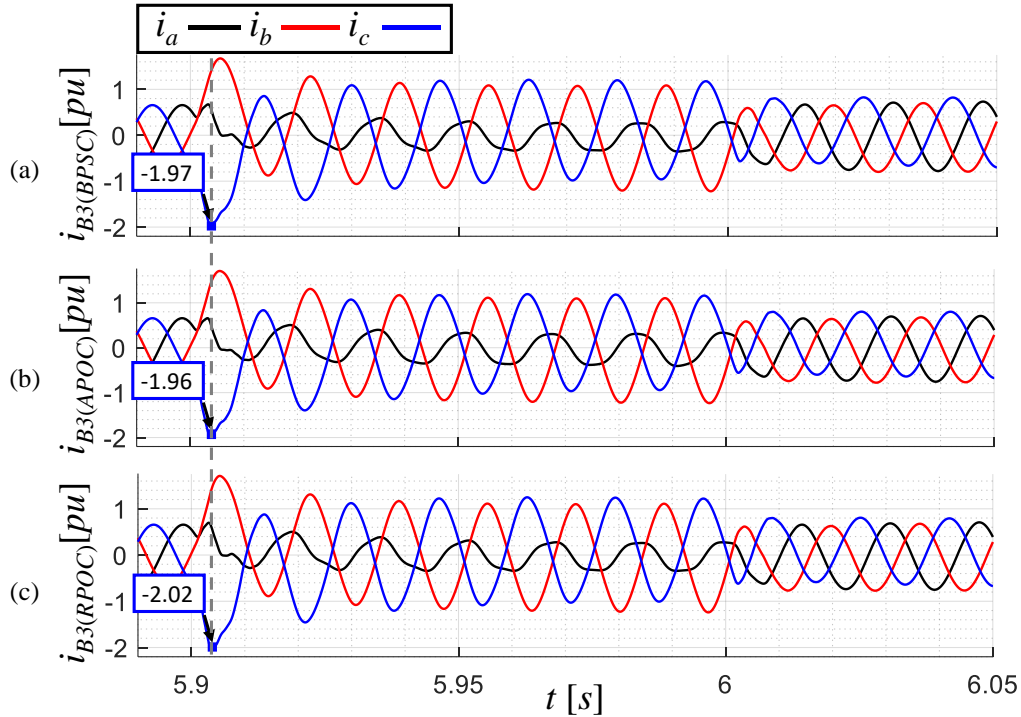
Fig. 4.19: Generator at bus 2 short-circuit current for (a) BPSC, (b) APOC and (c) RPOC. (Values normalized by the generator rated current).



Elaborated by the author (simulations results).

According to the results, changing the power control strategy does not impact the peak value of the short-circuit current of synchronous generators. But they also highlight the limitation of the contribution of wind turbines (Fig. 4.8), which is limited to 1[pu], in relation to synchronous machines.

Fig. 4.20: Generator at bus 3 short-circuit current for (a) BPSC, (b) APOC and (c) RPOC. (Values normalized by the generator rated current).



Elaborated by the author (simulations results).

4.5.3 Changing the WF location.

For a more comprehensive analysis of the parameter variations on voltage support, a series of simulations were conducted by altering the connection position of the WF along the transmission line between buses 6 and 9.

This involved adjusting the distance between the point of connection of the park relative to bus 6, thereby modifying the equivalent impedance and voltage at the wind farm's point of common coupling (PCC). The test criteria, including fault location, duration, and impedance, remain consistent with those described at the beginning of the previous section.

For pre-fault conditions, the active power and bus voltage regulation references were kept in accordance with Tab. 4.3. The reactive power references of wind turbines obtained from the load flow analysis are detailed in Tab. 4.4.

Tab. 4.4: WEC systems reactive power references for regulating the voltage at bus 11 in 1.03[pu] (values normalized by converter rated values)

WF connection in relation to bus 6 [%]	20	30	40	50	60	70	80
WEC reactive power [pu]	-0.31812	-0.29467	-0.26455	-0.24831	-0.22369	-0.19622	-0.16448

Elaborated by the author (simulation results)

Building upon the comprehensions gained from the previous section, the values during the fault are not constant. Therefore, the subsequent results pertain to average within the time range of 5.95[s] and 6[s], while the fault starts at $t = 5.9[\text{s}]$. This time interval ensures a comparison of variables under the steady state of the short circuit.

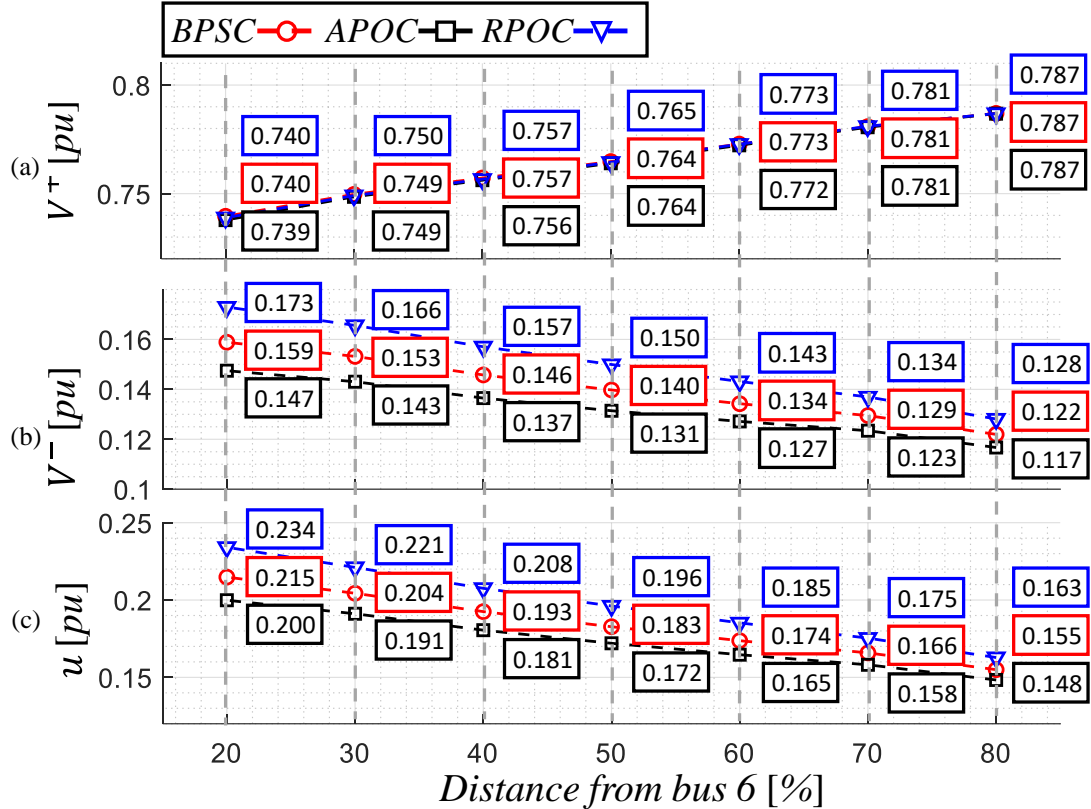
Fig. 4.21 presents the positive and negative sequence voltage, and the unbalance factor measured at the terminals of the WEC system. As the WF connection point moves away from bus 6 and further from the fault point, the effects of voltage sag and unbalance become milder. The different power control strategies present similar values for the positive sequence (Fig. 4.21(a)).

However, for the negative sequence (Fig. 4.21(b)), as the connection point approaches the fault, the difference between the magnitude of the voltages becomes larger, with the APOC strategy presenting the lowest values and the RPOC the highest ones. Consequently, the imbalance factor (Fig. 4.21(c)) is also lowest for the APOC strategy.

The active and reactive power generated by the wind turbine during the fault are depicted in Fig. 4.22. Due to the absence of negative sequence currents in the BPSC, its active power production (Fig. 4.22(a)) surpasses that of the other strategies. This difference is evident even at a connection point further away from bus 6, where the voltage imbalance is less pronounced. For reactive power (Fig. 4.22(b)), the difference between the strategies is not as prominent, but RPOC still presents the highest average value of reactive power among the strategies.

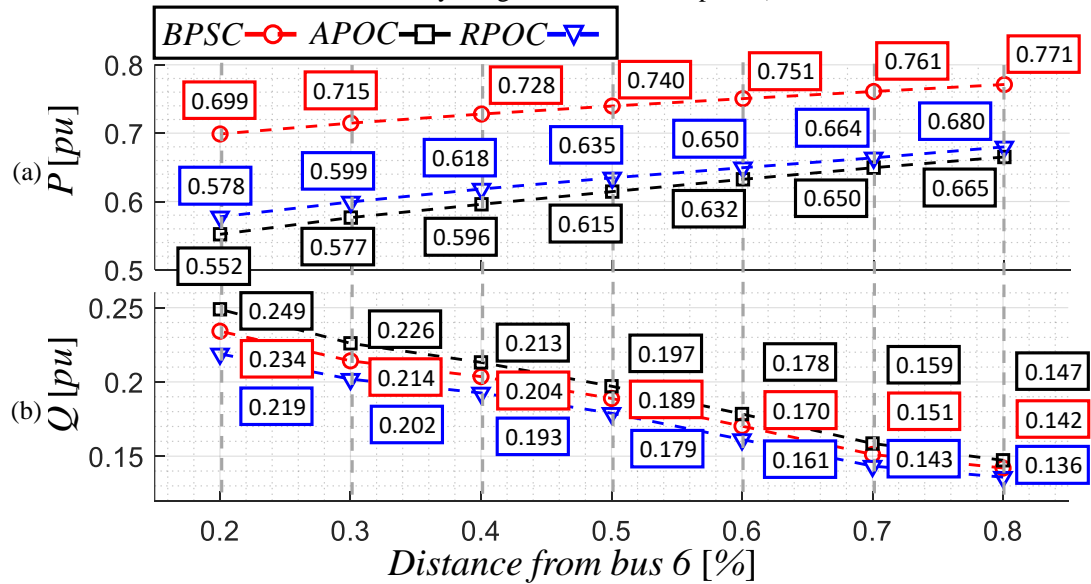
From the previous results, the synchronous generator connected to bus 3 was the most impacted by the change in the wind farm's power control strategies. The average active and reactive powers of this generator are shown in Fig. 4.23. Contrary to the WEC system, the BPSC strategy by the WF's wind turbines results in a smaller amount of active power produced by the synchronous generator (Fig. 4.23(a)), and the use of RPOC in the highest results active power for generator 3. For reactive power (Fig. 4.23(b)), the application of different strategies does not result in significant differences between them.

Fig. 4.21: WEC (a) positive, (b) negative and (c) unbalance factor for different power control strategies changing the location of wind farm. (Values normalized by the grid converter rated voltage).



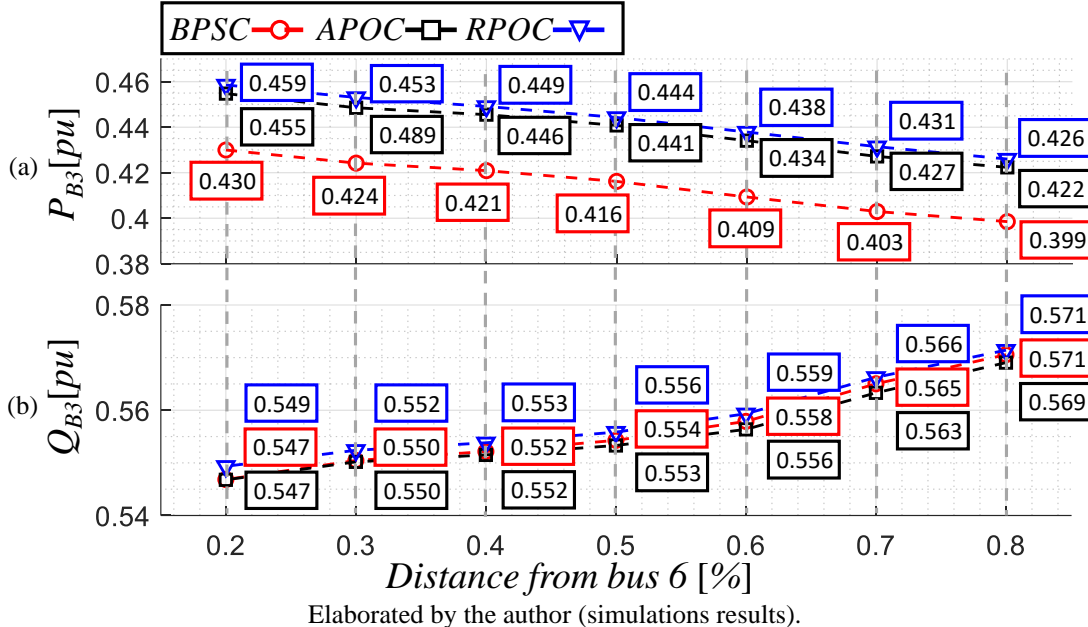
Elaborated by the author (simulations results).

Fig. 4.22: WEC average (a) active and (b) reactive power during the short-circuit. (Values normalized by the generator nominal power).



Elaborated by the author (simulations results).

Fig. 4.23: Synchronous generator at bus 3 average (a) active and (b) reactive power during the short-circuit. (Values normalized by the generator nominal power).



Elaborated by the author (simulations results).

4.6 Chapter conclusion

This chapter delved into examining the effects of power control strategies on the operation of the electrical system during unbalanced voltage sags. Mathematical models were specifically designed to explore how wind turbine technology, employing full-power converters, impacts short-circuit current and voltage support.

Irrespective of the chosen control strategy or the nature of the short circuit, the wind turbine's contribution remains limited to its nominal value. However, it can actively participate in the negative sequence, albeit within stringent constraints imposed by power control strategies.

In terms of voltage support, the model predictions, substantiated by simulation outcomes, underscore the efficacy of the Active Power Oscillation Cancellation (APOC) strategy. Not only does it nullify active power oscillations, but it also diminishes the magnitude of negative sequence voltage. Consequently, the APOC emerges as the most adept strategy in mitigating the effects of unbalanced sags on electronic converters, offering significant flexibility in voltage support while damping active power oscillations.

Furthermore, the APOC, coupled with positive sequence reactive current injection, presents a more enticing alternative compared to the requirements outlined in VDE AR N 4120. While offering greater flexibility in voltage support, VDE AR N 4120 fails to dump active power oscillations.

Finally, an intriguing observation is that strategies facilitating the circulation of negative sequence currents generate less active power compared to BPSC. This, in turn, bolsters the stability margin of synchronous generators, particularly in the vicinity of WFs.

Chapter V

CONCLUSIONS

5.1.1 Thesis conclusions

Wind energy conversion systems (WECS), specifically wind turbines employing full-power converters, exhibit different transient behaviors compared to synchronous machines. Due to the physical constraints of semiconductor devices, WECS display current source characteristics, posing both advantages and challenges, because while offering greater control flexibility, they also limit system support capabilities.

Grid codes mandate that during momentary voltage sags, wind turbines must inject reactive current to improve the voltage profile and extend their operation. However, during asymmetric faults, due to the physical limitations of the converter, there is a trade-off between damping power oscillations and flexibility in voltage support.

To address damping power oscillations, several power control strategies can be employed, such as Active Power Oscillation Cancellation (APOC), Reactive Power Oscillation Cancellation (RPOC), and Balanced Positive Sequence Control (BPSC). These strategies have been thoroughly discussed in this thesis.

Building upon grid codes and the need for instantaneous power oscillation cancellation during asymmetric faults, this thesis proposes an algorithm that prioritizes the following tasks:

- 1.** Compliance with voltage ride-through and RCI requirements.
- 2.** Limiting grid converter current to rated value.
- 3.** Control of active power production.
- 4.** Mitigation of power oscillations during unbalanced voltage sags.

The algorithm was validated through computational simulations of a 2.1[MW] WEC based on real data system. Results demonstrated that the algorithm kept converter current within rated limits under various operational conditions. Furthermore, it forecasted the maximum active power capacity that could be supplied to the grid, allowing for implementation of protection chopper circuit control to protect not only DC bus capacitors but also reduce their operational impacts.

An important point to highlight is canceling power oscillations is only feasible because the actual grid code just defines the behavior positive sequence reactive current, thereby providing three degrees of freedom that encompass negative sequence reactive current and positive and negative sequence active currents.

However, as demonstrated in this thesis, in more recent GCs, e.g., VDE AR N 4120, the behavior of both positive and negative sequence reactive currents is pre-established, and it is not possible to cancel power oscillations.

Tab. 5.1 summarizes the results of the test system during a unbalanced voltage sag with unbalance factor $u = 0.333$ and $|\mathbf{v}^+| = 0.6[\text{pu}]$. The better settings of current and voltage ripple in the capacitors, diode and IGBT losses are highlighted in blue on Tab. 5.1, and except for diodes losses, the APOC has all of them, reducing the current ripple ($I_{(120[\text{Hz}])}$) to 4.7[%] of the converter nominal current and 41.4[%] of IGBT nominal operation losses. Therefore, it proves to be the most effective in terms of reducing impacts on the converter.

Tab. 5.1: Summary results of power oscillation impact on the grid power converter

	BPSC	APOC	RPOC
Current ripple ⁽¹⁾	0.172	0.047	0.314
Voltage ripple ⁽²⁾	0.028	0.008	0.050
Diode losses ⁽³⁾	2.982	2.884	2.765
IGBT losses ⁽⁴⁾	0.726	0.414	0.489

Values normalized by: (1) converter nominal current, (2) DC bus operational voltage, (3)(2) losses in nominal operation condition.

In this work, the effects of different power control strategies on voltage support and their impacts on other generators within the electrical power system were evaluated. Tab. 5.2 summarizes the most important results obtained with the wind farm at the closest distance to the fault point (20% of the distance from the line to bus 6). This investigation was conducted through mathematical modeling, validated by computational simulations of the WSCC 9-bus system, incorporating a 73.5[MVA] wind farm based on real system data.

The three strategies present very similar values of voltage magnitude in the positive sequence. However, for the negative one, the APOC strategy presents the lowest value ($V = 0.147[\text{pu}]$), indicating that the voltage at the WEC terminals tends to be more balanced.

Regarding impacts on synchronous machines, due to its proximity to the wind farm, generator 3 is the most affected by the change in strategy. In this case, the RPOC provides the highest active power supply by this generator ($P = 0.459[\text{pu}]$), a result very close to that of the APOC strategy ($P = 0.455[\text{pu}]$), i.e., increasing the generator stability margin.

Tab. 5.2: Summary results of power control strategies on power system

	BPSC	APOC	RPOC
WEC positive seq. Voltage ⁽¹⁾	0.740	0.740	0.739
WEC negative seq. Voltage ⁽¹⁾	0.159	0.147	0.173
WEC active power ⁽²⁾	0.699	0.552	0.578
WEC reactive power ⁽²⁾	0.234	0.249	0.219
Gen. 3 active power ⁽³⁾	0.430	0.455	0.459
Gen. 3 reactive power ⁽³⁾	0.547	0.547	0.549

Values normalized by: (1) converter nominal voltage, (2) converter nominal power, (3) generator 3 nominal power.

The results obtained through models and computer simulations demonstrate that the APOC strategy not only reduces the impacts of sags on the converter but also provides the best voltage support among the strategies analyzed. This makes APOC an interesting alternative to more recent grid codes, such as VDE AR N 4120, which, despite offering greater flexibility in terms of voltage support, fail to dampen power fluctuations.

5.1.2 Author publications

The results presented in this thesis outcome in the following publications:

- R.M. Silva, A.F. Cupertino, G.M. Rezende, C.V. Sousa, V.F. Mendes, Power control strategies for grid connected converters applied to full-scale wind energy conversion systems during LVRT operation, Electric Power Systems Research. 184 (2020) 106279. <https://doi.org/10.1016/j.epsr.2020.106279>.
- R.M. Silva, C.V. Sousa, V.F. Mendes, Active Power Saturation for Full-Scale Renewable Power Converters during Voltage Ride Through Operation, in: 2021 14th IEEE International Conference on Industry Applications (INDUSCON), IEEE, São Paulo, Brazil, 2021: pp. 31–37. <https://doi.org/10.1109/INDUSCON51756.2021.9529450>.

5.2 Work continuity.

The following future works proposals are proposed:

- Deeper study of the power control effects on the converter lifetime, quantifying the thermal stress during the voltage sags.
- Extend the application of the active power curtailment algorithm so that it can also cover the requirements of VDE AR N 4120.
- Extending the analysis to inter-area electrical power systems.

REFERENCES

- AGHMADI, A.; MOHAMMED, O. A. Energy Storage Systems: Technologies and High-Power Applications. **Batteries**, v. 10, n. 4, p. 141, 20 abr. 2024.
- AKAGI, H.; WATANABE, E.; AREDES, M. **Instantaneous power theory and applications to power conditioning**. Second edition ed. Hoboken, New Jersey: IEEE Press/Wiley, 2017.
- ALGHAMDI, S. A. Improvement of Fault Ride-Through Capability of Grid Connected Wind Turbine Based on a Switched Reluctance Generator Using a Dynamic Voltage Restorer. **Sustainability**, v. 15, n. 14, p. 11061, 14 jul. 2023.
- AMIRNASER YAZDANI; REZA IRAVANI. **Voltage-Sourced Converters in Power Systems : Modeling, Control, and Applications**. [s.l.] Wiley-IEEE Press, 2010.
- ANDERSON, P. M. **Analysis of faulted power systems**. New York: IEEE Press, 1995.
- ANDRADE, V. D.; SORRENTINO, E. **Typical expected values of the fault resistance in power systems**. 2010 IEEE/PES Transmission and Distribution Conference and Exposition: Latin America (T&D-LA). *Anais...* Em: EXPOSITION: LATIN AMERICA. Sao Paulo, Brazil: IEEE, nov. 2010. Disponível em: <<http://ieeexplore.ieee.org/document/5762944/>>. Acesso em: 21 nov. 2023
- APPUNN, K. **The history behind Germany's nuclear phase-out**. News. Disponível em: <<https://www.cleanenergywire.org/factsheets/history-behind-germanys-nuclear-phase-out>>. Acesso em: 3 out. 2021.
- BERGER, M. et al. Dual Control Strategy for Grid-tied Battery Energy Storage Systems to Comply with Emerging Grid Codes and Fault Ride Through Requirements. **Journal of Modern Power Systems and Clean Energy**, v. 10, n. 4, p. 977–988, 2022.
- BU, S. Q. et al. Probabilistic Analysis of Small-Signal Stability of Large-Scale Power Systems as Affected by Penetration of Wind Generation. **IEEE Transactions on Power Systems**, v. 27, n. 2, p. 762–770, maio 2012.
- BUSO, S.; MATTAVELLI, P. **Digital control in power electronics**. 2nd edition ed. San Rafael, Calif.: Morgan & Claypool Publishers, 2015.
- CAMACHO, A. et al. Flexible Voltage Support Control for Three-Phase Distributed Generation Inverters Under Grid Fault. **IEEE Transactions on Industrial Electronics**, v. 60, n. 4, p. 1429–1441, abr. 2013a.
- CAMACHO, A. et al. Flexible Voltage Support Control for Three-Phase Distributed Generation Inverters Under Grid Fault. **IEEE Transactions on Industrial Electronics**, v. 60, n. 4, p. 1429–1441, abr. 2013b.

CAMACHO, A. et al. Reactive Power Control for Distributed Generation Power Plants to Comply With Voltage Limits During Grid Faults. **IEEE Transactions on Power Electronics**, v. 29, n. 11, p. 6224–6234, nov. 2014.

CAMACHO, A. et al. Control Strategy for Distribution Generation Inverters to Maximize the Voltage Support in the Lowest Phase During Voltage Sags. **IEEE Transactions on Industrial Electronics**, v. 65, n. 3, p. 2346–2355, mar. 2018.

CAMM, E. H. et al. **Wind power plant grounding, overvoltage protection, and insulation coordination: IEEE PES wind plant collector system design working group**. 2009 IEEE Power Energy Society General Meeting. Anais... Em: 2009 IEEE POWER ENERGY SOCIETY GENERAL MEETING. jul. 2009.

CASTILLA, M. et al. Grid-Fault Control Scheme for Three-Phase Photovoltaic Inverters With Adjustable Power Quality Characteristics. **IEEE Transactions on Power Electronics**, v. 25, n. 12, p. 2930–2940, dez. 2010.

CASTILLA, M. et al. Voltage Support Control Strategies for Static Synchronous Compensators Under Unbalanced Voltage Sags. **IEEE Transactions on Industrial Electronics**, v. 61, n. 2, p. 808–820, fev. 2014.

CASTILLA, M. et al. Avoiding overvoltage problems in three-phase distributed-generation systems during unbalanced voltage sags. **IET Power Electronics**, v. 13, n. 8, p. 1537–1545, jun. 2020.

CÉSAR A. SILVA, S. R. Current reference strategy with explicit negative sequence component for voltage equalization contribution during asymmetric fault ride through. **International Transactions on Electrical Energy Systems**, v. 25, p. 3449–3471, 22 dez. 2014.

CHEN, J. et al. **Lifetime assessment of DC link electrolytic capacitor of wind power converter based on operational condition**. 2016 IEEE International Conference on High Voltage Engineering and Application (ICHVE). Anais... Em: 2016 IEEE INTERNATIONAL CONFERENCE ON HIGH VOLTAGE ENGINEERING AND APPLICATION (ICHVE). Chengdu, China: IEEE, set. 2016. Disponível em: <<http://ieeexplore.ieee.org/document/7800694/>>. Acesso em: 17 jun. 2024

CHOU, S.-F. et al. **A reactive current injection technique for renewable energy converters in low voltage ride-through operations**. 2011 IEEE Power and Energy Society General Meeting. Anais... Em: 2011 IEEE POWER & ENERGY SOCIETY GENERAL MEETING. San Diego, CA: IEEE, jul. 2011. Disponível em: <<https://ieeexplore.ieee.org/document/6039096/>>. Acesso em: 19 jun. 2024

COMMISSION REGULATION (EU) 2016/631. Commission Regulation (EU) 2016/631 of 14 April 2016: establishing a network code on requirements for grid connection of generators. Official Journal of the European Union, , 14 abr. 2016. Disponível em: <<https://eur-lex.europa.eu/legal-content/EN/TXT/PDF/?uri=CELEX:32016R0631>>. Acesso em: 22 mar. 2022

CONROY, J. F.; WATSON, R. Low-voltage ride-through of a full converter wind turbine with permanent magnet generator. **IET Renewable Power Generation**, v. 1, n. 3, p. 182–189, set. 2007.

CUPERTINO, A. F. et al. Benchmarking of power control strategies for photovoltaic systems under unbalanced conditions. **International Journal of Electrical Power & Energy Systems**, v. 106, p. 335–345, 1 mar. 2019.

CZARNECKI, L. S. Orthogonal decomposition of the currents in a 3-phase nonlinear asymmetrical circuit with a nonsinusoidal voltage source. **IEEE Transactions on Instrumentation and Measurement**, v. 37, n. 1, p. 30–34, mar. 1988.

DE ANDRADE, E. G. et al. **Power losses in photovoltaic inverter components due to reactive power injection**. 2016 12th IEEE International Conference on Industry Applications (INDUSCON). Anais... Em: 2016 12TH IEEE INTERNATIONAL CONFERENCE ON INDUSTRY APPLICATIONS (INDUSCON). Curitiba, PR, Brazil: IEEE, nov. 2016. Disponível em: <<http://ieeexplore.ieee.org/document/7874587/>>. Acesso em: 26 jun. 2024

DEETJEN, T. A.; RHODES, J. D.; WEBBER, M. E. The impacts of wind and solar on grid flexibility requirements in the Electric Reliability Council of Texas. **Energy**, v. 123, p. 637–654, mar. 2017.

DESALEGN, B. et al. Onshore versus offshore wind power trends and recent study practices in modeling of wind turbines' life-cycle impact assessments. **Cleaner Engineering and Technology**, v. 17, p. 100691, dez. 2023.

ENERGINET. **Technical regulation 3.2.5 for wind power plants above 11kW**. Energinet, , jul. 2016.

ENTSO-E. **Fault current contribution from PPMS & HVDC**. Entso-e, , 16 nov. 2016. Disponível em: <https://eepublicdownloads.entsoe.eu/clean-documents/Network%20codes%20documents/NC%20RfG/161116_IGD_Fault%20Current%20Contribution%20from%20PPMs%20%20HVDC_for%20consultation_for%20publication.pdf>. Acesso em: 22 mar. 2023

ENTSOE, E. N. OF T. S. O. FOR E. **Need for synthetic inertia (SI) for frequency regulation**. entsoe, , 2 nov. 2017.. Acesso em: 10 out. 2021

ENTSOE, E. N. OF T. S. O. FOR E. **Short Circuit Contribution of New Generating Units Connected With Power Electronics and Protection Behaviour**. , 3 abr. 2019. Disponível em: <https://eepublicdownloads.entsoe.eu/clean-documents/SOC%20documents/190304_SOC_TOP_7.4_Short%20Circuit%20Contribution%20of%20Power%20Electronics%20Connecting%20Generators%20and%20Protection%20report.pdf>. Acesso em: 10 set. 2021

EPCOS. **Film Capacitors:General Technical Information**. EPCOS (TDK), , maio 2009. Disponível em: <https://www.tdk-electronics.tdk.com/en/web/%20generator/Web/Sections/ProductCatalog/Capacitors/FilmCapacitors/%20PDF/PDF__GeneralTechnicalInformation,property=Data__en.pdf;/PDF_GeneralTechnicalInformation.pdf>

EPE, E. DE P. E. Balanço Energético Nacional 2012: Ano base 2011 (Brazilian Energy Balance 2012 Year 2010): BEN. [s.l.] Ministério de Minas e Energia (MME), 2012. Disponível em: <<https://www.epe.gov.br/sites-pt/publicacoes-dados-abertos/publicacoes/PublicacoesArquivos/publicacao-131/topico-102/Relat%C3%ADrio%20S%C3%ADntese%202012.pdf>>. Acesso em: 1 jun. 2021.

EPE, E. DE P. E. Balanço Energético Nacional 2023: Ano base 2022 (Brazilian Energy Balance 2023 Year 2022): BEN. [s.l.] Ministério de Minas e Energia (MME), 2023. Disponível em: <<https://www.epe.gov.br/sites-pt/publicacoes-dados-abertos/publicacoes/PublicacoesArquivos/publicacao-748/topico-687/BEN2023.pdf>>. Acesso em: 1 jun. 2023.

ERLICH, I. et al. Effect of wind turbine output current during faults on grid voltage and the transient stability of wind parks. 2009 IEEE Power & Energy Society General Meeting. Anais... Em: ENERGY SOCIETY GENERAL MEETING (PES). Calgary, Canada: IEEE, jul. 2009. Disponível em: <<http://ieeexplore.ieee.org/document/5275626/>>. Acesso em: 2 dez. 2021

FEI WANG; DUARTE, J. L.; HENDRIX, M. A. M. Pliant Active and Reactive Power Control for Grid-Interactive Converters Under Unbalanced Voltage Dips. **IEEE Transactions on Power Electronics**, v. 26, n. 5, p. 1511–1521, maio 2011.

FEIX, G. et al. Simple methods to calculate IGBT and diode conduction and switching losses. 2009 13th European Conference on Power Electronics and Applications. Anais... Em: 2009 13TH EUROPEAN CONFERENCE ON POWER ELECTRONICS AND APPLICATIONS. Barcelona, Spain: IEEE, 10 set. 2009. Disponível em: <<https://ieeexplore.ieee.org/document/5278746>>

FENG, Y. et al. Power Oscillation Control of Grid-Feeding Converter Considering Next Generation Grid Code During Asymmetrical Faults. 2020 IEEE Energy Conversion Congress and Exposition (ECCE). Anais... Em: 2020 IEEE ENERGY CONVERSION CONGRESS AND EXPOSITION (ECCE). Detroit, MI, USA: IEEE, 11 out. 2020. Disponível em: <<https://ieeexplore.ieee.org/document/9235844>>. Acesso em: 20 jun. 2024

GANDHI, O. et al. Competitiveness of PV Inverter as a Reactive Power Compensator considering Inverter Lifetime Reduction. **Energy Procedia**, v. 150, p. 74–82, set. 2018.

GARNICA, M. et al. Optimal Voltage-Support Control for Distributed Generation Inverters in *RL* Grid-Faulty Networks. **IEEE Transactions on Industrial Electronics**, v. 67, n. 10, p. 8405–8415, out. 2020.

GOKSU, O. et al. Impact of wind power plant reactive current injection during asymmetrical grid faults. **IET Renewable Power Generation**, v. 7, n. 5, p. 484–492, set. 2013.

GÖKSU, Ö. et al. Instability of Wind Turbine Converters During Current Injection to Low Voltage Grid Faults and PLL Frequency Based Stability Solution. **IEEE Transactions on Power Systems**, v. 29, n. 4, p. 1683–1691, jul. 2014.

GOLESTAN, S.; GUERRERO, J. M.; VASQUEZ, J. C. Three-Phase PLLs: A Review of Recent Advances. **IEEE Transactions on Power Electronics**, v. 32, n. 3, p. 1894–1907, mar. 2017.

GOMES GUERREIRO, G. M. et al. Concerning Short-Circuit Current Contribution Challenges of Large-Scale Full-Converter Based Wind Power Plants. **IEEE Access**, v. 11, p. 64141–64159, 2023.

GRAB, R. et al. Modeling of Photovoltaic Inverter Losses for Reactive Power Provision. **IEEE Access**, v. 10, p. 108506–108516, 2022.

GRAUNGAARD TAUL, M. et al. Current Reference Generation Based on Next-Generation Grid Code Requirements of Grid-Tied Converters During Asymmetrical Faults. **IEEE Journal of Emerging and Selected Topics in Power Electronics**, v. 8, n. 4, p. 3784–3797, dez. 2020.

GUERREIRO, G. M. G. et al. Novel estimation framework for short-circuit current contribution of type IV wind turbines at transient and steady-state of the faults. **Electric Power Systems Research**, v. 234, p. 110679, set. 2024.

HASAN, S.; AGARWAL, V. An Unconstrained Voltage Support Scheme for Distributed Generation Connected to Resistive-Inductive Grid Under Unbalanced Conditions. **IEEE Transactions on Industry Applications**, v. 57, n. 4, p. 4253–4262, jul. 2021.

HE, X.; GENG, H.; MU, G. Modeling of wind turbine generators for power system stability studies: A review. **Renewable and Sustainable Energy Reviews**, v. 143, p. 110865, jun. 2021.

HIREMATH, R.; MOGER, T. Comprehensive review on low voltage ride through capability of wind turbine generators. **International Transactions on Electrical Energy Systems**, v. 30, n. 10, out. 2020.

ICSEG, I. C. FOR A S. E. G. **WSCC 9-Bus System**. , [s.d.]. Disponível em: <<https://icseg.iti.illinois.edu/wsc-9-bus-system/>>. Acesso em: 12 jan. 2021

IEEE STD 80. **IEEE Guide for Safety in AC Substation Grounding**. [s.l.] IEEE, [s.d.]. Disponível em: <<http://ieeexplore.ieee.org/document/7109078/>>. Acesso em: 21 nov. 2023.

IEEE-115. **IEEE Guide for Test Procedures for Synchronous Machines Including Acceptance and Performance Testing and Parameter Determination for Dynamic Analysis**. [s.l.] IEEE, [s.d.]. Disponível em: <<https://ieeexplore.ieee.org/document/9050934/>>. Acesso em: 9 nov. 2021.

IEEE-125. **IEEE Recommended Practice for Preparation of Equipment Specifications for Speed-Governing of Hydraulic Turbines Intended to Drive Electric Generators**. [s.l.] IEEE, [s.d.]. Disponível em: <<https://ieeexplore.ieee.org/document/4383553/>>. Acesso em: 19 out. 2021.

IEEE-421.5. IEEE Recommended Practice for Excitation System Models for Power System Stability Studies. [s.l.] IEEE, [s.d.]. Disponível em: <<http://ieeexplore.ieee.org/document/7553421/>>. Acesso em: 9 nov. 2021.

IEEE-1159. IEEE Recommended Practice for Monitoring Electric Power Quality. [s.l.] IEEE, [s.d.]. Disponível em: <<https://ieeexplore.ieee.org/document/5154067/>>. Acesso em: 8 dez. 2021.

INFINEON, T. Technical Information ModSTACK™ HD 6MS30017E43W33015. Infineon, , 4 abr. 2012. Disponível em: <https://www.infineon.com/dgdl/Infineon-6MS30017E43W33015-DS-v02_03-en_de.pdf?fileId=db3a304332fc1ee70133161f376c6f16>. Acesso em: 12 abr. 2020

INFINEON, T. Technical Information IGBT-Module FF1000R17IE4. Infineon, , 5 nov. 2013. Disponível em: <https://www.infineon.com/dgdl/Infineon-FF1000R17IE4-DS-v03_02-EN.pdf?fileId=db3a30431ff9881501201dc994a34980>. Acesso em: 10 nov. 2022

IRENA, I. R. E. A. Energy transition - Thechnology. <https://www.irena.org/Energy-Transition/TechnologyTechnology>, , [s.d.]. Disponível em: <<https://www.irena.org/Energy-Transition/>>. Acesso em: 10 ago. 2023

ISE, F. I. FOR S. E. S. Public net electricity generation in Germany 2011 and 2020. , [s.d.]. Disponível em: <<https://energy-charts.info/?l=en&c=DE>>. Acesso em: 1 jun. 2023

ISSAADI, I.; HEMSAS, K. E.; SOUALHI, A. Wind Turbine Gearbox Diagnosis Based on Stator Current. **Energies**, v. 16, n. 14, p. 5286, 10 jul. 2023.

JIA, J.; YANG, G.; NIELSEN, A. H. A Review on Grid-Connected Converter Control for Short-Circuit Power Provision Under Grid Unbalanced Faults. **IEEE Transactions on Power Delivery**, v. 33, n. 2, p. 649–661, abr. 2018.

JIA, K. et al. Analytical Calculation of Transient Current from an Inverter-Interfaced Renewable Energy. **IEEE Transactions on Power Systems**, p. 1–1, 2021.

JIABING HU et al. Coordinated strategy between positive- and negative-sequence currents of wind farms for transient stability enhancement of synchronous generators under asymmetrical grid faults. International Conference on Renewable Power Generation (RPG 2015). Anais... Em: INTERNATIONAL CONFERENCE ON RENEWABLE POWER GENERATION (RPG 2015). Beijing, China: Institution of Engineering and Technology, 2015. Disponível em: <<https://digital-library.theiet.org/content/conferences/10.1049/cp.2015.0421>>. Acesso em: 21 nov. 2021

JUNG, H. Y. et al. A New Circuit Design of Two-Switch Buck-Boost Converter. **IEEE Access**, v. 6, p. 47415–47423, 2018.

KARBOUJ, H.; RATHER, Z. H. A Novel Wind Farm Control Strategy to Mitigate Voltage Dip Induced Frequency Excursion. **IEEE Transactions on Sustainable Energy**, v. 10, n. 2, p. 637–645, abr. 2019.

KAUSHAL, A.; HERTEM, D. V. An overview of Ancillary Services and HVDC systems in European Context. **Energies**, v. 12, n. 18, p. 3481, 9 set. 2019.

KELLER, J.; KROPOSKI, B. **Understanding Fault Characteristics of Inverter-Based Distributed Energy Resources**. 1617 Cole Boulevard, Golden, Colorado 80401-3393: National Renewable Energy Laboratory, jan. 2010. Disponível em: <<http://www.osti.gov/bridge>>. Acesso em: 10 ago. 2023.

KIM, D. K. et al. Evaluation of energy storage technologies for efficient usage of wind power in the far-eastern region: A techno-economic analysis. **Journal of Energy Storage**, v. 39, p. 102595, jul. 2021.

KOUCHAKI, A.; NYMAND, M. Analytical Design of Passive LCL Filter for Three-Phase Two-Level Power Factor Correction Rectifiers. **IEEE Transactions on Power Electronics**, v. 33, n. 4, p. 3012–3022, abr. 2018.

KUNDUR, P.; BALU, N. J.; LAUBY, M. G. **Power system stability and control**. New York: McGraw-Hill, 1994.

LENZ, J. M.; PINHEIRO, J. R.; SARTORI, H. C. **DC-link electrolyte capacitor lifetime analysis for a PV boost converter**. 2017 IEEE 8th International Symposium on Power Electronics for Distributed Generation Systems (PEDG). **Anais...** Em: 2017 IEEE 8TH INTERNATIONAL SYMPOSIUM ON POWER ELECTRONICS FOR DISTRIBUTED GENERATION SYSTEMS (PEDG). Florianopolis, Brazil: IEEE, abr. 2017. Disponível em: <<http://ieeexplore.ieee.org/document/7972544/>>. Acesso em: 13 jun. 2019

LETAIEF, F. et al. A Comprehensive Approach to Flexible LVRT Strategies for Inverter-Based PPMs Enhancing Voltage-Support, Overcurrent Protection, and DC-Link Voltage Quality. **IEEE Access**, v. 12, p. 52990–53017, 2024.

LI, Z.; LIU, F. Frequency and voltage regulation control strategy of Wind Turbine based on supercapacitors under power grid fault. **Energy Reports**, v. 10, p. 2612–2622, nov. 2023.

LÓPEZ, M. A. G. et al. Control Strategy for Grid-Connected Three-Phase Inverters During Voltage Sags to Meet Grid Codes and to Maximize Power Delivery Capability. **IEEE Transactions on Power Electronics**, v. 33, n. 11, p. 9360–9374, nov. 2018.

MA, K.; LISERRE, M.; BLAABJERG, F. **Power controllability of three-phase converter with unbalanced AC source**. 2013 Twenty-Eighth Annual IEEE Applied Power Electronics Conference and Exposition (APEC). **Anais...** Em: 2013 IEEE APPLIED POWER ELECTRONICS CONFERENCE AND EXPOSITION - APEC 2013. Long Beach, CA, USA: IEEE, mar. 2013. Disponível em: <<http://ieeexplore.ieee.org/document/6520231/>>. Acesso em: 19 jun. 2024

MENDES, V. F. et al. Doubly-fed induction generator ride-through fault capability using resonant controllers for asymmetrical voltage sags. **IET Renewable Power Generation**, v. 9, n. 7, p. 783–791, 2015.

MENDES, V. F. et al. Low Voltage Ride-Through Capability Solutions for Permanent Magnet Synchronous Wind Generators. **Energies**, v. 9, n. 1, p. 59, jan. 2016.

MIRET, J. et al. Control Scheme With Voltage Support Capability for Distributed Generation Inverters Under Voltage Sags. **IEEE Transactions on Power Electronics**, v. 28, n. 11, p. 5252–5262, nov. 2013.

MIRET, J. et al. Reactive current injection protocol for low-power rating distributed generation sources under voltage sags. **IET Power Electronics**, v. 8, n. 6, p. 879–886, 2015.

MULJADI, E. et al. Different Factors Affecting Short Circuit Behavior of a Wind Power Plant. **IEEE Transactions on Industry Applications**, v. 49, n. 1, p. 284–292, jan. 2013.

NASIRI, M.; ARZANI, A. Robust control scheme for the braking chopper of PMSG-based wind turbines—A comparative assessment. **International Journal of Electrical Power & Energy Systems**, v. 134, p. 107322, jan. 2022.

NASIRI, M.; FARIDPAK, B.; FARROKHIFAR, M. **Low Voltage Ride Through Enhancement in PMSG-based Wind Turbines using De-loading Droop**. 2020 11th Power Electronics, Drive Systems, and Technologies Conference (PEDSTC). Anais... Em: 2020 11TH POWER ELECTRONICS, DRIVE SYSTEMS, AND TECHNOLOGIES CONFERENCE (PEDSTC). Tehran, Iran: IEEE, fev. 2020. Disponível em: <<https://ieeexplore.ieee.org/document/9088374/>>. Acesso em: 28 out. 2023

NASIRI, M.; MILIMONFARED, J.; FATHI, S. H. A review of low-voltage ride-through enhancement methods for permanent magnet synchronous generator based wind turbines. **Renewable and Sustainable Energy Reviews**, v. 47, p. 399–415, jul. 2015.

NASIRI, M.; MOHAMMADI, R. Peak Current Limitation for Grid Side Inverter by Limited Active Power in PMSG-Based Wind Turbines During Different Grid Faults. **IEEE Transactions on Sustainable Energy**, v. 8, n. 1, p. 3–12, jan. 2017.

NEJABATKHAH, F.; LI, Y. W.; WU, B. Control Strategies of Three-Phase Distributed Generation Inverters for Grid Unbalanced Voltage Compensation. **IEEE Transactions on Power Electronics**, v. 31, n. 7, p. 5228–5241, jul. 2016.

ONS, O. N. DO S. E. **Submódulo 2.10: Requisitos técnicos mínimos para a conexão às instalações de transmissão**. ONS, , 8 dez. 2020a. Disponível em: <https://apps08.ons.org.br/ONS.Sintegre.Proxy/ecmprsite/ecmfragmentsdocuments/Subm%C3%B3dulo%202.10-RQ_2020.12.pdf>. Acesso em: 10 jan. 2021

ONS, O. N. DO S. E. **Submódulo 2.11: Requisitos mínimos para os sistemas de proteção, de registro de perturbações e de teleproteção**. ONS, , 8 dez. 2020b. Disponível em: <https://apps08.ons.org.br/ONS.Sintegre.Proxy/ecmprsite/ecmfragmentsdocuments/Subm%C3%B3dulo%202.11-RQ_2020.12.pdf>. Acesso em: 10 jan. 2021

ONS, O. N. DO S. E. **Relatório de Análise de Perturbação (RAP): Análise da Perturbação do dia 15/08/2023 às 08h30min envolvendo o SIN**. [s.l.] ONS, 25 set. 2023. Disponível em: <<https://www.ons.org.br/AcervoDigitalDocumentosEPublicacoes/Minuta%20do%20RAP%202023.08.15.pdf>>. Acesso em: 23 nov. 2023.

OPPENHEIM, A. V.; SCHAFER, R. W. **Discrete-time signal processing**. 3rd ed ed. Upper Saddle River: Pearson, 2010.

PENA, R.; CARDENAS, R.; ASHER, G. **Overview of control systems for the operation of DFIGs in wind energy applications.** IECON 2013 - 39th Annual Conference of the IEEE Industrial Electronics Society. *Anais...* Em: IECON 2013 - 39TH ANNUAL CONFERENCE OF THE IEEE INDUSTRIAL ELECTRONICS SOCIETY. Vienna, Austria: IEEE, nov. 2013. Disponível em: <<http://ieeexplore.ieee.org/document/6699116/>>. Acesso em: 13 out. 2021

PHILLIPS, C. L.; HARBOR, R. D. **Feedback control systems.** 4. ed ed. Upper Saddle River, NJ: Prentice Hall, 2000.

PIMENTEL, C. **Falha em parques eólicos e solares no CE causou apagão de agosto.** Site de notícias governamentais. Disponível em: <<https://agenciabrasil.ebc.com.br/geral/noticia/2023-09/falha-em-parques-eolicos-e-solares-no-ce-causou-apagao-de-agosto>>.

PINTO, J. et al. Comparison of DSOGI-Based PLL for Phase Estimation in Three-Phase Weak Grids. **Electricity**, v. 2, n. 3, p. 244–270, 8 jul. 2021.

POLINDER, H. **Overview of and trends in wind turbine generator systems.** 2011 IEEE Power and Energy Society General Meeting. *Anais...* Em: 2011 IEEE POWER & ENERGY SOCIETY GENERAL MEETING. San Diego, CA: IEEE, jul. 2011. Disponível em: <<https://ieeexplore.ieee.org/document/6039342/>>. Acesso em: 11 nov. 2021

QUAN, H.; SRINIVASAN, D.; KHOSRAVI, A. Incorporating Wind Power Forecast Uncertainties Into Stochastic Unit Commitment Using Neural Network-Based Prediction Intervals. **IEEE Transactions on Neural Networks and Learning Systems**, v. 26, n. 9, p. 2123–2135, set. 2015.

QUINTERO, J. et al. The Impact of Increased Penetration of Converter Control-Based Generators on Power System Modes of Oscillation. **IEEE Transactions on Power Systems**, v. 29, n. 5, p. 2248–2256, set. 2014.

RAJENDRAN, S. et al. A Review of Generators and Power Converters for Multi-MW Wind Energy Conversion Systems. **Processes**, v. 10, n. 11, p. 2302, 5 nov. 2022.

REE, R. E. DE E. **Requisitos de respuesta frente a huecos de tensión de las instalaciones eólica.** REE, , out. 2006.

REE, R. E. DE E. **Generation data.** , mar. 2019. Disponível em: <<https://www.ree.es/en/datos/todate>>. Acesso em: 1 out. 2021

RODRIGUEZ, F. J. et al. **Discrete-time implementation of second order generalized integrators for grid converters.** 2008 34th Annual Conference of IEEE Industrial Electronics. *Anais...* Em: IECON 2008 - 34TH ANNUAL CONFERENCE OF IEEE INDUSTRIAL ELECTRONICS SOCIETY. Orlando, FL: IEEE, nov. 2008. Disponível em: <<http://ieeexplore.ieee.org/document/4757948/>>. Acesso em: 7 out. 2023

RODRIGUEZ, P. et al. **New Positive-sequence Voltage Detector for Grid Synchronization of Power Converters under Faulty Grid Conditions.** 37th IEEE Power Electronics Specialists Conference. *Anais...* Em: 37TH IEEE POWER ELECTRONICS SPECIALISTS

CONFERENCE. Jeju, Korea: IEEE, 2006. Disponível em: <<http://ieeexplore.ieee.org/document/1712059/>>. Acesso em: 23 dez. 2021

RODRÍGUEZ, P. et al. Reactive Power Control for Improving Wind Turbine System Behavior Under Grid Faults. **IEEE Transactions on Power Electronics**, v. 24, n. 7, p. 1798–1801, jul. 2009.

RODRIGUEZ, P. et al. **Current control method for distributed generation power generation plants under grid fault conditions**. IECON 2011 - 37th Annual Conference of the IEEE Industrial Electronics Society. **Anais...** Em: IECON 2011 - 37TH ANNUAL CONFERENCE OF IEEE INDUSTRIAL ELECTRONICS. Melbourne, Vic, Australia: IEEE, nov. 2011. Disponível em: <<http://ieeexplore.ieee.org/document/6119490/>>. Acesso em: 29 nov. 2018

RODRIGUEZ, P. . et al. Flexible Active Power Control of Distributed Power Generation Systems During Grid Faults. **IEEE Transactions on Industrial Electronics**, v. 54, n. 5, p. 2583–2592, out. 2007.

SAHOO, S.; TIMMANN, P. Energy Storage Technologies for Modern Power Systems: A Detailed Analysis of Functionalities, Potentials, and Impacts. **IEEE Access**, v. 11, p. 49689–49729, 2023.

SHAIR, J. et al. Power system stability issues, classifications and research prospects in the context of high-penetration of renewables and power electronics. **Renewable and Sustainable Energy Reviews**, v. 145, p. 111111, jul. 2021.

SILVA, R. M. et al. **Parameter determination of permanent magnet synchronous machine and sensorless algorithm implementation based on sliding mode observer**. 2018 Simposio Brasileiro de Sistemas Eletricos (SBSE). **Anais...** Em: 2018 SIMPOSIO BRASILEIRO DE SISTEMAS ELETRICOS (SBSE). maio 2018.

SILVA, R. M. et al. Power control strategies for grid connected converters applied to full-scale wind energy conversion systems during LVRT operation. **Electric Power Systems Research**, v. 184, p. 106279, jul. 2020.

SILVA, R. M.; SOUSA, C. V.; MENDES, V. F. **Active Power Saturation for Full-Scale Renewable Power Converters during Voltage Ride Through Operation**. 2021 14th IEEE International Conference on Industry Applications (INDUSCON). **Anais...** Em: 2021 14TH IEEE INTERNATIONAL CONFERENCE ON INDUSTRY APPLICATIONS (INDUSCON). São Paulo, Brazil: IEEE, 15 ago. 2021. Disponível em: <<https://ieeexplore.ieee.org/document/9529450/>>. Acesso em: 1 jan. 2022

SOSA, J. L. et al. Control Strategy to Maximize the Power Capability of PV Three-Phase Inverters During Voltage Sags. **IEEE Transactions on Power Electronics**, v. 31, n. 4, p. 3314–3323, abr. 2016.

SOUED, S.; RAMADAN, H. S.; BECHERIF, M. Effect of Doubly Fed Induction Generator on Transient Stability Analysis under Fault Conditions. **Energy Procedia**, v. 162, p. 315–324, abr. 2019.

SWANDARU, A.; ROTARU, M. D.; SYKULSKI, J. K. **The effectiveness of additional reactive current injection from a distributed energy resource unit to mitigate short voltage instability during extreme low voltage ride through.** 2017 International Conference on Modern Power Systems (MPS). *Anais...* Em: 2017 INTERNATIONAL CONFERENCE ON MODERN POWER SYSTEMS (MPS). jun. 2017.

SWANDARU, A.; ROTARU, M. D.; SYKULSKI, J. K. A simple method for estimating the effectiveness of reactive power-based low-voltage ride-through support of the distributed energy resources. **IET Renewable Power Generation**, v. 15, n. 6, p. 1149–1162, abr. 2021.

TDK. Aluminum Electrolytic Capacitors: General technical information. TDK, , ago. 2022. Disponível em: <<https://www.tdk-electronics.tdk.com/download/185386/e724fb43668a157bc547c65b0cff75f8/pdf-generaltechnicalinformation.pdf>>. Acesso em: 1 dez. 2022

TENNET TSO GMBH. Grid Code for High and Extra High voltage. Tennet, , nov. 2015.

TEODORESCU, R. et al. Proportional-resonant controllers and filters for grid-connected voltage-source converters. **IEE Proceedings - Electric Power Applications**, v. 153, n. 5, p. 750–762, set. 2006.

TOLMASQUIM, M. T. Energia renovável: hidráulica, biomassa, eólica, solar, oceânia. [s.l.] EPE - Empresa de Pesquisa Energética, 2016.

VARTANIAN, C. et al. Ensuring System Reliability: Distributed Energy Resources and Bulk Power System Considerations. **IEEE Power and Energy Magazine**, v. 16, n. 6, p. 52–63, nov. 2018.

VDE, V. D. E. VDE-AR-N 4120 Anwendungsregel:2018-11 - Technical requirements for the connection and operation of customer installations to the high voltage network (TAR high voltage). VDE, , nov. 2018. Disponível em: <<https://www.emissions-euets.com/internal-electricity-market-glossary/793-frequency-containment-reserve>>. Acesso em: 10 nov. 2020

WANG, H.; BLAABJERG, F. Reliability of Capacitors for DC-Link Applications in Power Electronic Converters—An Overview. **IEEE Transactions on Industry Applications**, v. 50, n. 5, p. 3569–3578, set. 2014.

WANG, Z. et al. Calculation of Rotor Currents for Doubly-Fed Induction Generation under Short Circuits in Power Grids. 2019 IEEE 3rd International Conference on Green Energy and Applications (ICGEA). *Anais...* Em: 2019 IEEE 3RD INTERNATIONAL CONFERENCE ON GREEN ENERGY AND APPLICATIONS (ICGEA). Taiyuan, China: IEEE, mar. 2019. Disponível em: <<https://ieeexplore.ieee.org/document/8880760/>>. Acesso em: 13 out. 2021

WEI, P. et al. Progress in Energy Storage Technologies and Methods for Renewable Energy Systems Application. **Applied Sciences**, v. 13, n. 9, p. 5626, 3 maio 2023.

WNA, W. N. A. Nuclear Power in Germany. Disponível em: <<https://world-nuclear.org/information-library/country-profiles/countries-g-n/germany.aspx>>. Acesso em: 2 out. 2021.

YANG, Y. et al. **Instantaneous thermal modeling of the DC-link capacitor in PhotoVoltaic systems.** 2015 IEEE Applied Power Electronics Conference and Exposition (APEC). Anais... Em: 2015 IEEE APPLIED POWER ELECTRONICS CONFERENCE AND EXPOSITION (APEC). mar. 2015.

YEPES, A. G. et al. Analysis and Design of Resonant Current Controllers for Voltage-Source Converters by Means of Nyquist Diagrams and Sensitivity Function. **IEEE Transactions on Industrial Electronics**, v. 58, n. 11, p. 5231–5250, nov. 2011.

ZHOU, A.; LI, Y. W.; MOHAMED, Y. Mechanical Stress Comparison of PMSG Wind Turbine LVRT Methods. **IEEE Transactions on Energy Conversion**, v. 36, n. 2, p. 682–692, jun. 2021.

Appendix A

NON-SINUSOIDAL POWER CONTROL STRATEGY

A.a Instantaneous active and reactive control (IARC)

The IARC strategy generates active (\mathbf{i}_p^*) and reactive (\mathbf{i}_q^*) reference currents directly proportional to the vectors \mathbf{v} and \mathbf{v}_\perp . This strategy is firmly rooted in the principles of instantaneous power theory and the calculus of these reference currents is described in equations (A.1) and (A.2) (RODRIGUEZ et al., 2007; RODRÍGUEZ et al., 2009).

$$\mathbf{i}_p^* = \frac{P^*}{|\mathbf{v}|^2} \mathbf{v}, \quad (\text{A.1})$$

$$\mathbf{i}_q^* = \frac{Q^*}{|\mathbf{v}|^2} \mathbf{v}_\perp, \quad (\text{A.2})$$

As $|\mathbf{v}|^2 = \mathbf{v} \cdot \mathbf{v} = \mathbf{v}_\perp \cdot \mathbf{v}_\perp$, it can be proven that the IARC strategy yields the most efficient set of currents to achieve the power set-points P^* and Q^* . This efficiency stems from the fact that there are no instantaneous power oscillations, even in the presence of unbalanced voltages, as demonstrated below:

$$p = \mathbf{v} \cdot (\mathbf{i}_p + \mathbf{i}_q) = \frac{P^*}{|\mathbf{v}|^2} \underbrace{\mathbf{v} \cdot \mathbf{v}}_{|\mathbf{v}|^2} + \frac{Q^*}{|\mathbf{v}|^2} \underbrace{\mathbf{v} \cdot \mathbf{v}_\perp}_0 = P^*, \quad (\text{A.3})$$

$$q = \mathbf{v}_\perp \cdot (\mathbf{i}_p + \mathbf{i}_q) = \frac{P^*}{|\mathbf{v}|^2} \underbrace{\mathbf{v}_\perp \cdot \mathbf{v}}_0 + \frac{Q^*}{|\mathbf{v}|^2} \underbrace{\mathbf{v}_\perp \cdot \mathbf{v}_\perp}_{|\mathbf{v}|^2} = Q^*. \quad (\text{A.4})$$

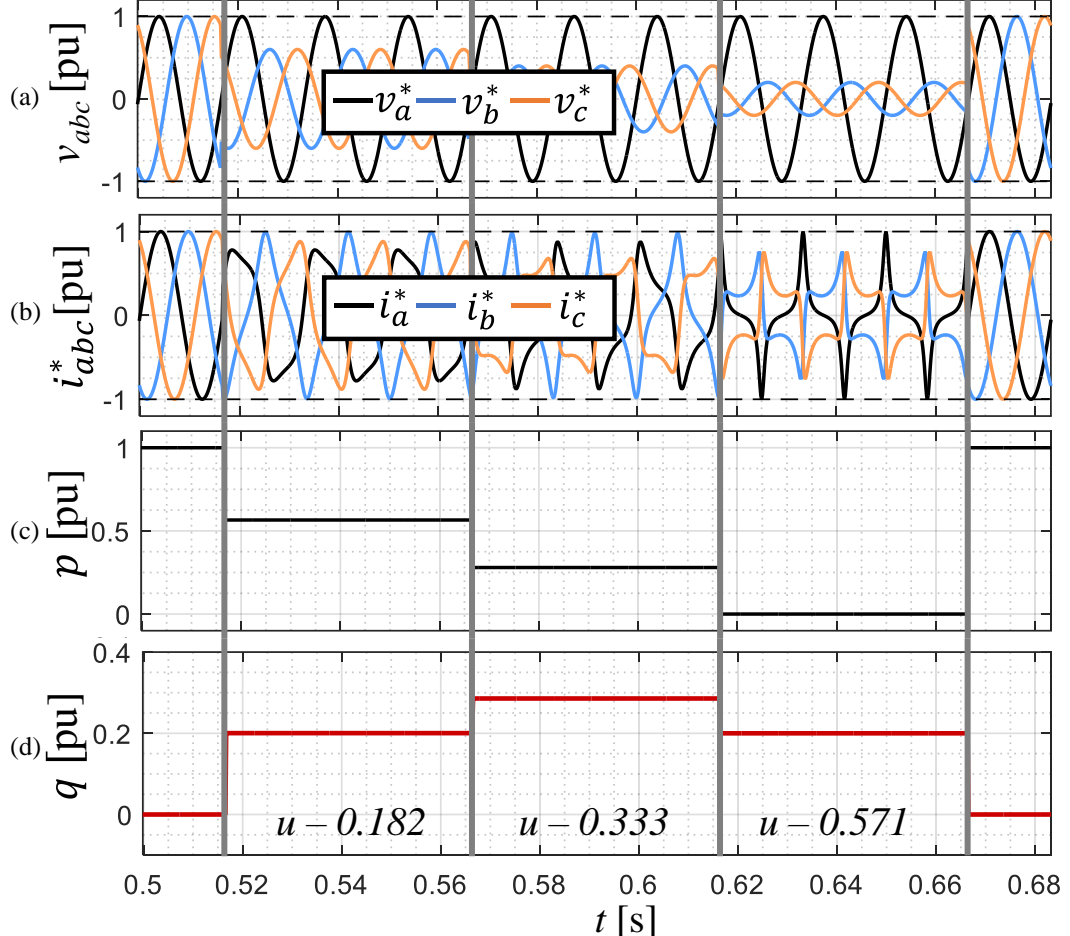
According to equation (2.6), the norm of vector $|\mathbf{v}|^2$ is not constant, leading to non-sinusoidal reference currents with a high total harmonic distortion (THD) value. In accordance with (CASTILLA et al., 2010), THD can be approximated using the expression (A.5), assuming only active power injection:

$$THD = \frac{u}{\sqrt{1-u^2}}. \quad (\text{A.5})$$

Applying the voltage profile displayed in Fig. A.1(a), the corresponding currents produced by the IARC strategy are illustrated in Fig. A.1(b). It is evident that as the voltage unbalance between phases increases, the current waveform becomes more distorted. Nevertheless, as

depicted in Fig. A.1(c) and Fig. A.1(d), there are no power oscillations for any of the tested conditions.

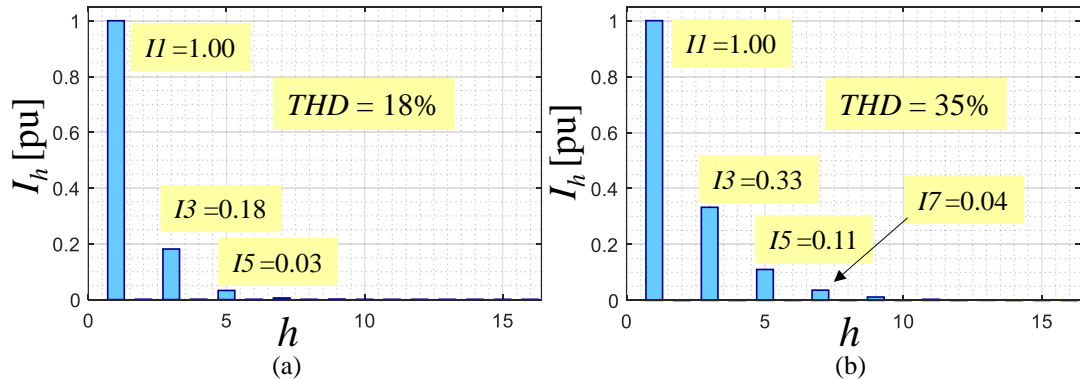
Fig. A.1: (a) voltages and (b) reference currents in natural frame, (c) active and (d) reactive instantaneous power for IARC strategy.

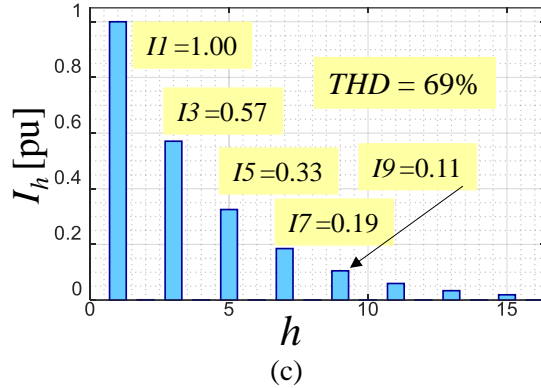


Elaborated by the author.

The frequency spectrums of the reference currents are depicted in Fig. A.2, and the voltage unbalance gives rise to odd harmonics, particularly the third and fifth order components.

Fig. A.2: Harmonic distortion for (a) $u = 0.182$, (b) $u = 0.333$ and (c) $u = 0.571$ using IARC strategy.

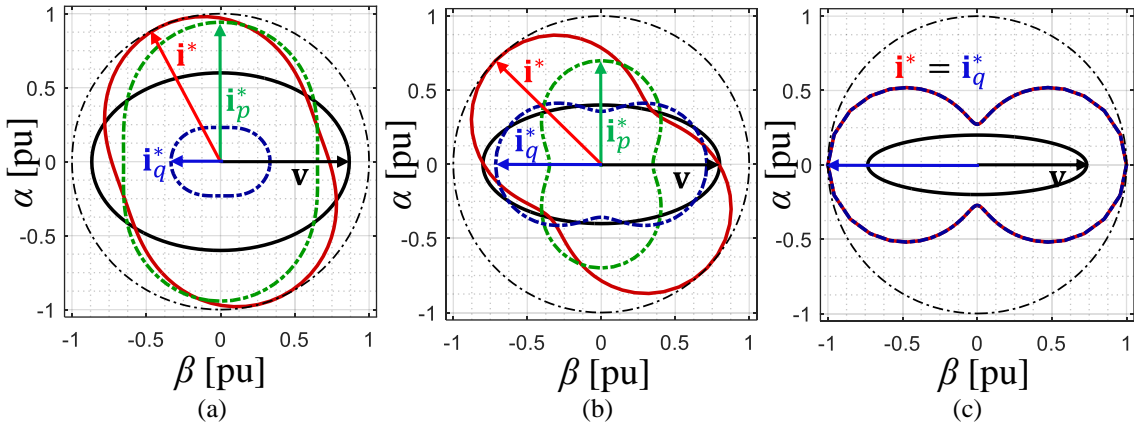




Elaborated by the author.

The current vector paths for different unbalance factors are depicted in Fig. A.3, they do not form circular or elliptical shapes; instead, they become more sinuous as the unbalance factor increases.

Fig. A.3: Current and voltage vector path during the voltage sag for (a) $u = 0.182$, (b) $u = 0.333$ and (c) $u = 0.571$ for IARC strategy.



Elaborated by the author.

A.b Instantaneously controlled positive sequence (ICSP)

The ICSP strategy is designed to inject the power set-points P^* and Q^* exclusively through the positive sequence, meaning there are no negative sequence components in the reference currents. This strategy was introduced with the consideration that only one of the power set-points is non-zero during the voltage sag, as described in (A.6) and (A.7) (RODRIGUEZ et al., 2007; RODRÍGUEZ et al., 2009):

$$\left. \begin{aligned} P^* &= \mathbf{v} \cdot \mathbf{i}_p^+ = \mathbf{v}^+ \cdot \mathbf{i}_p^+ + \mathbf{v}^- \cdot \mathbf{i}_p^+ \\ 0 &= \mathbf{v} \cdot \mathbf{i}_p^- = \mathbf{v}^+ \cdot \mathbf{i}_p^- + \mathbf{v}^- \cdot \mathbf{i}_p^- \end{aligned} \right\} \Rightarrow \mathbf{i}_q = 0, \quad (\text{A.6})$$

$$\left. \begin{aligned} Q^* &= \mathbf{v}_\perp \cdot \mathbf{i}_q^+ = \mathbf{v}_\perp^+ \cdot \mathbf{i}_q^+ + \mathbf{v}_\perp^- \cdot \mathbf{i}_q^+ \\ 0 &= \mathbf{v}_\perp \cdot \mathbf{i}_q^- = \mathbf{v}_\perp^+ \cdot \mathbf{i}_q^- + \mathbf{v}_\perp^- \cdot \mathbf{i}_q^- \end{aligned} \right\} \Rightarrow \mathbf{i}_p = 0. \quad (\text{A.7})$$

The reference currents calculated with ICSP are defined in (A.8) and (A.9):

$$\mathbf{i}_p^{+*} = \frac{P^*}{|\mathbf{v}^+|^2 + \mathbf{v}^+ \cdot \mathbf{v}^-} \mathbf{v}^+, \quad (\text{A.8})$$

$$\mathbf{i}_q^{+*} = \frac{Q^*}{|\mathbf{v}^+|^2 + \mathbf{v}^+ \cdot \mathbf{v}^-} \mathbf{v}_\perp^+, \quad (\text{A.9})$$

Replacing (A.6) and (A.7) in (2.11) and (2.12), it is obtained the instantaneous power equations as follows:

$$p = (\mathbf{v}^+ + \mathbf{v}^-) \cdot (\mathbf{i}_p^+ + \mathbf{i}_q^+) = \underbrace{\mathbf{v}^+ \cdot \mathbf{i}_p^+}_{P^*} + \underbrace{\mathbf{v}^- \cdot \mathbf{i}_p^+}_{0} + \underbrace{\mathbf{v}^+ \cdot \mathbf{i}_q^+}_{0} + \underbrace{\mathbf{v}^- \cdot \mathbf{i}_q^+}_{\tilde{p}}, \quad (\text{A.10})$$

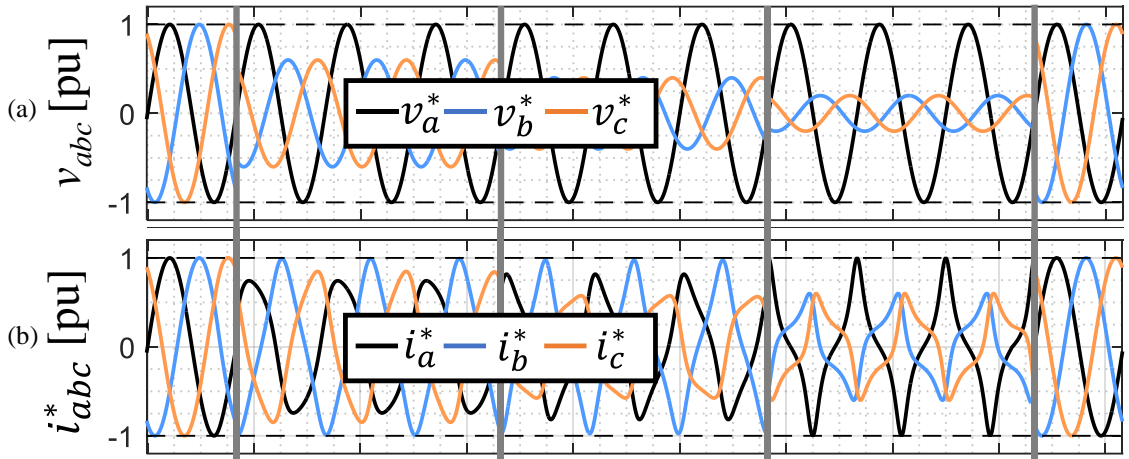
$$q = (\mathbf{v}_\perp^+ + \mathbf{v}_\perp^-) \cdot (\mathbf{i}_p^+ + \mathbf{i}_q^+) = \underbrace{\mathbf{v}_\perp^+ \cdot \mathbf{i}_q^+}_{Q^*} + \underbrace{\mathbf{v}_\perp^- \cdot \mathbf{i}_q^+}_{0} + \underbrace{\mathbf{v}_\perp^+ \cdot \mathbf{i}_p^+}_{0} + \underbrace{\mathbf{v}_\perp^- \cdot \mathbf{i}_p^+}_{\tilde{q}}. \quad (\text{A.11})$$

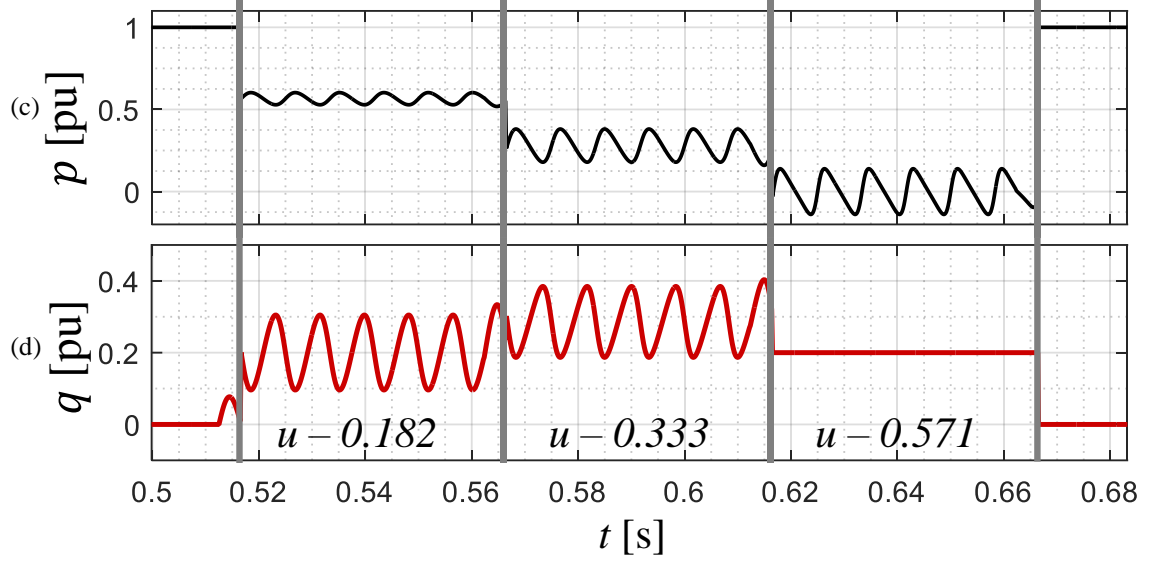
Then, the oscillations can be eliminated only if the orthogonal current component is zero. The internal products in the denominators of equations (A.8) and (A.9) lead to non-sinusoidal reference currents, where the THD, considering only active power injection, can be approximated using the equation (A.12) (CASTILLA et al., 2010):

$$THD = \sqrt{\frac{u^2}{2\sqrt{1-u^2}(1-\sqrt{1-n^2})}} - 1. \quad (\text{A.12})$$

The currents of ICSP for the voltage profile displayed in Fig. A.4(a) are illustrated in Fig. A.4(b). The currents present a less irregular shape in relation to IARC. The active and reactive power oscillations are not null in Fig. A.4(c) and Fig. A.4(d), and they are directly proportional to the orthogonal current component. In other words, active currents generate reactive power ripple, while reactive currents generate active power oscillations.

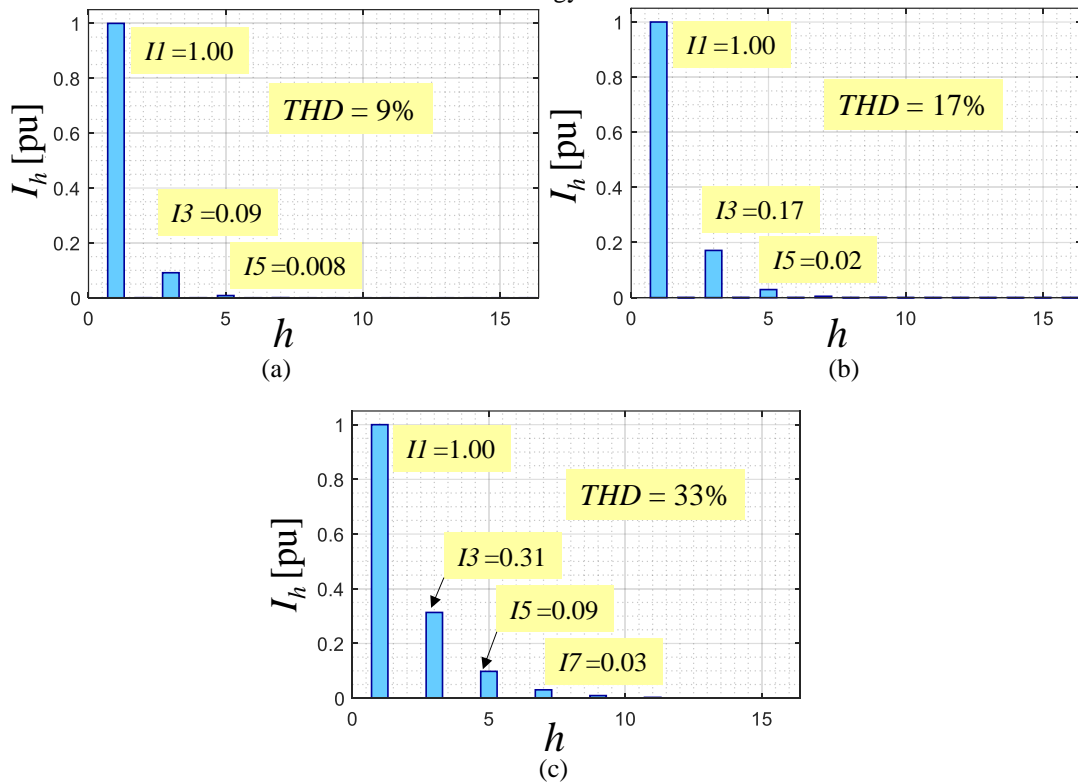
Fig. A.4: (a) voltages and (b) reference currents in natural frame, (c) active and (d) reactive instantaneous for ICPS strategy.





The current spectrums in Fig. A.5 it is possible to note that despite the high harmonic content the ICSP, it presents lower THD value in relation to the IARC. However, it cannot cancel the simultaneously active and reactive power oscillations.

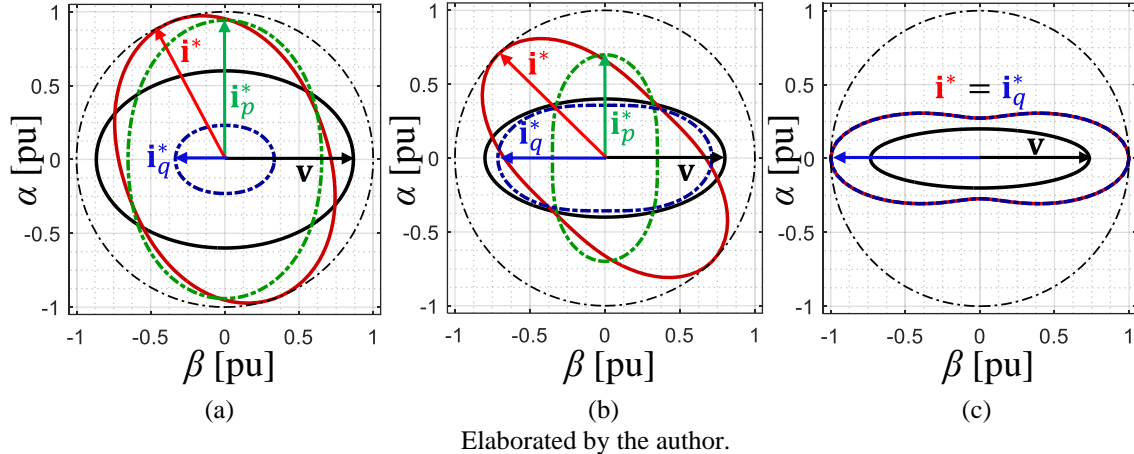
Fig. A.5: Harmonic distortion for (a) $u = 0.182$, (b) $u = 0.333$ and (c) $u = 0.571$ instantaneous for ICPS strategy.



Elaborated by the author.

Finally, the ICPS currents vector paths are shown Fig. A.6. Even though this strategy delivers currents exclusively through the positive sequence, these currents do not follow a circular trajectory in the complex plane.

Fig. A.6: Current and voltage vector path during the voltage sag for (a) $u = 0.182$, (b) $u = 0.333$ and (c) $u = 0.571$ for ICPS strategy.

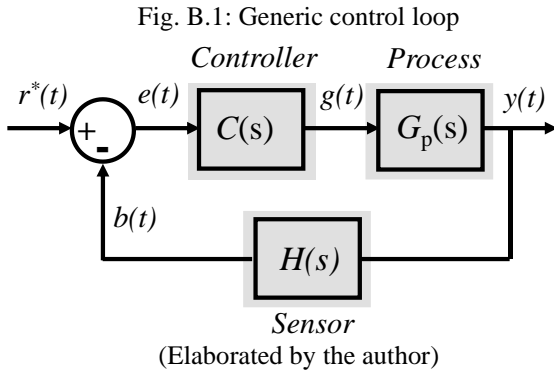


Appendix B

MODELING AND CONTROL

B.a Control Loop transfer function.

Consider the generic control loop illustrated in Fig. B..



- $C(s)$ is the system control or compensator, and its design will be discussed in this appendix.
- $G_p(s)$ is the process or plant transfer function.
- $H(s)$ is the process sensor that converts the physical variables into a range or variable that can be processed by the controller.
- $r^*(t)$ is the control system reference or the desired process output.
- $g(t)$ is the manipulated variable by the controller to achieve the desired response.
- $b(t)$ is controller feedback.
- $e(t)$ is the error, which represents the difference between the control variable and the control system reference.

Based in Fig. B.1, the closed loop transfer function of a classical control system is defined in (B.1).

$$T(s) = \frac{Y(s)}{R^*(s)} = \frac{G_p(s)C(s)}{1 + H(s)G_p(s)C(s)}. \quad (\text{B.1})$$

The stability of a linear system is defined based on the location of the poles (roots of the denominator equation) in the s-plane (PHILLIPS; HARBOR, 2000). Therefore, the stability margin of the control system (B.1) is defined by:

$$H(s)C(s)G_c(s) = -1, \quad (\text{B.2})$$

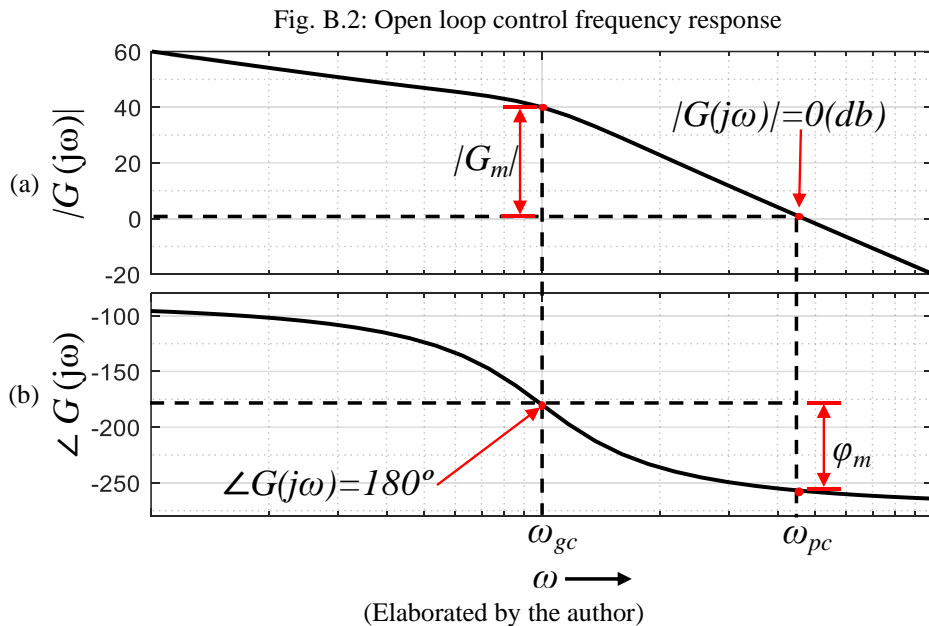
where $H(s)C(s)G_c(s)$ is the open loop transfer function. Rewriting the equation (B.2) in terms of magnitude and phase, the equations (B.3) and (B.4) define stability margin, which represents the boundaries where a linear control system becomes marginally stable.

$$|H(s)C(s)G_c(s)| = 1, \quad (\text{B.3})$$

$$\angle H(s)C(s)G_c(s) = \pm 180^\circ. \quad (\text{B.4})$$

Transfer functions in control theory are approximate mathematical models of physical phenomenon. Hence, due to inaccuracies in the mathematical model, it is desired that the control system not only be stable but also present stability margin (PHILLIPS; HARBOR, 2000).

The controller design described in this section is based on frequency response, therefore, stability criteria are estimated using the bode diagram, and the stability margin is related to the proximity of the point $|G(j\omega_{gc})| = 0[\text{db}]$ on the magnitude curve and $\angle G(j\omega_{pc}) = \pm 180^\circ$ on the phase curve, demonstrated in Fig. B.2(a) and Fig. B.2(b), respectively. Here, ω_{gc} is the frequency at which the transfer function magnitude becomes equal to 1 or 0[db], and ω_{pc} is the frequency at which the transfer function phase angle becomes equal to $\pm 180^\circ$.



The purpose is to determine the parameters of the controller $C(s)$ to introduce a specific phase margin ϕ_m at a given frequency ω_{gc} in the open loop transfer function. This can be expressed as:

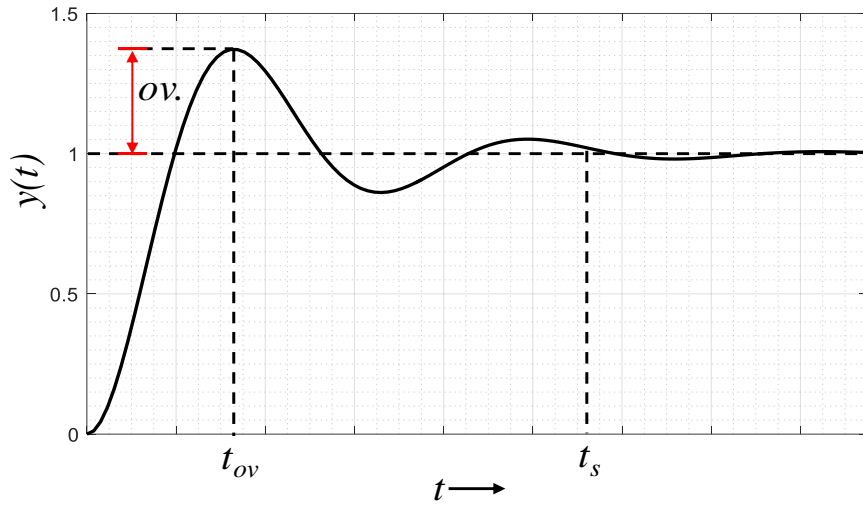
$$\theta = -180^\circ + \phi_m + \angle H(j\omega_{gc})G_c(j\omega_{gc}) = \pm 180^\circ, \quad (\text{B.5})$$

where θ is the phase shift introduced by the controller in the control loop. Now, let's consider the standard second-order transfer function in (B.6), where ζ is the damping coefficient, ω_n is the not-damped natural frequency.

$$G(s) = \frac{\omega_n}{s^2 + 2\zeta\omega_n s + \omega_n^2}, \quad (\text{B.6})$$

The temporal response of a second order system to a step input is described in Fig. B.3, where ov is the response overshoot and t_s is the settling time.

Fig. B.3: Second order system temporal characteristic response



(Elaborated by the author)

Therefore, according to the reference Phillips e Harbor (2000) is possible to establish a relationship between the relative stable margins and the temporal response characteristics, using the equations (B.7) to (B.10).

$$\phi_m = \tan^{-1} \left(\frac{2\zeta}{\sqrt{\sqrt{4\zeta^4 + 1} - 2\zeta^2}} \right) \approx 100\zeta, \quad (\text{B.7})$$

$$\omega_{gc} = \omega_n \sqrt{\sqrt{4\zeta^4 + 1} - 2\zeta^2} \approx \omega_n, \quad (\text{B.8})$$

$$ov. = \exp \left(-\frac{\pi\zeta}{\sqrt{1-\zeta^2}} \right), \quad (\text{B.9})$$

$$t_s = \frac{4}{\zeta\omega_n} = \frac{8}{\omega_{cg} \tan(\phi_m)}. \quad (\text{B.10})$$

B.b Proportional-Integral controller tuning

Due to its simple implementation and well-behaved response, the PI (proportional-integral) controller is one of the most used in industrial process control systems, including power electronic converters. The PI transfer function is defined in equation (B.11), where K_p is the proportional and K_I is the integral gain.

$$C(s) = K_p + \frac{K_I}{s} \quad (\text{B.11})$$

Hence, from the previously established concepts, it is possible to develop a Matlab script that allows to calculate the PI controller gains according to the desired response criteria, as follows:

```
% Proportional integral controller project
%%
% =====
% User entries
% =====
% process trasfer function
Dp = xx;
Np = xx;
% sensor transfer function
Dh = xx;
Nh = xx;
% desired overshoor
ov = xx ;
% desired gain croosing frequency
wgc = xx;
% ===== %
% minimum damping factor calculation
zeta = sqrt((log.ov)^2/(pi^2+(log.ov)^2));

% minimum phase margin calculation
phi_m = atand((2*zeta)/sqrt(sqrt(4*zeta^2+1)-2*zeta^2));

Gp = tf(Dp,Np) ; % process control transfer fnction
H = tf(Dh,Nh) ; % sensor transfer function
GMA = series(Gp,H); % open loop trnasfer fuction
% without compesation
% noncompesated system phase and magnitude in the
% desired crossing frequency
[Mag,ph] = bode(GMA,wgc);

% Compensator design
Mag_PI = 1/Mag ; % compesator agnitude
pha_PI = -ph - 180 + phi_m; % compesator phase

tau_PI = 1/(wgc) * tan((pha_PI+90)*pi/180);
Kpi = Mag_PI * wgc/(sqrt(1+(wgc*tau_PI)^2));
Kp = Kpi * tau_PI; % proportional gain
Ki = Kpi ; % Integral gain

Gc = tf([Kp Ki],[1 0]) ; % Controller transfer function
```

```

GMAC = series(GMA,Gc);

opts = bodeoptions('cstprefs');
opts.FreqUnits = 'Hz';

figure()
bode(GMAC,GMA,opts)

T = Gp*Gc/(1+Gp*Gc*H);
figure()
step(T);
%%

```

PI controllers design routine
(Elaborated by the author)

The control loops in power electronics converters are typically arranged in cascade. To ensure the decoupling between their responses, the outer loop cutoff frequency at least ten times slower than the inner loop. Moreover, it is worth emphasizing that the values calculated through the equations developed in the routine do not guarantee controller pole dominance, and it is necessary to adjust the gain values to achieve a better response.

B.c Resonant controller tuning

The PI controllers have a limited bandwidth, which is a significant drawback in stationary frame control where the variables have non-zero frequencies in steady state. To achieve a better dynamic response in steady state within the stationary frame, proportional resonant (PR) controllers will be utilized to track arbitrary sinusoidal references in positive and negative sequences simultaneously, with zero steady-state error. The damped PR transfer function is described in equation (B.12) (TEODORESCU et al., 2006; YEPES et al., 2011), where K_{lh} is the resonant gain, ω_b is the bandwidth and ω_h is the resonant frequency.

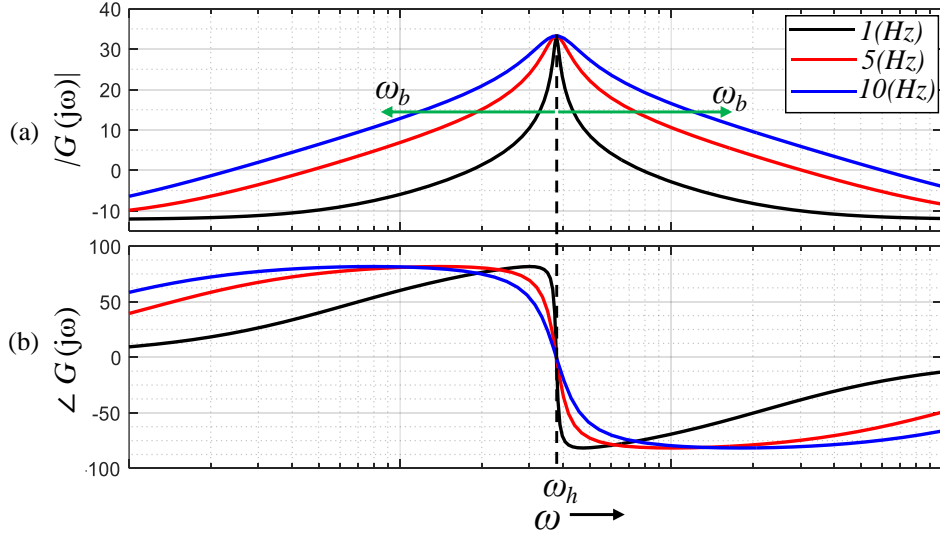
$$C(s) = K_{lh} \frac{\omega_b s}{s^2 + 2\omega_b s + \omega_h^2} + K_p, \quad (\text{B.12})$$

In the resonance frequency the PR controller presents similar characteristics to a PI in relation to relative stability, consequently the controller tuning can follow a similar procedure to the earlier section.

In addition to the gains K_p and K_{lh} , the bandwidth ω_b must be appropriately determined, and Fig. B.4 shows the proportional resonant controller bode diagram for different bandwidth ω_b values. In the magnitude curve (Fig. B.4(a)) the increase of ω_b results in the compensation of larger range of frequency near to the resonance. In the phase curve (Fig. B.4(b)), near to the resonance point, small frequency deviations result in significant phase margin variations, which is improved with the increase of the ω_b . However, when it is used

more than one PR controller, the bandwidth increase may cause the controller's response overlap, generating stability problems. Thus the ω_b determination must take in account the phase margin deterioration for more than one controller, and frequency deviation that the controller can compensate.

Fig. B.4: Resonant controller frequency response



(Elaborated by the author)

B.d Controller discretization

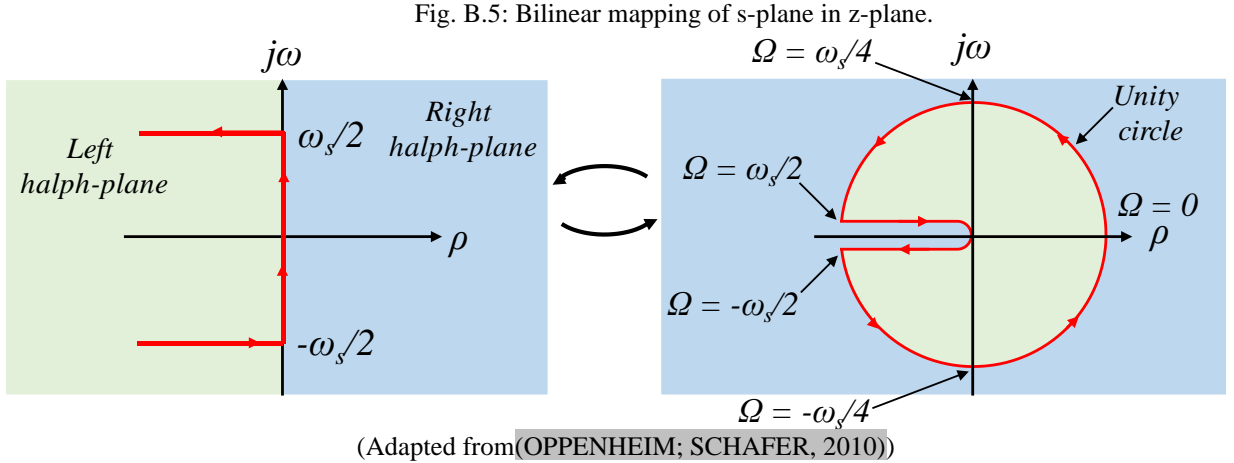
A linear time-invariant system can be discretized using mapping techniques to transition from the continuous-time domain (s-plane) to the discrete-time domain (z-plane). There are various mapping techniques available, and one of them is the bilinear transformation defined in equations (B.13), where T_s represents the sample time. The bilinear transformation is derived from the trapezoidal rule approximation, providing a close match between the system's frequency response in the continuous and discrete-time domains (OPPENHEIM; SCHAFER, 2010)

$$s = \frac{2}{T_s} \frac{1 - z^{-1}}{1 + z^{-1}} \Leftrightarrow z = \frac{1 + (T_s/2)s}{1 - (T_s/2)s} \quad (\text{B.13})$$

The graphical relationship between the s-plane and the z-plane, achieved through the bilinear transformation, is illustrated in Fig. B.5. Here, $\omega_s = 2\pi/T_s$ represents the sample frequency, and Ω is the equivalent discrete unity-circle frequency. In this mapping:

- The imaginary axis in the s-plane is mapped to the unit-circle boundary in the z-plane.
- The left half-plane in the s-plane corresponds to the inside of the unit circle in the z-plane.

- The right half-plane in the s-plane corresponds to the outside of the unit circle in the z-plane.



The imaginary axis that comprises the interval $-\infty \leq \omega \leq \infty$ in the continuous-time domain, it is compressed to the interval $-\pi \leq \Omega \leq \pi$ in the discrete time domain. Thus, the relation between the continuous-time (ω) and the discrete-time (Ω) is not linear (OPPENHEIM; SCHAFER, 2010), as defined by equation (B.14).

$$\omega = 2 \operatorname{atan} \left(\frac{\Omega T_s}{2} \right) \Leftrightarrow \Omega = \frac{2}{T_s} \tan \left(\frac{\omega}{2} \right). \quad (\text{B.14})$$

Therefore, to ensure the matching between the continuous and discrete-time system response in a specific frequency ω_d , it is necessary to use the frequency prewarping in the bilinear transformation, as follows.

$$s' = \frac{\omega_d}{\tan(\omega_d T_s / 2)} \frac{1 - z^{-1}}{1 + z^{-1}} \quad (\text{B.15})$$

B.d.i Proportional-integral controller discretization

The discretization of the proportional controller (equation (B.11)) results in (B.16), where $Y_p(z)$ and $E(z)$ are the proportional controller input and output, respectively.

$$C_p(z) = \frac{Y_p(z)}{E(z)} = K_p, \quad (\text{B.16})$$

Thus, since $k \in \mathbb{Z}$, the proportional controller difference equation is given by:

$$y_p(k) = K_p e(k), \quad (\text{B.17})$$

The discretization of integral part of PI controller (B.11), is obtained through the bilinear transformation in (B.18), with $Y_i(z)$ is the integral output.

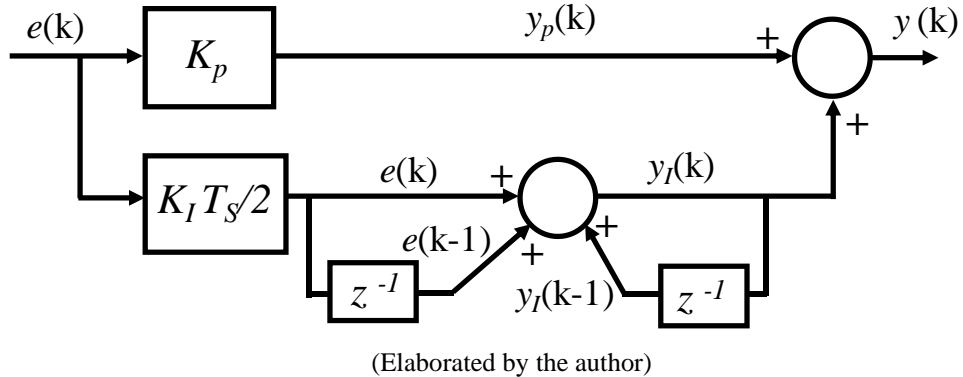
$$C_I(z) = \frac{Y_I(z)}{E(z)} = \frac{K_I T_s}{2} \frac{1 + z^{-1}}{1 - z^{-1}}, \quad (\text{B.18})$$

Then, the integral controller difference equation is given by:

$$y_I(k) = \frac{K_I T_s}{2} (e(k) + e(k-1)) + y_I(k-1), \quad (\text{B.19})$$

The PI controller block diagram is presented in Fig. B.6.

Fig. B.6: Discrete time PI controller block diagram



B.d.ii Anti-wind-up implementation

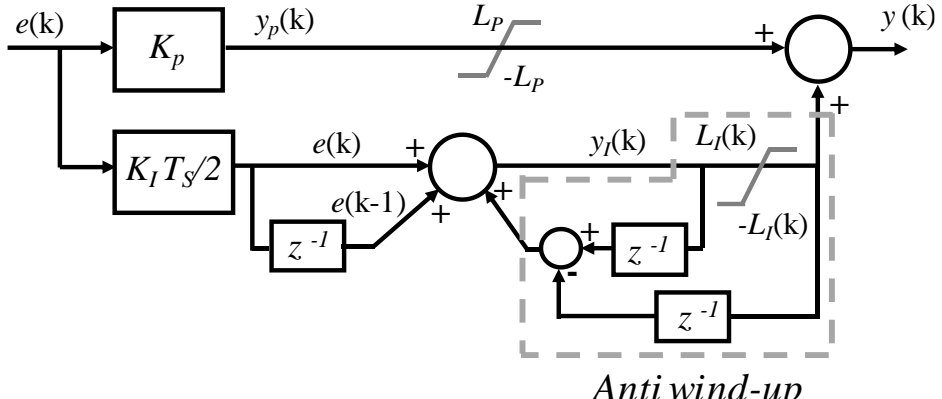
In a significant transition in the control system reference, the PI controller continues to accumulate error integration throughout the entire transient. Consequently, when a new set-point is established, the integral controller may significantly deviate from the current reference, leading to a transient overshoot.

The anti-wind-up is based on the dynamic saturation of the integral controller during the transitory operation. The proportional controller output is monitored and when its value becomes greater than the saturation limit L_p , the integral output is set to zero. The integration is resumed only when the proportional control falls below the saturation limit (BUSO; MATTAVELLI, 2015).

The PI controller with anti-wind-up implemented in the present work was based in the algorithm presented in the reference BUSO E MATTAVELLI (2015), where the discrete time block diagram is shown in Fig. B.7. The proportional (L_p) and integral (L_I) saturation limits relation is defined by the following equation.

$$L_I = L_p - (K_p e[k]). \quad (\text{B.20})$$

Fig. B.7: Discrete time PI controller block diagram with anti-wind-up diagram



(Adapted from (BUSO; MATTAVELLI, 2015))

B.d.iii Resonant controller discretization

Using $\sigma = \omega_d / \tan(\omega_d T_s / 2)$ in the pre-warping discretization, equation (B.15), and replace it into the resonant part of the PR controller transfer function, equation (B.12), the discrete-time transfer function is given by:

$$C_R(z) = \frac{Y_R(z)}{E(z)} = \frac{a_2 z^{-2} + a_1 z^{-1} + a_0}{b_2 z^{-2} + b_1 z^{-1} + b_0}, \quad (\text{B.21})$$

where:

$$a_0 = -a_2 = \frac{2\sigma\omega_b K_{Ih}}{\sigma^2 + 2\sigma\omega_b + (9\omega_h)^2}, \quad (\text{B.22})$$

$$a_1 = 0.$$

$$b_1 = -b_2 = \frac{-2\sigma^2 + 2(\omega_h)^2}{\sigma^2 + 2\sigma\omega_b + (\omega_h)^2},$$

$$b_0 = 1.$$

Then, the difference equation is defined as follows:

$$y_R(k) = a_2 e(k-2) + a_0 e(k) - (b_2 y(k-2) + b_1 y(k-1)) \quad (\text{B.23})$$

B.e GSC modelling

The grid-connected converter (GSC) serves as the primary interface between the wind energy conversion (WEC) system and the electrical power system. Its control structure comprises multiple cascaded loops, as depicted in Fig. 3.2 of Chapter 3. This section will delve into the detailed modeling of these control loops, outlining their functions and interactions within the overall system.

B.e.i GSC current control loop

The current control dynamic is dictated by the output filter of the GSC, and because of the relatively high impedance of the filter's shunt branch at fundamental frequency, its influence can be disregarded. Then, the voltage at the converter terminals are described in equations (B.24) and (B.25).

$$v_{(c)\alpha} = R_t i_\alpha + L_t \frac{di_\alpha}{dt} + v_{(g)\alpha}, \quad (\text{B.24})$$

$$v_{(c)\beta} = R_t i_\beta + L_t \frac{di_\beta}{dt} + v_{(g)\beta}, \quad (\text{B.25})$$

here, $v_{(c)}$ denotes the voltage at the converter terminals, while $v_{(g)}$ represents the mains voltage. Additionally, $L_t = L_1 + L_2$ and $R_t = R_1 + R_2$ symbolize the filter's equivalent inductance and resistance, respectively.

When linearizing the system around an operating point with the mains voltage $v_{(g)}$ held constant, the magnitude and phase deviations of the voltage $v_{(c)}$ prompt the circulation of current through L_t and R_t . Then, the transfer function governing this dynamic behavior is defined by equation (B.26).

$$\frac{I(s)}{V_c(s)} = \frac{1}{L_t s + R_t}. \quad (\text{B.26})$$

In the implementation of the current control loop, in Fig. 3.2, proportional-integral-resonant (PIR) controllers (TEODORESCU et al., 2006), the equations which is described in (B.12), were used, and a disturbance compensation action with voltage $v_{(g)}$ is introduced to the output of current controllers. Finally, the reference voltages $v_{(g)}^*$ are applied to modulation technique.

B.e.ii DC voltage control loop

The DC bus voltage control hinges on maintaining a balance between the input (P_{gen}) and output (P_c) power of the GSC, and any disparities between these quantities changes the energy stored in the capacitor, directly affecting the DC voltage level, i.e.:

$$\frac{C}{2} \frac{dv_{dc}^2}{dt} = P_{gen} - P_c. \quad (\text{B.27})$$

As depicted in Fig. 3.1, passive elements are interposed between the point where voltage is measured (v_g) and the converter terminals (v_c). Consequently, the relation between the active power at converter terminals (P_c) and that one which flows to the mains, disregarding the

losses in the GSC, is delineated in equation (B.28), where P_g and Q_g are active and reactive power feed into the mains (AMIRNASER YAZDANI; REZA IRAVANI, 2010).

$$\frac{C}{2} \frac{dV_{dc}^2}{dt} = P_{gen} - \left[P_g + \left(\frac{2LP_g}{3V_g^2} \right) \frac{dP_g}{dt} \right] - \left[Q_g + \left(\frac{2LQ_g}{3V_g^2} \right) \frac{dQ_g}{dt} \right]. \quad (\text{B.28})$$

Because the presence of $P_g dP_g/dt$ and $Q_g dQ_g/dt$, the equation (B.28) is non-linear. Then, linearizing them, the transfer function is described by set of equations (B.29), with $\overline{V_{dc}^2}$ the average value of square DC voltage magnitude and $\overline{P_{gen}}$ average primary source active power, both linearized at operational point.

$$\begin{aligned} \frac{V_{dc}^2(s)}{\overline{P_g}(s)} &= - \left(\frac{2}{C} \right) \frac{\tau_p s + 1}{s}, \\ \tau_p &= \frac{2L_t \overline{P_{gen}}}{3\overline{V_{dc}^2}}, \end{aligned} \quad (\text{B.29})$$

The time constant within equation (B.29) characterizes the power flow across the filter elements, and it can be safely neglected in cases where it becomes extremely small.

In the control loop for the DC bus voltage, in Fig. 3.2, to mitigate high frequency variations, moving average filters (MAV) are employed on the measured variables and they should be taken into account in the definition of control response time. The control loop uses a proportional-integral (PI) controller, and at the output of this controller, a feed-forward action considering the power originated from the primary source (P_{gen}) also using MAV is applied.

B.e.iii Reactive power control loop

The mean value of reactive power can be calculated by the product of grid voltage magnitude (V_g) by the reactive current magnitude (I_q), as follows:

$$Q = V_g I_q, \quad (\text{B.30})$$

In the calculation of voltage magnitude, it is essential to consider the delay introduced by the PLL loop calculation. Moreover, the inclusion of a filter is of utmost importance to effectively suppress high frequency components in the magnitude calculations. To represent these elements when linearizing the system around an operating point with a grid average voltage (\bar{V}_g), a first-order system with a time constant τ_q is employed, and the system transfer function is approached by (B.31).

$$\frac{Q(s)}{I_q(s)} = \frac{1}{\tau_q s + 1} V_g . \quad (\text{B.31})$$

In the reactive power control loop in Fig. 3.2, given its management of continuous variables, a PI controller is deployed, the output of this controller is the reactive current magnitude described as ($I^+_{q(\text{RCL})}$). It is important to emphasize that, when a voltage dip is detected through the PLL output voltage, this control loop is temporarily deactivated, since the priority is the direct control of the reactive current.

B.f Appointments

This chapter aims to delineate the design methodology of the controllers utilized in this study and GSC control loop modeling, detailing the equations requisite for achieving the desired control criteria based on predefined performance conditions, along with the discretization of the controllers for implementation in a digital signal processing system. It is imperative to note the following:

- In applications focused on power electronics, it is customary to employ control loops that operate in cascade. Consequently, to ensure decoupling between these loops, a standard is established wherein the external loop must possess a cutoff frequency at least 10 times slower than the subsequent internal loop.
- The control design methodology described does not guarantee the dominance of the controller's poles. In practical terms, this implies that the performance criteria may not necessarily be met solely through the calculated gains. Consequently, it may be necessary to adjust the controllers to achieve a better response during simulation or practical implementation.

Appendix C

WEC LOSSES AND BREAKING CHOPPER

C.a Semiconductor losses

Losses in semiconductor devices are comprised of conduction losses (E_{cond}) and switching losses (E_{sw}) (DE ANDRADE et al., 2016). Conduction losses occur when current passes through the semiconductor device in its on-state. These losses can be calculated using equation (C.1), where v_{on} represents the voltage drop, $i_{on(av)}$ is the average current, $i_{on(rms)}$ is the RMS current, and r_{on} is the on-state resistance of the semiconductor device.

$$E_{cond} = v_{on} \cdot i_{on,av} + r_{on} \cdot i_{on,rms}^2. \quad (\text{C.1})$$

For IGBTs, switching losses arise during the intervals when the device transitions from the on-state to the off-state and vice versa (FEIX et al., 2009). During these transitions, both voltage and current are present across the device, as represented in Fig. C.1, where v_{CE} is the voltage across the collector-emitter terminals, i_C the collector current, t_{on} and t_{off} are the device turn-on and turn-off times. The power dissipation can be approximated as the sum of the energy lost during the turn-on (E_{on}) and turn-off (E_{off}) processes, multiplied by the switching frequency (f_{sw}), as defined in (C.2).

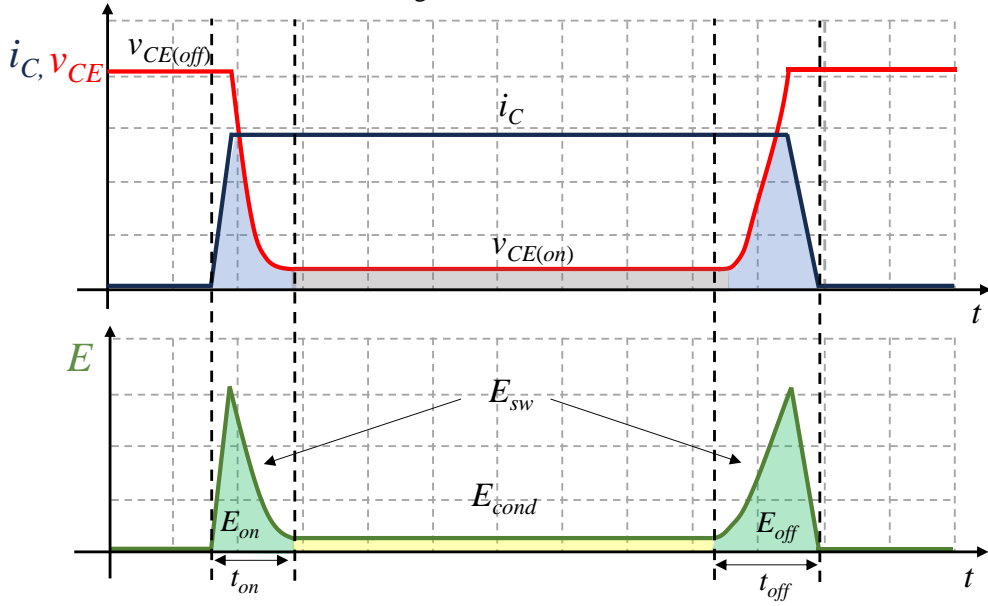
$$E_{sw(IGBT)} = (E_{on} + E_{off}) \cdot f_{sw}. \quad (\text{C.2})$$

For diodes, Fig. C.2 illustrates the losses during the transition from the on to the off state. When a reverse voltage (V_R) is applied to the cathode and anode terminals, the diode current starts to decay from the forward current (I_F) until reaches zero, during this interval, the voltage across the diode remains almost its forward (V_F) value. After the current reaches zero, it continues to flow in the opposite direction, the voltage across the diode also reverses direction and increases until reaches its maximum reverse value (V_{RM}). After this, it decreases and oscillates around V_R .

The interval which the diode conducts in reverse is the reverse recovery time (t_{rr}). The recovery charge (Q_{rr}) is defined as the integral of the current flowing through the diode during the t_{rr} interval (JUNG et al., 2018). The diode switching losses can then be defined by (C.2):

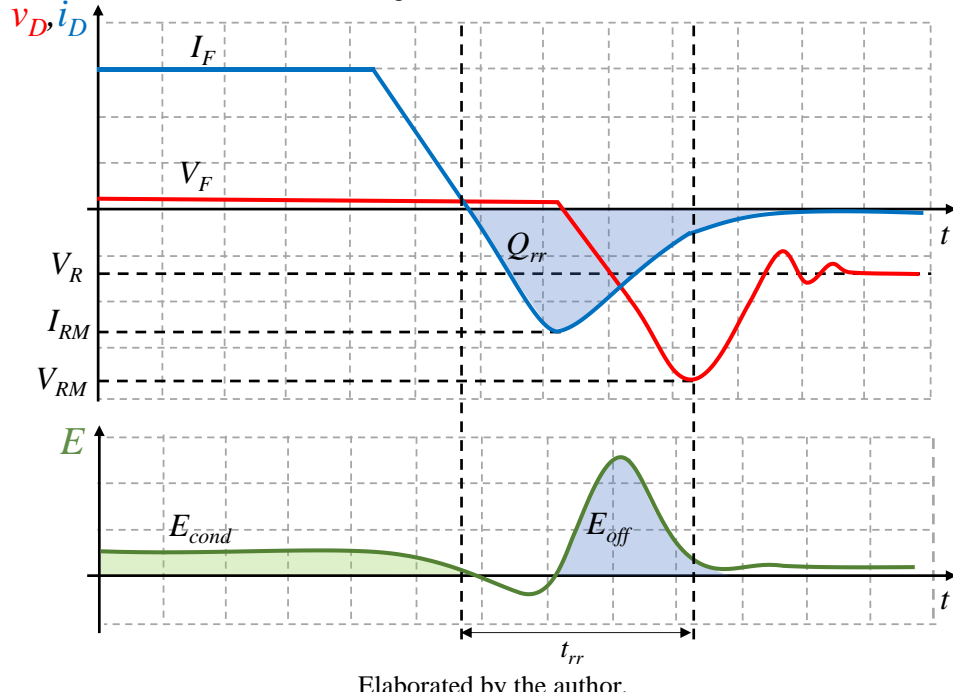
$$E_{sw(diode)} = V_R \cdot Q_{rr} \cdot f_{sw}. \quad (\text{C.3})$$

Fig. C.1: IGBT losses



Elaborated by the author.

Fig. C.2: Diode losses.



Elaborated by the author.

C.b DC bus capacitors losses

DC bus capacitors in grid converters serve as energy storage elements and they are crucial for maintaining a balance between the energy input from the primary source and the AC output power, absorbing the instantaneous differences between these two energy sources (WANG; BLAABJERG, 2014; YANG et al., 2015). Additionally, the capacitors help mitigate

the high-frequency ripple produced by the pulse-width modulation (PWM) converters (YANG et al., 2015).

During transient events in the electrical mains, the mechanical inertia of the wind turbine can lead to great energy variations in the converter's DC bus, which result in overvoltage that pose stress on the capacitors' dielectric properties (NASIRI; ARZANI, 2022). Additionally, many converters operate in environmental conditions characterized by high humidity and temperature.

Lifetime and reliability of a DC capacitor depends to a large extent on the capacitor's temperature (TDK, 2022). Then, it is very important to evaluate the losses in the capacitors to their operating temperature remains within the values defined by the manufacturer.

C.b.i Power losses in DC capacitors

The power dissipated in a electrolytic capacitor (P_{loss}) primarily consists of resistive (P_R) and dielectric (P_D) losses (EPCOS, 2009). The P_R is defined by the product of the equivalent series resistance (ESR_f) by the RMS current ripple I_f^{\sim} for a frequency f , as described in (C.4):

$$P_R = \sum_{f=1}^n ESR_f (I_f^{\sim})^2, \quad (\text{C.4})$$

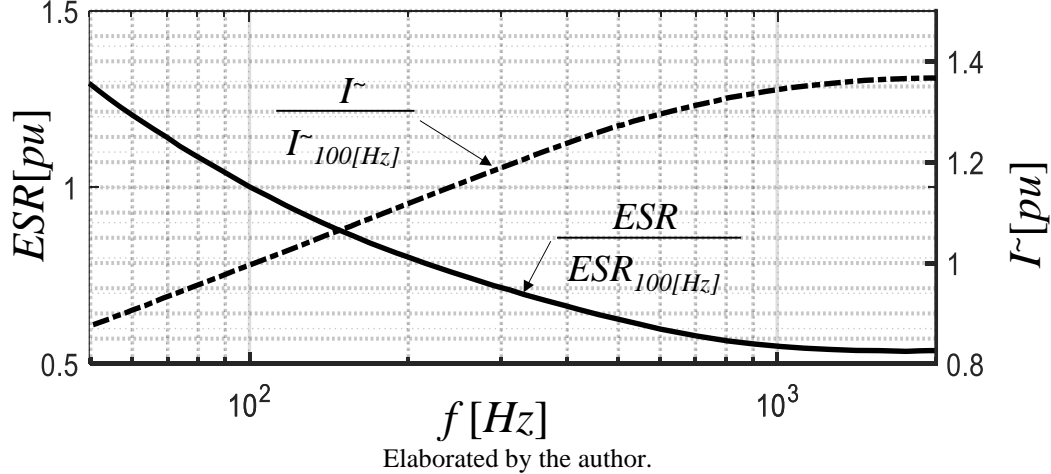
The ESR_f represents the parasitic resistance of the capacitor electrodes and contacts, and its values according to the frequency of the current ripple, as illustrated in Fig. C.3, where the ESR tends to decrease as the frequency increases. Consequently, low-frequency current ripple generates higher losses, and to maintain capacitor losses within its nominal value, I_f^{\sim} tends to decrease.

Dielectric losses (P_D) are primarily influenced by the peak of a symmetrical alternating voltage i.e. the dielectric losses increase with both the frequency and magnitude of the voltage ripple, as defined in (C.5).

$$P_D = \hat{v}_{ac} \pi f_0 C \tan (\delta_0), \quad (\text{C.5})$$

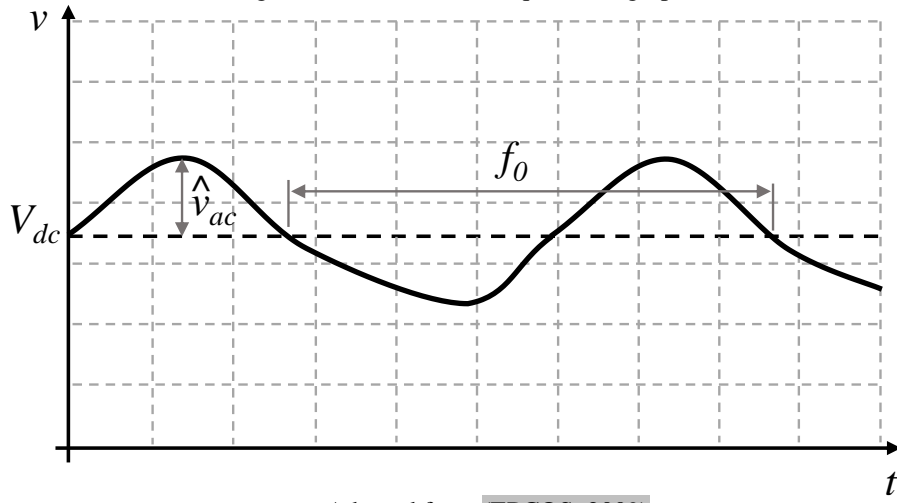
where \hat{v}_{ac} is the peak value of the symmetrical AC voltage and f_0 is the a.c. voltage ripple frequency, where these parameters are measured as illustrated in Fig. C.4, and finally the $\tan (\delta_0)$ represents the dissipation factor of the dielectric.

Fig. C.3: ESR vs. frequency and permissible current ripple characteristic of a dielectric capacitor.



Elaborated by the author.

Fig. C.4: Dielectric losses quantities graphical definition.



Adapted from (EPCOS, 2009).

C.c Braking chopper

The braking chopper protection circuit is composed of a resistor connected to the converter's DC bus via a static switch. Its primary function is to assist in maintaining energy balance on the converter's DC bus by dissipating surplus energy generated by the wind turbine that cannot be feed-in to the grid.

The braking helps prevent an increase in bus voltage, making it a crucial component in avoiding disconnection of the wind turbine during voltage ride-through operation, and their design must accommodate the full power of the generator for a sufficient duration, allowing time for the blade angle control system to act and reduce mechanical power without adversely affecting the turbine's physical structure (MENDES et al., 2016). This response time could be more than a few seconds and consequently, the resistor used in this circuit needs to have a large volume and is relatively costly (NASIRI; ARZANI, 2022).

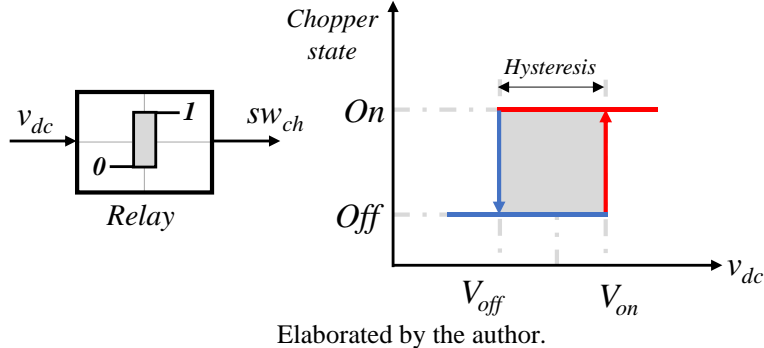
Alternative protection methods, such as pitch angle control (NASIRI; FARIDPAK; FARROKHIFAR, 2020) or control function exchange between the GSC and MSC (NASIRI; MOHAMMADI, 2017), have been proposed in the literature. However, these alternatives do not eliminate the need for a braking chopper and may not perform optimally in all types of voltage sags. As a result, the braking chopper remains the simplest and most effective protection method (NASIRI; ARZANI, 2022).

This work will explore two modes of operation for controlling this protection circuit: hysteresis-based control using voltage levels and pulse-width modulation (PWM) based on power balance.

C.c.i Hysteresis control

Chopper control using hysteresis, depicted in Fig. C.5, operates by monitoring the DC bus voltage. When the voltage exceeds a threshold limit V_{on} , the switch is turned on. It remains in this state until the voltage falls below threshold voltage V_{off} . Within the voltage range between V_{on} and V_{off} , the switch maintains its previous state (dead band).

Fig. C.5: Hysteresis control diagram.

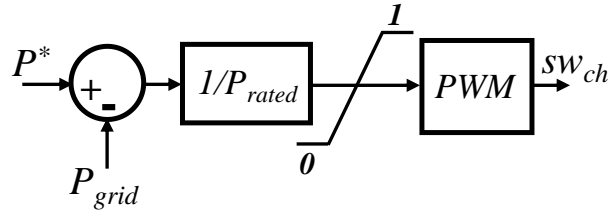


Elaborated by the author.

C.c.ii PWM control

The PWM control discussed in this section was specifically designed for integration with the active power curtailment algorithm detailed in Chapter 3 to enhance the power balancing process. This control strategy involves comparing the active power reference (P^*) received from the output of DC bus control loop (Fig. 3.2) with the maximum active power that can be feed-in to the grid (P_{grid}), calculated by the curtailment algorithm. The difference between them is normalized by the converter rated power (P_{rated}) and utilized as a modulation index for the PWM of the chopper drive, where the modulation index is limited between 0 and 1. The chopper PWM control is depicted in Fig. C.6.

Fig. C.6: PWM control diagram.



Elaborated by the author.

C.d Simulations results

To make a comparison of the chopper control schemes, computer simulations were conducted using PLECS software (version 4.5.6). Detailed information about the simulation setup can be found in Tab. D. and Tab. D.2, and the chopper-related data is presented in Tab. C.1. For the simulations, the BPSC strategy was employed in conjunction with the active power limitation algorithm outlined in Chapter 3, as it aligns with the current RCI requirements.

The system was submitted to the voltage profile depicted in Fig. 3.18, which yielded a positive sequence voltage of 0.6[pu] and an unbalance factor of 0.3333[pu], then the WEC could inject active and reactive currents.

Tab. C.1: Chopper components parameters

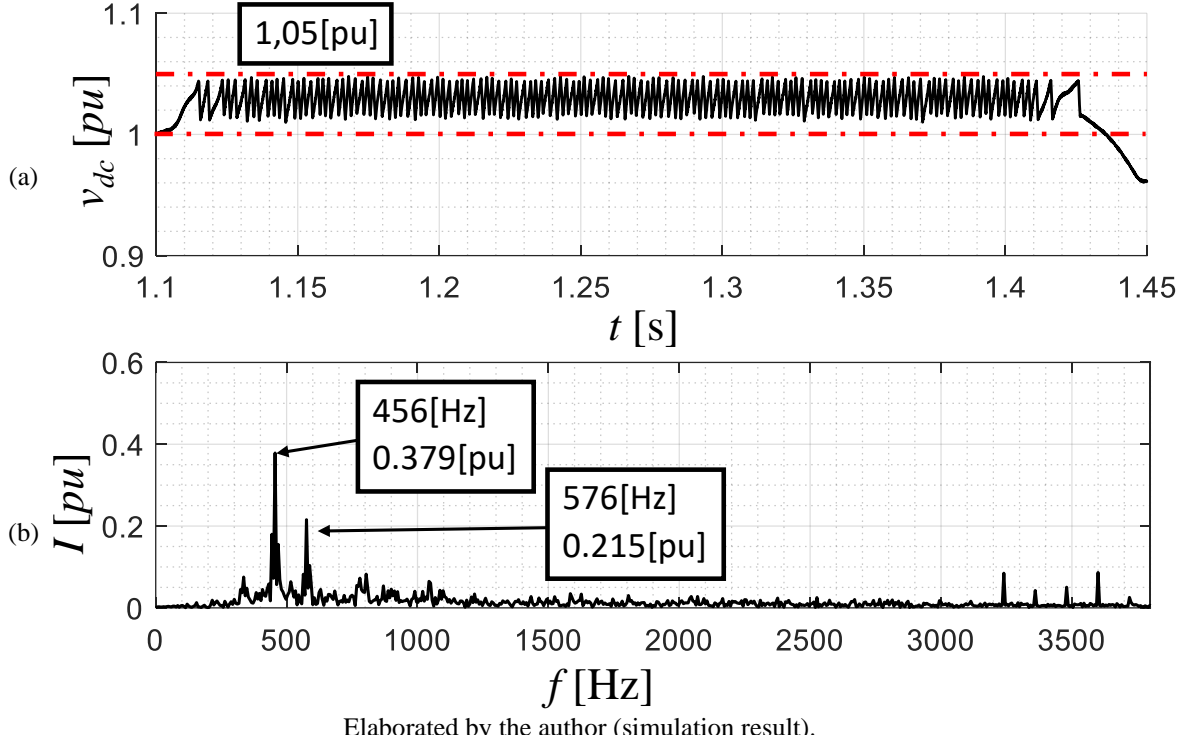
Parameter	Symb.	Value	Unity
Chopper resistance	R _{ch}	0.55	Ω
Braking resistor capacity	E _{ch}	40	MJ
IGBT blocking voltage	V _{max}	1.7	kV
IGBT rated current	I _{sw}	2	kAmps

C.d.i Hysteresis control

When using hysteresis control, the DC voltage profile exhibited a pattern as shown in Fig. C.7(a), with the steady-state voltage reaching maximum values of 1.05[pu]. The chopper switching process introduces distortions in the bus voltage waveform, where the transition between the switch states depends on several factors such as the time constant derived from the chopper resistance and the bus capacitor values, the generated active power and feed-in to the grid.

The frequency spectrum of the current in the DC bus, depicted in Fig. C.7(b), revealed the presence of low-frequency components (up to 1000[Hz]). Notably, it highlighted frequencies of 456[Hz] with a magnitude of 0.379[pu] and 576[Hz] with a current magnitude of 0.215[pu].

Fig. C.7: DC bus (a) voltage and (b) capacitors' current spectrum for chopper hysteresis control (values normalized by the converter rated values)



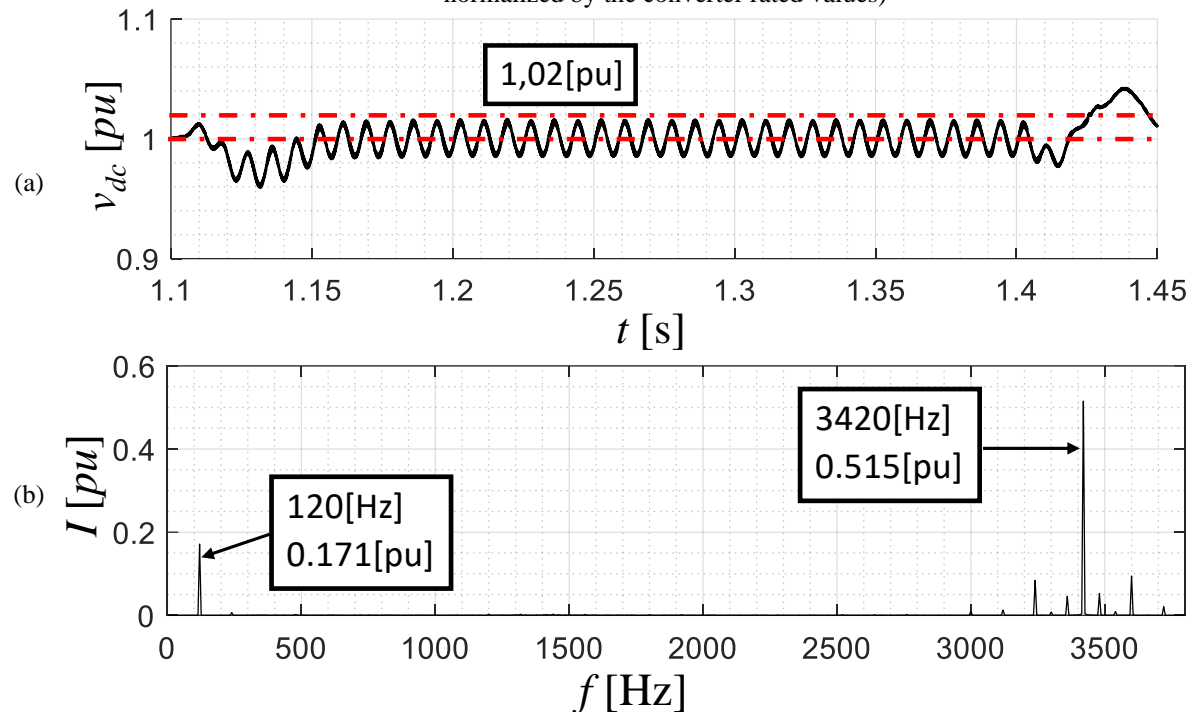
Elaborated by the author (simulation result).

C.d.ii PWM control

The PWM control operates with a switching frequency of 3420[Hz], the same of the converter, and the average value of the steady-state voltage remains at 1[pu]. The 120[Hz] oscillations observed in the voltage profile in Fig. C.8(a), are attributed to the use of the BPSC strategy.

The current frequency spectrum of the bus capacitors is presented in Fig. C.8(b), and it displays two significant components. The first is at 120[Hz] with a magnitude of 0.172[pu], which corresponds to grid active power oscillations. The second component is at the chopper switching frequency of 3420[Hz], with a magnitude of 0.515[pu]. The latter component is attributed to chopper switching, and unlike hysteresis control, this frequency is fixed (does not depend on external factors), and the current magnitude is influenced by the grid and generator power balance.

Fig. C.8: DC bus (a) voltage and (b) capacitors' current spectrum for chopper PWM control (values normalized by the converter rated values)



Elaborated by the author (simulation result).

Appendix D

WEC AND POWER SYSTEM DATA

D.a Wind energy conversion system data.

The data for the wind energy conversion (WEC) system used in the simulation for this study are described in Tab. D.. It represents a real full power converter wind turbine equipped with a permanent magnet synchronous generator, a back-to-back power converter with a power stack Infineon 6MS30017E43W33015 (INFINEON, 2012) with IGBT modules FF1000R17IE4 (INFINEON, 2013).

Tab. D.1: 2.1[MW] WEC system parameters

Parameter	Symb.	Value	Unity
Line nominal voltage	V_n	0.69	kVrms
Grid frequency	f_{grid}	60	Hz
Generator Rated Power	P_{gen}	2	MW
Generator Rated Current	I_{gen}	1.67	kArms
Converter Rated Power	P_n	2.1	MW
Converter Rated Current	I_{rated}	1.76	kArms
D.C. bus capacitor	C_{dc}	35.7	mF
D.C. bus nominal voltage	V_{dc}	1.15	kV
Chopper resistance	R_{ch}	0.55	Ω
GSC filter inductor	L_f	80	μ H
Transformer inductance	L_t	25.26	μ H
Filter capacitor	C_f	147	μ F
Damping resistor	R_d	0.1	Ω
Damping inductor	L_d	20	μ H
Switching frequency	f_{sw}	3.42	kHz
IGBT blocking voltage	V_{max}	1.7	kV
IGBT rated current	I_{sw}	2	kArms

The controller gains and saturation limits are detailed in Tab. D.2, while their modeling and structures can be found in Chapter 3.

D.b Wind farm (WF).

The simulation model used in this work includes a wind farm (WF) composed of 35 wind turbines which structure is graphically detailed on Fig. 1.6. The WF is connected to the

electrical power system via a 10.7 km transmission line, and the transmission line's specifications are outlined in Tab. D.3. The connection between the transmission line and the WF's point of common coupling (PCC), two power transformers are employed, and their specifications are provided in Tab. D.4.

Tab. D.2: 2.1[MW] WEC system controllers' parameters

Parameter	Symb.	Value	Unit
Sample freq.	fs	6.84	kHz
Current controller prop.	IKp	0,2179	mho
Current controller int.	IKi	129,913	
Current controller ress. a0	$Ia0$	0,01534	
Current controller ress. a1	$Ia1$	0,0	
Current controller ress. a2	$Ia2$	-0,01534	
Current controller ress. b0	$Ib0$	1	
Current controller ress. b1	$Ib1$	-1,98604	
Current controller ress. b2	$Ib2$	0,99817	
Current controller wind-up	IKc	1	
Current controller sat.	$IOutMax$	690	
Voltage controller prop.	$V2Kp$	3,5236	
Voltage controller int.	$V2Ki$	287,0118	
Voltage controller sat.	$V2OutMax$	2,31	MW
Voltage controller wind-up	$V2Kc$	1	
React. Power controller prop.	QKp	0,00000001	
React. Power controller int.	QKi	0,0002	
React. Power controller wind-up	QKc	1	
React. Power controller sat.	$QOutMax$	2584,4	

Tab. D.3: Transmission line (TL) parameters

Parameter	Value	Unity
Length	10.7	km
Resistance	0.0908	Ω/km
Reactance	0.4954	Ω/km
Susceptance	0.3009	$M\Omega/km$

Tab. D.4: Power transformer parameters

Parameter	Value	Unity
Nominal Power	87	MVA
Winding type	Ynd	-
High line voltage	230	kV
Low line voltage	34.5	kV
Percentual impedance	10	%

The WF's medium-voltage distribution system comprises 8 feeders of 34.5 kV, and each feeder associated with a specific number of generators and corresponding electrical parameters. These details can be found in Tab. D.5. Additionally, each generator is linked to a medium-to-low-voltage transformer, facilitating the connection to the respective feeder, and these transformer specifications are provided in Tab. D.6.

Tab. D.5: Wind farm medium voltage feeder

Feed.	Number of Gen.	Length [km]	Resist. [pu]	Reac. [pu]	Sucep. [MVAr]
1	7	3.669	0.028465	0.036068	0.0046
3	7	6.694	0.028465	0.036068	0.0046
5	7	4.451	0.028465	0.036068	0.0046
7	7	6.7	0.012241	0.033170	0.0050
8	7	7.9	0.012241	0.033170	0.0050

Tab. D.6: Wind generators interface transformer parameters

Parameter	Value	Unity
Nominal Power	2.5	MVA
Winding type	Yy	-
High line voltage	34.5	kV
Low line voltage	0.69	kV
Percentual impedance	10	%

D.c WSSC 9-bus System

The Western System Coordinating Council (WSCC) 9-bus test case serves as an approximation of an equivalent system featuring nine buses and three generators, as described in (ICSEG, [s.d.]). The system diagram can be visualized in Fig. D..

The power system comprises three synchronous generators, with characteristics outlined in Tab. D.7, Tab. D.8 and Tab. D.9. The generator connected to bus 1 (GEN1) is a salient pole machine. It operates as the slack bus, providing the system's angular reference and closing the energy balance. The generator at bus 2 (GEN2) is a round rotor machine, tt functions as the PV bus, regulating the bus voltage and producing active power. Lastly, the generator at bus 3 (GEN3) is also a round rotor synchronous machine and operates in PV mode. The excitation systems for these generators are of type DC1A, with their control loop parameters standardized in (IEEE-421.5, [s.d.]) and it parameters are described in Tab. D.10. For transient analysis, the speed governors were replaced by active power static values.

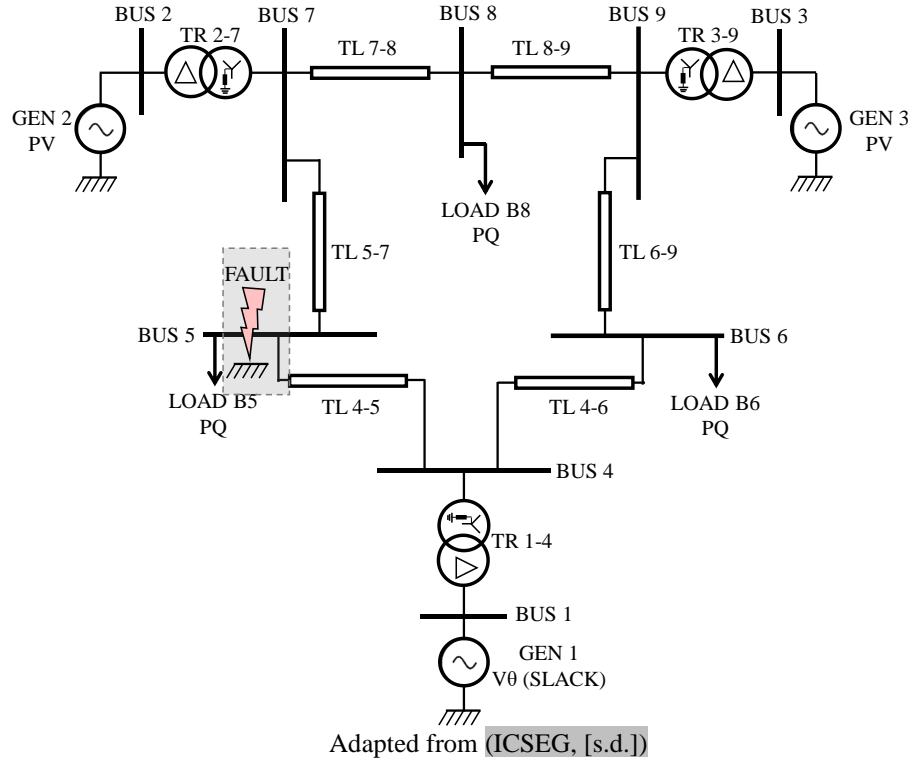
The 230[kV] transmission lines parameters are described in Tab. D.11 and Tab. D.12, All of them are modeled through equivalent PI lumped model. The transformers that connect the synchronous generators to the transmission lines are provided in Tab. D.13. The system has three loads connected to BUS8, BUS5 and BUS6 and their parameters describes in Tab. D.14.

Under normal operating conditions, the generators have the reference values:

- Bus 1: bus voltage 1.04[pu].

- Bus 2: bus voltage 1.025[pu], active power 163[MW].
- Bus 3: bus voltage 1.025[pu], active power 85[MW].

Fig. D.1: WSCC 9-bus system single line diagram.



Tab. D.7: Bus 1 synchronous generator parameters

Parameter	Symb	Value	Unity
Nominal line Voltage	V_{gn}	16.5	kV
Nominal power	S_n	247.5	MVA
Nominal frequency	f_n	60	Hz
Direct axis reactance	X_d	0.361	pu
Direct axis reactance (transitory)	X_d'	0.1504	pu
Direct axis reactance (sub transitory)	X_d''	0.099	pu
Quadrature axis reactance	X_q	0.2398	pu
Quadrature axis reactance (sub transitory)	X_q''	0.099	pu
Dispersion reactance	X_l	0.062	pu
Direct transitory time constant (transitory)	T_{do}'	8.96	s
Direct transitory time constant (sub transitory)	T_{do}''	0.01	s
Quadrature transitory time constant (sub transitory)	T_{qo}''	0.01	s
Poles pairs	N_p	20	
Inertia	J	9.55	kgm ²

Tab. D.8: Bus 2 synchronous generator parameters

Parameter	Symb	Value	Unity
Nominal line Voltage	V_{gn}	18	kV
Nominal power	S_n	192	MVA
Nominal frequency	f_n	60	Hz
Direct axis reactance	X_d	1.72	pu
Direct axis reactance (transitory)	X_d'	0.23	pu
Direct axis reactance (sub transitory)	X_d''	0.1728	pu
Quadrature axis reactance	X_q	1.65	pu
Quadrature axis reactance (transitory)	X_q'	0.23	pu
Quadrature axis reactance (sub transitory)	X_q''	0.1728	pu
Dispersion reactance	X_l	0.4224	pu
Direct transitory time constant (transitory)	T_{do}'	6	s
Direct transitory time constant (sub transitory)	T_{do}''	0.01	s
Quadrature transitory time constant (transitory)	T_{q0}''	0.53	s
Quadrature transitory time constant (sub transitory)	T_{q0}'''	0.001	s
Poles pair	N_p	1	
Inertia	J	3.33	kgm ²

Tab. D.9: Bus 3 synchronous generator parameters

Parameter	Symb.	Value	Unity
Nominal line Voltage	V_{gn}	13.8	kV
Nominal power	S_n	128	MVA
Nominal frequency	f_n	60	Hz
Direct axis reactance	X_d	1.68	pu
Direct axis reactance (transitory)	X_d'	0.2321	pu
Direct axis reactance (sub transitory)	X_d''	0.19	pu
Quadrature axis reactance	X_q	1.61	pu
Quadrature axis reactance (transitory)	X_q'	0.2321	pu
Quadrature axis reactance (sub transitory)	X_q''	0.19	pu
Dispersion reactance	X_l	0.314	pu
Direct transitory time constant (transitory)	T_{do}'	6	s
Direct transitory time constant (sub transitory)	T_{do}''	0.01	s
Quadrature transitory time constant (transitory)	T_{q0}''	0.53	s
Quadrature transitory time constant (sub transitory)	T_{q0}'''	0.001	s
Poles pair	N_p	1	
Inertia	J	2.35	kgm ²

Tab. D.10: DC1A excitation system (AVR) parameters

Parameter	Symb	Value	Unity
Voltage regulator gain	K_a	20.0	pu
Voltage regulator time constant	T_a	0.2	s
Maximum field voltage	V_{fmax}	-3.0	pu
Minimum field voltage	V_{fmin}	3.0	pu
Damping filter gain	k_f	0.063	pu
Damping filter time constant	T_f	0.35	s
Exciter gain	K_e	1.0	pu
Exciter time constant	T_e	0.314	s

Tab. D.11: 9-bus system transmission lines parameters

From bus	To bus	Length [km]	Resistance R [Ω/km]	Inductance L [mH/km]	Capacitance B [$\mu F/km$]
4	6	97.336	0.0924	1.33	0.00901
6	9	179.86	0.115	1.33	0.00998
7	8	76.176	0.059	1.33	0.00981
8	9	106.646	0.059	1.33	0.00983
5	7	170.338	0.0994	1.33	0.00901
4	5	89.93	0.0588	1.33	0.00981

Tab. D.12: 9-bus system transmission lines parameters (zero sequency)

From bus	To bus	Length [km]	Resistance R0 [Ω/km]	Inductance L0 [mH/km]	Capacitânce B0 [$\mu\text{F/km}$]
4	6	97.336	0.924	3.98	0.00541
6	9	179.86	1.15	3.98	0.00599
7	8	76.176	0.59	3.98	0.00589
8	9	106.646	0.59	3.98	0.0059
5	7	170.338	0.994	3.98	0.00541
4	5	89.93	0.588	3.98	0.00589

Tab. D.13: Generators' transformers parameters

From bus	To bus	Parameter	Symb.	Value	Unity
1	4	Hight voltage	V_H	230	kV
		Low voltage	V_X	16.5	kV
		Impedance	Z	5.76	%
7	2	Hight voltage	V_H	230	kV
		Low voltage	V_X	18	kV
		Impedance	Z	6.25	%
3	9	Hight voltage	V_H	230	kV
		Low voltage	V_X	13.8	kV
		Impedance	Z	5.86	%

Tab. D.14: 9-bus system loads parameters.

Bus	Active power [MW]	Reactive power [MVAr]
5	125	50
6	90	30
8	100	35